



The
University
Of
Sheffield.

The optical properties of photonic-crystal nanocavities containing plasmonic nanoparticles.

By:

Khalid Namiq Sediq

A thesis submitted in partial fulfilment of the requirements for the degree of
Doctor of Philosophy

The University of Sheffield
Faculty of Physics and Astronomy
Department of Physics

Submission Date

March 2016

*This thesis is dedicated to my parents for their
patience and my wife for her support*

Acknowledgements

I owe the deepest gratitude to my supervisor, Professor David Lidezy for guiding me through my thesis work. His patience, unconditional support, and generosity. Without his guidance and persistent help this dissertation would not have been possible.

In addition, I was fortunate enough to have had Dr. Kieran Deasy and Dr. Mohamed Murshidy whom helped me a lot in the experimental part of the dissertation. I get tremendously benefit from their constant advice and guidance.

I sincerely thank Dr. David Coles for his efforts in theoretical part of the dissertation. Also I wish to express my gratitude to Dr. Paul Fry in the Centre for Nanoscience and Technology and all EPMM group members in University of Sheffield for their help and support.

Finally, I wish to thank the ministry of higher education and scientific research in Kurdistan regional government (KRG) for their financial support and providing this opportunity to study in the University of Sheffield.

Contains

Chapter 1

Introduction and Thesis plan.....	1
1.1 Introduction	1
1.2 Thesis Plan	2
References	5

Chapter 2

Two dimensional photonic crystal theoretical background.....	8
2.1 Introduction	8
2.2 Maxwell's Equations in dielectric Medium	9
2.3 Photonic Band Structures	11
2.4 Important parameters affecting photonic crystal properties	16
2.5 Light confinement in a two dimensional photonic crystal.....	19
2.6 The Quality factor and dielectric losses	21
2.7 Light inside a cavity	24
2.8 Enhancement of spontaneous emission inside a cavity.....	25
2.8.1 Weak coupling	27
2.8.2 Strong coupling	27

2.9 Nanocavity applications	28
References	29
 Chapter 3	
Plasmonic nano structure: theoretical background	37
3.1 Introduction	37
3.2 Localized Surface Plasmon resonance (LSPR)	38
3.3 Metallic nanoparticles inside an electromagnetic	39
3.4 The optical properties of metals and metals nanoparticles.....	41
3.4.1 Free gas (Drude-Sommerfeld) model.....	41
3.4.2 Interband model	43
3.4.3 Mie theory	44
3.4.4 Dipole approximation (DA)	46
3.4.5 Mass-and-spring model	48
3.5 The effect of particle size.....	49
3.6 The effect of nanoparticle Shape	52
3.7 The effect of the surrounding medium	54
3.8 Some applications of Noble metal nanoparticles	55
References	57

Chapter 4

Experimental methods.....	64
4.1 Introduction	64
4.2 Cavity substrates	64
4.3 Electron Beam Lithography (EBL)	65
4.4 Sample preparation	67
4.5 E-beam resist	67
4.6 Proximity effect	68
4.7 Resist Development	70
4.8 Dry etching	70
4.9 Plasma system (ICP and RIE)	72
4.10 Photoluminescence (PL) Spectroscopy	77
4.11 Dark field spectroscopy	79
4.12 Printing gold nanoparticles on Silicon Nitride substrate.....	80
4.12.1 Optical printing method	80
4.12.2 Electron beam lithography (EBL)	82
4.13 Printing gold nanodisk inside L3 nanocavity using EBL method.....	85
4.14 Langmuir-Schaefer film deposition method (LS)	87
4.15 Monolayer formation	87
4.16 Atomic force microscope (AFM)	89
4.17 Finite Difference time domain (FDTD) modelling	90

References	91
-------------------------	-----------

Chapter 5

The Optical properties of L3 nanocavities optimizing the Q-factor of SiN based Structures	94
5.1 Introduction	94
5.2 Silicon Nitride Nanocavities	95
5.3 SiN Slab thickness	97
5.4 Design of an L3 Two Dimensional SiN Based Photonic Crystal Nanocavity	100
5.5 Nanocavity modes	101
5.6 Experimental results and discussion	103
5.6.1 Optical Prosperities of the SiN Based L3 Nanocavity ...	103
5.6.2 Fundamental mode position vs. air hole size and lattice constant	104
5.6.3 The effect of side holes of the fundamental cavity mode	109
5.6.4 Position of the Fundamental mode and Q factor vs. cavity side hole shift	109
5.7 Towards higher Q-factors	113
5.7.1 High Q-factor cavity Design	114
5.7.2 The Optical Properties of a Modified L3 Nanocavity ...	114
5.8 Summary and Conclusions	121

References	122
Chapter 6	
A chemical sensor based on a photonic-crystal L3 nanocavity defined into a silicon-nitride membrane	128
6.1 Introduction	128
6.2 Using Lumogen Red as a testbed	130
6.3 Experimental methods	132
6.4 L3 Cavity design	132
6.5 Effect of Lumogen Red monolayers on L3 nanocavity mode wavelength	133
6.6 Detection limit vs. number of monolayers	139
6.7 Using an L3 nanocavity as a Chemical Sensor	140
6.7.1 Porphyrins	140
6.7.2 Selection of Porphyrin materials as a chemical sensor to detect acid vapours	141
6.7.3 PP1 monolayer thickness vs. vapour exposure	144
6.8 Using an L3 nanocavity as a chemical sensor	147
6.8.1 Experimental results	147
6.8.2 Modelling cavity response	148
6.9 Conclusions	150
References	152

Chapter 7

Photonic-crystal L3 nanocavity containing Plasmonic nanoparticle using Laser-printing technique 158

7.1 Introduction158

7.2 The optical characteristics of a single gold nanosphere 160

7.3 Optical printing technique 161

7.4 Printing single gold nanosphere onto L3 nanocavity surface ... 162

7.4.1 Silicon Nitride as a platform for gold nanoparticle
Printing..... 163

7.4.2 Limitations to the laser printing technique 163

7.5 Experimental Results 164

7.6 Theoretical calculations 166

7.7 Conclusions..... 170

References 172

Chapter 8

The fabrication and characterization of gold nanoparticles and nanoparticle dimers and their incorporation into Photonic nanocavities 175

8.1 Introduction 176

8.2 Single gold nanodisk 176

8.3 Gold nanodisk dimers 181

8.4 Gold nanodisk dimers printed inside L3 nanocavity using EBL	188
8.5 Experimental methods	189
8.6 Results and discussions	191
8.7 conclusions	197
References	199
 Chapter 9	
Conclusions and Future work	204
9.1 Conclusions	204
9.2 Suggestions for future work	206
Publications	208

1.1 Introduction

In order gain understanding of light matter interactions, it is desirable to create an environment of intense confined electromagnetic (EM) field in a small volume. Two-dimensional (2D) photonic crystal (PC) technology can confine light to volumes that are smaller than a cubic wavelength by introducing a physical defect (such as one or more missing “holes”) known as a nanocavity into a photonic crystal [1]. The optical properties of such structures can be precisely controlled by nanoscale engineering design [2]. The majority of experimental work on nanocavities is based on semiconductor and dielectric materials that emit or absorb light at near infrared and telecommunication wavelengths, such as Silicon (Si) or Gallium Arsenide (GaAs) [3-6]. However, there is growing interest in structures that operate at other regions of the electromagnetic spectrum, including visible wavelengths. 2D-PC working at visible wavelengths are considered a promising tool to improve the performance of photonic devices, such as nano scale lasers [7], biosensors [8], chemical sensors [9], and single photon light sources [10]. Here, I focus on using silicon nitride (SiN) as a platform material for the fabrication of 2D PC nanocavities. SiN possess a number of important characteristics, such as transparency at visible wavelengths with a relatively high refractive index ($n = 2.1$), photoluminescence emission covering a wide spectra range, and a compatibility with silicon based technologies.

Noble metal nanoparticles (NPs) are plasmonic structures that can also create an intense confined electromagnetic field that is concentrated into a volume smaller than the diffraction limit [11]. Here, the electromagnetic field is produced by the oscillation of conduction electrons under the influence of an external electromagnetic field. The generated EM field is restricted to a region

near to the nanoparticle and is known as a localized surface plasmon resonance (LSPR) [12]. The LSPR peak position is tuneable and depends on number of parameters, such as NPs size, shape, chemical composition, environment optical properties and NP configuration [13]. Metal NPs have been widely explored for various applications in fields such as biology [14], medicine [15], diagnostics and therapy [16], EM field enhancement [17], photovoltaic enhancement [18] and surface enhancement Raman spectroscopy (SERS) [19].

In this thesis, I make a detailed study of the interaction between the optical fields in a nanocavity, and those of a plasmonic element placed within the cavity. This represents one of the first studies to explore methods and technologies to couple such types of excitation. The motivation here is to develop new ways to funnel energy from a photonic structure into a plasmonic structure, potentially providing a platform for new types of sensor devices.

1.2 Thesis plan

Chapter 2, discusses the fundamentals of two dimensional photonic crystals (2D PC) nanocavities. The parameters that effect the properties of a 2D PC are described. Light- matter interaction phenomena within a 2D PC nanocavity and some applications are introduced.

In Chapter 3, the plasmon resonance of noble metal nanoparticles (NPs) and their interaction with an applied electromagnetic field is introduced. A series of analytical solutions of the plasmon resonance of NPs are given, together with parameters that effect plasmon resonance. Some applications of plasmonic nanoparticles are also presented.

In Chapter 4, the fabrication process used to define a two-dimensional photonic crystals and the printing of gold NPs within the 2D PC nanocavity processes are presented. The experimental techniques and operational basis of the equipment used in sample characterisation are described.

Chapter 5, discusses the optical properties of silicon nitride (SiN) based L3 nanocavities. The optimisation of a 2D PC nanocavity design to achieve high Q-factor L3 SiN based nanocavities is introduced. It is shown that by modification of the holes around the L3 nanocavity, it is possible to produce a significant improvement in cavity Q-factor compared with an unmodified cavity.

In Chapter 6, the use of a silicon nitride (SiN) based L3 nanocavity PC as a chemical sensor is demonstrated. A thin functionalized polymer layer (a porphyrin based polymer known as PP1) is coated onto the surface of a SiN L3 nanocavity. It is shown that the PC nanocavity acts as an ultra- sensitive nano-optical device to detect changes in the optical properties of a film at the cavity surface, with a small change in cavity volume being detected as the polymer swells in response to exposure to an acidic vapour.

In Chapter 7, the optical properties of an L3 nanocavity are discussed after printing a single gold NP having a diameter of 150 nm onto the cavity surface. The printing processes is achieved by using laser-printing method with the optical properties of the structure being modelled using FDTD software. It is shown that electromagnetic field energy that initially stored in the nanocavity is dissipated through excitation of a localized surface plasmon.

In Chapter 8, electron beam lithography (EBL) is used to print metal nanodisks. The optical properties of single and dimer nanodisks are then discussed. Dimeric gold nanodisks are positioned with high accuracy inside an L3 nanocavity using

the same technique, and their effect on the optical properties of the cavity is studied. It is shown that the size and shape of the NPs influence their optical properties of the cavity. The effect of the separation distance between the printed dimer gold nanodisks on the nanocavity resonance is explored and again compared with an FDTD model.

In Chapter 9, results are summarized and future work is suggested.

References:

1. J. Joannopoulos, S. Johnson, J. Winn, and R. Meade, "Photonic Crystals: Molding the flow of Light", (2008), Princeton University Press, ISBN 978-0-691-12456-8, Princeton and Oxford.
2. Y. Akahane, T. Asano, B.S. Song, and S. Noda, "Fine-Tuned High-Q Photonic-Crystal Nanocavity," *Optics Express*, **13**, 4, 1202-1214 (2005).
3. Z. Wu, Z. Mi, P. Bhattacharya, T. Zhu, and J. Xu, "Enhanced spontaneous emission at 1.55 μm from colloidal PbSe quantum dots in a Si photonic crystal microcavity," *Applied Physics Letters*. **90**, 171105 (2007).
4. A. R. A. Chalcraft, S. Lam, D. O'Brien, T. F. Krauss, M. Sahin, D. Szymanski, D. Sanvitto, R. Oulton, M. S. Skolnick, A. M. Fox, D. M. Whittaker, H. Y. Liu, and M. Hopkinson, "Mode structure of the L3 photonic crystal cavity", *Applied Physics Letters*, **90**, 241117 (2007).
5. A. Badolato, K. Hennessy, M. Atature, J. Dreiser, E. Hu, P. M. Petroff, A. Imamoglu, "Deterministic Coupling of Single Quantum Dots to Single Nanocavity Modes", *Science*, **308**, 1158-1161 (2005).
6. T. Yoshie, J. Vuckovic, and A. Scherer, "High quality two-dimensional photonic crystal slab cavities", *Applied Physics Letters*, **79**, 26, (2001).
7. Bryan Ellis, "Ultralow-threshold electrically pumped quantum dot Photonic-crystal nanocavity laser" *Nature Photonics*, **5**, 297-300 (2011).
8. X. Fan, I. M. White, S. I. Shopova, H. Zhu, J. D. Suter, and Y. Sun, "Sensitive optical biosensors for unlabeled targets: a review," *Analytica Chimica Acta*, **620**, 8 – 26 (2008).
9. M. Loncar, A. Scherer, Y. Qiu, "Photonic crystal laser sources for chemical detection", *Applied Physics Letters*, **82**, 26, (2003).

10. M. D. Birowosuto , H. Sumikura , S. Matsuo , H. Taniyama , P. J. van Veldhoven, R. Notzel, M. Notomi, “Fast Purcell-enhanced single photon source in 1,550-nm telecom band from a resonant quantum dot-cavity coupling”, *Scientific Reports*, **2**, 321, (2012).
11. S. A. Maier, “*Plasmonics Fundamentals and Applications*”. Springer Science Business Media LLC (2007).
12. E. Petryayeva, U. J. Krull, “Localized surface plasmon resonance: Nanostructures, bioassays and biosensing A review”, *Analytica Chimica Acta* **706**, 8–24 (2011).
13. K. Lance Kelly, E. Coronado, L. Zhao, and G. C. Schatz, “The Optical Properties of Metal Nanoparticles: The Influence of Size, Shape, and Dielectric Environment”, *Journal of Physical Chemistry B*, **107**, 668-677 (2003).
14. J. Chen, F. Saeki, B. J. Wiley, H. Cang, M. J. Cobb, Z. Y. Li, L. Au, H. Zhang, M. B. Kimmey, X. Li and Y. Xia, “Gold Nanocages: Bioconjugation and Their Potential Use as Optical Imaging Contrast Agents”, *Nano Letters*, **5**, 473-477 (2005).
15. P. Ghosh, G. Han, M. De, C. K. Kim, V. M. Rotello, “Gold nanoparticles in delivery applications”, *Advanced Drug Delivery Reviews*, **60**, 1307–1315 (2008).
16. X. Huang, M. A. El-Sayed, “Gold nanoparticles: Optical properties and implementations in cancer diagnosis”, *Journal of Advanced Research*, **1**, 13–28 (2010).

17. T. Okamoto, I. Yamaguchi, T. Kobayashi, “Local plasmon sensor with gold colloid monolayers deposited upon glass substrates”, *Optics Letters*, **25**, 6, 372–374 (2000).
18. C. Clavero, “Plasmon-induced hot-electron generation at nanoparticle/metal-oxide interfaces for photovoltaic and photocatalytic devices”, *Nature Photonics* **8**, 95–103 (2014).
19. A. Swarnapali, D. S. Indrasekara , B. J. Paladini , D. J. Naczynski ,V. Starovoytov, P.V. Moghe , and L. Fabris, “Dimeric Gold Nanoparticle Assemblies as Tags for SERS Based Cancer Detection”, *Advanced Healthcare Materials*, **2**, 10, 1370-1376 (2013).

Chapter Two

Two dimensional photonic crystal theoretical background

2.1 Introduction

A Photonic Crystal (PC) is an optical nanostructure in which the material refractive index is varied periodically on a length scale compared to the wavelength of light. The name “Photonic Crystal” is derived from “electronic crystal”, in which the term “crystal” signifies periodic arrangement, with “photonic” signifying the effect of structure design on photon propagation properties.

When an electromagnetic wave (EM) passes through a two dimensional Photonic Crystal (2D PC) structure it undergoes scattering at the interface between the different dielectric regions. Such scattering can be coherent in certain directions and frequencies. Due to the alternation of the dielectric constant, light at certain frequencies travelling in certain direction will not be able to propagate through the PC structure. The range of frequencies that are unable to propagate is known as a photonic band gap (PBG). In 3D PC design it is possible to realize a region of energies where light cannot propagate regardless of their direction and polarization. This band gap is known as complete photonic band gap (PBG).

The forbidden energies can be strongly localized and highly confined by introducing a physical defect such as a “cavity” inside a PC structure [1]. The cavity then permits a perfect control of light propagation and radiation, which can be used in many applications such as controlling the spontaneous emission of emitter located inside a PC cavity [2], and to better study light-matter interactions [3].

2.2 Maxwell's Equations in dielectric Medium

To understand the behaviour of EM waves that propagate through a dielectric medium, we start with Maxwell's equations, which are given by [4]:

$$\begin{aligned}\nabla \cdot \vec{B} &= 0 \\ \nabla \cdot \vec{D} &= \rho \\ \nabla \times \vec{E} + \frac{\partial \vec{B}}{\partial t} &= 0 \quad \dots\dots\dots 2.1 \\ \nabla \times \vec{H} - \frac{\partial \vec{D}}{\partial t} &= J\end{aligned}$$

Here, \vec{E} and \vec{B} are the electric and magnetic fields, \vec{D} is the electric field displacement, \vec{H} is the magnetic induction field, and J and ρ are the electrical current and charge densities respectively.

Let us assume that EM waves propagate through a dielectric medium (i.e. no free charges and current densities $\rho = 0$, $J = 0$) that is non-dispersive or isotropic (ϵ , μ are not function of frequency and not depend on the direction of propagation respectively) and transparent (i.e. $\epsilon(\mathbf{r})$ is positive and real). Therefore, both electric field displacement and magnetic field can be written as:

$$\begin{aligned}\vec{D}(\vec{r}) &= \epsilon_0 \epsilon(\vec{r}) \vec{E}(\vec{r}) \quad \dots\dots\dots 2.2 \\ \vec{B}(\vec{r}) &= \mu_0 \mu(\vec{r}) \vec{H}(\vec{r})\end{aligned}$$

Here: ϵ and μ are the permittivity and permeability respectively. The refractive index n can be expressed as $= \sqrt{\epsilon\mu}$, but for most dielectric media where $\mu \approx \mathbf{1}$ we can write $\mathbf{n} = \sqrt{\epsilon}$. By substituting eq. 2.2 in to equations 2.1 we obtain:

$$\begin{aligned}\nabla \cdot \vec{H}(\vec{r}, t) &= 0 \\ \nabla \times \vec{E}(\vec{r}, t) + \mu_o \frac{\partial \vec{H}(\vec{r}, t)}{\partial t} &= 0 \\ \nabla \times \vec{H}(\vec{r}, t) + \epsilon_o \epsilon(\vec{r}) \frac{\partial \vec{E}(\vec{r}, t)}{\partial t} &= 0 \quad \dots\dots\dots 2.3 \\ \nabla \cdot [\epsilon(\vec{r}) \vec{E}(\vec{r}, t)] &= 0\end{aligned}$$

Here, both \vec{E} and \vec{H} are time and space dependent functions, and can be written using as:

$$\begin{aligned}\vec{H}(\vec{r}, t) &= \vec{H}(\vec{r}) e^{-i\omega t} \\ \vec{E}(\vec{r}, t) &= \vec{E}(\vec{r}) e^{-i\omega t} \quad \dots\dots\dots 2.4\end{aligned}$$

Here, ω is the angular frequency of the propagating wave.

The divergence in equations 2.3 is can be set to zero, and indicates that there are no point sources of electromagnetic (light) inside the medium. By substituting equations 2.4 in to equations 2.3 the curl equations of $E(r)$ and $H(r)$ become:

$$\begin{aligned}\nabla \times \vec{E}(\vec{r}) - i\omega\mu_o \vec{H}(\vec{r}) &= 0 \\ \nabla \times \vec{H}(\vec{r}) + i\omega\epsilon_o \epsilon(\vec{r}) \vec{E}(\vec{r}) &= 0 \quad \dots\dots\dots 2.5\end{aligned}$$

Rearranging equation 2.5 and substituting $c = 1/\sqrt{\epsilon\mu_o}$ we get:

$$\nabla \times \left(\frac{1}{\epsilon(\vec{r})} \nabla \times \vec{H}(\vec{r}) \right) = \left(\frac{\omega}{c} \right)^2 \vec{H}(\vec{r}) \quad \dots\dots\dots 2.6$$

Equation (2.6) represents the master equation of electromagnetic wave propagation through a dielectric medium. Equation (2.6) is an eigen equation, whose eigenvalues are $(\omega/c)^2$ with the Eigen operator being $\nabla \times \left(\frac{1}{\epsilon(r)} \right) \nabla \times$. Thus equation (2.6) can be written as:

$$\Theta H(r) = \left(\frac{\omega}{c} \right)^2 H(r) \quad \dots\dots\dots 2.7$$

Here, Θ is a linear Hermitian operator and has the same form in all directions.

2.3 Photonic Band Structure

Photons that propagate through a homogenous and isotropic dielectric medium are represented by the dispersion relation ($\omega = ck/n$), where, ω is photon angular frequency, k is the photon wave vector ($k=2\pi/\lambda_0$), c is the velocity of light in vacuum and n is the refractive index of the dielectric material. The dispersion relation shows that the angular frequency (or photon energy) depends linearly on the ratio between the wave vector and the material refractive index regardless of direction inside the medium. In a medium in which refractive index varies with the direction, the dispersion relation is different in each direction.

In a photonic crystal, there is a periodic modulation of the dielectric constant $\epsilon(r)$ in one, two or three dimensions as shown in figure 2.1, thus the dielectric ($\epsilon(r)$) function becomes a periodic function for multiples of a fixed step length called the lattice constant **a**. Photons that propagate in such periodic structure are given by.

$$H(\mathbf{r}) = e^{i\mathbf{k}_r \cdot \mathbf{r}} u_{\mathbf{k}}(\mathbf{r}) \quad \dots\dots\dots 2.8$$

Here, $H(\mathbf{r})$ is the wave function, $u_{\mathbf{r}}(\mathbf{r})$ is periodic envelop function of the real space lattice. Equation 2.8 is known as a Bloch function [5]. In Bloch theory, the wave vector \mathbf{k}_r can be translated to the first Brillouin zone (BZ) in reciprocal space.

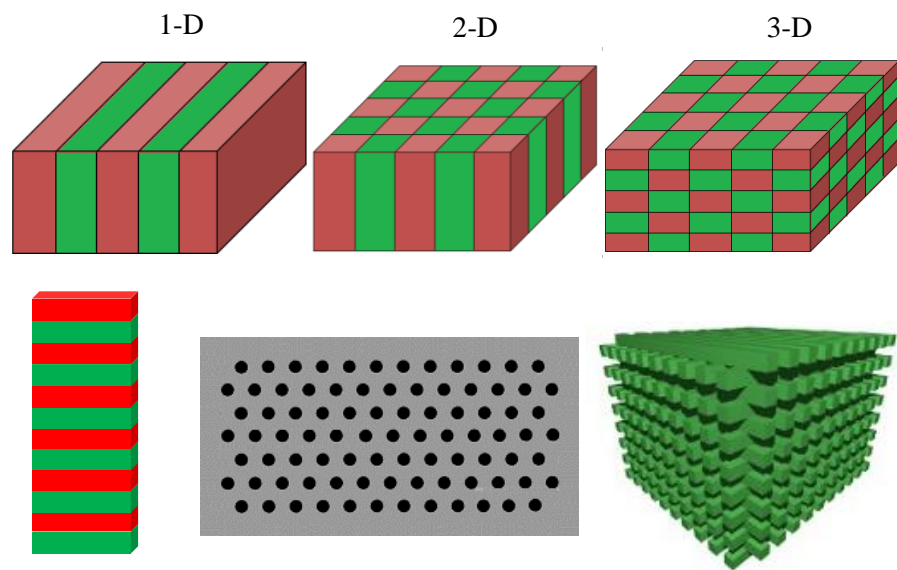


Figure 2.1: one, two and three dimensional photonic crystals. Different colours represented materials with different dielectric constant.

In a 2D PC having a hexagonal array of holes, there are three high symmetry points in the BZ defined as Γ , K and M which are known as the irreducible BZ as shown in figure 2.2. Therefore, the dispersion relation for photons propagating through a 2D PC is dependent on this direction within the BZ.

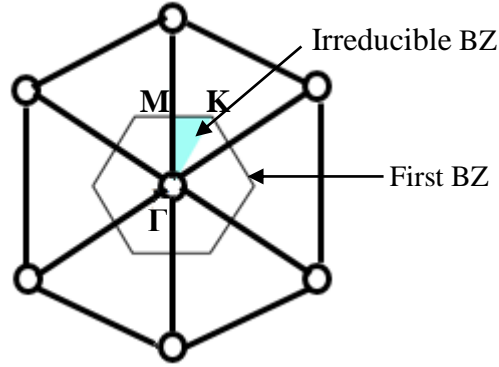


Figure 2.2: A hexagonal lattice and irreducible Brillouin zone (blue).

By substituting eq.2.8 into the master equation (eq. 2.6) we obtain:

$$(ik + \nabla) \times \left[\frac{1}{\epsilon(r)} (ik + \nabla) \times u_k(r) \right] = \left[\frac{\omega(k)}{c} \right]^2 u_k(r) \quad \dots \quad 2.9$$

Here, $(\omega(k)/c)^2$ is an eigenvalue of eigenequation 2.9. The result of solving equation 2.9 for K_r inside the first Brillouin zone in both the Γ - M and Γ - K directions is a discrete set of eigenvalues (energies). By plotting the dispersion relation in a periodic structure we can explain the emergence of a **photonic band gap** (PBG) structure.

The effect of a PBG was first proposed by Yablonovitch and John (1987) separately [6, 7]. Ho et al (1990) reported that a three dimensional (3D) diamond lattice is a suitable candidate to create a photonic band gap [8], while Yablonovitch experimentally fabricated a 3D PC working at microwave frequencies [9].

Usually, 2D PCs are defined using a triangle or a square array arrangement of air holes. Although both shapes have their own applications, a triangular 2D PC has a wider photonic band gap (PBG) than does a square one. The reason behind this is attributed to the greater symmetry and smooth Brillouin zone of the

triangular lattice [10-15]. Furthermore, a wide photonic band gap provides a stronger light confinement [14, 15].

Generally, the optical modes in 2D PC structure are classified in to two sets; transverse electric field TE-like modes and transverse magnetic field TM-like modes [5]. For instance, in photonic crystal slabs the transverse magnetic field TM-like modes, the electric field vector components (E_x and E_y) are confined in plane direction, and corresponding (H_z) field parallel to the z-axis as shown in figure 2.3.

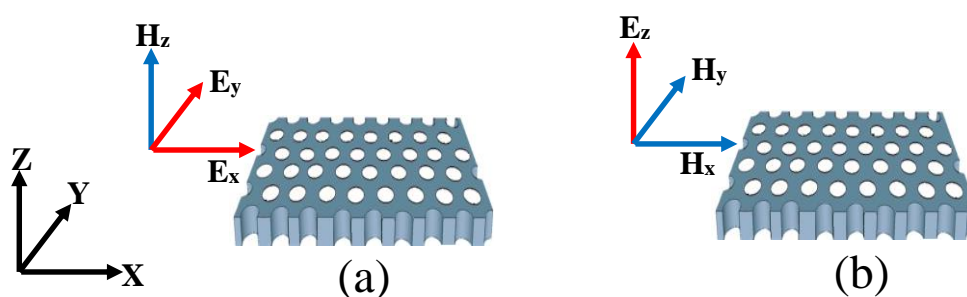


Figure 2.3: shows the orientation of electromagnetic field vector components for in plane propagation in triangular lattice of air holes. (a) TM polarization (b) TE polarization

To illustrate the optical properties of a PC the optical band gap position of a two-dimension photonic crystal structure was calculated using Maxwell's equations using a plane wave basis (MPB) method [16]. The parameters used in the calculation were a lattice constant $a = 260$ nm, hole radius $r = 0.288a$, slab thickness $0.77a$ and a refractive index of the slab $n = 2.1$ (SiN). The electric (TE) field is calculated in the $x, y, z = 0$ plane. The results of this calculation are shown in figure 2.4, with a photonic band gap (PBG) predicted for TE polarized light between 607.3 nm and 678.3 nm.

The photonic band gap of a PC design is most usually characterized by its position and size. The PBG position is determined by the middle of photonic band

gap wavelength. The PBG size is usually determined by the gap to mid-gap ratio ($\Delta\lambda/\lambda$, $\Delta E/E$ or $\Delta\omega/\omega$) and is expressed in the form of a percentage (e.g., a 20% gap refers to $\Delta\lambda/\lambda = 0.2$). The ($\Delta\lambda/\lambda$) ratio is independent on the size of the PC [5].

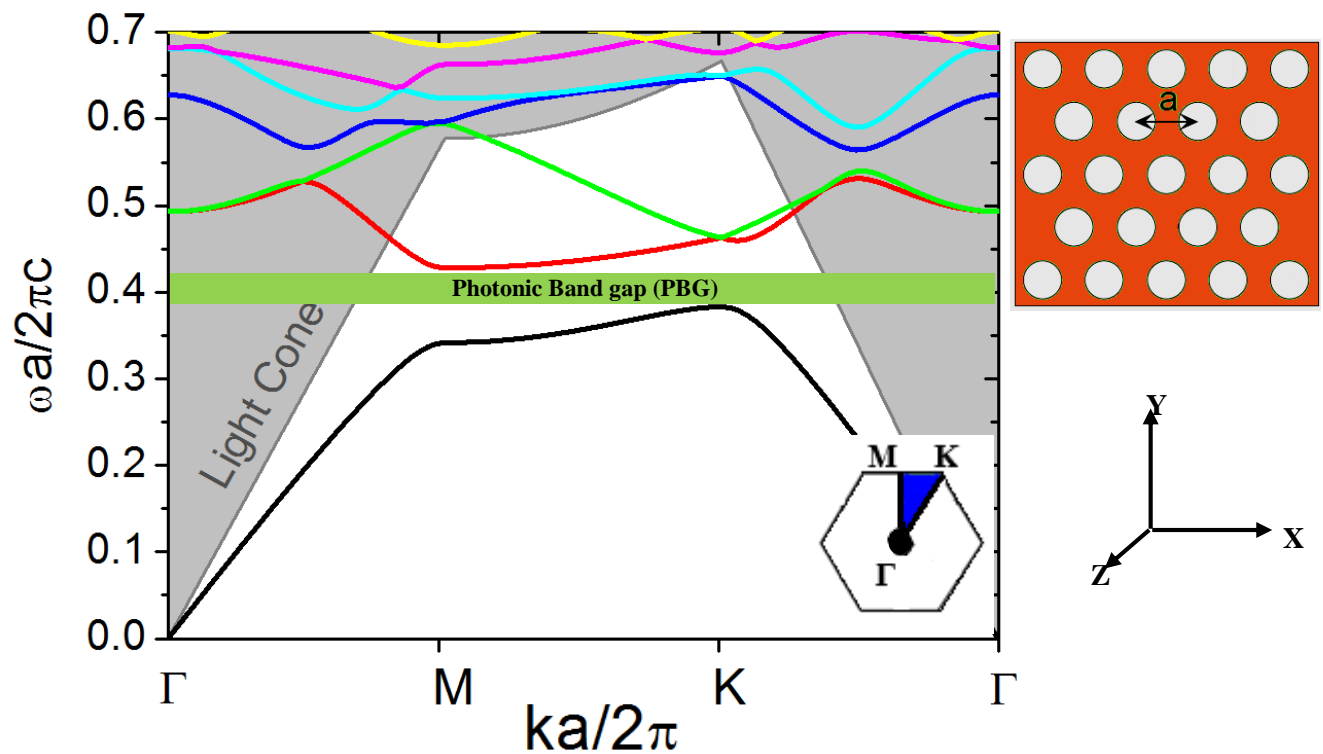


Figure 2.4: (a) Band diagrams for TE polarized light and photonic band gap for hexagonal lattices of air holes ($r = 0.288a$) in dielectric SiN slab with $n=2.1$ and centre- centre periodicity (lattice constant) $a= 260$ nm. The frequencies are plotted around the boundary of the irreducible Brillouin zone (inset scheme). (b) Hexagonal lattice of 2D PC diagram showing lattice constant.

2.4 Important parameters affecting photonic crystal properties

There are a number of important features and parameters that must be taken into account when designing a photonic crystal with a specific band behavior. Figure 2.5 shows the main parameters that affect photonic crystal properties.

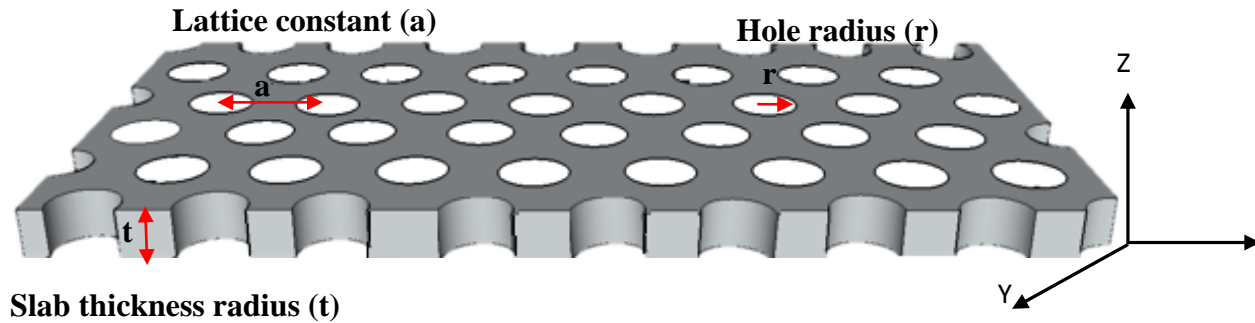


Figure 2. 5: sketch of hexagonal 2D PC structure L3 nanocavity showing the parameters effect on PC properties.

- **Symmetry**, or lattice shape. There are two main arrangements of 2D PC; square and triangular.
- **Photonic crystal dimensionality**. Refractive index periodicity determines the dimensionality of the photonic crystal, with either one 1D, two 2D, or three 3D dimensional lattice possible.
- **The slab thickness**. The optimum thickness of SiN based 2D photonic crystal membrane is around $0.7a$, where (**a**) is the lattice constant [17]. However, the slab thickness effects the mid-gap position of PBG [18, 19]. It has been observed that the frequency of the mid-gap increase with decreasing the slab thickness.
- **Filling fraction (FF)**: also known as packing fraction in solid state physics [20]. This is defined as the fraction of the scattering object compared to the total unit cell volume [21]. In most cases the hole size in

a PC is proportional to the FF. The effect of the hole size scaled by r/a ratio was studied using plane wave basis (MPB) method. The results of such a calculation are shown in figure 2.6. It is found that by increasing the hole radius from $0.269a$ to $0.288a$ both the mid-gap position and the gap size also increase.

- **Relative Refractive index** (n) is the ratio between the high and low refractive index materials of the periodic structure. The width of the band-gap increases and shifts toward lower energy as the refractive index of the slab increases [22]. In addition, PC modes are very sensitive to any alternation of the environmental refractive index. This approach allows a PC to be used as a refractive index sensor [23].
- **Lattice constant** is defined as the distance between two adjacent air holes in 2D PC structure. Both hole size and the lattice constant are the most flexible parameters that can be used to tune the PBG energy. However, for a PC structure having a constant hole size, the peak position of the cavity mode undergoes a red shift as the lattice constant increases. [24].

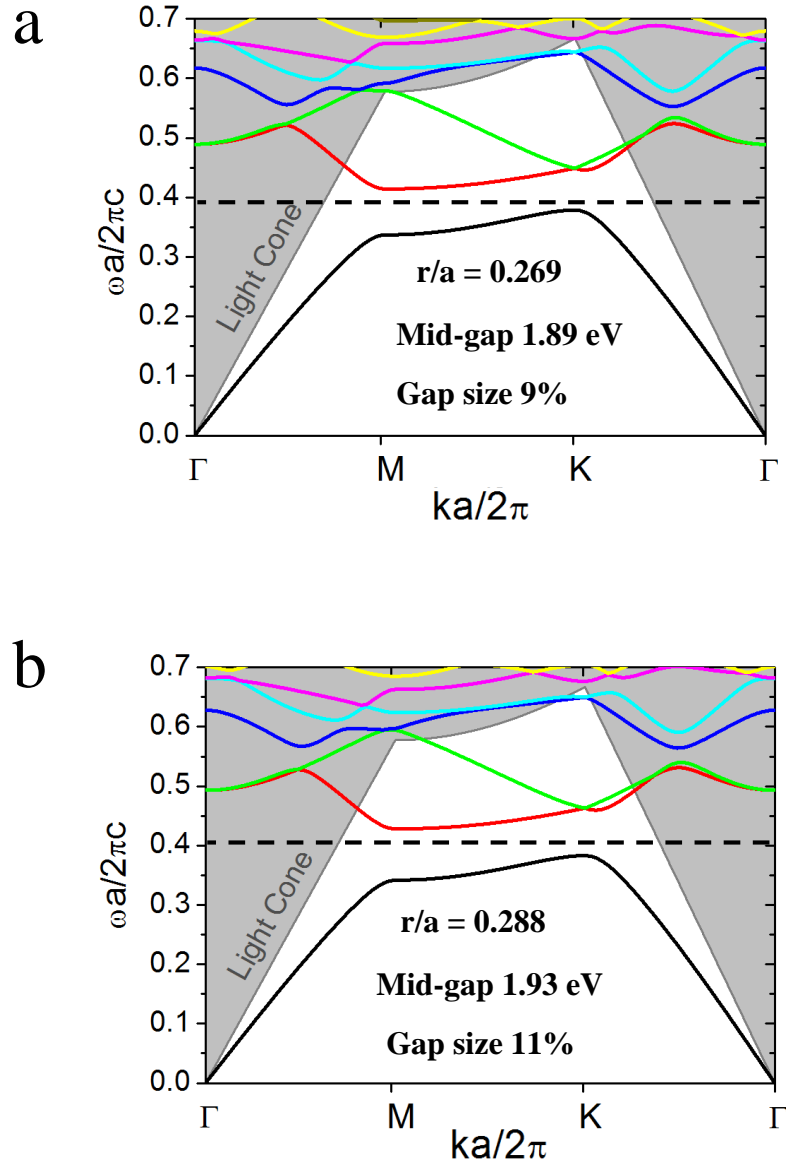


Figure 2. 6: A comparison of the position and the size of the photonic band gap of TE polarized light and for hexagonal lattices SiN ($n=2.1$) based 2D PC having lattice constant $a = 260$ nm, slab thickness $0.77a$ and hole size (a) $0.269a$ and (b) $0.288a$ respectively.

2.5 Light confinement in a two dimensional photonic crystal (2D PC)

The confinement of light in an ultra-small volume of the order of $(\lambda/n)^3$ can be achieved by introducing a physical defect into a periodic structure. This defect then acts as a “trap” for light within the optical band-gap.

As a consequence of the size of an optical nanocavity, light is confined in a small volume that is defined by spatially integrating the total electric field energy and normalizing it by the maximum electric field energy density [25].

$$V = \frac{\iiint \epsilon(\mathbf{r})|\mathbf{E}(\mathbf{r})|^2 dV}{\max[\epsilon(\mathbf{r})|\mathbf{E}(\mathbf{r})|^2]} \dots\dots\dots 2.10$$

Here, $\mathbf{E}(\mathbf{r})$ is the electric field strength and $\epsilon(\mathbf{r})$ is the dielectric constant.

The criterion for effective light confinement in a small volume is the ratio between the cavity quality factor Q and the spatial mode volume (Q/V). The Q factor of a cavity is usually defined as the ratio between the stored radiation energy inside the cavity and the output radiation energy per cycle [26], and can be expressed in terms of line width of an optical mode at energy E (linewidth ΔE)

$$Q = \frac{E}{\Delta E} = \frac{\omega_o}{\Delta\omega} \dots\dots\dots 2.11$$

Equation 2.11 can be re-written as:

$$Q = \frac{\lambda_o}{\Delta\lambda} \dots\dots\dots 2.12$$

A high (Q/V) ratio leads to an enhanced spontaneous emission rate through the Purcell effect [27].

In a two dimensioned photonic crystal there are two mechanisms by which light is confined as shown in figure 2.7. The first is in-plane confinement in the (x, y) direction. This confinement mechanism occurs as a result of the periodicity of

dielectric layers around the cavity that acts as a distributed Bragg Reflector (DBR) and increases the strength of light reflected toward the cavity. The second is an out of plane or normal direction confinement mechanism. This mechanism occurs as a result of total internal reflection (TIR) of the confined light waves inside the cavity that propagate with a different angles of incidence. The waves that propagate beyond the critical angle of the PC slab material undergo total internal reflection (TIR) and are trapped inside the cavity. Therefore, light confinement in the out of plane direction is limited by specific angle of incidence. The total waveguide quality factor Q_w can be divided in to two parts, in plane Q_{in} (parallel to x, y direction) and out of plane Q_{out} in the z direction, as summarized by equation.

$$\frac{1}{Q_w} = \frac{1}{Q_{in}} + \frac{1}{Q_{out}}$$

By introducing a sufficient numbers of holes around the nanocavity, Q_{in} can be increased significantly [28], while the use of relatively thick waveguide slab can offer high vertical confinement as suggested by Pugh et al [29].

Optical nanocavities have great scientific and engineering interest, such as systems to generate large Purcell enhancements, [30, 31], as high-resolution sensors [32], as threshold less nano lasers [33], ultra-small filters [34], quantum information processing device [35], and devices to control light/matter interactions at the nano-scale [36].

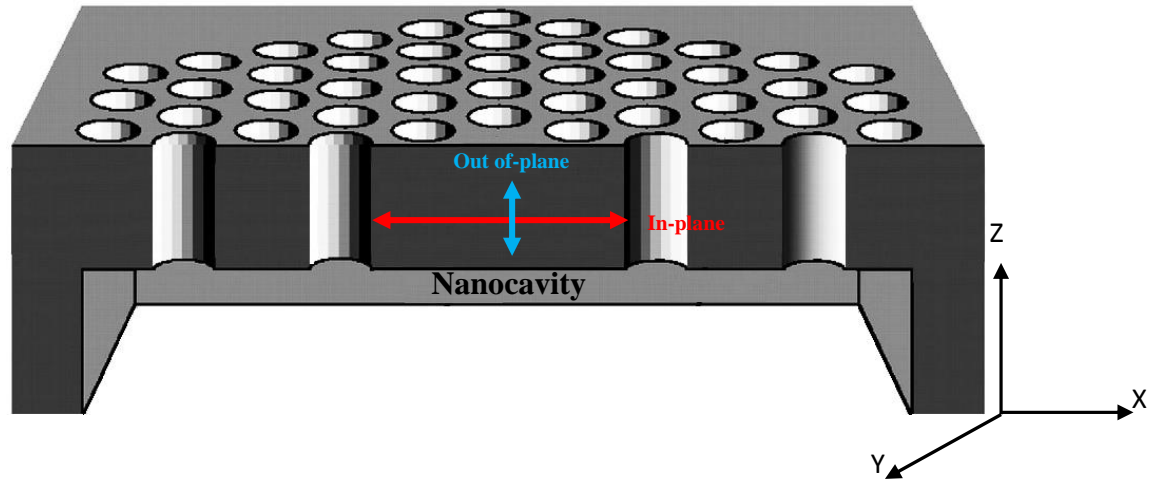


Figure 2.7: sketch of 2D PC nanocavity shows light confinement directions, in-plane (red) and out of plane (blue).

2.6 The quality factor and dielectric losses.

Confining light in a volume having a fraction of wavelength volume is not straightforward, and presents a number of difficulties. One of the most important difficulties is loss due to the total internal reflection. Indeed, light that is confined inside a cavity is composed of many plane waves that are incident with different angles at the air-slab interface. Light rays that do not fulfill the TIR condition will escape from the slab surface. Such modes are known as the leakage field or light cone. These leaky modes reduce the magnitude of the confined field within the cavity. In order to store energy in the cavity efficiently, it is necessary to increase the Q- factor. To achieve a high cavity quality factor, the leakage fields can be reduced by modifying the periodicity of the holes around the cavity. This can be achieved through a slight displacement of the holes around the cavity, leading to significant suppression of the leakage fields [26].

Experimentally, Q-factor determines the damping rate of an oscillating system, i.e. a high Q-factor is an indication of low damping rate of the system and vice versa [37]. Therefore, the cavity quality factor is dependent on the lifetime of the cavity mode. Mathematically, Q-factor can be expressed as the number of optical periods inside a cavity multiplied by 2π before the density of the stored energy drops by a factor of e^{-1} compared to its original value.

Assuming an electric field is confined inside a cavity, the density of the stored energy will thus decay by factor of e^{-Kt} where K is loss rate of the cavity can be expressed as

$$U(t) = U_0 e^{-Kt} \quad \dots\dots\dots 2.14$$

Here, U_0 is initial density of stored energy. From the definition of Q factor:

$$Q = \frac{\text{energy stored}}{\text{energy dissipated per cycle}} = -\omega_0 \frac{U(t)}{\frac{dU(t)}{dt}} = \frac{\omega_0}{K} \quad \dots\dots 2.15$$

Here, ω_0 is the angular frequency of light at the nanocavity optical mode [26, 37]. From equation 2.15 it can be seen that Q factor of a cavity is inversely proportional to optical loss in the cavity. In addition, the identity between equation 2.11 and 2.15 shows that the output cavity mode profile (see figure 2.8) depends on the photon lifetime inside a cavity and thus the frequency broadening of the cavity mode can be expressed as:

$$K = \Delta\omega = (FWHM) \quad \dots\dots\dots 2.16$$

Where FWHM is full width half maximum.

It is known that optical losses inside a nanocavity can result from absorption or scattering or experimental imperfections introduced during the fabrication process that reducing the total Q factor of a nanocavity. Therefore, the total Q factor for a nanocavity can be represented by the sum of the waveguide and dielectric material Q factors and expressed as [38]:

$$\frac{1}{Q_{total}} = \frac{1}{Q_w} + \frac{1}{Q_d} \quad \dots\dots\dots 2.17$$

In order to increase the total nanocavity Q factor it is important to use materials having low optical losses, as well as employing techniques to suppress leaky modes.

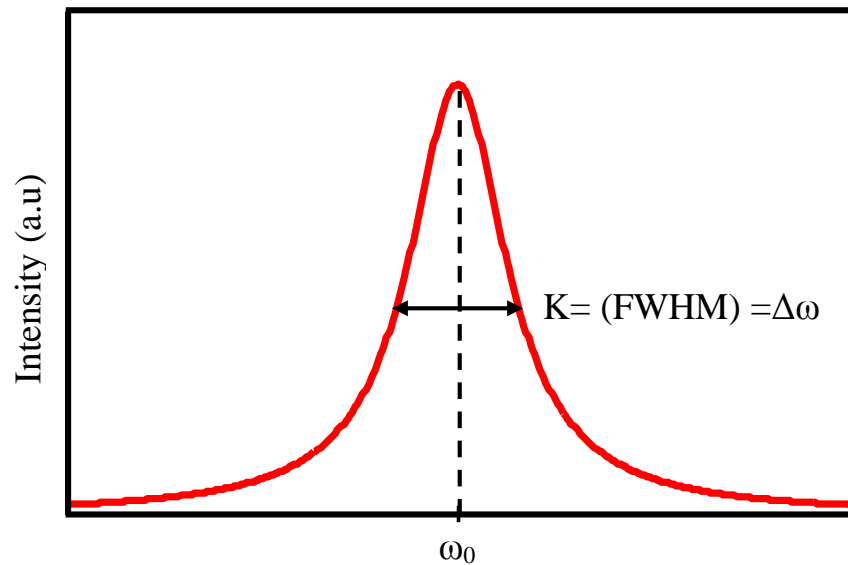


Figure 2.8: spectral line of output mode shows the frequency distribution vs. photon energy and the (FWHM)

2.7 Light inside a cavity

In the early years of last century, Albert Einstein proposed that light-matter interactions could be divided into three processes: spontaneous emission, stimulated emission, and photon-absorption. Each process is described by a probability [39]. Assuming a two-level system containing states with a density (number per unit volume) N_1 and N_2 , the probability by which transitions between states can be expressed as:

$$\text{spontaneous emission } W_{21} = A_{21}N_2$$

$$\text{stimulated emission } W_{21} = B_{21}\rho_\omega N_2 \quad \dots\dots\dots 2.18$$

$$\text{stimulated absorption } W_{12} = B_{12}\rho_\omega N_1$$

Here, A and B are Einstein's coefficients, and ρ_ω is the energy density per unit angular frequency interval in the region containing N_2 states in the upper level and N_1 states in the lower level.

Equation 2.18 indicates that spontaneous emission occurs when an electron in an excited state returns back to the initial or ground state, accompanied by the emission of a photon.

However, it was observed that the rate of spontaneous emission of an excited state is dependent on the electromagnetic environment. Therefore, great interest has been given to structures in which electromagnetic environments can be controlled such as micro-cavities and optical resonators [40]. By careful design, cavities can be created that can trap light for significant time periods and have a controllable optical density of states, making it possible to modify light-matter interactions.

2.8 Enhancement of spontaneous emission inside a cavity.

We now consider the spontaneous emission rate of a two level atomic system placed in a confined electromagnetic field. Atom field interaction leads to coupling between states of 1 and 2, and their population is said to be “dressed” by the electromagnetic field with angular frequency which is known as the Rabi frequency. The Rabi frequency can be expressed in term of electric field strength \vec{E}_0 and dipole moment $\vec{\mu}$ by the following expression [41]:

$$g = \frac{\vec{\mu} \cdot \vec{E}_0}{\hbar} \quad \dots\dots\dots 2.19$$

However, the strength of coupling g between an emitter located inside a confined cavity electromagnetic field is determined by two dissipative processes. The first is the decay rate of light inside the cavity that is represented by K , and as discussed earlier, it is related to the cavity Q factor and the cavity resonance frequency using

$$K = \frac{\omega_o}{Q} \quad \dots\dots\dots 2.20$$

The second process is the spontaneous emission Γ rate of an atom in which a photon is emitted out of the cavity mode resonance. We can also express the coupling strength as a function of the cavity mode volume V [42]:

$$g = \frac{1}{n} \left(\frac{\hbar\omega}{2\varepsilon_o V} \right)^{1/2} \quad \dots\dots\dots 2.21$$

Here, n is the index of refraction of the medium inside the cavity.

In the case of an atom coupling to a number of modes inside cavity, the integrated probability of a transition to each single cavity mode can be calculated by

applying Fermi's Golden Rule which states that the spontaneous emission rate Γ is proportional to the optical density of states, $\rho(\omega)$, using [43]:

$$\Gamma_{i \rightarrow f} = \frac{2\pi}{\hbar} \langle f | \vec{E} \cdot \vec{\mu} | i \rangle^2 \quad \dots\dots 2.22$$

Fermi's Golden Rule describes the enhancement or suppression of optical transitions. Purcell predicted that the spontaneous emission rate of a cavity could be enhanced by placing an atomic transition at resonance in a cavity [27]. The ratio between cavity spontaneous emission rate and bulk spontaneous emission rate (Γ_{free}) can be used to calculate the enhancement of EM field (Γ_{cav}) inside a nanocavity as expressed using [44, 45]:

$$\Gamma = \frac{\Gamma_{cav}}{\Gamma_{free}} = \frac{3}{4\pi^2} \left(\frac{\lambda}{n}\right)^3 \frac{Q}{V} \left(\frac{\vec{E}_r \cdot \vec{\mu}}{|\vec{E}_{max}| \cdot |\vec{\mu}|} \right)^2 \times \frac{\Delta\lambda_{cav}^2}{4(\lambda - \lambda_{cav})^2 + \Delta\lambda_{cav}^2} \quad \dots 2.23$$

It is known that the photonic bandgap in a photonic crystal (where the electromagnetic density of states is zero) can be used to suppress spontaneous emission [6]. In equation 2.23 at the point of maximum spatial and frequency alignment between the two-level system and the cavity mode, (i.e. the atomic transition frequency equal to the cavity resonance i.e. $(\lambda = \lambda_{cav})$, when the position of the emitter is located at the maximum electric field) a significant enhancement of electromagnetic field inside the cavity is achieved and is expressed by the Purcell factor [46]:

$$F = \frac{3}{4\pi^2} \left(\frac{\lambda}{n}\right)^3 \frac{Q}{V} \quad \dots\dots\dots 2.24$$

It is clear from equation 2.24 that electromagnetic field enhancement is dependent on the Q/V ratio of the nanocavity. A PC nanocavity can confine light in a very small volume, and it is possible to align the emitter dipole moment and

vacuum field to achieve good coupling. Cavities that have a high Purcell factor are desirable for many applications such as low threshold nano-cavity lasers [47] and single-photon sources [48]. Cavity spontaneous emission rate has been enhanced by 75 times using GaAs based an H1 cavity [49]. Recently, spontaneous emission rates have been enhanced by 25 times using a GaP based S1 cavity having a Q-factor of 3800 contain a diamond single NV centers located inside cavity [50]. High Purcell enhancement (around 90) was demonstrated using a H1 SiN based nanocavity [51]. High Q/V characteristics make a PC with nanocavity an attractive system to study light-matter interactions [6] in both the strong and weak coupling regimes.

2.8.1 Weak coupling

As discussed in section 2.8, the strength of atom-cavity coupling depends on photon dissipation rate for the photon (K) and the emitter decay rate (Γ). When the strength of coupling is less than K and Γ i.e., $g \ll (K, \Gamma)$ the system said to be weakly coupled. This is irreversible process, in which the atomic excited states decay rapidly and the emitted photon is coupled into the continuum and escapes from the cavity. In the weak coupling regime, spontaneous emission can be suppressed or enhanced on resonance by the Purcell effect or by increasing the Q/V value [52].

2.8.2 Strong coupling

In this regime, the strength of coupling is greater than the dissipation (K) and the emitter decay rate (Γ), i.e., $g \gg (K, \Gamma)$. This means that there is a high probability that the emitted photon from excited atom is again reabsorbed by the atom, rather than decaying incoherently. Thus, a reversible exchange of energy between an

excited atom and the cavity is predicted until the correlation between them eventually vanishes. A cavity with large Q/V ratio (where $g \propto \frac{Q}{\sqrt{V}}$) is important to satisfy the strong coupling condition. The emitted spectrum of the coupled system shows two resonance peaks that are split by Rabi frequency. A strong coupling between quantum dots QDs and L3 type cavity mode at room temperature was demonstrated by Yoshie et. al [53]. Also photoluminescence (PL) emission was also used to evidence a QD-cavity anti crossing as the temperature was tuned through the L3 cavity mode [54]. Mujumdar et al showed that the two-level system of a series of QDs can be dressed by a strong pump laser [55].

2.9 Nanocavity applications

In communication applications, a fiber optics based PC was used as an efficient tool to transfer light with low losses for long distance and even through sharp bends [56, 57]. The high speed, compactness and low power consuming properties of PCs nanocavity also make them a good candidate for applications such as optical integrated circuits [58].

Due to the high Q/V ratio property of a PC nanocavity, the high spontaneous emission enhancement rate [59, 60] makes them a good platform for use in low threshold nanocavity laser devices [61].

The ability of integrating PCs nanocavities on one chip, makes them a promising system for applications such as biosensors [62, 63] and chemical sensors [64]. In addition, the PL output of a PCs nanocavity is sensitive to changes in the local environment, making them useful as sensor for refractive index changes [65, 23] and relative humidity sensors [66, 58].

References:

1. S. Strauf, K. Hennessy, M.T. Rakher, Y.S. Choi, A. Badolato, L.C. Andreani, E.L. Hu, P.M. Petroff, and D. Bouwmeester, "Self-Tuned Quantum Dot Gain in Photonic Crystal Lasers", *Physical Review Letters*, **96**, 12, (2006).
2. Bryan Ellis, "Ultralow-threshold electrically pumped quantum dot Photonic-crystal nanocavity laser" *Nature Photonics*, **5**, (2011).
3. D. Englund, A. Faraon, I. Fushman, N. Stoltz, P. Petroff, and J. Vuckovic, "Controlling Cavity Reflectivity with a Single Quantum Dot," *Nature*, **450**, 7171, 857-861 (2007).
4. J. D. Jackson "classical electrodynamics", (1999), John Wiley & Sons, 3rd Ed.
5. J. Joannopoulos, S. Johnson, J. Winn, and R. Meade, "Photonic Crystals: Molding The flow of Light", (2008), Princeton University Press, ISBN 978-0-691-12456-8, Princeton and Oxford.
6. E. Yablonovitch, "Inhibited Spontaneous Emission in Solid-State Physics and Electronics," *Physical Review Letters*. **58**, 20, 2059-2062 (1987).
7. S. John, "Strong Localization of Photons in Certain Disordered Dielectric Superlattices," *Physical Review Letters*, **58**, 23, 2486-2489 (1987).
8. K.M. Ho, C.T. Chan, and C.M. Soukoulis, "Existence of a Photonic Gap in Periodic Dielectric Structures," *Physical Review Letters*, **65**, 25, 3152-3155 (1990).
9. E. Yablonovitch, T.J. Gmitter, and K.M. Leung, "Photonic Band-Structure - the Face-Centered-Cubic Case Employing Nonspherical Atoms," *Physical Review Letters*, **67**, 17, 2295-2298 (1991).

10. P.R. Villeneuve and M. Piche, "Photonic Band-Gaps in 2-Dimensional Square and Hexagonal Lattices," *Physical Review B*, **46**, 8, 4969-4972 (1992).
11. K.J. Vahala, "Optical microcavities", *Advanced Series in Applied Physics*, **5**, (2003).
12. M. Loncar, T. Doll, J. Vuckovic, and A. Scherer, "Design and Fabrication of Silicon Photonic Crystal Optical Waveguides", *Journal of Lightwave Technology*, **18**, 10, 1402-1411 (2000).
13. J. Zha, Z.Y. Zhong, H.Zhang, Q. Wen, and Y. Li, "Differences of Band Gap Characteristics of Square and Triangular Lattice Photonic Crystals in Terahertz Range" *Journal of Electronic and Technology of China*, **7**, 3, (2009).
14. Y. Akahane, T. Asano, B.S. Song, and S. Noda, "High-Q Photonic Nanocavity in a Two-Dimensional Photonic Crystal," *Nature*, **425**, 6961, 944-947 (2003).
15. T. Yoshie, J. Vuckovic, A. Scherer, H. Chen, and D. Deppe, "High Quality Two-Dimensional Photonic Crystal Slab Cavities," *Applied Physics Letters*, **79**, 26, 4289-4291 (2001).
16. Steven G. Johnson and J. D. Joannopoulos, "Block-iterative frequency-domain methods for Maxwell's equations in a planewave basis," *Optics Express* **8**, 3, 173-190 (2001).
17. S. G. Johnson, S. Fan, P. R. Villeneuve, L. A. Kolodziejski, J. D. Joannopoulos "Guided modes in photonic crystal slabs", *Physical Review B* **60**, 8, 5751-5758 (1999).
18. F. Pisanello, A. Quattieri, T. Stomeo, L. Martiradonna, R. Cingolani, A. Bramati, and M. De Vittorio, "High-Purcell-Factor Dipolelike Modes at

-
- Visible Wavelengths in H1 Photonic Crystal Cavity," *Optics Letters*, **35**, 10, 1509-1511 (2010).
19. O. Painter, J. Vuckovic, and A. Scherer, "Defect Modes of a Two-Dimensional Photonic Crystal in an Optically Thin Dielectric Slab," *Journal of the Optical Society of America B-Optical Physics*, **16**, 2, 275-285 (1999).
20. Y. Kalra, R. K. Sinha, *Pramana Journal of Physics*, **67**, 6, 1155–1164 (2006).
21. Jin Hou, David S. Citrin, "Slab-Thickness Dependence of Photonic Bandgap in Photonic-Crystal Slabs," *IEEE Journal of Selected Topics in Quantum Electronics*, **18**, 6 (2012).
22. A.M. Adawi, A.R.A. Chalcraft, D.M. Whittaker, and D.G. Lidzey, "Refractive Index Dependence of L3 Photonic Crystal Nano-Cavities," *Optics Express*, **15**, 22, 14299-14305 (2007).
23. D. F. Dorfner, T. Hürlimann, T. Zabel, L. H. Frandsen, G. Abstreiter, J. J. Finley, "Silicon photonic crystal nanostructures for refractive index sensing", *Applied Physics Letters*, **93**, 181103 (2008).
24. M. Kitamura, S. Iwamoto, and Y. Arakawa, "Enhanced Light Emission from an Organic Photonic Crystal with a Nanocavity," *Applied Physics Letters*, **87**, 15, (2005).
25. M. Notomi, "Manipulating Light with Strongly Modulated Photonic Crystals," *Reports on Progress in Physics*, **73**, 9, (2010).
26. Y. Akahane, T. Asano, B.S. Song, and S. Noda, "Fine-Tuned High-Q Photonic-Crystal Nanocavity," *Optics Express*, **13**, 4, 1202-1214 (2005).
27. E. Purcell, M, "Spontaneous Emission Probabilities at Radio Frequencies," *Physical Review*, **69**, 11, 681 (1946).
28. I. Bayn, . J. Salzman, "Ultra high-Q photonic crystal nanocavity design: The effect of a low ϵ slab material", *Optics Express*, **16**, 4972-4980 (2008).

29. J. R. Pugh, Y.L. D. Ho, E. Engin, C. Railton, J. G. Rarity, M. J. Cryan “Novel high-Q modes in thick 2D photonic crystal slabs”, *Journal of Optics*, **15**, (2013).
30. Y. Gong, J. Vučković “Design of plasmon cavities for solid-state cavity quantum electrodynamics applications,” *Applied Physics Letters*, **90**, 033113 (2007).
31. X. Yang, A. Ishikawa, X. Yin, X. Zhang. “ Hybrid Photonic-Plasmonic Crystal Nanocavities” *ASC Nano*, **5**, 4, 2831–2838 (2011).
32. M. Lončar, A. Scherer, and Y. Qiu, “Photonic crystal laser sources for chemical detection,” *Applied Physics Letters*, **82**, 4648-4650 (2003).
33. O. Painter, R. K. Lee, A. Scherer, A. Yariv, J. D. O’Brien, P. D. Dapkus, and I. Kim, “Two-dimensional photonic band-gap defect mode laser,” *Science* **284**, 1819-1821 (1999).
34. H. Takano, Y. Akahane, T. Asano, and S. Noda, “In-plane-type channel drop filter in a two-dimensional photonic crystal slab,” *Applied Physics Letters*, **84**, 2226-2228 (2004).
35. P. Michler, A. Kiraz, C. Becher, W. V. Schoenfeld, P. M. Petroff, L. Zhang, E. Hu, and A. Imamoglu, “A quantum dot single-photon turnstile device,” *Science*, **290**, 2282-2285 (2000).
36. V. Giannini, A.I. Fernandez-Dominguez, Y. Sonnefraud, T. Roschuk, R. Fernandez-Garcia, and S.A. Maier, "Controlling Light Localization and Light-Matter Interactions with Nanoplasmonics," *Small*, **6**, 22, 2498-2507 (2010).
37. P. Lalanne, C. Sauvan and J. P. Hugonin, “Photon confinement in photonic crystal nanocavities”, *Laser & Photonics Review*, **2**, 6, 514–526 (2008).

38. T. Xu, M. S. Wheeler, H. E. Ruda, M. Mojahedi, J. S. Aitchison “The influence of material absorption on the quality factor of photonic crystal cavities”, *Optics Express*, **17**, 10, (2009).
39. R. C. Hilborn, "Einstein coefficients, cross sections, f values, dipole moments, and all that", *American Journal of Physics*, **50**, 11, (1982).
40. P. Goy, J. M. Haimond, M. Gross, and S. Haroche, “Observation of Cavity-Enhanced Single-Atom Spontaneous Emission”, *Physical Review Letters*, **50**, 24, (1983).
41. A.M .Fox, “Quantum Optics”, (2006), Oxford University Press, 1st edition.
42. G. Khitrova, H. M. Gibbs, M. Kira, S. W. Koch, and A. Scherer, “Vacuum Rabi splitting in semiconductors," *Nature Physics*, **2**, (2006).
43. M. Boroditsky, R. Vrijen, T. F. Krauss, R. Coccioli, R. Bhat, E. Yablonovitch, “Spontaneous Emission Extraction and Purcell Enhancement from Thin-Film 2-D Photonic Crystals”, *Journal of Lightwave Technology*, **17**, 11, (1999).
44. D. Englund, D. Fattal, E. Waks, G. Solomon, B. Zhang, T.Nakaoka, Y. Arakawa, Y. Yamamoto, J. Vučković, “Controlling the Spontaneous Emission Rate of single Quantum Dots in two dimensional photonic crystal”, *Physical Review Letters*, **95**, 013904, (2005).
45. H. Iwase, D. Englund, J. Vučković , “Analysis of the Purcell effect in photonic and plasmonic crystals with losses”, *Optics Express*, **18**, 16, 16546 (2010).
46. H. Y. Ryu and M. Notomi, “Enhancement of spontaneous emission from the resonant modes of a photonic crystal slab single-defect cavity”, *Optics Express*, **28**, 23, (2003).

47. X. Wang, “Low threshold laser cavities of two dimensional photonic crystal line defect mode”, *Optik*, **122**, 1042–1045 (2011).
48. M. D. Birowosuto, H. Sumikura, S. Matsuo, H. Taniyama, P. J. van Veldhoven, R. Notzel, M. Notomi, “Fast Purcell-enhanced single photon source in 1,550-nm telecom band from a resonant quantum dot-cavity coupling”, *Scientific Reports*, **2**, 321, (2012).
49. L. Sanchis, M. J. Cryan, J. Pozo, I. J. Craddock, and J. G. Rarity, “Ultra-high Purcell factor in photonic crystal slab microcavities”, *Physical Review B*, **76**, 045118 (2007).
50. T. van der Sar, J. Hagemeyer, W. Pfaff, E. C. Heeres, S. M. Thon, H. Kim, P. M. Petroff, T. H. Oosterkamp, D. Bouwmeester, R. Hanson, “Deterministic nanoassembly of a coupled quantum emitter–photonic crystal cavity system”, *Applied Physics Letters*, **98**, 193103, (2011).
51. F. Pisanello, A. Quattieri, T. Stomeo, L. Martiradonna, R. Cingolani, A. Bramati, M. De Vittorio, “High-Purcell-factor dipolelike modes at visible wavelengths in H1 photonic crystal cavity”, *Optics Letters*, **35**, 1509-1511 (2010).
52. J. P. Reithmaier, G. Sek, A. Löffler, C. Hofmann, S. Kuhn, S. Reitzenstein, L. V. Keldysh, V. D. Kulakovskii, T. L. Reinecke, A. Forchel, “Strong coupling in a single quantum dot-semiconductor microcavity system”, *Nature*, **432**, 197–200 (2004).
53. T. Yoshie, A. Scherer, J. Hendrickson, G. Khitrova, H.M. Gibbs, G. Rupper, C. Ell, O.B. Shchekin, and D.G. Deppe, "Vacuum Rabi Splitting with a Single Quantum Dot in a Photonic Crystal Nanocavity," *Nature*, **432**, 7014, 200-203 (2004).

54. D. Englund, A. Majumdar, A. Faraon, M. Toishi, N. Stoltz, P. Petroff, J. Vuckovic, "Resonant Excitation of a Quantum Dot Strongly Coupled to a Photonic Crystal Nanocavity", *Physical Review Letters*, **104**, 073904, (2010).
55. A. Majumdar, A. Papageorge, E. D. Kim, M. Bajcsy, H. Kim, P. Petroff, J. Vuckovic, "Probing of single quantum dot dressed states via an off-resonant cavity", *Physical Review B*, **84**, 085310, (2011).
56. A. Mekis, J.C. Chen, I. Kurland, S.H. Fan, P.R. Villeneuve, J.D. Joannopoulos, "High Transmission through Sharp Bends in Photonic Crystal Waveguides," *Physical Review Letters*, **77**, 18, 3787-3790 (1996).
57. P. Russell, "Photonic-Crystal Fibers", *IEEE Journal of Light Wave Technology*, **24**, 12, 4729 (2006).
58. M. Y. Mohd Noor, N. M. Kassim, A. S. M. Supaat, M. H. Ibrahim, A. I. Azmi, A. S. Abdullah, G. D. Peng, "Temperature-insensitive photonic crystal fibre interferometer for relative humidity sensing without hygroscopic coating", *Measurements Science and Technology*, **24**, 105205 (2013).
59. H.Y. Ryu, M. Notomi, E. Kuramoti, T. Segawa, "Large Spontaneous Emission Factor (> 0.1) in the Photonic Crystal Monopole-Mode Laser," *Applied Physics Letters*, **84**, 7, 1067-1069 (2004).
60. Pisanello, F., A. Quattieri, T. Stomeo, L. Martiradonna, R. Cingolani, A. Bramati, M. De Vittorio, "High-Purcell-factor dipole like modes at visiblewavelengths in H1 photonic crystal cavity", *Optics Express*, **35**, 1509-1511 (2010).
61. B. Ellis, M. A. Mayer, G. Shambat, T Sarmiento, J. Harris, E. E. Haller, J.Vuckovic, "Ultralow-threshold electrically pumped quantum dot Photonic-crystal nanocavity laser", *Nature Photonics*, **5**, 297-300 (2011).

62. X. Fan, I. M. White, S. I. Shopova, H. Zhu, J. D. Suter, and Y. Sun, "Sensitive optical biosensors for unlabeled targets: a review," *Analytica Chimica Acta*, **620**, 8 – 26 (2008).
63. J. B. Fan, M. S. Chee, K. L. Gunderson, "Highly parallel genomic assays", *Nature Review Genetics*, **7**, 8, 632 (2006).
64. M. Loncar, A. Scherer, Y. Qiu, "Photonic crystal laser sources for chemical detection", *Applied Physics Letters*, **82**, 26, (2003).
65. I.M. White, X. Fan, "On the Performance Quantification of Resonant Refractive Index Sensors," *Optics Express*, **16**, 2, 1020-1028 (2008).
66. J. Mathew, Y. Semenova, G. Rajan, G. Farrell, "Humidity sensor based on photonic crystal fibre interferometer", *Electronics Letters*, **46**, 19, (2010).

Chapter three

Plasmonic nanoparticles: theoretical background

3.1 Introduction

Noble metal nanoparticles (NPs) having sizes between 1 and 100 nm have unusual characteristics that result in unique properties that are not observed in ordinary materials [1]. A long time ago (before the optical properties of metallic nano metal were understood) artists in the Roman Empire (4th century AD), imbedded gold and silver nanoparticles into glass to create brilliant colours as exemplified by the Lycurgus cup [2]. This cup appears red or green depending on the illumination as shown in Figure 3.1. Analytical measurements shown that the particles used in the artwork had size in the range of 15-100 nm [3].

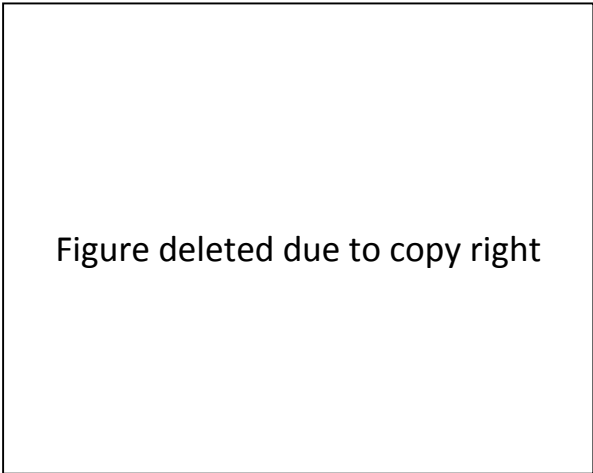


Figure deleted due to copy right

Figure 3.1: Lycurgus cup, from reference [2]

As will be discussed below, the size of the NPs determines their colour and appearance [4]. The colour of a collection of NPs results from the interactions between the incident light and the NPs through absorption or scattering processes. These processes result from the presence of a plasmon resonance (PR) which is defined as the collective oscillation of the free electrons in the

conduction band of the NP under the influence of an external incident electromagnetic field [5]. In this chapter, the plasmon resonance of metal NPs and their interaction with an applied electromagnetic field is introduced. Analytical solutions such as Mie theory [6] of plasmon resonance of NPs as well as environmental effects that effect resonance frequency will be discussed. Finally, the applications of plasmonic nanoparticles will be briefly presented. These include Raman Spectroscopy (SERS) [7], bio sensing [8], dark-field microscopy [9] and in plasmonic photonic crystal nano cavities [10, 11].

3.2 Localized Surface Plasmon resonance (LSPR)

A surface plasmon resonance (SPR) can be defined as the collective oscillation of the electron cloud in the conduction band of a noble metal particle which is stimulated by an incident electromagnetic field. The condition of resonance is achieved when the frequency of the external field matches the natural oscillation frequency of the electrons inside the metallic nanoparticle [13] as shown in Figure 3.2.

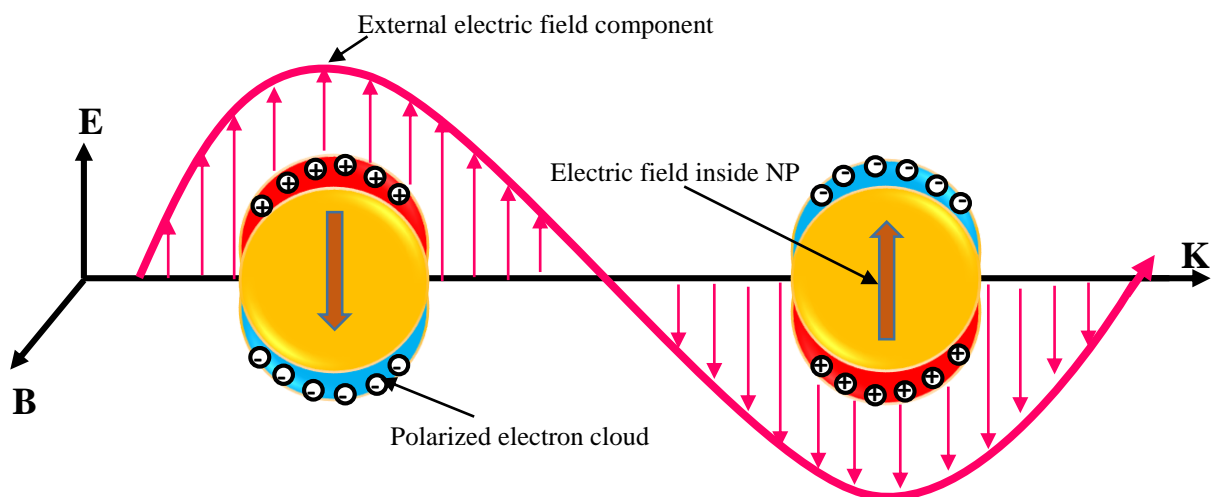


Figure 3.2: Scheme of the light interaction with a metallic NP. Electric dipole created by the accumulation of positive and negative charges under the influence of the exciting electric field of the light.

The electromagnetic field produced by the oscillating electron cloud is localized and does not propagate far from the NP surface, and hence the plasmon resonance of a metallic NP is known as a localized surface plasmon resonance (LSPR). Because of this, metallic nanoparticles can confine or squeeze electromagnetic energy into a volume smaller than the diffraction limit $(\lambda_0/2n)^3$. Here, n is medium refractive index and is expressed using $n = \sqrt{\epsilon}$ [5]. For gold NPs, the plasmon resonance exist at visible wavelengths and so their bright colours are a consequence of the absorption and scattering of incident light.

3.3 Metallic nanoparticles inside an electromagnetic field

The interaction of metal NPs with an electromagnetic field can be described using Maxwell equations as given in equations 2.1 along with specific boundary conditions to give us an appropriate analysis of the nature of the plasmon resonance.

For a metallic NP, we can use boundary condition appropriate for linear, isotropic and non-magnetic media. For electrical displacement \vec{D} and magnetic field \vec{B} , the displacement includes a term describing the dielectric constant $\epsilon(\omega)$. This term is dependent on the angular frequency of the EM field, and is generally described as complex function.

Following equation 2.2, we can write down an expression

$$\epsilon(\omega) = \epsilon_1(\omega) + i\epsilon_2(\omega) \quad \dots\dots\dots 3.1$$

Similarly, the refractive index of a medium can be described using

$$\tilde{n}(\omega) = n(\omega) + i\Omega \quad \dots\dots\dots 3.2$$

Using $n = \sqrt{\epsilon}$, it is straightforward to show

$$\varepsilon_1 = n^2 - \Omega^2 \quad \dots\dots\dots 3.3$$

$$\varepsilon_2 = 2n\Omega \quad \dots\dots\dots 3.4$$

$$n^2 = \frac{\varepsilon_1}{2} + \frac{1}{2} \sqrt{\varepsilon_1^2 + \varepsilon_2^2} \quad \dots\dots\dots 3.5$$

Here, Ω is the extinction coefficient and determines the absorption of the electromagnetic waves propagating through the medium. For a light beam propagating through a medium, its intensity is attenuated exponentially as defined by Beer's law:

$$I(x) = I_o e^{-\alpha x} \quad \dots\dots\dots 3.6$$

Here, α is absorption coefficient and is linked to extinction coefficient by:

$$\alpha(\omega) = \frac{2\Omega(\omega)\omega}{c} \quad \dots\dots\dots 3.7$$

From equations (3.4) and (3.7) it is clear that the imaginary part ε_2 of the dielectric function determines the magnitude of the absorption. For $\varepsilon_1 \gg \varepsilon_2$ the real part of the refractive index (n) determines the decrease in the phase velocity of a propagating beam inside a medium. In addition, the absorption losses depend on the conductivity of the material $\sigma(\omega)$ which is related to the imaginary part of the complex frequency-dependent dielectric function by $\varepsilon_2 = \sigma(\omega)/\varepsilon_o(\omega)$. For a metal, these losses occur close to the surface (within a distance of 10s of nm) over a region called the penetration depth [14].

3.4 The optical properties of metals and metal nanoparticles.

To understand the response of metallic NPs to an applied electromagnetic field and the parameters that determine such a response, a number of theories and analytical solutions have been developed. These are discussed in the next sections. These allow the optical properties of metals to be understood over a wide range of frequencies.

3.4.1 Free gas (Drude-Sommerfeld) model.

Consider a gas of free electrons each having a charge e and a number of free electrons per unit volume N oscillating against a background of heavy fixed positive ion cores. The electrons oscillate under the influence of an applied electromagnetic field $E(t) = E_0 \exp(-i\omega t)$, with their motion being damped as a consequence of collisions. The collision frequency is described using $\gamma = 1/\tau$, where τ is the relaxation time of the free electron gas (typically $\tau = 10^{-14}$ sec at room temperature). We start with the equation of motion for an electron gas in an applied external field

$$m_e \ddot{x} + m_e \gamma \dot{x} = -e E(t) \dots\dots\dots 3.8$$

The solution of this equation is

$$x(t) = \frac{e}{m_e(\omega^2 + i\gamma\omega)} E(t) \dots\dots\dots 3.9$$

The electron gas that is displaced around the fixed ion-core background generates a polarization (P) given by

$$P = -Nex \dots\dots\dots 3.10$$

This can be related to the dielectric constant ϵ by

$$D = \varepsilon_o E + P = \varepsilon_o \varepsilon E \dots\dots\dots 3.11$$

Using equations (3.9), (3.10) and (3.11) the dielectric function of the free electron gas can be obtained [16-17].

$$\varepsilon(\omega) = 1 - \frac{\omega_p^2}{\omega^2 + i\gamma\omega} \dots\dots\dots 3.12$$

Here, $\varepsilon(\omega)$ is a complex dielectric function and ω_p is the bulk plasmon frequency, $\omega_p = Ne^2/m_e\varepsilon_o$. For gold, $\omega_p = 13.8 \times 10^{15}$ Hz and $\gamma = 1.075 \times 10^{14}$ Hz [7]. For high frequencies, the damping rate (γ) can be neglected and equation 3.15 is reduced to.

$$\varepsilon(\omega) = 1 - \frac{\omega_p^2}{\omega^2} \dots\dots\dots 3.13$$

The metal gold for instance has a plasmon resonance at visible wavelengths, and has a dielectric function as function of incident wavelength as shown in figure 3.3.

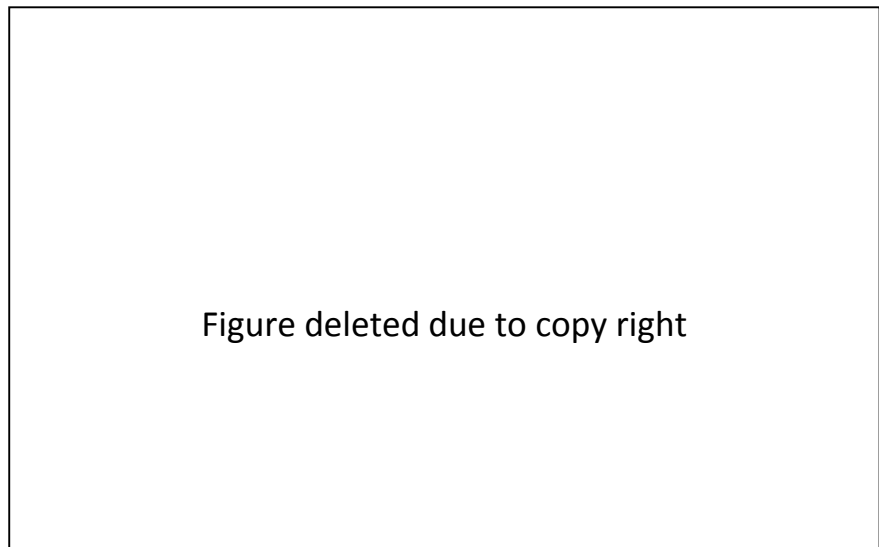


Figure 3.3. Permittivity of gold as a function of wavelength. Figure taken from reference 17.

It can be seen that the real part totally dominates the dielectric function and it is negative. This implies that light at such frequencies can only penetrate a very small distance into a metal. The imaginary part represents energy dissipation by inter-electron motion [18]. However, the damping rate constant γ is directly proportional to the Fermi velocity V_F and inversely proportional to the electron mean free path l and is given by [19]:

$$\gamma = \frac{v_F}{l} \dots\dots\dots 3.14$$

3.4.2 Interband model

The Drude-Sommerfeld model describes the free electron gas contribution to the dielectric response, but neglects the contribution of inter band transitions of bound electrons inside the metal. However, photons at high energy (especially above 2.25 eV) can excite inter-band (valance band) electrons to higher lying conduction bands. The material dielectric function can be therefore described using an interband model [18, 20]:

$$\varepsilon(\omega)_{interband} = 1 + \frac{\tilde{\omega}_p^2}{(\omega_o^2 - \omega^2) - \omega i \tilde{\gamma}} \dots\dots 3.18$$

Here, $\tilde{\omega}_p = \tilde{N}e^2/m_e\varepsilon_0$, \tilde{N} is the density of bound electrons and $\tilde{\gamma}$ is the bound electron damping rate. The difference between the Drude and interband models occurs at the resonance frequency ω_o , where the imaginary part of the dielectric function increases sharply, leading to a high damping rate. For gold NPs, as shown in figure 3.4 the dielectric function is obviously following the interband transition model for wavelengths below 650 nm. While for wavelengths above 650 nm the Drude model is dominated the dielectric function behaviour. To

describe experimentally obtained the metal dielectric function contributions both interband (equation 3.18) and Drude models (equation 3.15) have to be taken in to account in the metal dielectric function.

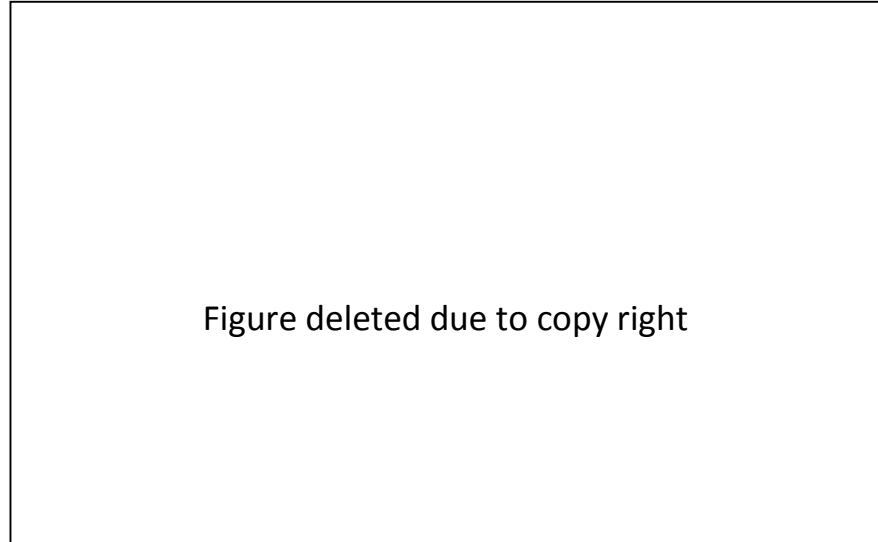


Figure 3.4: the effect of interband electrons on the gold dielectric function. At resonance frequency the dielectric function increases rapidly [20]

3.4.3 Mie theory

The plasmon resonance of a metal sphere interacting with an incident plane wave was first calculated by Gustav Mie [6]. Mie solved Maxwell's equations to calculate the extinction cross section by assuming a metal sphere with a given radius imbedded in a linear, isotropic, homogeneous medium. The amount of light removed from the incident light is known as the extinction cross section and occurs through two processes: scattering and absorption. The cross section for these processes are shown in figure 3.5. The solution of the internal and scattered fields can be expanded into a set of normal modes represented by vector harmonics [5]. The extinction cross section of a spherical NP is given by the following expression [1]:

$$\sigma_{ext} = \frac{\lambda^2}{2\pi} \sum_{L=0}^{\infty} (2L + 1) \cdot \text{Re}(a_L + b_L) \quad \dots\dots\dots 3.16$$

Here:

$$a_L = \frac{\Psi_L(\beta) \Psi'_L(n\beta) - n\Psi_L(n\beta) \Psi'_L(\beta)}{\xi_L(\beta) \Psi'_L(n\beta) - n\Psi_L(n\beta) \xi'_L(\beta)} \quad \dots\dots\dots 3.17$$

$$b_L = \frac{n\Psi_L(\beta) \Psi'_L(n\beta) - \Psi_L(n\beta) \Psi'_L(\beta)}{n\xi_L(\beta) \Psi'_L(n\beta) - \Psi_L(n\beta) \xi'_L(\beta)}$$

Here, β is the size parameter $\beta = \frac{\pi d n_o}{\lambda_o}$. where λ_o is the incident wavelength with respect to vacuum, and n, n_o the refractive index of the medium and the surrounding medium respectively. L is index (0, 1, 2, ...), and Ψ and ξ are the cylindrical Bessel–Riccati functions. The derivation of the equation can be found in reference [21]. FDTD software has been used to calculate the extinction, scattering and absorption cross section based on the solution of Mie equation in three dimensions for a 150 nm gold nanoparticle as shown in figure 3.5.

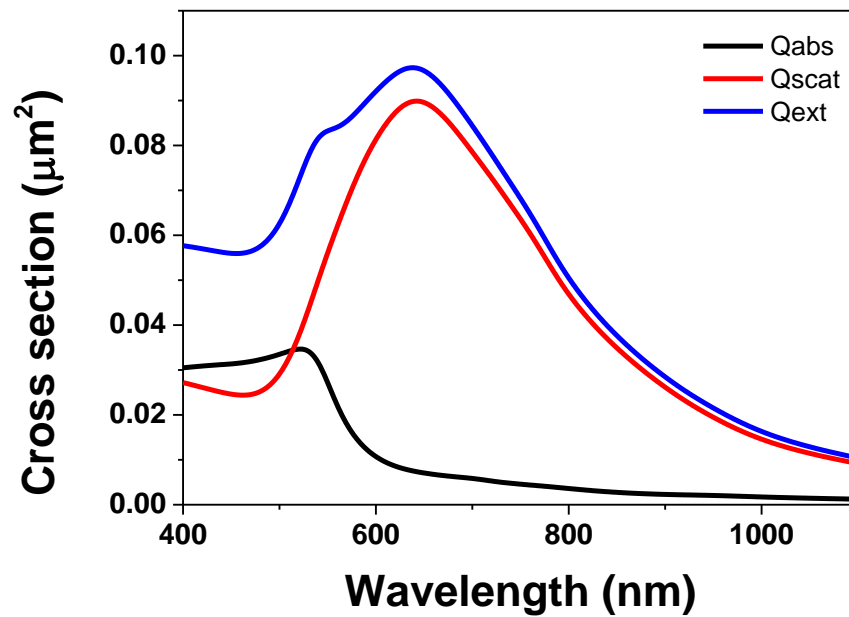


Figure 3.5: FDTD calculation shows the contributions to NP total scattering cross section from absorption and of a spherical 150 nm Au NP in water.

3.4.4 Dipole approximation (DA).

A dipole approximation (DA) can be applied to particles having a size that is comparatively less than the wavelength of the applied electromagnetic field. At visible wavelengths, this corresponds to particles having a diameter of ~50 nm.

For $2r \ll \lambda$ (where r is the radius of the particles and λ is the wavelength of the light in the surrounding media), the extinction cross-section depends only on contributions from the electric dipole [12, 22]. The Mie theory, outlined in equation 3.16 reduces to the following relationship [23].

$$Q_{ext} = 9 \frac{\omega}{c} \varepsilon_m^{3/2} V \frac{\varepsilon_1(\omega)}{[\varepsilon_1(\omega) + 2\varepsilon_m(\omega)]^2 + [\varepsilon_2(\omega)]^2} \dots\dots 3.18$$

Here, V is the volume of a spherical particle, ω is the angular frequency of the exciting light and c its velocity, ε_m is the dielectric function of the surrounding medium, $\varepsilon_1, \varepsilon_2$ are the real and imaginary parts of the material dielectric functions respectively. Equation 3.18 is originally derived from the sum of scattering and absorption cross sections $Q_{ext} = Q_{abs} + Q_{scat}$ [5] where.

$$Q_{abs} = 4\pi k r^3 \text{Im}\left(\frac{\varepsilon_p - \varepsilon_m}{\varepsilon_p + 2\varepsilon_m}\right) \dots\dots\dots 3.19$$

$$Q_{scat} = 8\pi k^4 r^6 \left| \frac{\varepsilon_p - \varepsilon_m}{\varepsilon_p + 2\varepsilon_m} \right|^2 \dots\dots\dots 3.20$$

It is clear from equations 3.19 and 3.20 that both the absorption and scattering cross sections are scaled by the particle radius r [5]. For particle radius $r \ll \lambda$, the absorption cross section dominates over the scattering cross section, and thus the extinction cross section $Q_{ext} \approx Q_{abs}$. Indeed, the scattering contribution can usually be neglected for gold and silver particles with $r \leq 20$ nm [24]. Figure 3.6

plots of FDTD calculations of Mie scattering for gold spheres with varying radius (17, 25, 37, 50, and 75 nm). The results show the scattering contribution can be neglected for particles below $r \approx 25$ nm, while it exceeds the absorption cross section at $r > 50$ nm.

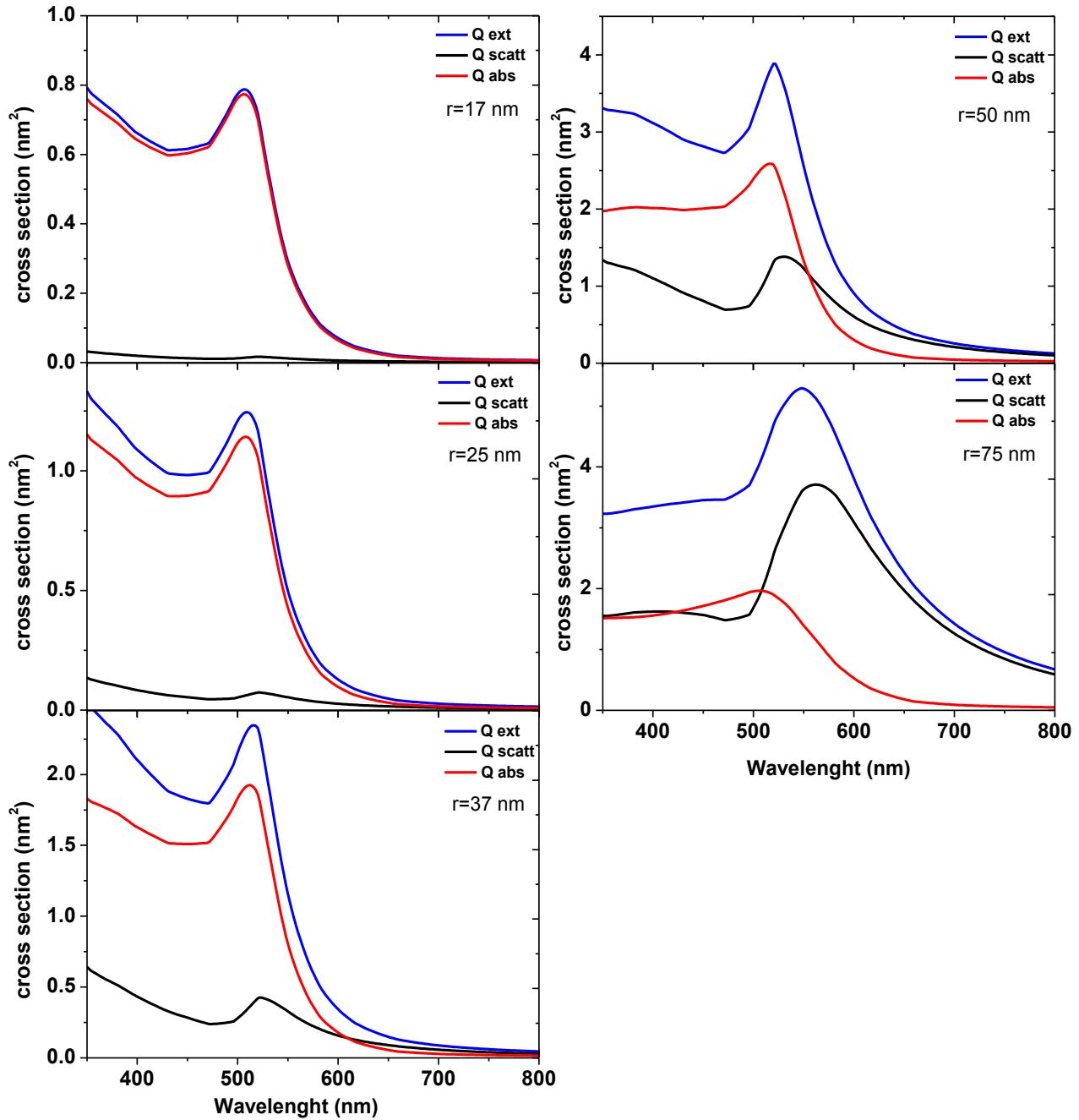


Figure 3.6: FDTD calculation using Mie theory, showing the extinction, scattering and absorption cross sections for gold spheres having different value of radius.

3.4.5 Mass-and-spring model

Although the quasi-static solutions of Mie theory are able to describe the interactions between the incident field and a metal nano particle, they are less successful in describing the optical response of non-spherical particles. To understand the physics of non-spherical plasmonic particles, a mass-spring model was developed [25, 26]. This model assumes that the displaced electron cloud around a heavy positive charged nucleus under the influence of an external field could be expressed as simple harmonic oscillation. This is similar to a classical mass connected to spring of spring constant G , as shown in figure 3.7. To estimate the restoring force on the charge carriers that accumulate at the opposite ends of a nanoparticle (displaced by a distance Δx), they can be considered as point-like charges. At the resonance frequency, we start from the equivalence of the restoring force and Coulomb force equations, thus;

$$F(\Delta x) = -\frac{1}{2\pi\epsilon_0} (ne)^2 \frac{A^2}{d} \Delta x = -G\Delta x \dots\dots\dots 3.21$$

Here n is the charge carrier density, A is cross-sectional area and e is the elementary charge. By solving equation 3.21, the resonance frequency ω_{res} of the plasmon on an elongated particle can be expressed as.

$$\omega_{\text{res}} = \frac{\omega_p}{2\sqrt{2}} \frac{1}{R} \dots\dots\dots 3.22$$

where, R is the nanoparticle aspect of ratio.

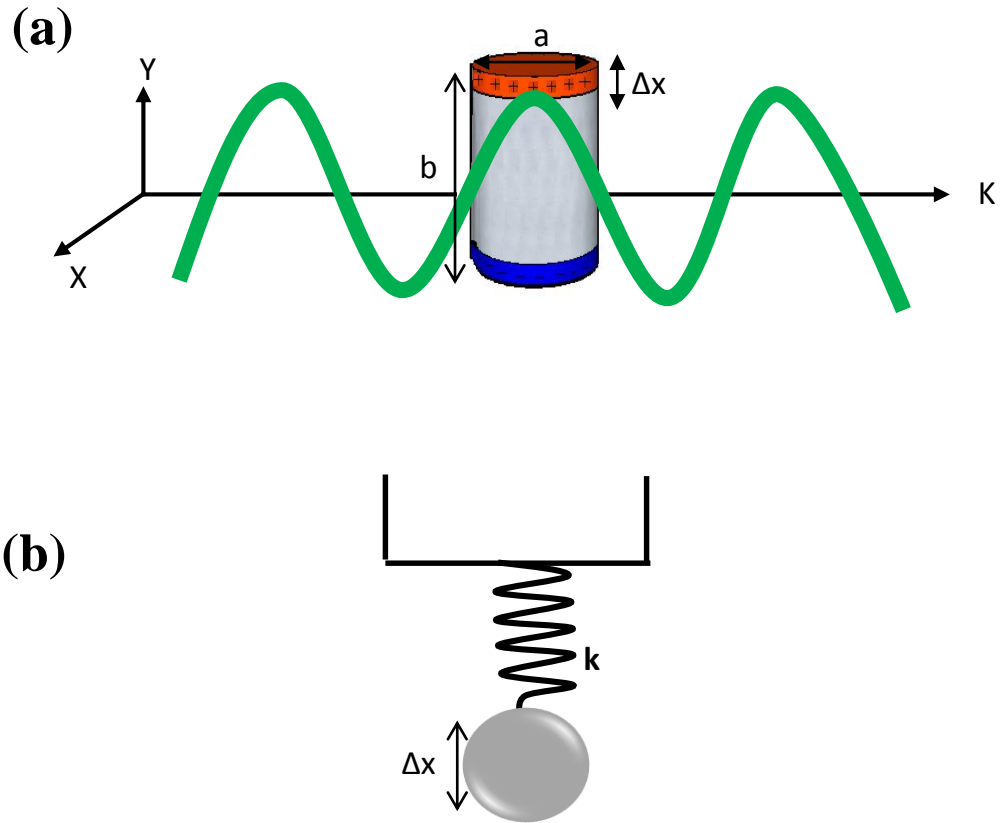


Figure 3.7: Mass-and-spring model for a plasmonic resonances: (a) Sketch of an elongated plasmonic particle with charge accumulated at its ends. (b) The oscillation can be represented by an effective spring constant k and an effective mass m of the moving electron cloud.

3.5 The effect of particle size

Nanoparticles are a collection of atoms bound together having a size intermediate between that of a single atom and a bulk material [27]. The quantum size of a metallic nanoparticle gives rise to a distinctive optical response and electrodynamic interactions. For instance, solutions of colloidal noble metal nanoparticles have different colours, such as silver, gold, and copper [28]. Generally, the response of a NP surface plasmon resonance frequency (SPR) depends on its size.

In a semiconductor nanoparticle (a quantum object) the onset of the first electron transition shifts to higher energy (i.e. the band gap size increase) as the particle size is reduced [29]. Similarly, for metal NPs, the separation between the energy levels (conduction and valance bands) increases sharply as the particle size is decreased. In addition, in particles smaller than the mean free path of conduction electrons, the damping constant γ increases resulting from the collision of free conduction electrons with the boundaries of the particle [30]. This effect reduces the intensity of the SPR [31]. Figure 3.8 shows the change in the dielectric constant of gold NPs as a function of particle size.

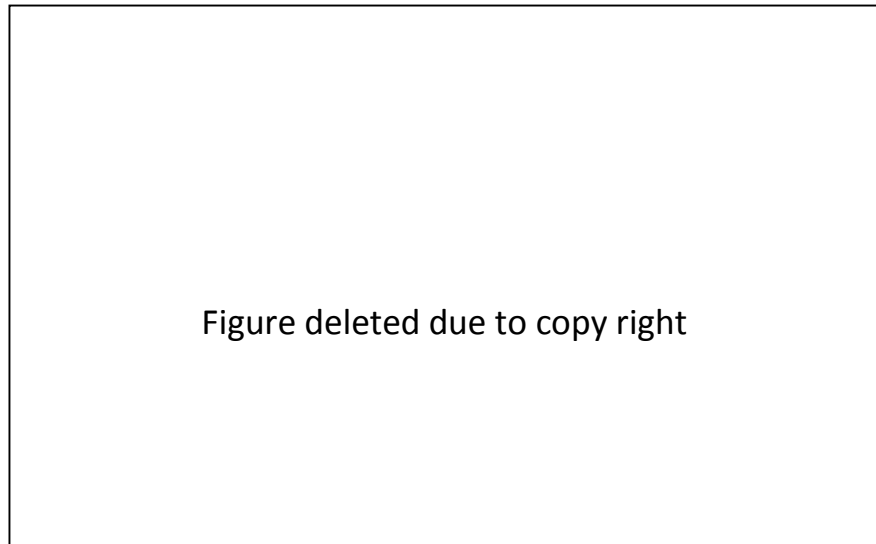


Figure 3.8: Dielectric function of gold illustrates the size effect [19]

For large NPs (having a radius of more than 20 nm), where several plasmon resonance bands are degenerate, the NPs are described as a multipole rather than a dipole (as used to describe small NPs) [28]. Here, as the particle size increases in comparison with the wavelength of the incident light, the dipole approximation model is no more valid. Rather the SPR wavelength becomes dependent on radius r . In addition, higher order SPR peaks appear at lower energies resulting in a red shift as shown in figure 3.9 (a) and (b) [32] as a consequence of phase retardation

[17, 33, 34]. Also the contribution of the scattering cross -section increases significantly as the particle size increases (see section 3.4.4 figure (3.6)). Figure 3.9 (a) shows the red shift of the extinction cross section as a function of the particle size.

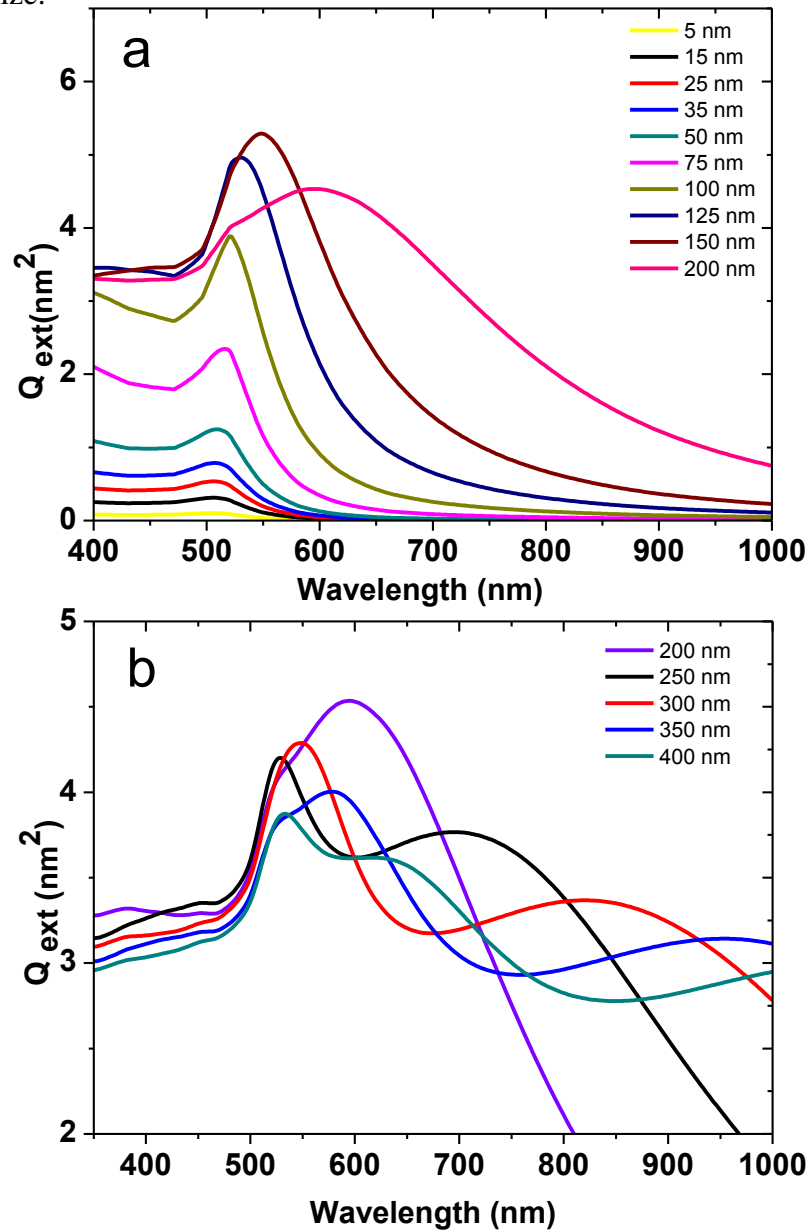


Figure 3.9: (a) FDTD calculation showing red shift of extinction cross section peak with increasing particle diameter from 5 nm to 200 nm. (b) Particle diameter increases from 200 nm to 400 nm, and multimode extinction cross section peaks appear.

Note that the dielectric function values in all Mie calculations have been taken from data produced by John and Christy [35].

3.6 The effect of nanoparticle Shape.

In addition to size effects, the shape of a NP has a significant effect on its optical extinction, absorption and scattering spectrum peaks as shown in Figure 3.10. The sharp ends of a NP can result in high charge accumulation via strong enhancement of SPR [36], as has been observed in nanorods [37] and stars [38]. For nanorod or cylindrical shaped NPs, the extinction resonance band is split into two bands that corresponded to electrons oscillating parallel or perpendicular to the major axis (long axis) of the NP [12, 19, 22, 36]. A high resonance frequency band referred to as transverse plasmon modes, results from electrons oscillating in a perpendicular direction to the long axis, with the other low resonance frequency band referred to as a longitudinal plasmon that results from electrons oscillating parallel to the long axis [12, 40].

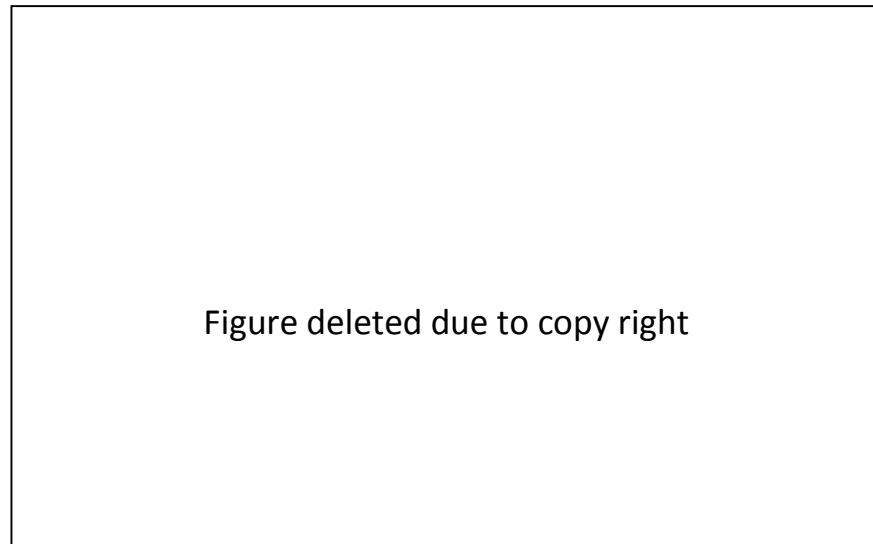


Figure 3.10: Normalized extinction, absorption, and scattering cross sections for three different shape of Ag nanoparticles in a vacuum [40].

For elliptical particles having a fixed length, the longitudinal plasmon modes are red-shifted as the aspect ratio (the ratio between long to short axis see figure 3.11) increases [17, 33]. The plasmon resonance is dependent on NP shape and can be described using extended Mie theory known as Gans theory. This describes the depolarization factor along each axis of a nanorod or spheroid particle depending on its aspect ratio. A red shift is observed for longitudinal plasmon modes as the aspect ratio increases, while the transverse plasmon modes undergoes a small blue shift [12, 22, 33, 36]. This is shown in Figure 3.12.

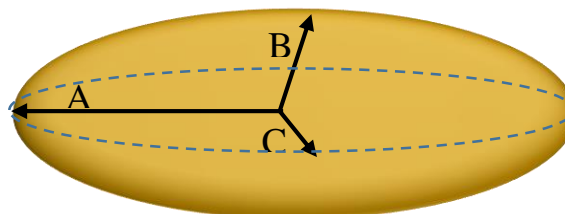


Figure 3.11: illustrate the axes of ellipsoid shape, here A is the long axis B and C are the short axes. For $A > B = C$ the aspect of ratio = A / B .

Figure deleted due to copy right

Figure 3.12: Normalized absorption plasmon resonance spectra of Au nanorods of different aspect ratio. The figure shows the high sensitivity of longitudinal modes to a change in the aspect ratio [41].

3.7 The effect of the surrounding medium.

The dipole approximation (DA) (equation 3.21) indicates that the dielectric constant of the surrounding medium around a metal NP plays a significant role in determining both the intensity and the plasmon resonance peak position [23, 33]. For particle sizes within the DA approximation, Okamoto et.al, showed that the peak position of the absorption cross section for a 20.2 nm gold NPs monolayer is increased and red shifts as the refractive index of the host environment increases [42]. This effect is shown in Figure 3.13. This result has been confirmed theoretically by applying DA calculation to 10 nm gold NP immersed in liquids also with various refractive indices [43].

It has also been shown that the longitudinal mode of a (60 x 20) nm gold nano-ellipsoid, undergoes a red-shift as the refractive index of the environment increases [33], as shown in figure 3.14. The SPR wavelength is thus highly sensitive to surrounding media and can be used to construct plasmonic chemical and biological sensors [44].

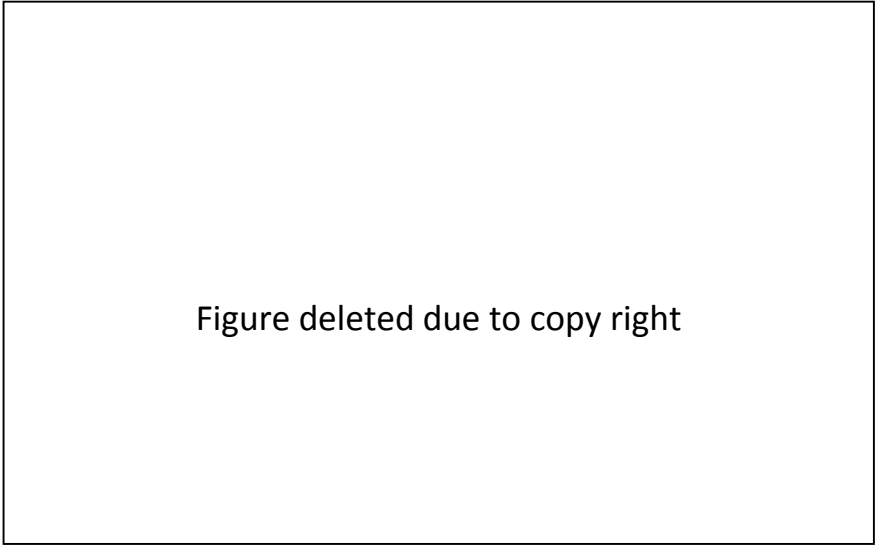


Figure deleted due to copy right

Figure 3.13: the absorption cross section of a 20.2 nm gold colloid monolayer immersed in liquid samples of various refractive index [42].

Figure deleted due to copy right

Figure 3.14: Calculated absorption cross section of a gold nano ellipsoid with varying medium dielectric constant. The inset shows a plot of the maximum of the longitudinal plasmon band as a function of the medium dielectric constant [33].

3.8 Some applications of Noble metal nanoparticles.

There are many applications of noble metal nanoparticles in different fields which are highlighted briefly. The development of synthesis methods to fabricate metallic nanoparticles opens a wide range of potential applications. The most developed applications of plasmonic NPs are in biology. Gold is a material of choice for biological applications due to its inert character (resistance to oxidation), with its plasmon resonance existing at visible frequencies [12]. Moreover, noble metal NPs can be synthesised having a size similar to other biological structures, such as DNA chains, bacteria and biological cells. This enables them to interact with such structures and to act as therapeutic agents [45, 46]. For instance, metal NPs are used widely in cancer diagnosis and photothermal therapy [47, 41]. In photothermal therapy, the extinction resonance peak which positioned at infrared wavelengths can be used to heat up localized

cells, permitting cancerous tumours to be eliminated [48, 49]. Metal NPs can also be used as a fluorescent label for imaging of biological tissues instead of using organic or inorganic dyes. Here, the long life time and reduced excitation power are an advantage [50]. Metallic NPs have also been used as biosensors [51, 52], bio detectors [53] and in drug delivery applications [54].

The plasmonic excitation of noble metal NPs have high local electric field intensity. This permits them to be used to detect a single molecule by enhancing the Raman scattering cross sections, a process known as Surface Enhanced Raman spectroscopy (SERS) [55, 56].

Metal NPs have also been used to increase the efficiency of photovoltaic devices. This was achieved by promoting total internal reflection inside an active layer by trapping the photons using their large optical scattering cross section [57, 58]. Thin film composites of noble metal NPs have also been developed for use as a selective optical absorber [58, 59]. Metal NPs having sharp ends, such as so-called bow-tie shapes can be used to achieve extreme field enhancement and produce extreme ultraviolet light (EUV) down to 47 nm [60]. Finally, a hybrid plasmon- photonic crystal resonance has been demonstrated as biochemical sensor. This technique has shown to reduce the size and cost of a biochemical sensor and can be used as an alternative to the traditional optical spectrometer for resonance spectral measurements [61, 62].

In summary, in this chapter, I have discussed the basic physics of plasmon resonance in metallic nanoparticles, and have highlighted the different physical methods used to describe their optical dielectric properties. These results are used in the rest of this thesis, particularly in chapters 7 and 8.

References

1. Ki Young Kim, "Plasmonics: Principles and Applications", Chapter 11, V.A.G. Rivera, F.A. Ferri and E. Marega Jr, "Localized Surface Plasmon Resonances: Noble Metal Nanoparticle Interaction with Rare-Earth Ions", ISBN 978-953-51-0797-2, 558 pages, Publisher: InTech, Chapters published under CC by 3.0, license, DOI: 10.5772/2633 (2012).
2. I. Freestone, N. Meeks, M. Sax, C. Higgitt, "The Lycurgus Cup – A Roman Nanotechnology", *Gold Bulletin*, **40**, 270-277 (2007).
3. I.C. Barber, and D.J. Freestone, "An investigation of the origin of the colour of the Lycurgus cup by analytical transmission electron microscopy", *Archaeometry*, **32**, 33-34 (1990).
4. L. J. E. Anderson, C. M. Payne, Yu-Rong Zhen, P. Nordlander, and Jason H. Hafner, "A Tuneable Plasmon Resonance in Gold Nanobelts", *Nano Letters*, **11**, 5034–5037 (2011).
5. S. A. Maier, "Plasmonics Fundamentals and Applications". Springer Science Business Media LLC (2007).
6. G. Mie, "Beitrage zur Optik truber Medien, speziell kolloidaler Metallosungen" *Annalen der Physik*, **25**, 3, 377–445 (1908).
7. J. F. Li, Y. F. Huang, Y. Ding, Z. L. Yang, S. B. Li, X. S. Zhou, F. R. Fan, W. Zhang, Z. Y. Zhou, D. Y. Wu, B. Ren, Z. L. Wang and Z. Q. Tian, "Shell-isolated nanoparticle-enhanced Raman spectroscopy", *Nature Letters*, **464**, (2010).
8. J. N. Anker, W. P. Hall, O. Lyandres, N. C. Shah, J. Zhao and R. P. Van Duyne, "Biosensing with plasmonic nanosensors", *Nature Materials*, **7**, (2008).
9. J.J. Mock, M. Barbic, D.R. Smith, D.A. Schultz, and S. Schultz, "Shape Effects in Plasmon Resonance of Individual Colloidal Silver Nanoparticles," *Journal of Chemical Physics*, **116**, 15, 6755-6759 (2002).

10. R. M. Gelfand, L. Bruderer, and H. Mohseni, “Theoretical Design for a Plasmon-Polariton Photonic Crystal”, 21st Annual Meeting of the IEEE Lasers and Electro-Optics Society, 143–144 (2008).
11. T. Xing and D. Z. Chao, “Optimization of nanocavity field enhancement using two-dimensional plasmonic photonic crystals”, Chinese Science Bulletin, **57**, 1, 77-82 (2012).
12. Sujit Kumar Ghosh and Tarasankar Pal, “Interparticle Coupling Effect on the Surface Plasmon Resonance of Gold Nanoparticles: From Theory to Applications”, Chemical Review, **107**, 11, 4797-4862 (2007).
13. K. Lance Kelly, Eduardo Coronado, Lin Lin Zhao, and George C. Schatz, “The Optical Properties of Metal Nanoparticles: The Influence of Size, Shape, and Dielectric Environment”, Journal of Physical Chemistry **B**, **107**, 668-677 (2003).
14. J. D. Jackson. *Classical Electrodynamics*. John Wiley and Sons, New York, 3 Edition, (1999).
15. P. B. Johnson and R. W. Christy, “Optical constant of the noble metals”, Physical Review **B**, **6**, 12, 4370-4379 (1972).
16. P. Kvasnička and J. Homola, “Optical sensors on spectroscopy of localized surface plasmons”, Biointerphases, **3**, 3, (2008).
17. V. Myroshnychenko, J. Rodriguez-Fernandez, I. Pastoriza-Santos, A. M. Funston, C. Novo, P. Mulvaney, L. M. Liz-Marzan and F. J. G. de Abajo, “Modelling the optical response of gold nanoparticles”, Chemical Society Reviews, **37**, 1792–1805 (2008).
18. L. Novotny and B. Hecht, *Principles of Nano-Optics*. Cambridge University Press, UK, (2006), ISBN 978-0521832243.
19. T. Okamoto, “Near-field Optics and Surface Plasmon Polaritons”, Topics in Applied Physics, **81**, 97–122, Springer (2001).

20. G. M. Wysin, V. Chikan, N. Young and R. K. Dani, "Effects of interband transitions on Faraday rotation in metallic nanoparticles", *Journal of Physics: Condensed Matter*, **25**, 325302 (2013).
21. C. F. Bohren and D. R. Huffman, "Absorption and scattering of light by small particles", Wiley-Interscience, (1983), ISBN 978-0471293408.
22. S. Link and M. A. EL-Sayed, "Shape and size dependence of radiative, non-radiative and photothermal properties of gold nanocrystals", *International Reviews in Physical Chemistry*, **19**, 3, 409-453(2000).
23. A. Moores and F. Goettmann, "The plasmon band in noble metal nanoparticles: an introduction to theory and applications", *New Journal of Chemistry*, **30**, 1121–1132 (2006).
24. B. Khlebtsov , A. Melnikov , V. Zharov and N. Khlebtsov, "Absorption and scattering of light by a dimer of metal nanospheres: comparison of dipole and multipole approaches", *Nanotechnology* **17**, 1437–1445 (2006).
25. P. Biagioni, J-S Huang, B Hecht, "Nanoantennas for visible and infrared radiation", *Reportes on Progress in Physics*, **75**, 024402 (2012).
26. Y. S. Joe, A. M. Satanin, and C. S. Kim, "Classical analogy of Fano resonances" , *Physica Scripta*, **74**, 259–266 (2006).
27. G. Schmid, L. F. Chi, "Metal Clusters and Colloids", *Advanced Matererial*, **10**, 7, (1998).
28. J. Zheng, C. Zhou, M. Yu and J. Liu, "Different sized luminescent gold nanoparticles", *Nanoscale*, **4**, 4073–4083 (2012).
29. Y. Wang and N. Herron, "Nanometer-Sized Semiconductor Clusters: Materials Synthesis, Quantum Size Effects, and Photo physical Properties", *The Journal of Physical Chemistry*, **95**, 2, (1991).

30. L. B. Scaffardi and J. O. Tocho, "Size dependence of refractive index of gold nanoparticles", *Nanotechnology*, **17**, 1309–1315 (2006).
31. K. B. Mogensen and K. Kneipp, "Size-Dependent Shifts of Plasmon Resonance in Silver Nanoparticle Films Using Controlled Dissolution: Monitoring the Onset of Surface Screening Effects" *The Journal of Physical Chemistry C*, **118**, 28075–28083 (2014).
32. R. Jin, Y. Cao, C. A. Mirkin, K. L. Kelly, G. C. Schatz, J. G. Zheng, "Photoinduced conversion of silver nanospheres to nanoprisms", *Science*, **294**, 1901–1903 (2001).
33. S. Link, Z. L. Wang and M. A. El-Sayed, "Simulation of the Optical Absorption Spectra of Gold Nanorods as a Function of Their Aspect Ratio and the Effect of the Medium Dielectric Constant", *The Journal of Physical Chemistry B*, **103**, 16, 3529 (1999).
34. L. Gunnarsson, T. Rindzevicius, J. Priekulis, B. Kasemo, and M. Kall, "Confined Plasmons in Nanofabricated Single Silver Particle Pairs: Experimental Observations of Strong Interparticle Interactions", *Journal of Physical Chemistry B* **109**, 3, (2005).
35. P. B. Johnson and R. W. Christy, "Optical constant of the noble metals", *Physical Review B* **6**, 12, 4370-4379 (1972).
36. C. L. Nehl and J. H. Hafner, "Shape-dependent plasmon resonances of gold nanoparticles", *Journal of Materials Chemistry*, **18**, 2415–2419 (2008).
37. S. Eustis and M. El-Sayed, "Aspect Ratio Dependence of the Enhanced Fluorescence Intensity of Gold Nanorods: Experimental and Simulation Study", *Journal of Physical Chemistry B* **109**, 16350-16356 (2005).
38. C. L. Nehl, H. Liao, and J. H. Hafner, "Optical Properties of Star-Shaped Gold Nanoparticles", *Nano Letters*, **6**, 4, 683-688 (2006).

39. C. J. Orendorff, T.K. Sau, and C. J. Murphy, “Shape-Dependent Plasmon-Resonant Gold Nanoparticles”, *Small*, **2**, 5, 636 – 639 (2006).
40. V. Giannini, A. I. Fernandez-Dominguez, Y. Sonnefraud, T. Roschuk, R. Fernandez-Garcia, and S. A. Maier, “Controlling Light Localization and Light-Matter Interactions with Nanoplasmonics”, *Small*, **6**, 22, 2498–2507 (2010).
41. X. Huang, I. H. El-Sayed, W. Qian and M. A. El-Sayed, “Cancer cell imaging and photothermal therapy in the near-infrared region by using gold nanorods”, *Journal of the American Chemical Society*, **128**, 128 2115 (2006).
42. T. Okamoto, I. Yamaguchi, T. Kobayashi, “Local plasmon sensor with gold colloid monolayers deposited upon glass substrates”, *Optics Letters*, **25**, 6, 372–374 (2000).
43. M A Garcia, “Surface plasmons in metallic nanoparticles: fundamentals and applications”, *Journal of Physics D: Applied Physics*, **44**, 283001 (2011).
44. H. Chen, X. Kou, Z. Yang, W. Ni, and J. Wang, “Shape- and Size-Dependent Refractive Index Sensitivity of Gold Nanoparticles” *Langmuir*, **24**, 10, 5233-5237 (2008).
45. M. Hu, J. Chen, Z. Y. Li, L. Au, G. V. Hartland, X. Li, M. Marquez, Y. Xia, “Gold nanostructures: engineering their plasmonic properties for biomedical applications”, *Chemical Society Reviews*, **35**, 1084-1094 (2006).
46. F. S. Rosarin and S. Mirunalini, “Nobel Metallic Nanoparticles with Novel Biomedical Properties”, *Journal of Bioanalysis and Biomedicine*, **3**, 4, 85-91 (2011).
47. X. Huang, M. A. El-Sayed, “Gold nanoparticles: Optical properties and implementations in cancer diagnosis” *Journal of Advanced Research* **1**, 13–28 (2010).

48. T. B. Huff, L. Tong, Y. Zhao, M. N. Hansen, J. X. Cheng, A. Wei, “Hyperthermic effects of gold nanorods on tumour cells”, *Nanomedicine*, **2**, 1, 125-132 (2007).
49. R. S. Ningthoujam, R. K. Vatsa, A. Kumar, B. N. Pendey, “Heating Tumors to Death using Functionalized Fe₃O₄ Magnetic Nanoparticles”, *Research Article*, **323**, (2011).
50. J. Chen, F. Saeki, B. J. Wiley, H. Cang, M. J. Cobb, Z. Y. Li, L. Au, H. Zhang, M. B. Kimmey, X. Li and Y. Xia, “Gold Nanocages: Bioconjugation and Their Potential Use as Optical Imaging Contrast Agents” *Nano Letters*, **5**, 473-477(2005).
51. J. J. Shi, Y. F. Zhu, X. R. Zhang, W. R. G. Baeyens and A. M. Garcia-Campana, “Recent developments in nanomaterial optical sensors”, *Trends in Analytical Chemistry*, **23**, 5. 351-360 (2004).
52. C. Lumdee, B. Yun, and P. G. Kik, “Wide-Band Spectral Control of Au Nanoparticle Plasmon Resonances on a Thermally and Chemically Robust Sensing Platform”, *the Journal of Physical Chemistry C*, **117**, 19127–19133 (2013).
53. W. Fritzsche and T. A. Taton, “Metal nanoparticles as labels for heterogeneous, chip-based DNA detection”, *Nanotechnology*, **14**, R63-R73 (2003).
54. P. Ghosh, G. Han, M. De, C. K. Kim, V. M. Rotello, “Gold nanoparticles in delivery applications”, *Advanced Drug Delivery Reviews*, **60**, 1307–1315 (2008).
55. A. Swarnapali, D. S. Indrasekara, B. J. Paladini, D. J. Naczynski, V. Starovoytov, P.V. Moghe , and L. Fabris, “ Dimeric Gold Nanoparticle Assemblies as Tags for SERS Based Cancer Detection”, *Advanced Healthcare Materials*, **2**, 10, 1370-1376 (2013).

56. K. D. Alexander, M. J. Hampton, S. Zhang, A. Dhawan, H. Xu, R. Lopez, “A high-throughput method for controlled hot-spot fabrication in SERS-active gold nanoparticle dimer arrays”. *Journal of Raman Spectroscopy* **40**, 12, 2171-2175 (2009).
57. H. A. Atwater and A. Polman, “Plasmonics for improved photovoltaic devices”, *Nature Materials*, **9**, 205-213 (2010).
58. T. Soga, “Nanostructured Materials for Solar Energy Conversion” First edition Copyright Elsevier B.V. (2006).
59. P. Oelhafen and A. Schuler, “Nanostructured materials for solar energy conversion”, *Solar Energy*, **79**, 110-121 (2005).
60. S. Kim, J. Jin, Y. J. Kim, I. Y. Park, Y. Kim, S. W. Kim, “High-harmonic generation by resonant plasmon field enhancement”, *Nature*, **453**, (2008).
61. M. Iwanaga and B. Choi, “Heteroplasmon Hybridization in Stacked Complementary Plasmon-Photonic Crystals”, *Nano Letters*, **15**, 1904–1910 (2015).
62. H. Guo and J. Guo, “Hybrid plasmon photonic crystal resonance grating for integrated spectrometer biosensor”, *Optics Letters*, **40**, 2, (2015).

Chapter four

Experimental methods

4.1 Introduction

In this chapter the fabrication and characterization of two-dimension photonic crystal nanocavities (2D PC NC) is discussed. This technique involves E-beam lithography and dry etching. The PC NCs are characterised using far field spectroscopy. The deposition of gold nano structures inside a cavity is also discussed. Here, two techniques have been used, optical printing using a focused laser and electron beam lithography (EBL).

4.2 Cavity substrates

Optical nanocavities (NCs) were fabricated onto a freestanding silicon nitride (SiN) membrane purchased from Silson Ltd. The membrane was prepared at Silson Ltd by depositing a thin layer of silicon nitride onto a 381 μm thick silicon wafer. The sample was then chemically etched to produce a freestanding SiN membrane (or SiN window) as shown in figure 4.1. The size of the SiN window used was 0.5 X 0.5 mm^2 having a refractive index and thickness of 2.1 and 200 nm respectively. Such thin membranes are very fragile; therefore, great care needs to be shown in handling samples during the fabrication process.

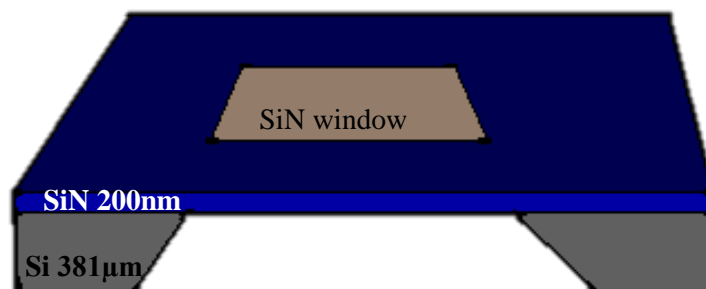


Figure 4.1: A schematic diagram of a freestanding SiN membrane

4.3 Electron Beam Lithography (EBL)

Lithography is a process whereby a desired structure or design is transferred to a surface. Depending on the required feature size, the radiation source used to create the image can be thermal, optical or electron beam radiation. For instance, optical lithography can be used to print features having sub-micron size. EBL can be used to create features having a size of tens of nanometres [1]. EBL techniques also have the advantage that a pattern can be changed and improved readily in the system software, unlike optical photolithography where physical mask-plates are needed. This therefore reduces costs and time delays associated with mask production. However, EBL is a serial technique in which patterned features are written pixel-by-pixel, therefore exposure may consume many hours when writing large and complex designs. Also EBL systems are expensive and highly complex, and require substantial ongoing maintenance to optimize performance.

In this thesis EBL is used to create photonic crystal nanocavities. The machine system used (Raith-150) was housed in the Centre for Nanoscience and Technology at the University of Sheffield as shown in figure 4.2.

Raith-150 software has its own built-in design tools based on the GDSII format. The GDSII editor allows basic structures to be drawn such as circles, polygons, open paths, single dots and filled rectangles. The advantage of using the GDSII editor is its ability to build small structures and collect them together into a final design form. Moreover, it can arrange different elements of a structure into levels, which allows more flexibility to control the surface dose rate.



Figure 4.2: EBL system at the Centre for Nanoscience and Technology University of Sheffield

Three main layers were used in designing photonic crystal nanocavities (PC NCs). The first was a “text” layer. This layer was used to label the PC NC properties. The second layer was the PC NCs design, while the third layer was known as “manual marks” and was used to determine the border of membrane area. An image of the PC NC design on a SiN membrane is shown in figure 4.3. The EBL exposure parameters that have been used in this work are shown in Table (4.1).

Table 4.1 EBL parameters used for PC fabrication

E-beam energy (KV)	E-beam current (μA)	Dose ($\mu\text{C}/\text{cm}^2$)	Dose factor
30	0.038-0.04	240	1.3

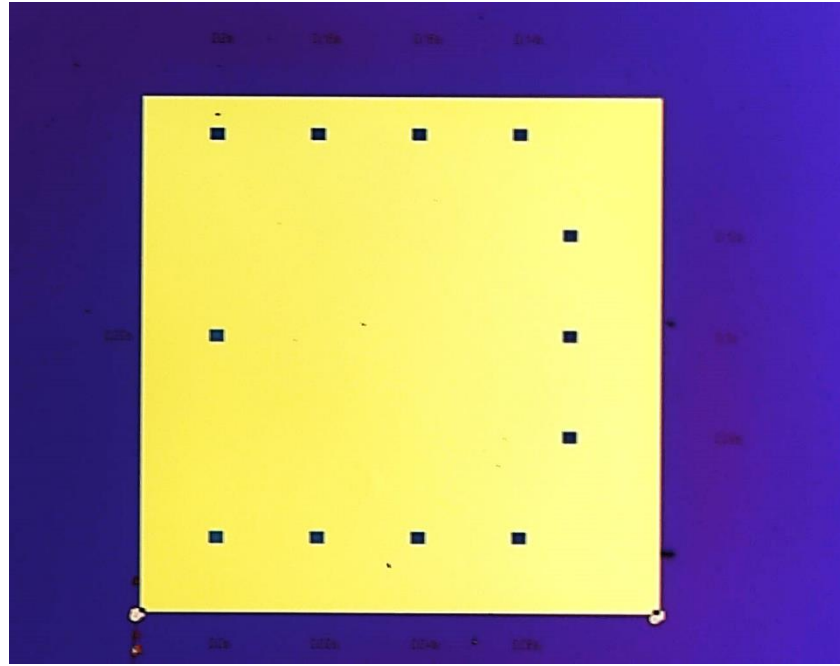


Figure 4.3 SiN membrane window containing 12 PC NCs

4.4 Sample preparation

Before depositing a resist layer onto the sample surface, it must have cleaned to remove any surface contamination or dust particles. Firstly, the sample is rinsed in heated acetone, followed by isopropyl alcohol (IPA). It is then dried using a N₂ gas jet. Finally, the sample is placed on a hot plate at 100 °C for one minute in order to evaporate any residual solvent.

4.5 E-beam resist

To achieve high resolution using e-beam lithography, polymethyl-methacrylate (PMMA) resist was used having a molecular weight of 950kDa. Before the sample was coated with the e-beam resist, it was first baked on a hot plate for one minute at 100° C. The PMMA resist was then spun on to the SiN membrane for 30 seconds at speed of 3500 rpm, creating a thin PMMA layer of thickness \approx 200

nm. The substrate was then baked on a hot plate at 180 °C for 10 minutes in order to harden the resist by removing any residual solvent. Finally, the sample was ready for electron beam exposure.

There are two types of an EBL resist; positive and negative. In a positive photoresist, the area exposed to the e-beam becomes soluble in a developer and can thus be used to produce positive image of the exposed pattern. In a negative photoresist, the area exposed to the e-beam becomes insoluble in a developer and can thus be used to produce negative image of the exposed pattern as shown in figure 4.4.

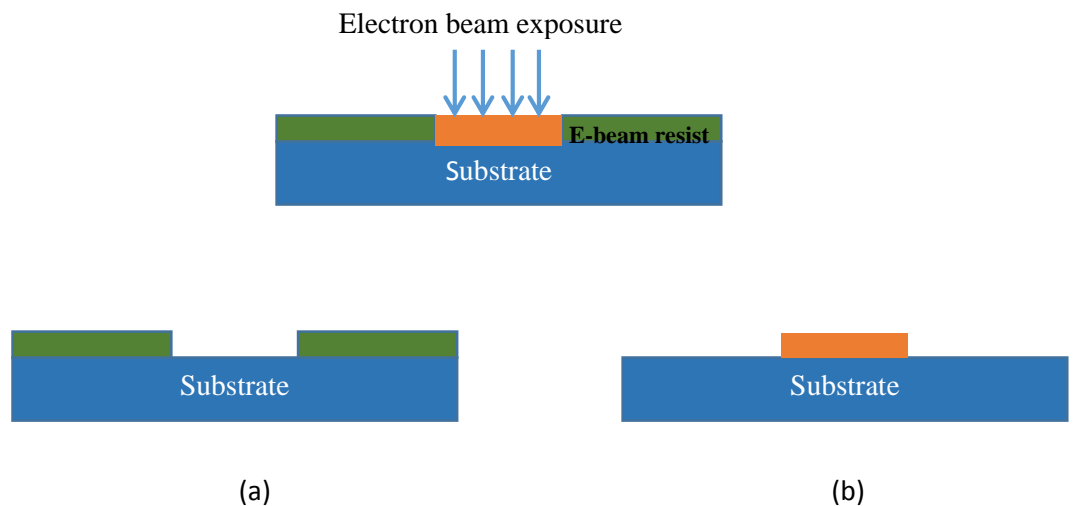


Figure 4.4: (a) a positive resist and (b) a negative resist

4.6 Proximity effect

During the lithography process, the scattering of the focused electron-beam affects the resolution of the features that are written into the resist. There are two mechanisms by which the e-beam is scattered. The first is forward scattering of the e-beam in the resist material. This broadens the beam diameter and affects

the size of the printed pattern. The second scattering mechanism is back scattering. Here, the electron beam reaches the surface of the substrate and undergoes back scattering. As a result, areas that are nearby the incident beam are also exposed, leading to a reduction in the received dose across the exposed area [2]. The combination of both types of scattering are called proximity effects. Proximity-effect-correction (PEC) is achieved by employing Monte Carlo simulation methods that compute electron trajectories penetrating both the resist layer and substrate. However, the energy density absorbed in the resist as a function of acceleration voltage and resist thickness can be modelled to adjust the electron-beam dose to achieve a suitable exposure [3, 4] as shown in figure 4.5.

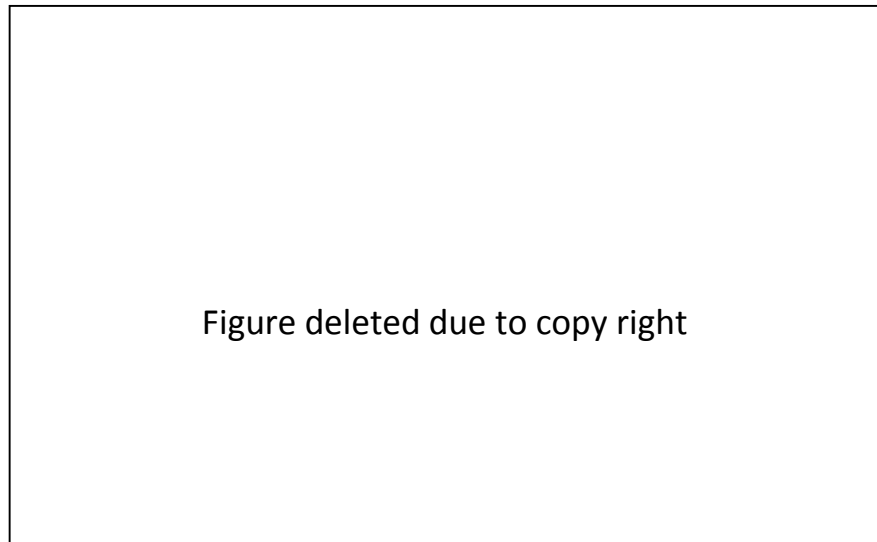


Figure 4.5: Monte Carlo simulation of electron scattering in a PMMA resist on a silicon substrate at (a) 10 kV and (b) 20 kV. Figure reproduced from [5]

4.7 Resist Development

To transfer a pattern into the resist, the sample is developed in a solution called a developer. It is important to choose a high resolution developer to ensure that the side-wall of resist features are vertical. There are two parameters that effect the side walls of the resist features; excessive e-beam dose and inadequate or excessive resist development. On exposure, the resist becomes soluble in the developer solution. A common developer for PMMA is MIBK: IPA 1:3 (methyl isobutyl ketone: isopropyl alcohol) solution. To develop the PMMA, the sample is immersed for 30 seconds in a developer solution after which it is dried with a N₂ gas jet for 30 seconds.

4.8 Dry etching

An etching process is used to transfer the patterns written into a resist after development on to the sample surface. There are two type of etching processes; wet and dry etching.

In wet etching, a chemical solution is used to remove the substrate material not covered by the patterned resist. Although this method is cost effective with high selectivity, it is not suitable for etching small sized features (sub tens of nanometres). In a dry etching process, a chemical reaction of gasses or plasmas are used to remove unwanted material using a high-energy ion beam. Therefore, this technique is the optimum choice to create features sizes of sub-tens of nanometres. There are additional advantages to using a dry etching technique, including:

-
- 1- Isotropic etching (equal etching rates in both vertical and horizontal directions) or anisotropic etching (etching proceeds faster in one plane than in another).
 - 2- High selectivity between etched and non-etched layers.
 - 3- Automated process and better control.
 - 4- No inadvertent elongation during the etching process.
 - 5- Reduced handling of hazardous acids and solvents.

There are however few disadvantages to the dry etching technique, including:

- 1- Use of toxic and corrosive gases.
- 2- Use of expensive equipment.

Generally, dry etching is divided into two major types. One type of process relies on non-plasma based etching using fluoride or interhalogen gases. This process is used to etch Si, has high selectivity to resist layers, and does not require plasma-processing equipment. A second type of dry etching is called plasma based etching. This technique needs a RF field to drive the highly reactive chemicals toward the target. There are a number of plasma based dry etching processes:

- 1- Physical etching, based on bombarding the target by energized ions or atoms, leading to dislocation of atoms in the substrate (here the energy of the ions produced exceeds their binding energy).
- 2- Chemical etching, based on chemical reaction between atoms radicals and ions with atoms in the substrate. The chemicals are absorbed by the substrate leading to chemical reaction and desorption of by-products or volatile products.

-
-
- 3- Inductively Coupled Plasma etching (ICP).
 - 4- Reactive Ion Etching (RIE).

4.9 Plasma system (ICP and RIE).

ICP and RIE can achieve fast etch rates, uniformity, clean chemistries, high vertical profile, and low device damage [6]. Oxford Instruments Ltd. supplied the Inductively Coupled Plasma (ICP) and Reactive Ion Etching (RIE) etcher used. The gases used to etch silicon nitride (Si_3N_4) are either fluorine and/or chlorine based gases such as CHF_3 [7, 8]. This process creates radicals and ions, which react with Si in Si_3N_4 to convert it to volatile products [9].

The RIE chamber is supplied with two coils as shown in figure 4.6 (a). These coils create an electromagnetic field inside the chamber through the radio frequency (RF) (13.56 MHz) currents that flow in the coils. For low pressure gas flows rate, these coils produce a plasma (electron, ions and radicals) as well as directing, accelerating ions and electrons inside the chamber toward the surface of the substrate [7]. The free radicals enhance chemical reactions with atoms in the substrate while the energetic ions enhance the anisotropic etching of the substrate surface [10].

In addition to the RF coils, the ICP system includes a 2.54 GHz plasma source to increase electromagnetic induction and generate a high density of ions [11] as shown in figure 4.6 (b). The gas recipes for both RIE and ICP are illustrated in Table 4.2. The residual PMMA that remain after the etching process is then removed using an oxygen plasma asher tool. The whole fabrication process used to create a two dimensional photonic crystal L3 cavity is summarized in figure 4.7.

Figure 4.8 (a) and (b) shows a number of scanning electron microscope (SEM) images of SiN based photonic crystal L3 nanocavities that were fabricated. The creation of holes having a circular shape is an indication of the existence of straight side-walls and thus high cavity quality factor. This can be attributed to using a high EBL beam energy (30 kV) and a dry etch technique. Figure 4.8 (c) and (d) shows SEM images of the topside and the underside of a typical PC. Analysis of this image suggested that holes had a size of 140 nm at the top of the membrane, a value reduced to 119 nm for holes at the bottom side, corresponding to a taper angle of 5.42° . This angle is considered to be typical with that reported in previous work on SiN based PC nanocavities, where taper angles were reported ranging from 4° to 8° [12]. Excessive taper angles are the main reason that some of the structures studied in this thesis had a relatively low Q factor.

Table 4.2 the recipes of ICP and RIE used in this work

Tool	Gas	Rate (sccm)	Pressure(mTorr)	RF Power (W)	Etching time(min)
ICP	CHF3	30	35	480	20
RIE	CHF3	30	35	70	16

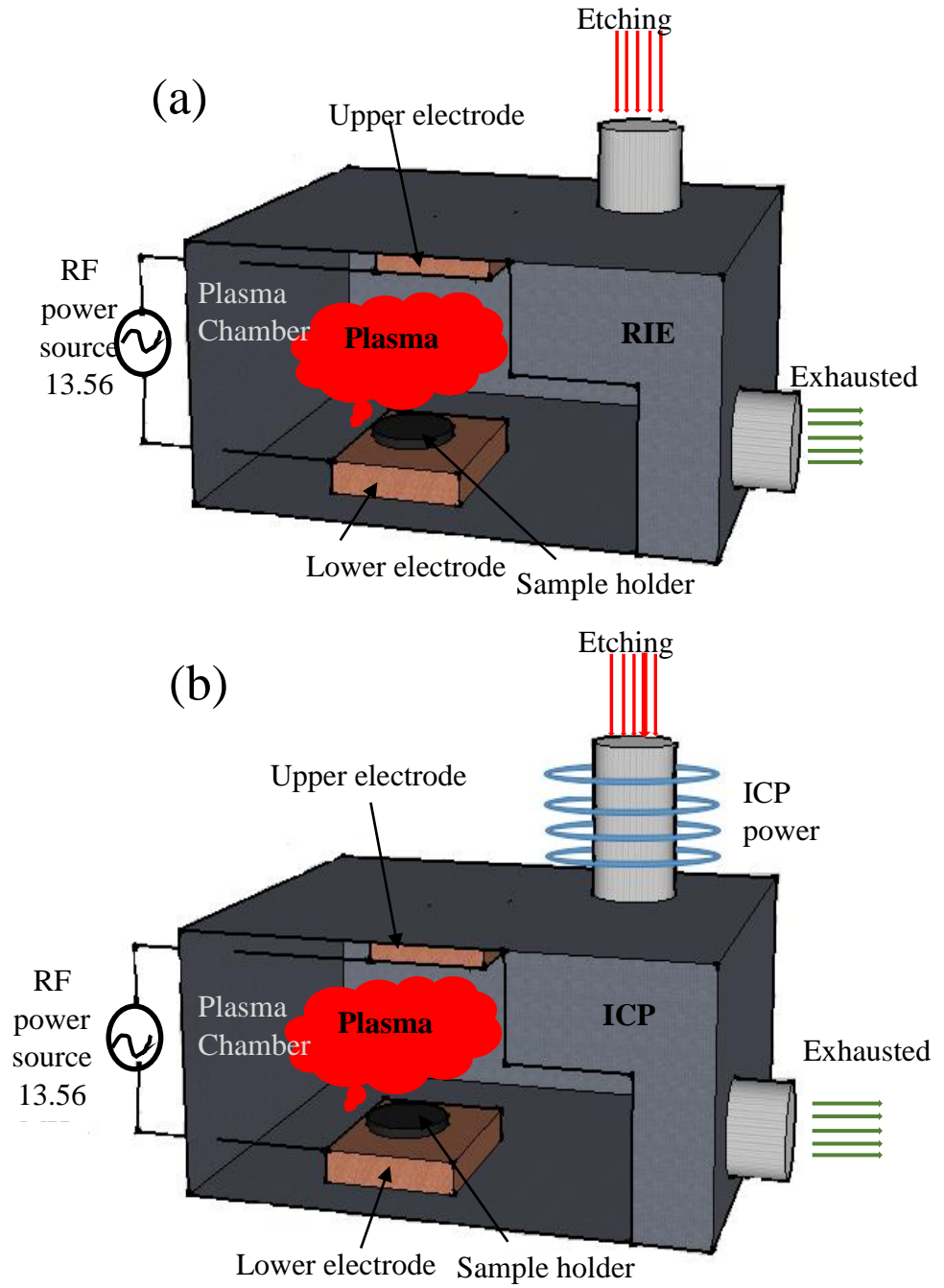


Figure 4.6: schematic of (a) RIE, (b) ICP tool

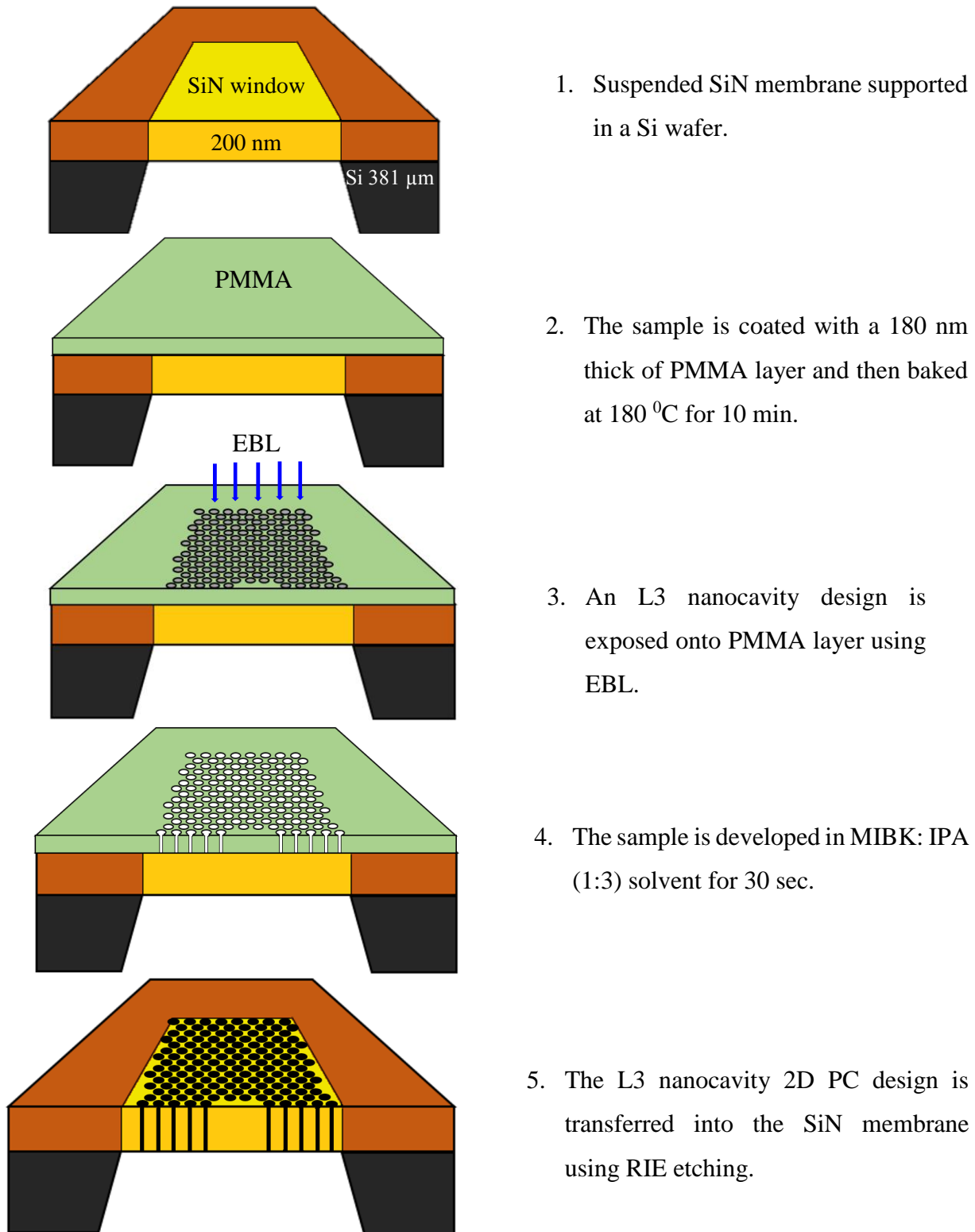


Figure 4.7: Schematic illustrating the fabrication of a 2D PC L3 nanocavity.

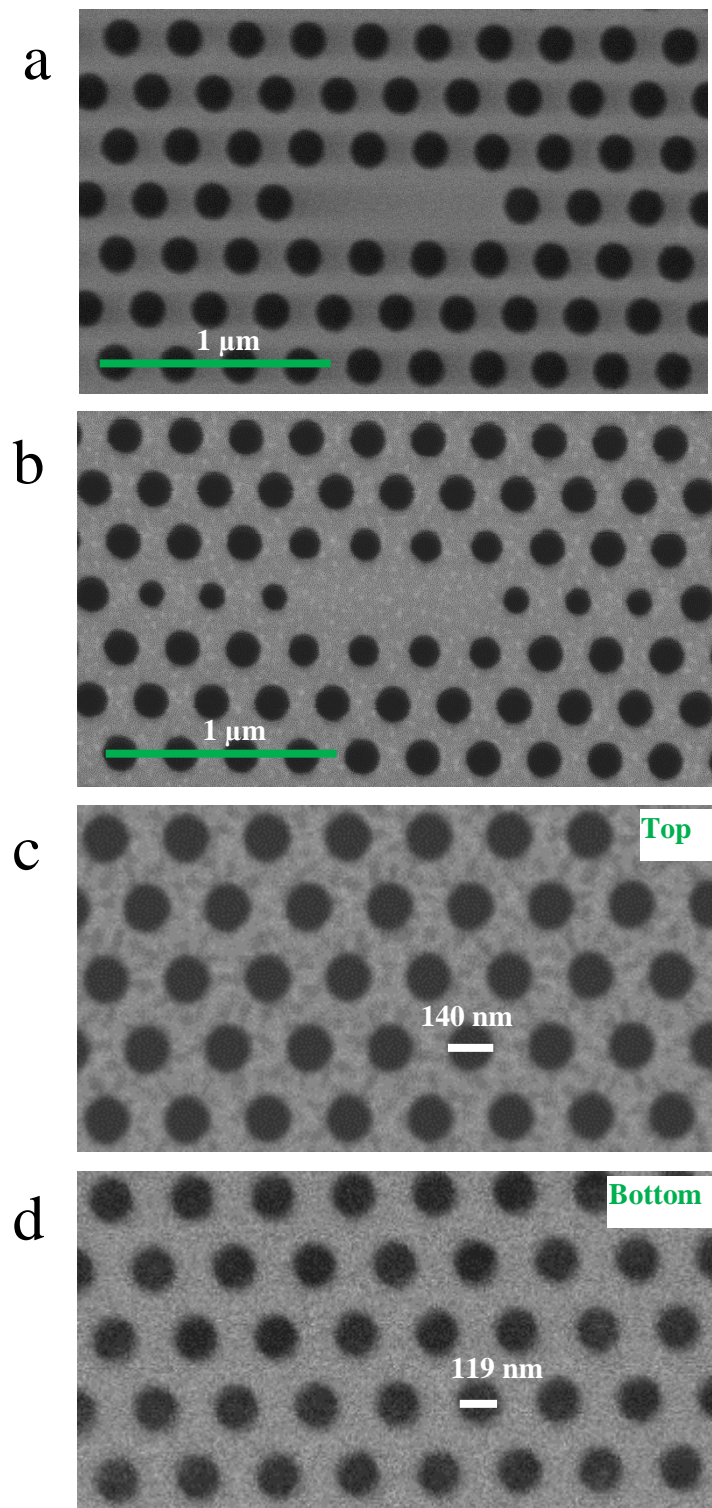


Figure 4.8: (a) and (b) Scanning electron micrographs (SEM) images for two type of L3 nanocavities design used in this work. (c) and (d) SEM image of top and bottom surface of a typical structure, used to estimate the verticality of the hole side wall. The white spots that appear in (b) and (c) are residual PMMA resist

4.10 Photoluminescence (PL) Spectroscopy

Far field optical spectroscopy was used to explore the optical properties of the nanocavities. The system used is shown schematically in Figure 4.9. Fluorescence spectroscopy was performed using a diode pumped solid state (DPSS) laser at 532 nm focused through a 100X long working distance objective lens (6 mm) having a 0.77 numerical aperture (NA) to a 2.5 μm diameter spot on the cavity surface. A neutral density filter was used to control the intensity of the incident beam. The objective lens was mounted on a three-dimensional piezo motor stage (Piezosystem Jena Tritor 100, Micro XYZ Positioner stage NV 40/3s controller) allowing the lens to move relative to the sample. The sample was excited at normal incident angle and the emitted photoluminescence PL collected at the same angle. The emitted PL from the structure was passed through a polarizer and long pass filter with a cut-off wavelength at 532 nm to reject the excitation laser, before it entered the spectrometer. The emitted light from the structure was directed to a spectrometer (Jobin Yvon Triax 320) through a 0.08 mm wide slit, which controlled the spectrometer resolution. Inside the spectrometer, light was dispersed (analysed) using two different gratings having 1200 and 300 line/mm giving spectral resolution of 0.07 and 0.3 nm respectively. Finally, the dispersed light was imaged onto a nitrogen cooled CCD. A white light source was used to align the laser spot on the PC.

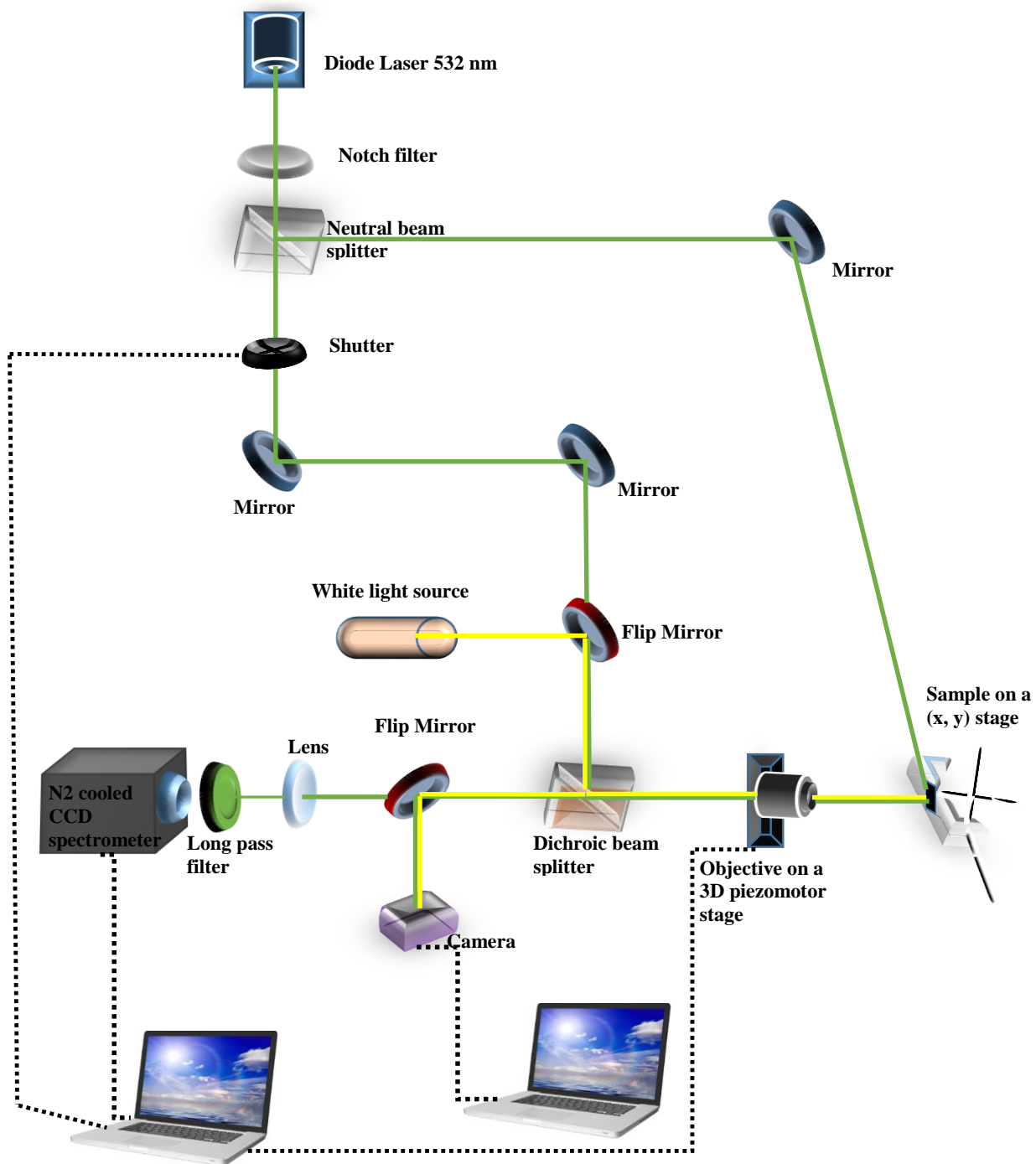


Figure 4.9: A schematic of the PL system used.

4.11 Dark field spectroscopy

Dark field spectroscopy was performed using an inverted microscope with oil immersion lens, as shown in Figure 4.10. This microscope was used to measure the scattered radiation from gold nano disks printed on SiN membranes. A small drop of immersion oil ($n = 1.515$) was dispensed on the sample and the sample was placed face down on the microscope stage. The objective lens was brought into contact with the oil on the sample. The NA of the objective (0.5) is less than that of the condenser lens (0.8-0.95) so only the scattered light is collected. The dark-field scattering measurements was done with the assistance of Mr. Alastair Humphrey and Prof. Bill Barnes at the University of Exeter.

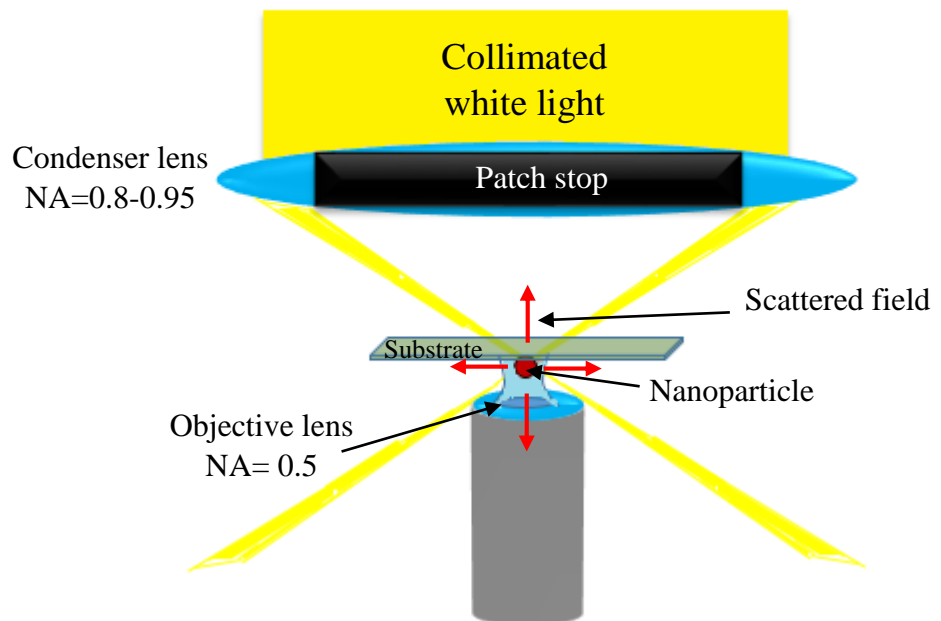


Figure 4.10: Dark field scattering spectroscopy system

4.12 Printing gold nanoparticles on Silicon Nitride substrate

To create plasmonic structures, metal nanoparticles were patterned onto dielectric substrates. Here, two techniques were used to deposit gold nanoparticles on a structure of interest. The first method used optical printing as described in section 4.12.1 to place single gold NPs onto a cavity surface [13]. Gold were also dimers patterned directly into a nanocavity surface using electron beam lithography (EBL) as discussed in section 4.12.2.

4.12.1 Optical printing method

Single Au NPs were patterned onto the surface of a nanocavity using a modification of an optical printing technique [13]. This work was done with assistance of Jaekown Do at Ludwig-Maximilians-University Munich. Figure 4.11 (a) shows a schematic of the system used to pattern the NPs. Here, the nanocavity was placed under a dark-field microscope (DFM) and a drop of an aqueous dispersion of 150 nm Au NPs was deposited on the cavity surface. On entering the region illuminated by a 1064 nm Gaussian beam, a gold NP first experiences a radial force (resulting from the absorption and scattering forces) that brings it towards the beam centre. The NP then experiences an axial force (known as a gradient force) that pushes it toward the region of highest beam intensity, i.e. toward the substrate (see calculated force map in Figure 4.11(b)). The magnitude of the absorption and scattering forces are however lower than the gradient force resulting from the small absorption and scattering cross section of a 150 nm spherical Au NP at 1064 nm. Figure 4.12 shows a successful printed gold NP inside L3 nanocavity.

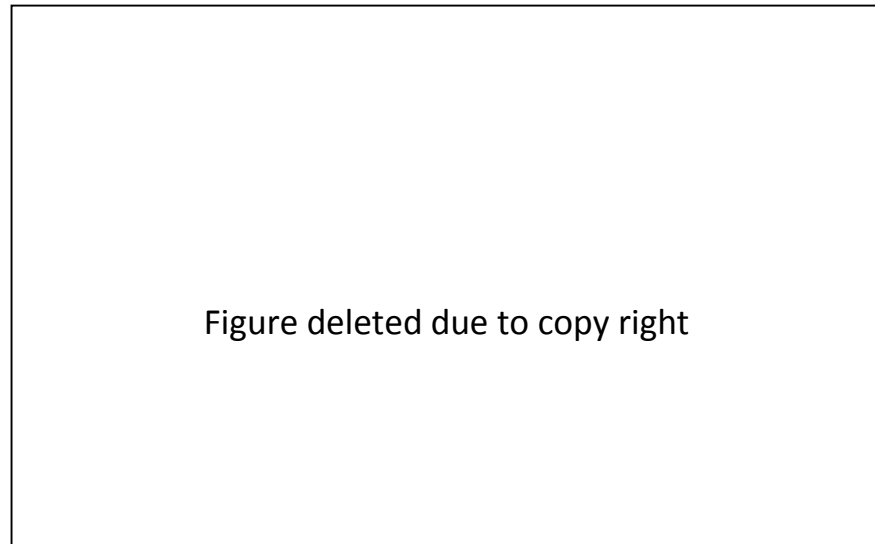


Figure 4.11: (a) Schematic figure of the experimental setup used to pattern Au NPs onto the nanocavity surface. (b) Calculated force map (in units of pN) acting on a single spherical gold nanoparticle (150 nm diameter) at the focus of a 1064 nm CW laser. Figure taken from reference [14].

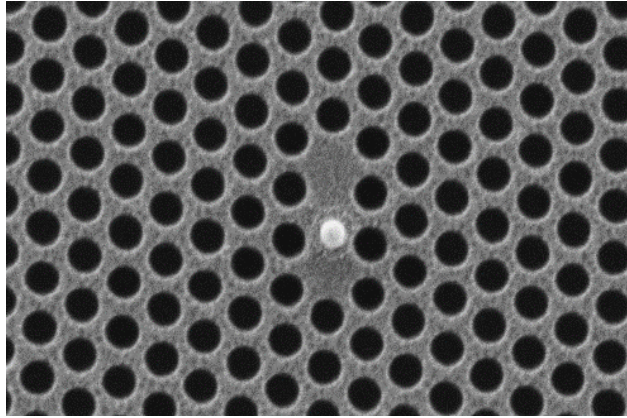


Figure 4.12: Au NP of 150 nm size printed onto L3 nanocavity surface using an optical printing method. Figure taken from reference [14]

4.12.2 Electron beam lithography (EBL) printing method.

The nanofabrication of gold nanoparticles on a silicon nitride membrane using EBL uses a process that is similar to the fabrication of photonic crystals. The fabrication steps are illustrated in figure 4.13. A thin layer (~ 180 nm) of a high resolution and electron-sensitive PMMA resist was coated on a freestanding silicon nitride membrane, and then baked at 180⁰ C for 10 minutes. It was then patterned using EBL to create the region in which the metallic dimers will eventually located. The exposed resist was developed and removed selectively using (MIBK: IPA) developer. A thin layer of gold (80-100 nm) was then deposited at a rate of (5 nm / sec) thermal evaporation to cover the sample. Finally, a piranha (H₂SO₄+ H₂O₂) acid solution was used to lift-off the remaining resist to leave holes filled with metal as shown in figure 4.14. It is important to note that a number of gold nanostructures did not survive the lift-off process as shown in figure 4.15. To solve this problem, two actions were developed. The first involved creating shallow holes (\approx 10 nm) on the SiN membrane surface using ICP through the resist. This tended to help to fix the

NPs in position. In addition to this, a thin layer of titanium (typically less than 5 nm) was used as adhesion layer. It was found that a thick layer of titanium increased the attenuation of the surface plasmon [15]. Chromium (Cr) was also explored for this purpose [16].

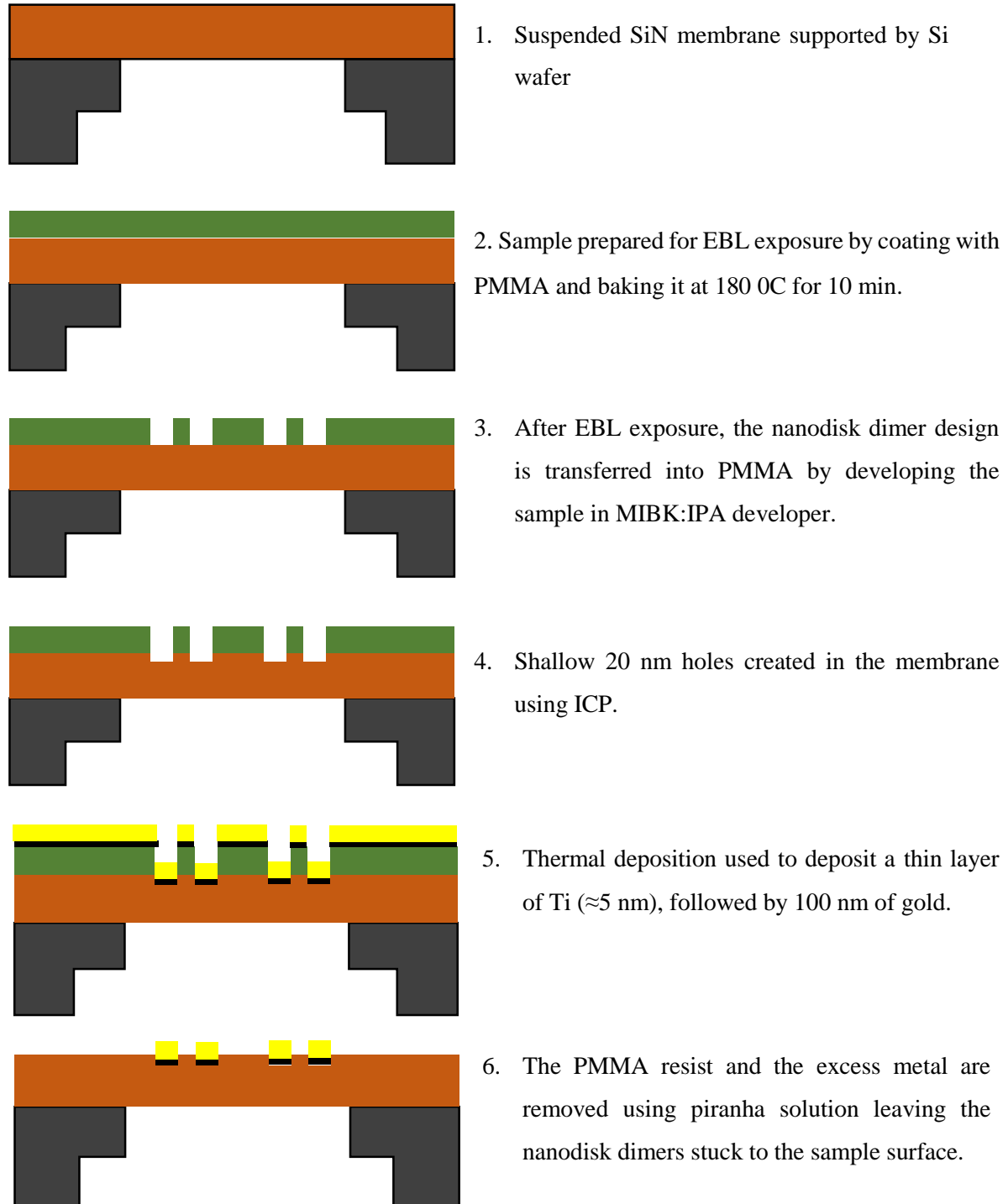


Figure 4.13. Schematic illustrating the fabrication steps to create gold nano structure on a SiN membrane.

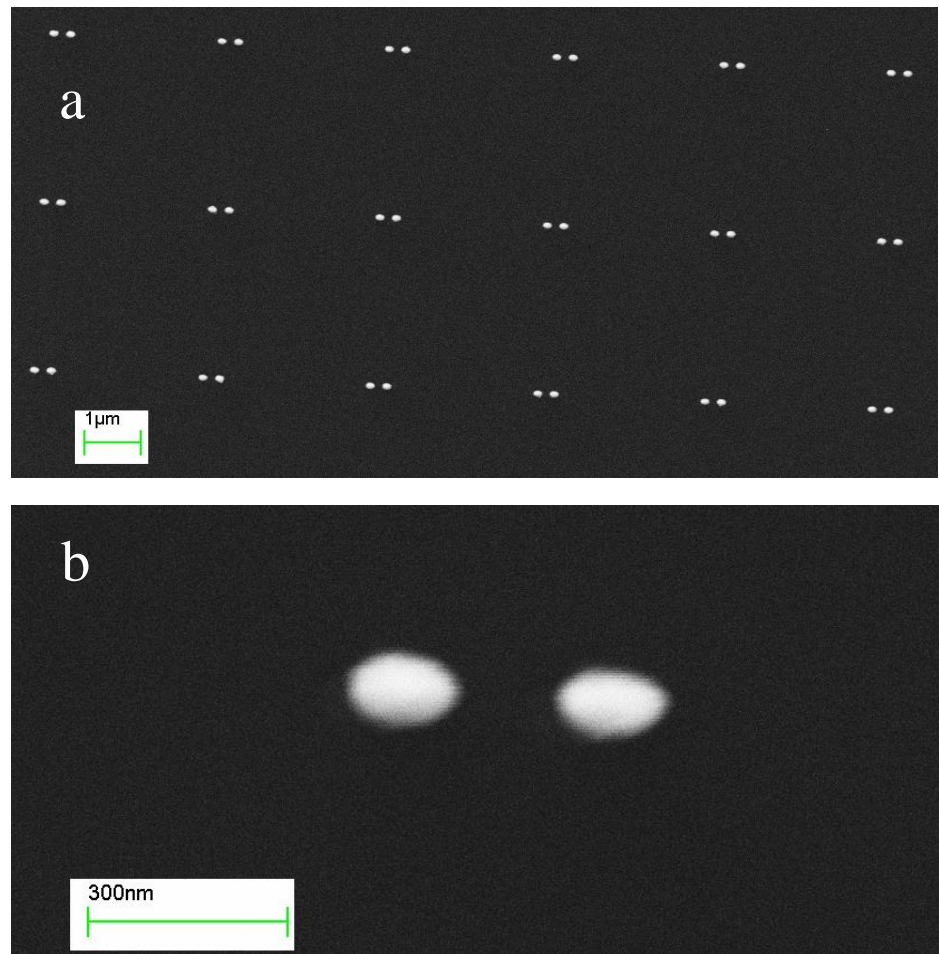


Figure 4.14: (a) An array of printed gold nano disk dimers on SiN membrane.
(b) Magnified image of gold nano disk dimers.

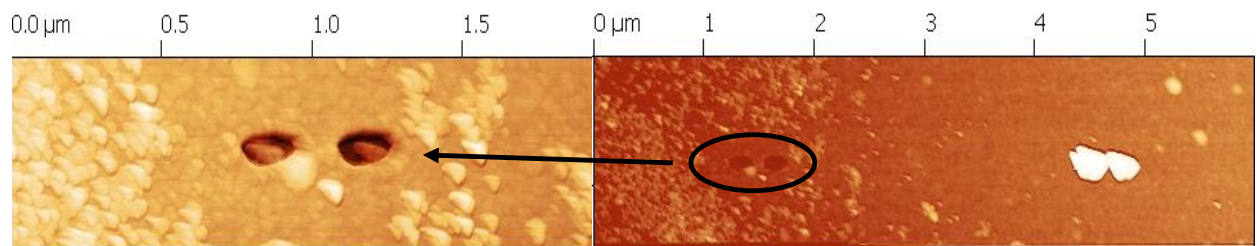


Figure 4.15. AFM image of missing gold nano disk dimers a SiN surface removed during the lift-off process.

4.13 Printing gold nanodisk inside L3 nanocavity using EBL method.

To print gold nano structures into an L3 nanocavity requires high (sub-micron) precision, and registration between process steps indeed, it has been necessary to combine two fabrication processes: namely two dimensional photonic crystal L3 nanocavity (2D PC L3 NC) fabrication and printing of gold nanostructures. To create the hybrid photonic-plasmonic nanocavity, the structure was designed using CAD tools. Four specific marks (crosses) were made around the area in which the L3 nanocavity would be printed. Each part of the structure was then arranged in a layer as shown in Figure 4.16.

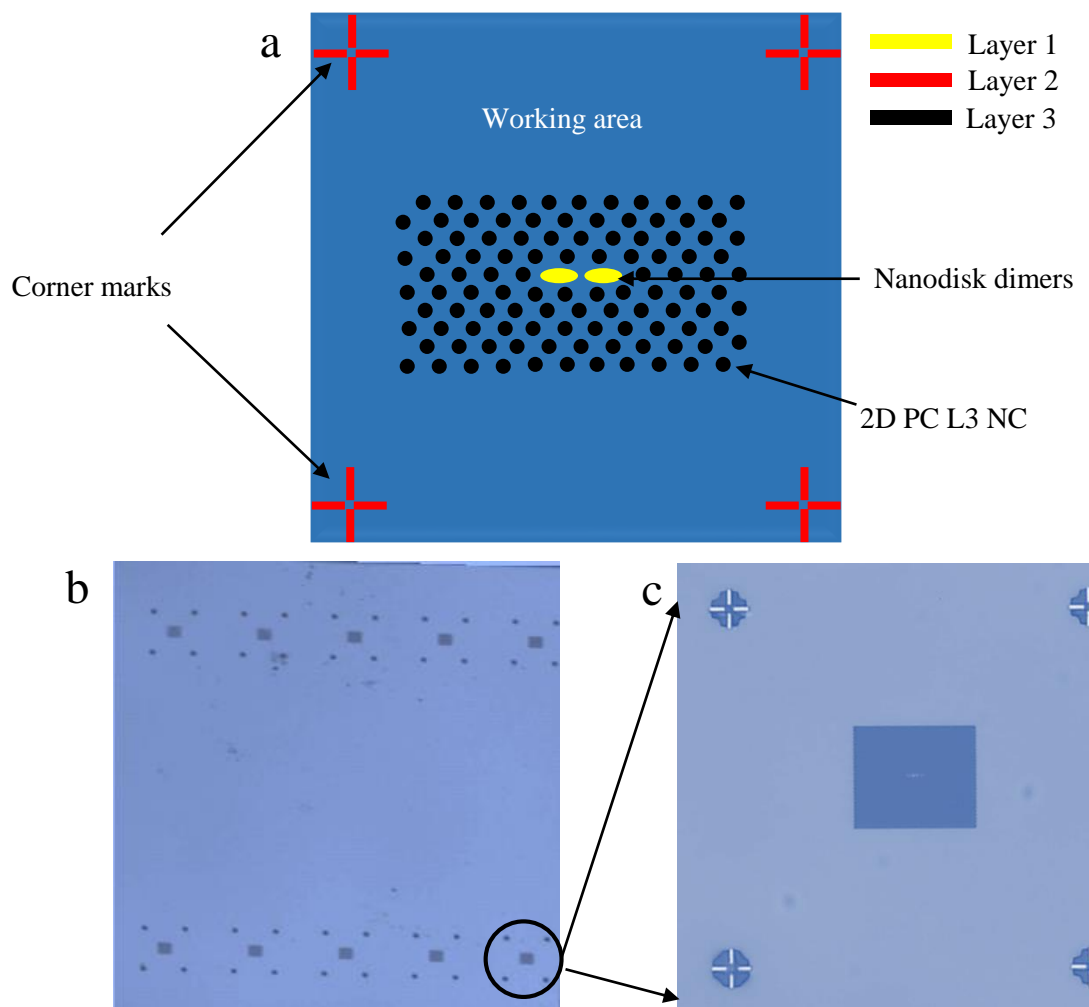


Figure 4.16: (a) Schematic of printed nanodisk dimer inside L3 nanocavity showing the reference marks around the working area. (b) & (c) showing optical microscope images of SiN membranes containing a series of printed PC arrays and a magnified view of a single PC array respectively.

The placement of the corner markers around the working area is critical to allow the position of the dimer to be located, then allowing the L3 nanocavity to be printed around the nano dimer with high accuracy. Thus both gold nanodisk and corner marks are printed first followed by the L3 NC fabrication. Finally, a plasma asher was used to clean the sample surface and remove any contamination or residual resist. A successfully printed pair of gold dimer nanodisks is shown in figure 4.17 (a). As discussed previously, the printing of gold nanostructures requires two fabrication stages, therefore there is a high probability that they are removed or shifted from their position, as shown in figure 4.17(b) & (c). In addition, a slight shift of the position nanostructure location (as identified by the corner marks), can lead to large mismatch between the NC and the dimers as shown in figure 4.17d.

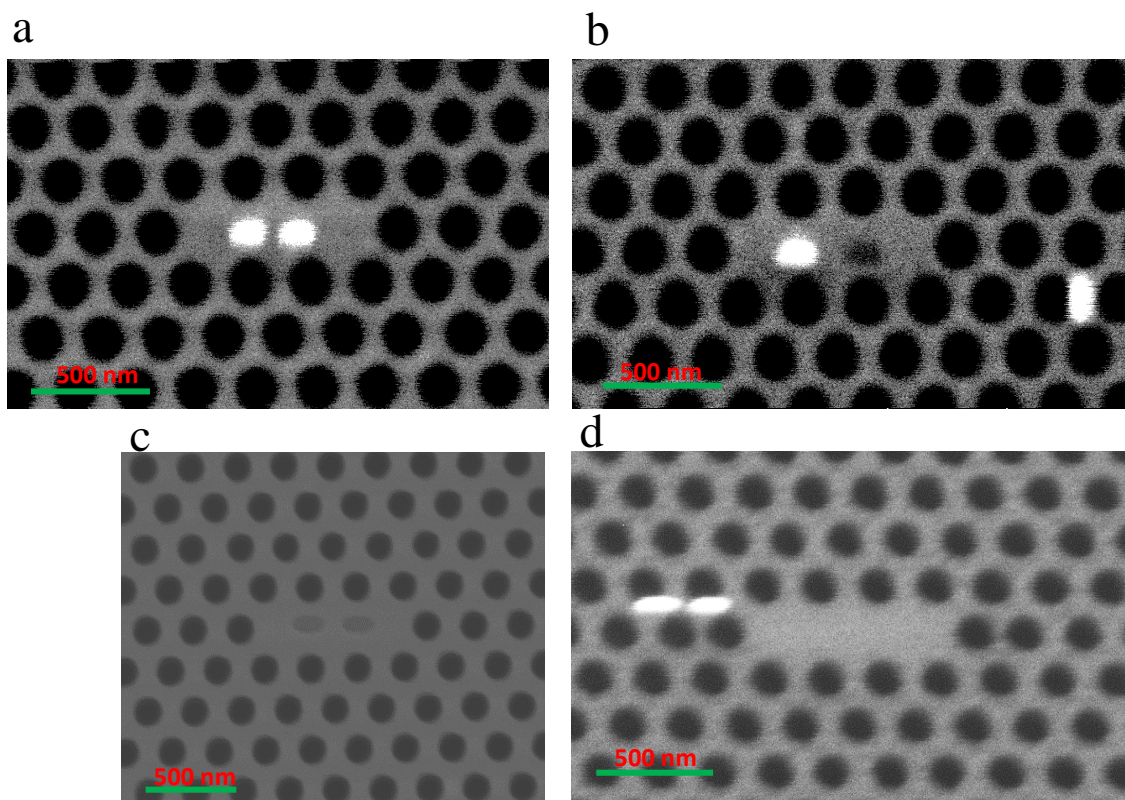


Figure 4.17: (a) A successful attempt to printing gold nanodisk dimers inside L3 NC. (b) and (c) a structure in which one of the printed gold nanodisks has been displaced far from the cavity or when both of them were removed during lift-off process. (d) Shows a structure in which there is a large unintentional mismatch between the location of nanodisks dimer and the nanocavity centre.

4.14 Langmuir-Schaefer film deposition method (LS)

The ability to combine organic molecules in a nanoscale cavity permits a system to be created that is electrically and optically active. Such components can then be used as chemical sensors [17, 18] and detectors [19].

The Langmuir-Schaefer deposition technique is a method used to deposit one or more monolayers of a material from an air-liquid interface onto a solid substrate. Here, a thin film is formed by dipping a solid substrate in a floating material either horizontally (Langmuir-Schaefer) or vertically (Langmuir-Blodgett) [21] as shown in Figure 4.18. The advantage of the L-S and L-B deposition techniques are a high control of film thickness, homogenous deposition over a large area and the deposition of multilayers of different materials.

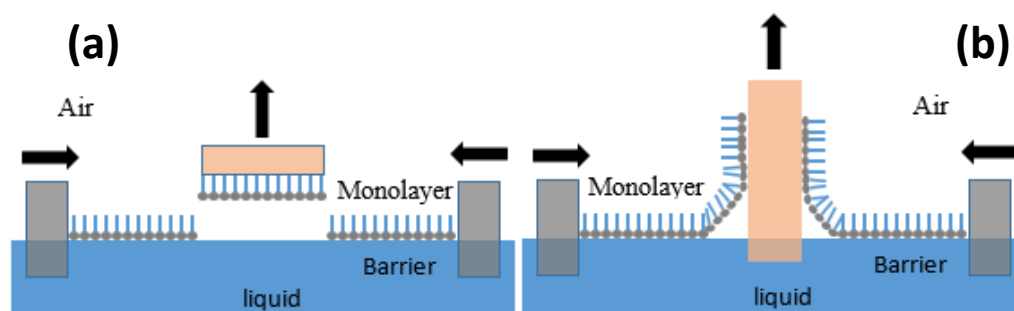


Figure 4.18: scheme a) Langmuir-Schaefer b) Langmuir-Blodgett monolayer deposition

4.15 Monolayer formation

Organic compounds can be divided into two categories; water soluble compounds (polar) and non-soluble compounds (nonpolar) [17]. Polarity arises due to the non-uniform (asymmetrical) distribution of charges across the molecular structure, resulting in the formation of a permanent electric dipole

moment. The best example of a polar compound is water. Here, two hydrogen atoms share electrons with an oxygen atom having a strong electron-withdrawing tendency. This causes a separation between charges and results in a permanent electric dipole. When a component is dissolved in water, solvation occurs as a consequence of the interaction between the dipole moments of the solvent and solute. In contrast, dipoles on symmetrical molecules in which the distribution of charges between two atoms are equally shared, such as C-C and C=C, do not result in the formation of dipoles. Most of such non-polar compounds are therefore insoluble in water at room temperature.

In the Langmuir-Schaefer deposition method, it is necessary to identify a material in which the molecules have a hydrophilic and a hydrophobic component. The molecules can arrange themselves at an air water interface, with the hydrophilic head immersed in the liquid and hydrophobic tail extending into the air [20] as shown in figure 4.19.

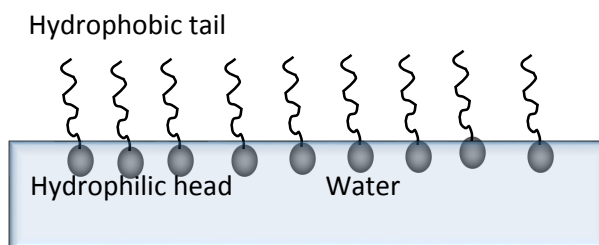


Figure 4.19: surfactant arrangement at air water interface.

A monolayer film can be transferred onto a substrate using the Langmuir-Schaefer (or Langmuir-Blodgett) technique, leading to reduction in the number of the molecules at the air-water interface. A constant density can however be maintained at the surface by compressing the surfactant through controlling the surface pressure [17].

4.16 Atomic force microscope (AFM)

An atomic force microscope (AFM) is an imaging instrument that is capable of recording high-resolution image of a surface at sub-nanometre length scale in both horizontal and vertical directions. Here, a Veeco-Dimension 3100 was used, operating in tapping mode as shown in figure 4.20. AFM works by measuring the alternation in the reflected laser signal produced as a micron-sized sharp tip scans across a surface. A silicon cantilever was used having force constant of 40N/m and resonant frequency between 200–400 kHz. In tapping mode, a piezo stack excites the cantilever causing the cantilever to oscillate vertically. Although, the cantilever oscillates continuously with same energy (in which energy is supplied by a piezo stack), the tip deflects as it touches the surface. As a result of this deflection the reflected laser beam, or “return signal” (when imaged onto a photodiode) generates an electronic signal that reveals information about the vertical height of the specimen surface [22]. This process is detailed schematically in figure 4.21.



Figure 4.20: Veeco-Dimension 3100 AFM device at the University of Sheffield

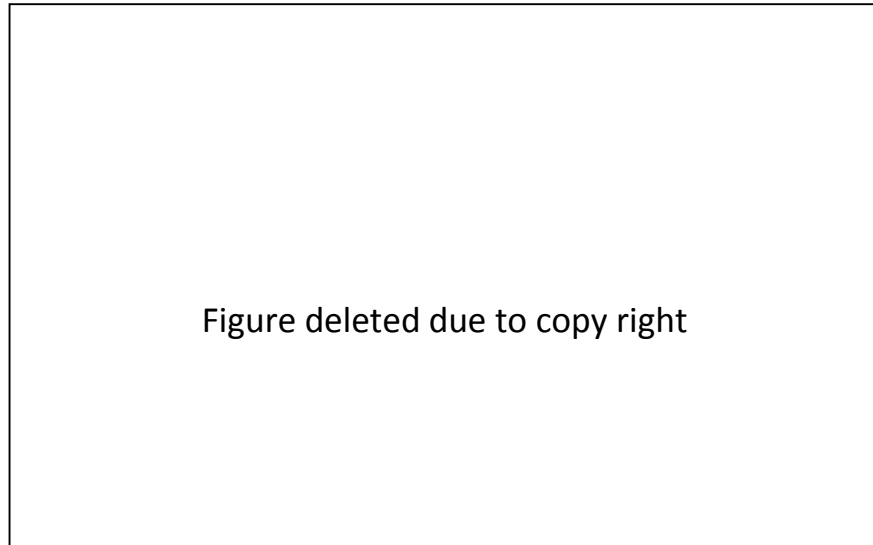


Figure 4.21: AFM tapping mode shows the deflection of the cantilever and return signal from sample surface [22].

4.17 Finite Difference time domain (FDTD) modelling

Finite Difference time domain (FDTD) is a computational electrodynamics modelling method. It was first introduced by Kane Yee in his original paper in 1966 [23], while the FDTD acronym was first named by Allen Taflove in 1980 [24]. This method is a time-traveling algorithm used to solve Maxwell's curl equations on a discretized spatial grid. FDTD calculations start by dividing the structure into a small discrete grid (smaller than smallest feature in the structure). As the space between the grids is decreased the resolution of the output result increase. Maxwell's curl equations are solved in a relay manner; the electric field E is solved at a given instant of time, followed by the magnetic field with the process being repeated until the time steps are have finished. In this work, the optical properties of nanocavity structures were calculated using the 3D FDTD code (CrystalWave) produced by Photon Design Ltd [25].

References

1. D.R. Allee, and A.N. Broers, "Direct nanometer scale patterning of SiO₂ with electron beam irradiation through a sacrificial layer", *Applied Physics Letters*, **57**, 2271-2273 (1990).
2. M. Urbanek, V. Kolarik, S. Kratky, M. Matejka, M. Horacek, J. Chlumska, "Monte-carol simulation of proximity effect in e-beam lithography", Brno, Czech Republic, EU, Nano conference (16 – 18/10 / 2013).
3. D.F. Kyser, N.S.Viswanathan, "Monte Carlo simulation of spatially distributed beams in electron –beam lithography", *Journal of Vacuum Science and Technology*, **12**, 1305-1308 (1975).
4. M. Urbanek, V. Kolarik, M. Matejka, F. Matejka, J. Bok, P. Miksik, J. Vasina, "Shaped e-beam Nano patterning with proximity effect correction", Brno, Czech Republic, EU, Nano conference (23 – 25/10 / 2012).
5. P. Rai Choudhury, "Handbook of Microlithography, Micromachining and Microfabrication", *Microlithography, Section 2.3 Electron-Solid Interactions*, **1**, (1997).
6. Dry Etching of InP Based Materials using High Density Inductively Coupled Plasma (ICP) by Oxford Instruments Plasma Technology.
<http://www.azonano.com/article.aspx?ArticleID=2716>
7. Y. X. Li, P. J. French, and R. F. Wolffenbuttel, "Selective reactive ion etching of silicon nitride over silicon using CHF₃ with N₂ addition", *Journal of Vacuum Science Technology*. **B 13**, 5, (1995).
8. C. Gatzert, a A. W. Blakers, and Prakash N. K. Deenapanrayb, "Investigation of reactive ion etching of dielectrics and Si in CHF₃ /O₂ or CHF₃ /Ar for photovoltaic applications", *Journal of Vacuum Science Technology*, **A 24**, 5, (2006).

-
9. B. D. Pant and U. S. Tandon, “Etching of Silicon Nitride in CCl_2F_2 , CHF_3 , SiF_4 , and SF_6 Reactive Plasma: A Comparative Study”, *Plasma Chemistry and Plasma Processing*, **19**, 4, (1999).
 10. T. Okumura, “Inductively Coupled Plasma Sources and Applications” Hindawi Publishing Corporation, *Physics Research International*, Volume 2010, Article ID 164249, doi:10.1155/2010/164249.
 11. http://www.cse.wustl.edu/~vgruev/cse/506/slides/w4_dry_etching.pdf .
 12. Barth, M , J Kouba, J Stingl, L chel, and O. Benson, Modification of visible spontaneous emission with silicon nitride photonic crystal nanocavities, *Optics Express*, **15**, 17231-17240 (2007)
 13. A. S. Urban , A. A. Lutich , F. D. Stefani , J. Feldmann, “Laser Printing Single Gold Nanoparticles”, *Nano Letters*, **10** , 4794 – 4798 (2010).
 14. J. Do , K. N. Sediq , K. Deasy , D. M. Coles , J. Rodríguez-Fernández, J. Feldmann , and D. G. Lidzey, “Photonic Crystal Nanocavities Containing Plasmonic Nanoparticles Assembled Using a Laser-Printing Technique”, *Advance Optical Mater*, **1**, 946–951 (2013).
 15. H. Aouani, J. Wenger, D. Ge´rard,H. Rigneault, E. Devaux, T. W. Ebbesen, F. Mahdavi, T. Xu, and S. Blair, “Crucial Role of the Adhesion Layer on the Plasmonic Fluorescence Enhancement” *American Chemical Society Nano*, **3**, 7, 2043–2048 (2009).
 16. G. Zorinants and W. L. Barnes, “Fluorescence enhancement through modified dye molecule absorption associated with the localized surface plasmon resonances of metallic dimers”, *New Journal of Physics*, **10**, 105002 (2008).
 17. S. Malik, C. C. Tripathi, “Thin Film Deposition by Langmuir Blodgett Technique for Gas Sensing Applications”, *Journal of Surface Engineered Materials and Advanced Technology*, **3**, 235-241(2013).

-
18. G. Giancane, L. Valli, “State of art in porphyrin Langmuir–Blodgett films as chemical sensors”, *Advances in Colloid and Interface Science*, **171–172**, 17-35 (2012).
 19. M. Ferreira, L. R. Dinelli , K. Wohnrath , A. A. Batista , O. N. Oliveira Jr, “Langmuir–Blodgett films from polyanilineyruthenium complexes as modified electrodes for detection of dopamine”, *Thin Solid Films* **446**, 301–306 (2004).
 20. C.P.L. Rubinger, R.L. Moreira, L.A. Cury, G.N. Fontes , B.R.A. Neves , A. Meneguzzi, C.A. Ferreira,” Langmuir–Blodgett and Langmuir–Schaefer films of poly (5-amino-1-naphthol) conjugated polymer “, *Applied Surface Science* **253**, 543–548 (2006).
 21. R. J. Farn, “Chemistry and Technology of Surfactants” copyright by Blackwell Publishing Ltd. (2006).
 22. Di Dimension 3100 Manual, NanoScope Software Version 5, Copyright ©Veeco Instruments Inc (2004).
 23. K. S. Yee, “Numerical solution of initial boundary value problems involving Maxwell’s equations in isotropic media”, *IEEE Transactions on Antennas and Propagation*, **14**, 3, 302-307 (1966).
 24. A. TAFLOVE, “Application of the Finite-Difference Time-Domain Method to Sinusoidal Steady-State Electromagnetic-Penetration Problems”, *IEEE Transition on Electromagnetic Compatibility*, **22**, 3, (1980).
 25. <http://www.photond.com>

Chapter Five

The Optical properties of L3 nanocavities optimizing the Q-factor of SiN based Structures

5.1 Introduction

Two-dimensional (2D) photonic crystals (PC) defined into a thin dielectric slab are of significant interest for their ability to control the propagation of light. By introducing a physical defect (cavity) into a photonic crystal, the light field can be localized within an extremely small volume [1, 2]. Cavities that confine light can be used to generate a number of quantum electrodynamic (QED) phenomena, such as enhancement of spontaneous emission [3], Rabi-splitting [4] and low-threshold lasing [5].

The majority of previous work on microcavities has focused on the use of materials having high refractive index, such as, Si and GaAs [6-11]. These materials are transparent at near infrared spectral regions and have strong optical absorption at viable wavelengths. In contrast low refractive index materials such as polymers (i.e. PMMA, polystyrene, etc) are transparent at visible wavelengths, but result in large optical losses when used as the dielectric medium for a PC cavity and thus result in low Q factor. Therefore, to create nanocavity device working at visible wavelengths, it is necessary to use a transparent material that is transparent in that region having a relatively high refractive index (to provide adequate optical confinement). Materials that here so far been explored for visible operation in nanocavities include GaN and AlN, that emit at violet-green wavelengths [12, 13]. Red emission can also be generated using InGaAlP [14]. Furthermore, PCs based on materials, such as diamond [15] and SiN [16, 17]

have been used to generate multimode emission in the yellow to red spectral region. In comparison to III-V semiconductors, the processes used to fabricate silicon-based PhCs are fully compatible with complementary metal-oxide semiconductor (CMOS) technology. This potentially provides low manufacturing costs and makes them easier to integrate with electronic components on the same chip [17- 19].

This chapter explores the use of SiN as a flexible platform to design a PC nanocavity at visible wavelengths. The parameters that affect the cavity optical modes will be presented and discussed. Finally, a modified PhC L3 cavity design used to optimise cavity Q factor will be presented. It is found that by modifying the air holes around the cavity, the Q- factor of the fundamental mode increased significantly to 890; a fourfold improvement in comparison with an unmodified cavity.

5.2 Silicon Nitride Slabs.

Silicon nitride (SiN) is a chemical component of silicon and nitrogen. It is transparent at visible wavelengths and has a refractive index in the range from 2 to 2.2, as shown in figure 5.1[20]. SiN also has broad PL emission peaking around 605 nm, with a full width at half maximum of ~ 215 nm as shown in figure 5.2. SiN is a material that is with compatible CMOS technology and has been explored as a promising material system especially for photonic applications such as photonic crystal nanocavity design [21-25]. Generally, optical confinement in a 2D PC slab within a nanocavity can be achieved by two mechanisms; laterally through the photonic band gap produced by air holes (DBR-like), and vertically through the total internal reflection at the slab-air interface. The total quality factor of a cavity (neglecting intrinsic absorption), is determined by the radiation

loss out of the cavity surface. This radiation loss can be reduced by selecting relatively high refractive index materials [26] or through modifying the design of holes around the nano-cavity [27, 28].

Adawi et al. [26] demonstrated that L3 nanocavities could be created from materials having a refractive index between 1.6 to 3.4. For cavities having no modifications to the shape or location of the holes surrounding the cavity, calculations predicted that the cavity quality factor increases super linearly with the refractive index of PhC membrane. For instance, by increasing the slab refractive index from 1.6 to 3.4, the Q-factor increased from 300 to 3900.

Makarova et al. [17] explored the emission from Si-rich SiN PC membranes. They showed that an L3 nanocavity having optical modes between 600–800 nm with quality factors in the range of 200–300 underwent a sevenfold enhancement of PL in comparison with bare Si-rich SiN membrane.

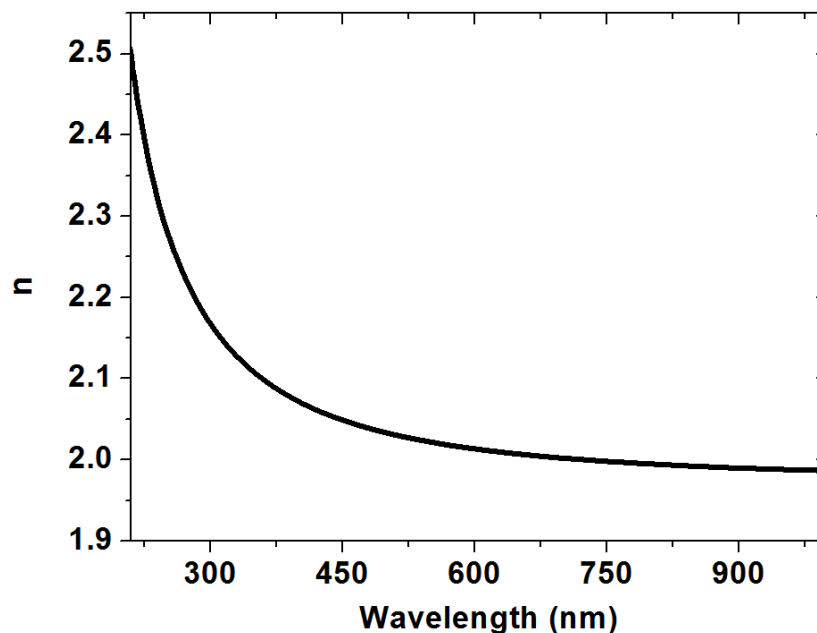


Figure 5.1: The refractive index of Si_3N_4

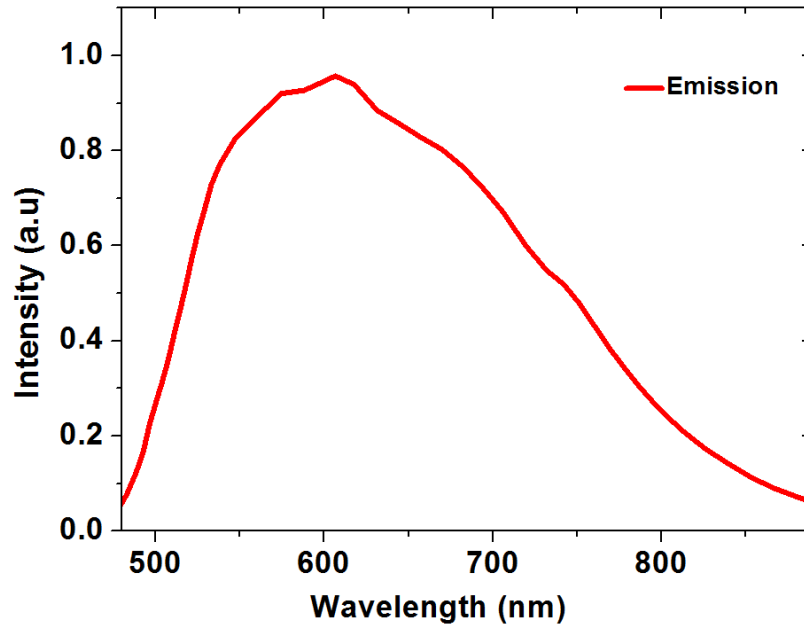


Figure 5.2: Photoluminescence (PL) emission of SiN membrane having a thickness of 200 nm.

5.3 SiN Slab thickness

The photonic band gap (PBG) of a 2D PC operates over a certain frequency range with light undergoing complete reflection as a consequence of diffractive interference at the interface between the air holes and the dielectric medium. Generally, PC properties can be characterised by the dispersion diagram of the electromagnetic waves that propagate through the PC structure, as well as by the transmittance and reflectance spectrum of the PC slab [29].

Slab thickness has a great impact on the size of the PBG and its position [30]. For instance, if the PC slab is too thick, the higher-order modes will overlap with the lower-order modes, and will prevent the formation of a PBG (see figure 5.4). If the slab is too thin, the cavity modes strongly couple with leaky modes at air-slab

interface, leading to weak light confinement within the cavity [31]. Johnson et al. estimated an optimum slab thickness (t) using the following equation [31]:

$$t \sim \frac{1}{2\omega_{gap-bottom}\sqrt{\epsilon}} \quad \dots\dots 4.1$$

Here, the thickness is in units of (a), where a is the lattice constant, $\omega_{gap-bottom}$ is the angular frequency in (a/c) unit, and c is speed of light. ϵ is the effective dielectric constant.

Pisanello et al. [3] investigated effect of SiN slab thickness on the photonic band gap of the 2D PC. It was shown that the PBG exists for $t = 0.7a$ and disappears when the slab thickness is increased to $1.55a$. Figure 5.3 shows the effect of PC membrane thickness on the PBG size calculated using plane wave basis (MPB) method.

In a 2D PC, it is important to select a free standing membrane thickness in which the reflectivity is greatest at the wavelengths corresponding to the desired photonic band gap wavelengths [29]. Here, a 200 nm thick suspended SiN membrane has been used, with the reflectance spectrum covering the visible spectrum (450 nm to 750 nm) and peaks at 540 nm. Reflectivity was calculated using the complex-matrix form of the Fresnel equations [32] as shown in figure 5.4.

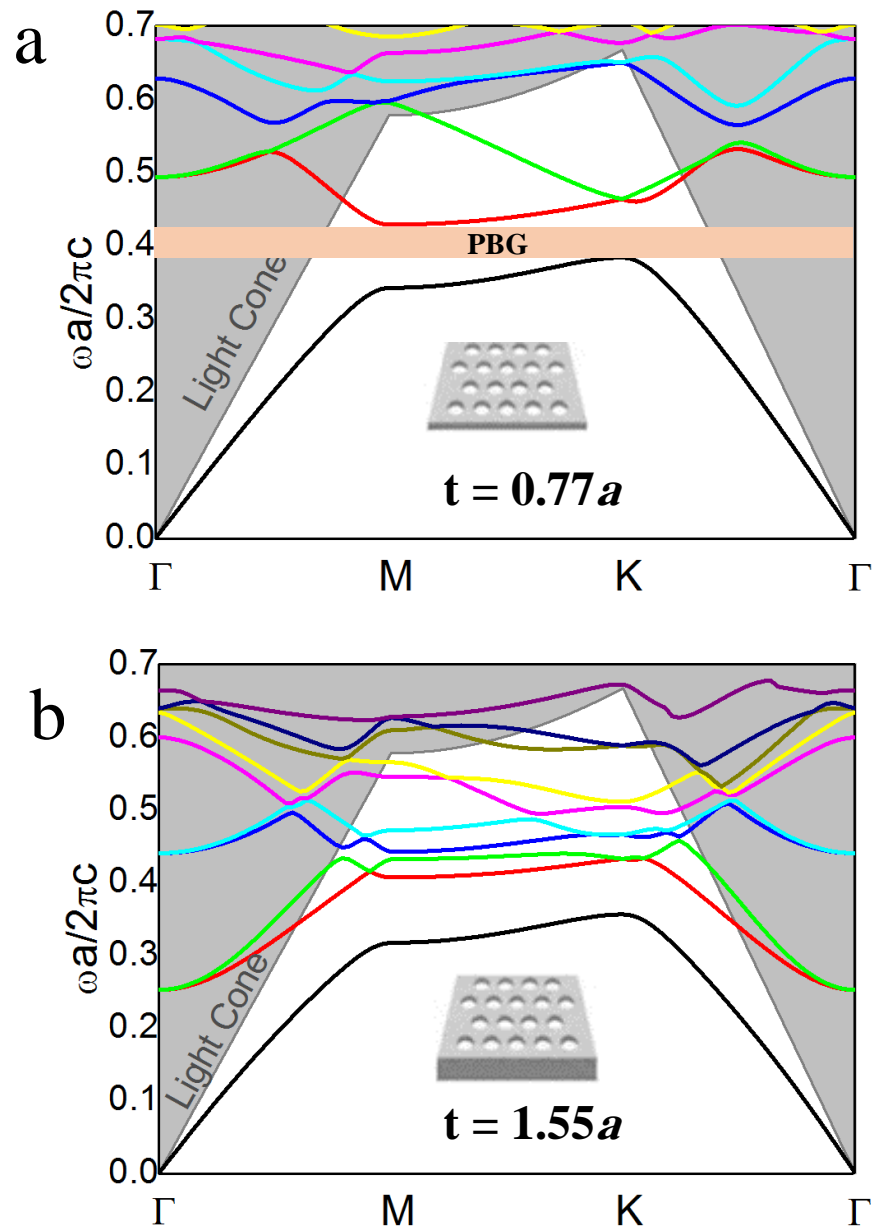


Figure 5.3: (a) Photonic band structure has a well-defined (PBG) for the structure thickness $t = 0.77a$. (b) The thickness increased to $t = 1.55a$ the PBG disappear the high-order modes overlap with low order modes.

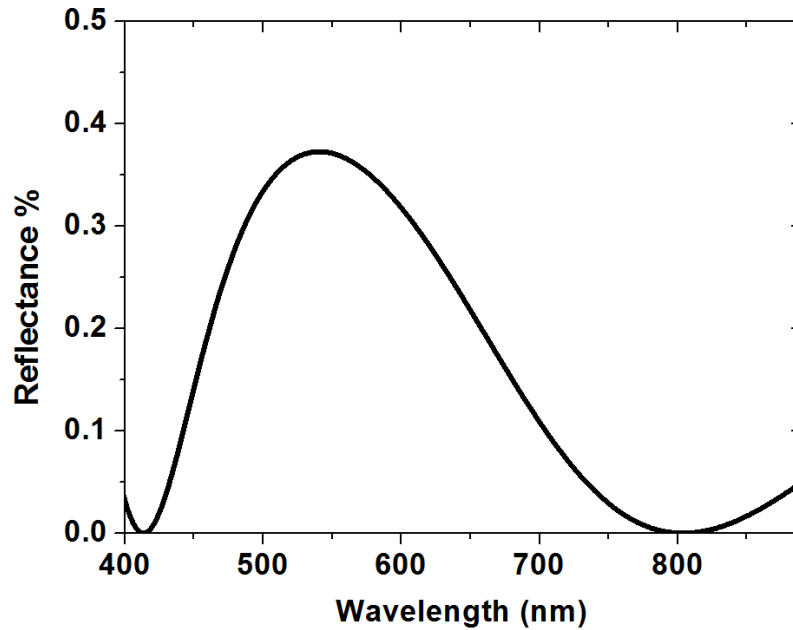


Figure 5.4: the reflectance of 200 nm thick SiN membrane

5.4 Design of an L3 Two Dimensional SiN Based Photonic Crystal Nanocavity

The structure that has been explored in this chapter is the so-called L3 nanocavity (three missing holes in a row) defined in a hexagonal 2D PC membrane. This type of cavity was used first explored by Akahane *et al* [1], and was based on a Si PC membrane having side holes around the cavity that were shifted out from the centre by a fraction of the lattice constant parameters. Experimentally, a Q-factor 45,000 was obtained for a shift in side holes of $S = 0.15a$, with the Q factor being around 10 times higher compared to the unmodified cavity. Peng *et al* [33] studied a GaAs L3 nanocavity with an imbedded single layer of InAs quantum dots as an active internal light source. They explored a structure that supported a multitude of modes, and showed experimentally for end-hole displacements $s = 0.15a$ the Q- factor increased from 1600 to 2500 respectively.

In this work, the L3 nanocavity 2D PhC with modified air holes was investigated as shown in figure 5.5, and the effect of a shift in side holes of the cavity on the mode position and Q- factor was explored. The PhC structure used in this work was based on a SiN ($n = 2.1$) membrane of thickness $t = 0.77 a$, lattice constant $a = 260$ nm and hole radius $r = 0.288a$. Here, the lateral PC structure size was $38a \times 30a$ with the L3 nanocavity located in the centre of the PC. The whole PC structure size was chosen to be larger than $28a \times 14\sqrt{3}a$, in order to avoid lateral (in-plane) losses due to the weaker lateral confinement [19].

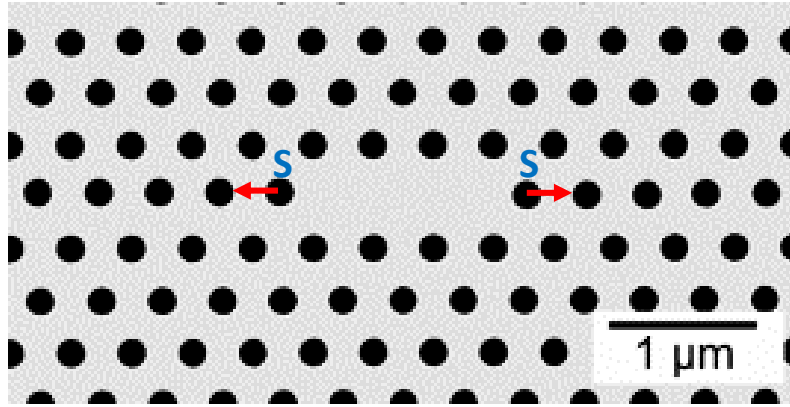


Figure 5.5: A schematic diagram of the L3 nanocavity having a hexagonal lattice of air holes of lattice constant $a = 260$ and radius $r = 0.288a$. The slab thickness is $t = 0.77a$ and S is the cavity side hole shift.

5.5 L3 nanocavity modes

For the design shown in figure 5.5, FDTD calculations confirmed that an unmodified cavity ($S = 0$) L3 nanocavity can support a number of confined modes. This result agrees well with other calculations obtained using a guided mode expansion method (GME) [34] and the plane wave expansion (PWE) techniques [33, 35]. The cavity modes exist at visible wavelengths (between 626 nm and 666 nm) as shown in figure 5.6. As a result of the 2D PC being defined into SiN slab, an optical bandgap only exists for TE-modes with light confined

within the PC cavity having Ex, Ey and Hz field components [36]. Figure 5.7 shows the L3 cavity field distributions of the highest order M1 mode (fundamental mode). The FDTD calculation also indicates that the fundamental mode M1 has the highest Q factor, and is clearly spectrally separated from the other modes (see figure 5.6). The fundamental mode is of significant interest in a range of applications, such as, nanocavity lasers [37] and for the selective excitation of quantum dots embedded within the cavity [38, 39]. I will therefore focus on the fundamental mode throughout this study of the optical properties of the modified L3 cavity as discussed in section 5.6.4.

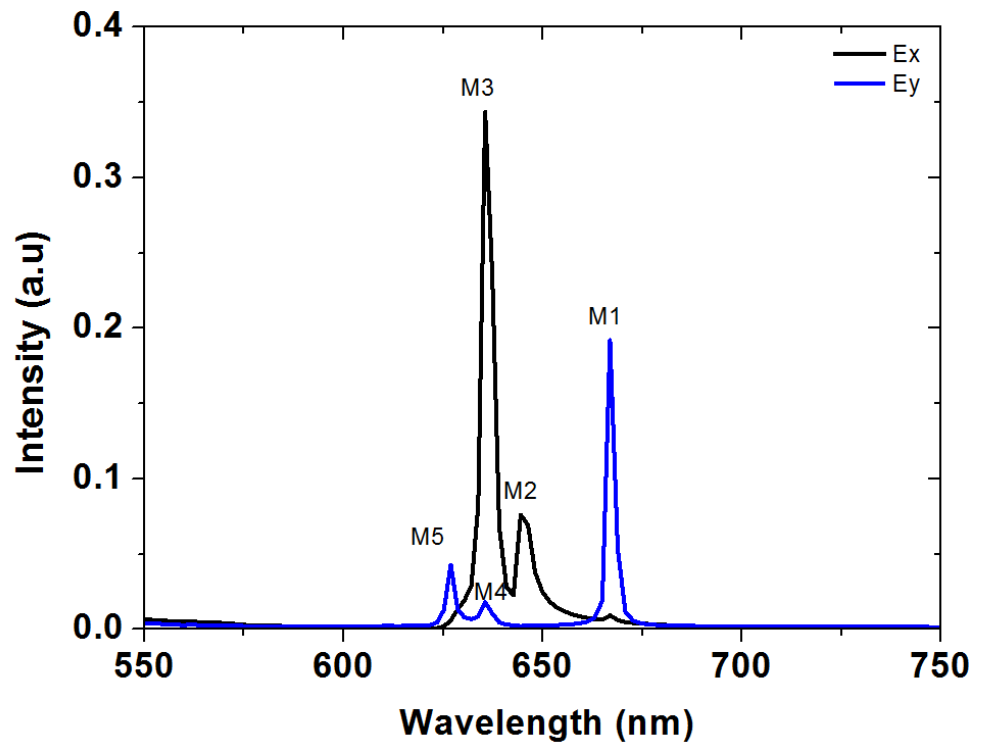


Figure 5.6: FDTD calculation shows multimode emission from an unmodified ($S=0$) L3 nanocavity, lattice constant $a = 260$ and radius $r = 0.288a$. The slab thickness is $t = 0.77a$. Here M1 is the fundamental mode.

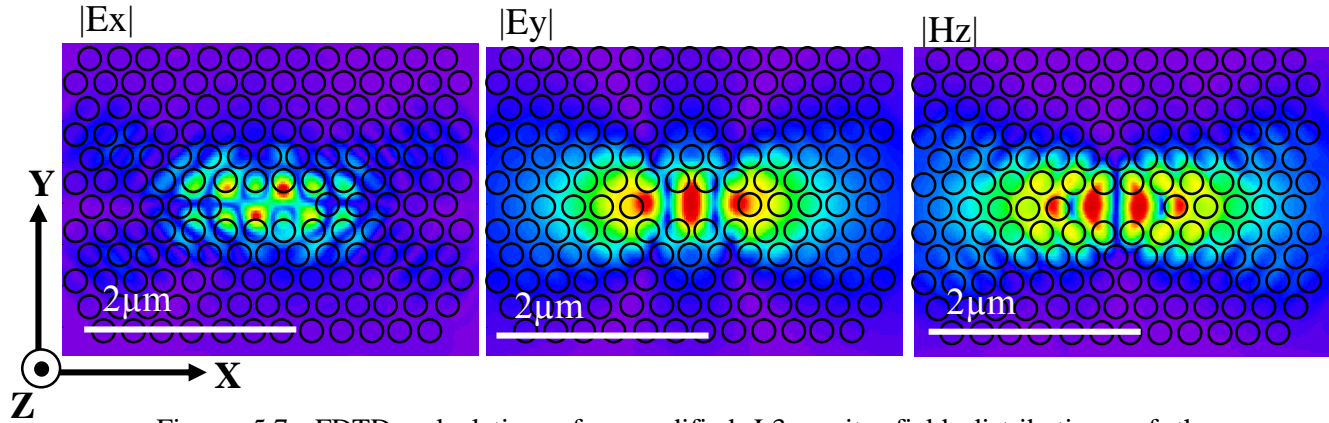


Figure 5.7: FDTD calculation of unmodified L3 cavity field distributions of the fundamental mode M1. The image dimension is $4\mu\text{m} \times 4\mu\text{m}$.

5.6 Experimental results and discussion

5.6.1 Optical Prosperities of the SiN Based L3 Nanocavity

Before exploring the effect of modification of the holes around the cavity on its optical modes, the unmodified ($S = 0$) L3 cavity was first studied. The structure constructed and modelled had a lattice constant $a = 260$ nm, hole radius and slab thickness $r = 0.288a$ and $t = 0.77a$ respectively as shown in figure 5.8. Generally, L3 cavities based on a high refractive index slab material have four modes as observed previously [17, 19]. Far field optical spectroscopy was used to study the nanocavity optical properties. The peak of the optical mode measured experimentally was compared with the calculated modes. The FDTD calculations indicated four modes, two of them mainly polarized in x-direction (denoted as M2 and M3) and in the y-direction (denoted as modes M1 and M4), respectively as shown in figure 5.9 a. The corresponding PL emission spectrum from an L3 SiN nanocavity was recorded from two different areas; either inside the cavity region, or out of the PC structure as shown in figure 5.9 b. The SEM image shown in the inset indicates the points at which the spectrum was recorded. It can be

seen that, sharp and intense optical modes can be seen from area A, while no optical peaks were recorded from area B or the bare SiN substrate area C. This enhancement of the optical field from area A results from the high optical field confinement inside the L3 nanocavity. Comparing the peak intensity of the modes with the surrounding background photoluminescence, it appears that modes M_1 and M_2 at 653 nm and 627 nm have enhanced emission intensity compared to bare SiN by a factor of 3 and 6 times respectively.

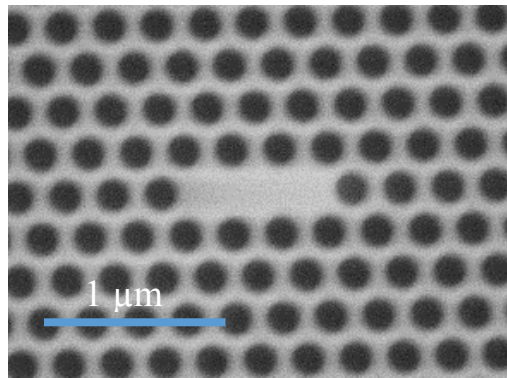


Figure 5.8: SEM image for unmodified L3 nanocavity

5.6.2 Fundamental mode position vs. air hole size and lattice constant

The hole size of 2D PC nanocavity is an important parameter, as it controls mode wavelength. Indeed, a small deviation in the hole size from that intended by just a few nanometres can result a shift of tens of nanometres in the mode wavelength. For example, by changing hole diameter by 4 nm will tune mode wavelength by around 10 nm at 1550 nm [40].

I have explored a large variety of different PC structures, varying the hole radii r from $0.23a$ to $0.32a$, where $a = 260$ nm is the lattice constant. Figure 5.10 (a) shows y - polarization peaks as a function of hole radius. It can be seen that the peaks shift toward smaller wavelengths as the hole radius is increased. This

allows the peak corresponding to the fundamental cavity mode to be tuned within the visible spectrum from 632 nm to 682 nm.

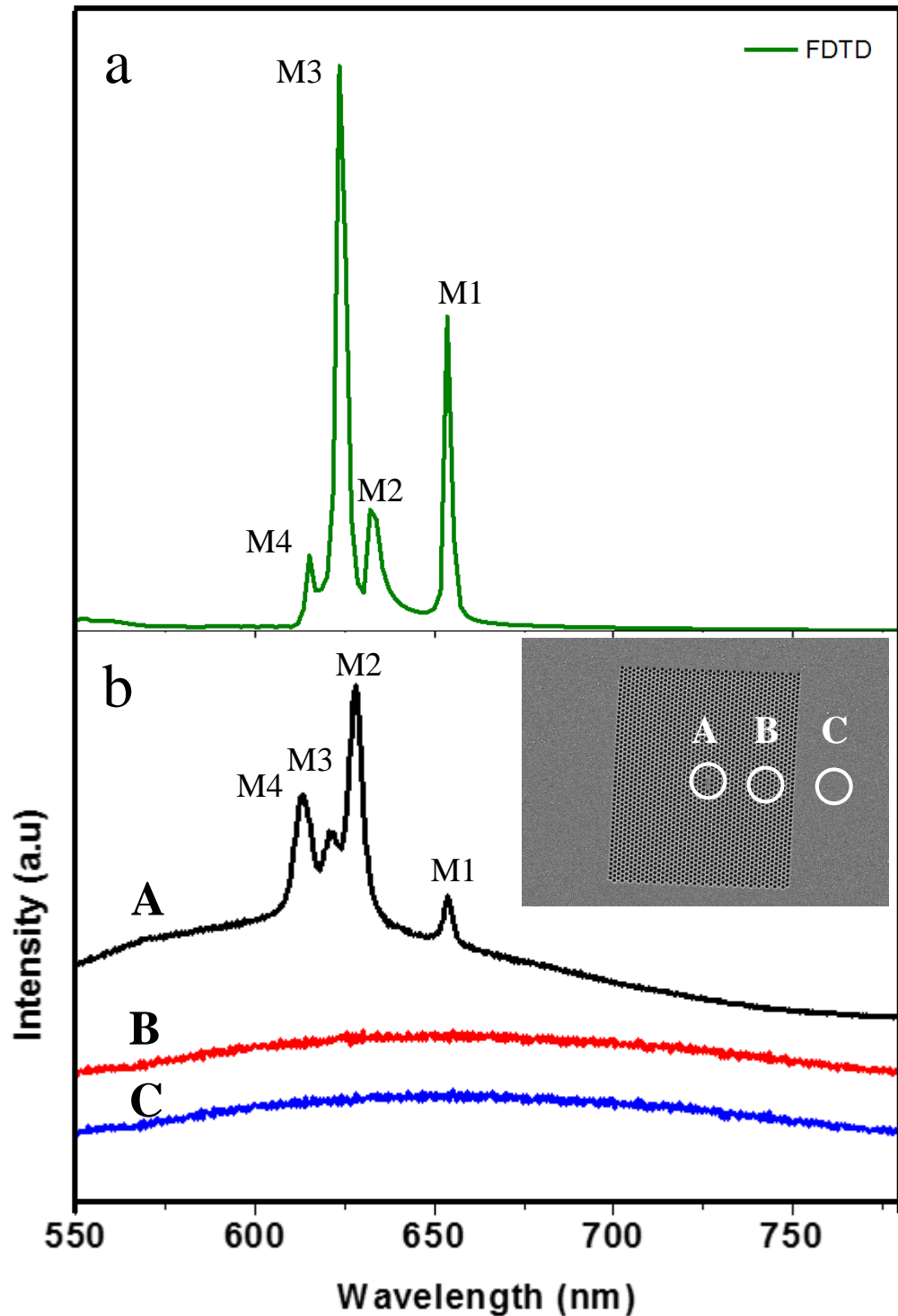


Figure 5.9: (a) FDTD calculation for unmodified L3 nanocavity, here $a = 260$ nm, $r = 0.288a$ and $t = 0.77a$. (b) PL emission spectra recorded at the positions marked A, B, and C on the SEM image shown in the inset.

Such experimental results are in good agreement with the FDTD calculation as shown in figure 5.10 (b). Here it is found that increasing the hole radius by around 5 nm results in a 10 nm shift in the fundamental mode peak position. A similar conclusion was reached by Barth et al using 2D PC L3 nanocavity SiN based having a lattice constant $a = 270$ nm [19].

The position of the fundamental mode also can be controlled by changing the lattice constant [27]. Figure 5.11(a) shows the PL emission spectra from PCs having various values of lattice constant. Here the hole radius of the PhC structure was set at $0.288a$ (as determined from SEM measurement) with the lattice constant being tuned from 240 nm to 290 nm. PL measurements on such structures indicates that the position of the fundamental mode varied linearly from 599 to 728 nm with increasing lattice constant. The FDTD calculation plotted in figure 5.11(b) shows good agreement with experimental results. Here the red shift of the fundamental mode with lattice constant indicates an ability to tune the PhC nanocavities wavelength.

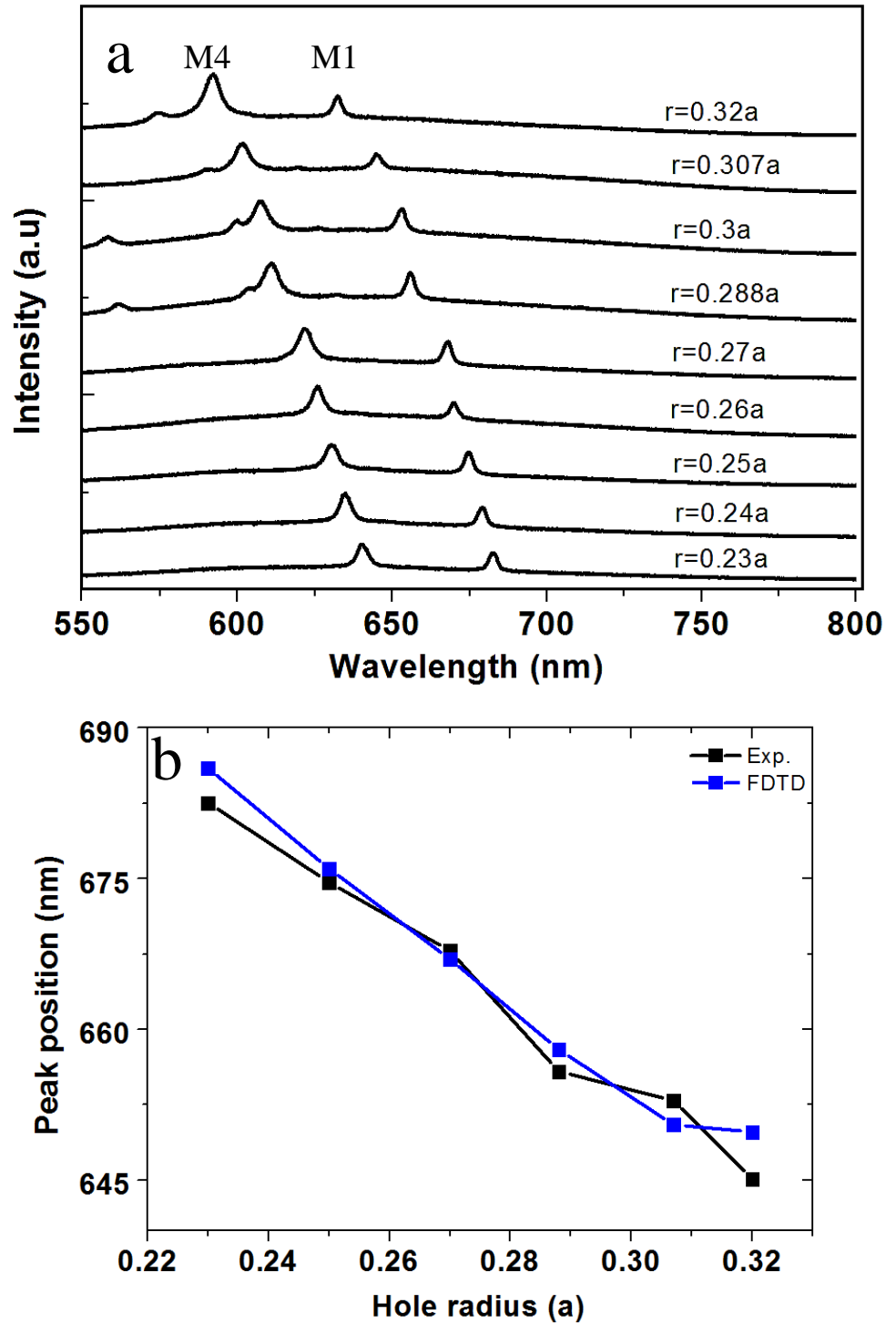


Figure 5.10: (a) shows a red shift in the fundamental mode (M1) peak position with reduced PhC hole radius. (b) Comparison between experimental measurements and FDTD calculations for the fundamental mode peak position as a function of air hole radius.

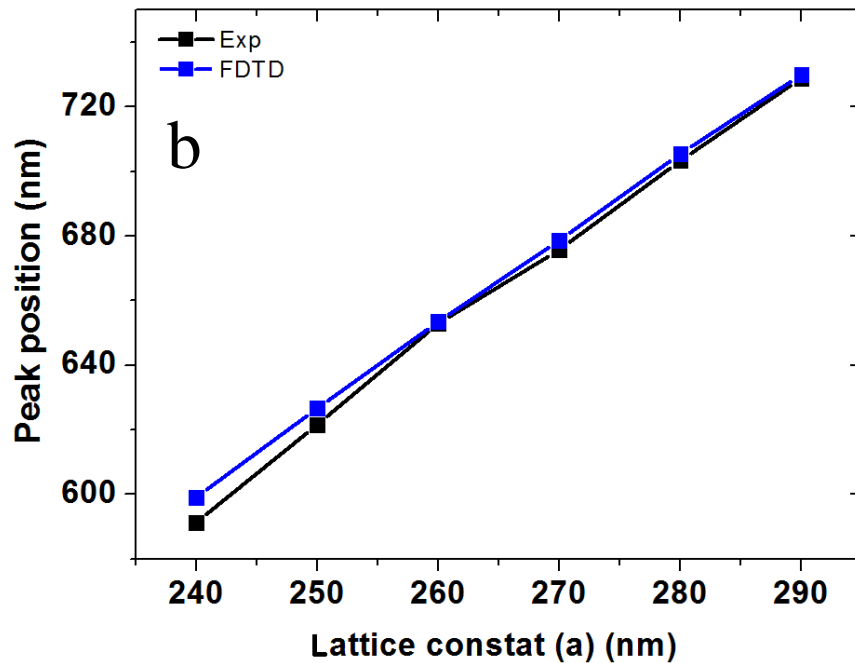
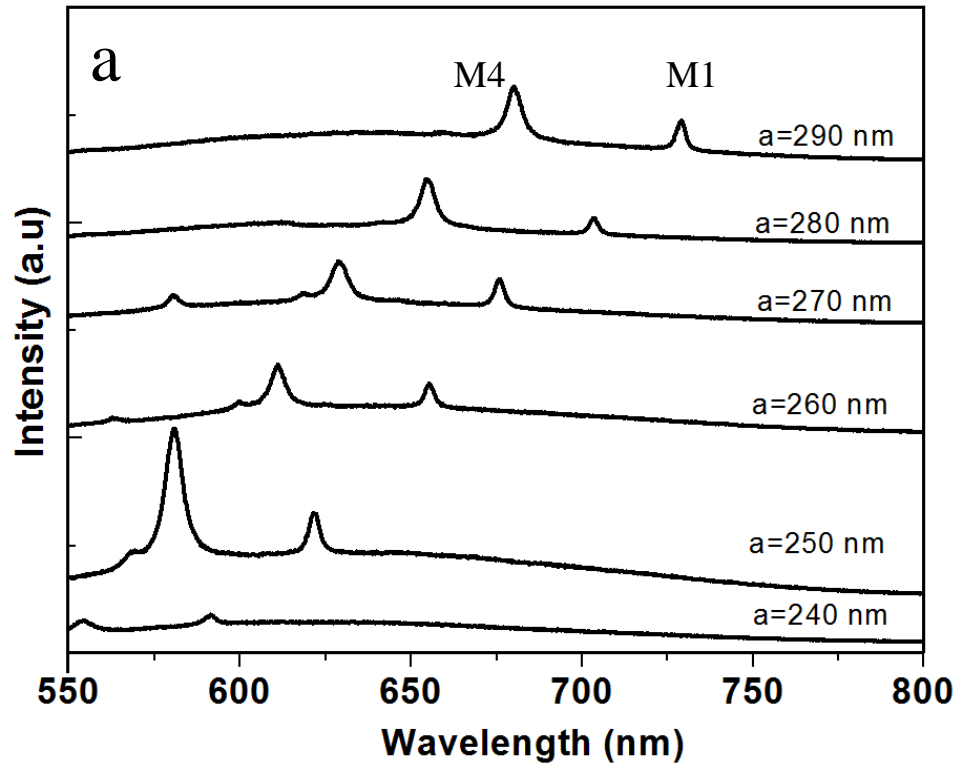


Figure 5.11: (a) Red shift of the fundamental mode M1 peak position with increased PhC lattice constant. (b) Comparison between experimental measurements and FDTD calculation for the fundamental mode peak position as a function of various lattice constant.

5.6.3 The effect of side holes of the fundamental cavity mode.

As mentioned previously, light confinement within a 2D PC L3 cavity results from two mechanisms; laterally by the periodic air holes and vertically by total internal reflection (TIR). In a small cavity, and at the cavity-air interface it is hard to satisfy the TIR conditions as the confined light consists of large number of plane wave components having different directions of wavevectors (k). Light can escape to air clad from the cavity slab as the TIR condition is not fulfilled as indicated by shaded region in figure 5.12 (e) (f). In contrast, light is strongly confined when $|k_{\parallel}|$ is larger than $2\pi/\lambda_0$.

By moving the side holes of a cavity by a small amount, the k_{\parallel} vector components that couple into the leaky regions are relatively reduced (see figure 5.12 (e) (f)), and the electric field decays more gently into the surrounding PhC structure, leading to reduced vertical losses as shown in figure 5.12 (c) and (d) [1, 28].

5.6.4 Position of the Fundamental mode and Q factor vs. cavity side hole shift

The effect of shifting the cavity air hole on the mode wavelength of the 2D PhC L3 nanocavity was explored. The first holes along the cavity long axis were shifted outwards from $S = 0$ to $S = 0.22a$. The experimental values of the measured Q-factor of the fundamental mode M1 as a function of the cavity side hole shift was determined by a Lorentzian fit to the polarised PL emission

spectrum where $Q = \lambda/\Delta\lambda$, where λ is the mode wavelength and $\Delta\lambda$ is its full width at half maximum as in plotted in Figure 5.13(a).

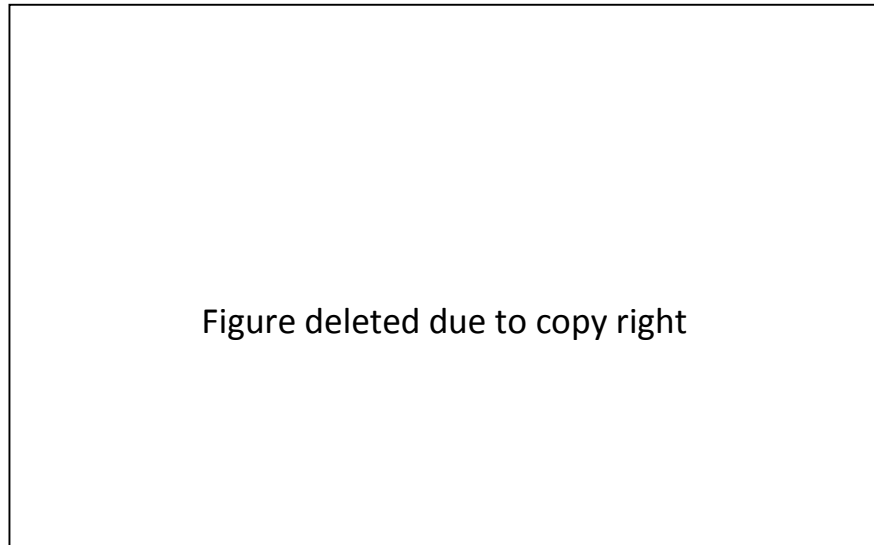


Figure 5.12: (a), (b) schematic of unmodified and modified L3 nanocavity respectively. (c), (d) electric field profile within the cavity (e) and (f) the spatial FT spectra respectively for the fundamental mode of a cavity modified by $S = 0.15a$ [taken from 1].

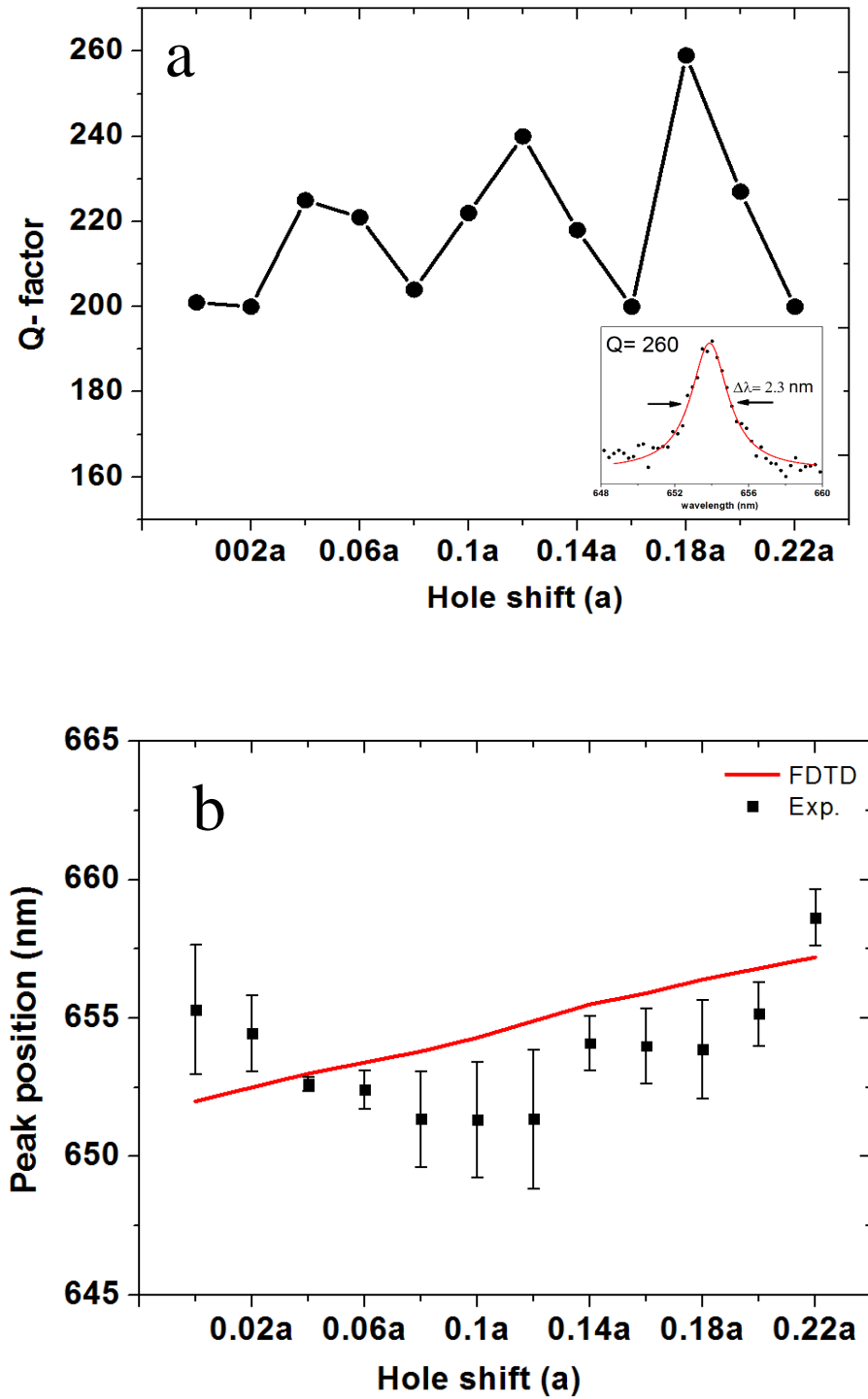


Figure 5.13: (a) Q -factor and (b) peak position of the fundamental mode as a function of the cavity side hole shift. The inset in part (a) shows the PL spectrum corresponding to a cavity having the maximum Q -factor. The red line in part (b) is the calculated wavelength of the M1 cavity mode calculated using FDTD.

Here, it was found that the highest Q-factor of 260 could be obtained for a side hole displacement of $S/a = 0.18$. This value of Q-factor is in reasonable agreement in comparison with previous works on SiN based L3 nanocavities [17, 19]. This value can however be increased significantly to 1375 as reported Murshidy using the same parameters with a slightly difference in hole size [41]. The main reason for the observed reduction in the cavity Q- factor seen here result from the taper angle of the 2D PhC air holes that surround the cavity. As discussed previously, the taper angle in this structure was estimated to be 5.4° (see Chapter four). It has been observed that increasing taper angle by one degree reduces the Q-factor value by over 10 % [42, 43] or by 40% for a 5° taper-angle [19]. Increasing the taper-angle of the air holes reduces cavity structure symmetry in the vertical direction which couples TE- like modes (in plane) and TM- like modes (out plane), breaks their orthogonality and causes propagation losses [42].

Figure 5.13 (b) illustrates the relation between the peak position of the cavity mode wavelength and the side hole shift. It can be seen that as the cavity side holes shift outwards, the position of the mode peak undergoes a small red shift. Notably, there is a small deviation between experimental results and calculated values (shown using red line); a result that probably results from disorder within the 2D PC air hole lattice.

5.7 Towards higher Q-factors.

High Q-factor nanocavities are of a significant interest, as high Q/V ratio nanocavities can create a significant enhancement in the spontaneous emission rate of a surface emitters via the Purcell effect [44]. A number of different designs have been introduced to create a high Q-factor 2D PhC nanocavities. McCutcheon and Loncar fabricated a SiN based nanobeam PhC nanocavity in which the cavity had an ultra-small mode volume of $0.78(\lambda/n)^3$ with a Q-factor exceeding one million [25]. Y-J Fu et al, fabricated a H1 nanocavity in a GaAs PhC membrane [21] with Q-factor of 11,700 achieved by modification of the six nearest cavity holes. The highest value of Q factor of 318,000 was reported by Tanabe et al using a single point defect between two coupled waveguides [45]. Barth et al [19] designed an L3 nanocavity SiN based with experimental Q factor 1500 by resizing the two long axis cavity air holes. They also investigated double-heterostructure cavities using the same material, creating cavities with a Q factor of 3400 [22]. Adawi et al [46] fabricated SiN L3 nanocavity having modified side holes and achieved a Q factor of 2650. It was concluded that this high Q value resulted from the small taper angle of the PhC holes. Indeed, this considered as a high value for such a low refractive index material ($n \approx 2.1$), while Q-factor can reach 12,000 as reported by Rivoire et al using high refractive index material such as GaAs ($n \approx 3.43$) [47]. Recently, Lai et al fabricated a modified Si based L3 nanocavity ($n = 3.46$) where the five nearest edge holes were shifted outwards along the cavity axis [48]. They recorded a Q-factor of 2×10^6 which represents the highest Q factor value yet reached using such design. Finally, Sekoguchi [49] reported the highest Q factor value of 9 million using Si based PhC formed by a

line defect of 17 missing air holes with the lattice constant varying along in the cavity long axis direction every two periods.

5.7.1 High Q-factor Cavity Design

To increase a cavity Q-factor, there are two mechanisms that can be explored; either increasing the PhC slab refractive index [26] or by modification of the air holes around the cavity [1, 19, 28]. Here, the modification of air holes surrounding an L3 nanocavity was selected. Figure 5.14 (a) shows an SEM image of an L3 2D PC nanocavity introduced into a SiN slab having lattice constant $a = 260$ nm, slab thickness of $t = 0.77a$, and the air hole radius of $r = 0.278a$. The radius of the four boundary air holes along the ‘long-edge’ above and below the cavity was reduced to $0.24a$, with the radius of the three air holes at the ends of the cavity reduced to $0.192a$. Figure 5.14 (b) shows a schematic of the modified air holes around the cavity highlighted using blue and green circles respectively. The first air hole at the ends of both sides of the cavity is displaced away from the cavity centre by a distance of S in the range ($0 \leq S/a \leq 0.28$).

5.7.2 The Optical Properties of a Modified L3 Nanocavity

The PL emission spectrum of a modified L3 nanocavity for non-displaced ($S/a = 0$) air holes is shown in figure 5.15. As it can be seen, there are five modes located within the TE bandgap of the PC membrane, three of them polarized mainly in y-direction (the short cavity axis modes) M1 (the fundamental mode), M3 and M5. The others are mainly polarized in x-direction (the long cavity axis modes) M2 and M4. It is clear that the x and y polarized modes are well separated, a result that can be attributed to a reduction in the taper angle of the air holes surrounding the cavity and increased vertical symmetry of

the slab structure. Thus both TE-like and TM-like cavity modes become more distinct [43, 44] and higher Q-factor modes are realised.

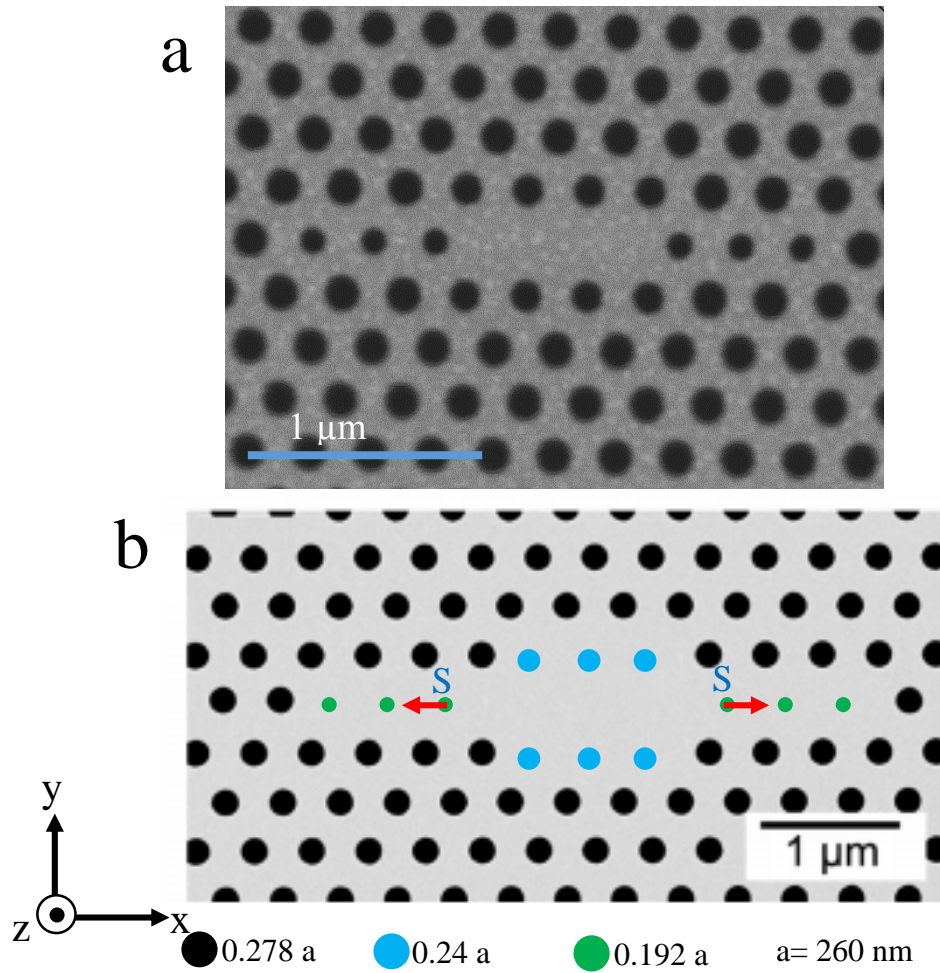


Figure 5.14: (a) SEM image of the SiN based modified L3 photonic crystal nanocavity.

(b) A schematic diagram of the location and design of the air holes around the modified L3 nanocavity

The first long edge air hole in both cavity side are now displaced by a distance of S in the range ($0 \leq S/a \leq 0.28$). Figure 5.16 shows the experimentally measured PL of the cavity modes polarized in y - direction. It can be seen that there are three modes that appear at 682, 650 and 623 nm (M1, M3, M5). It can also be seen that these modes shift towards longer wavelengths and their intensity drops gradually as the shift of the air holes increases.

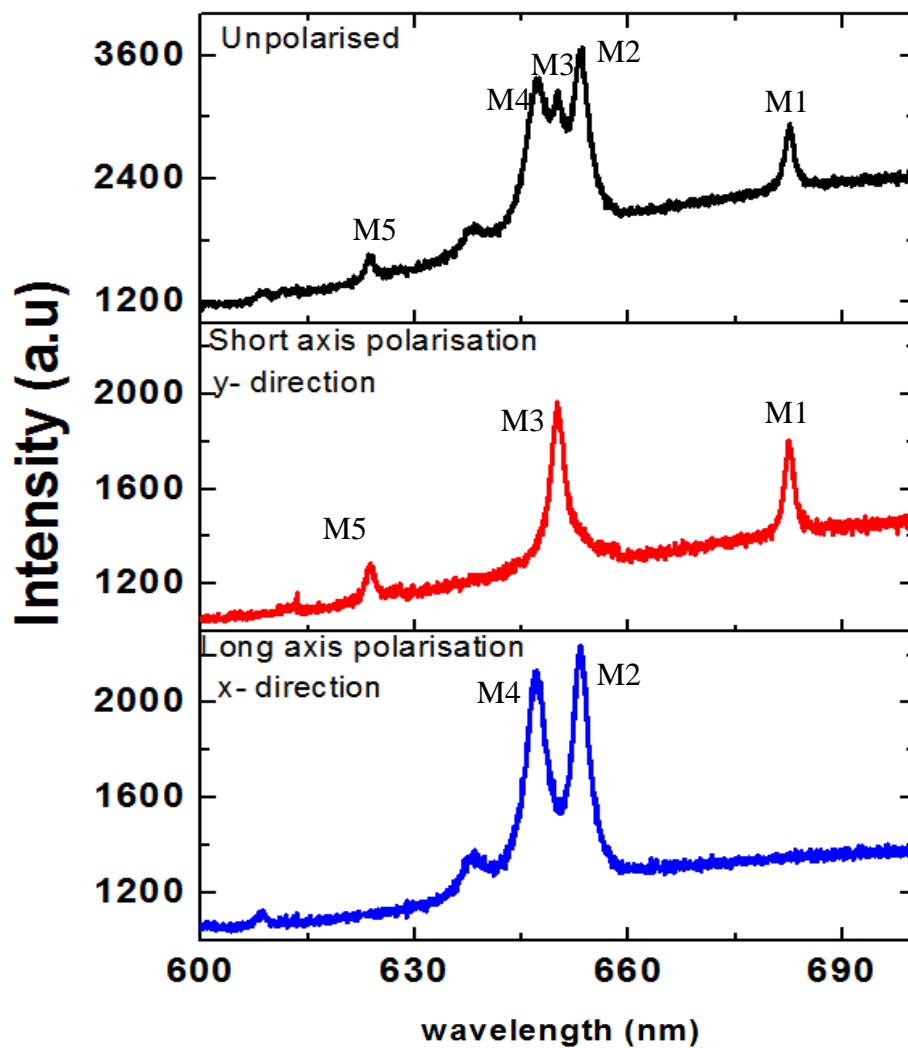


Figure 5.15: PL emission of modified L3 nanocavity with non-displaced air hole ($S/a = 0$).

Modes are well defined for both polarisation directions.

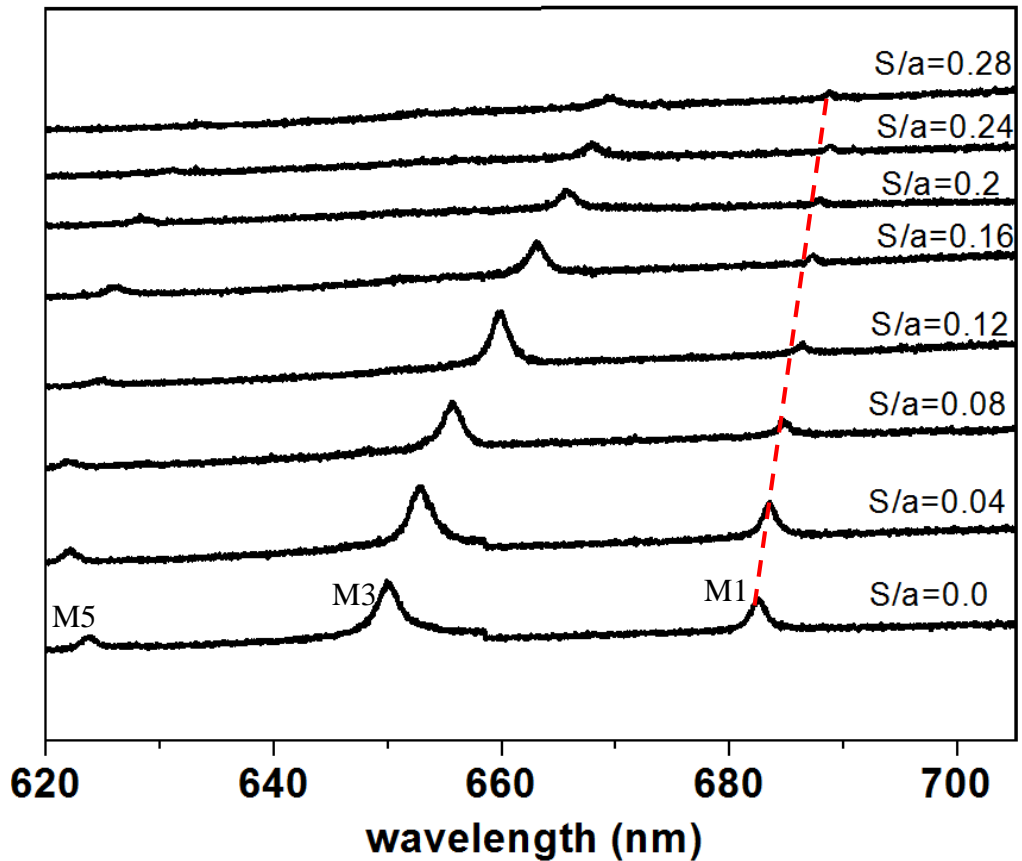


Figure 5.16: PL emission of modified L3 nanocavity. The y-component are linearly polarized and red shifted as a function of air –hole displacement.

The measured emission spectra of the y-polarized mode was compared with the result of FDTD simulation as shown in figure 5.17 (a). It can be seen that the FDTD emission spectrum contains three optical modes at 678, 653 and 640 nm. Despite the improvement in the side wall taper angle, the high Q-factor indicated by calculation is not achieved in practice. It is very likely that imperfection and disorder during the fabrication process is responsible for the deviation. Indeed, FDTD calculations indicate that mode M1 should have a Q-factor of 1,050; a value reasonably close to the measured value of 890. This close agreement suggests a high vertical confinement in our cavity structures.

Figure 5.17 (b) shows a plot of the calculated electromagnetic field amplitude of the X, Y and Z components at the nanocavity surface for the fundamental mode M1. It is clear that the fields associated with the M1 mode are confined within the cavity region. For an L3 nanocavity, the Y component of the electric field distribution of the fundamental mode M1 has a field maxima (anti-node) at the cavity centre. In contrast, the electric field distribution of the X component has a field minima (node) at the cavity centre [1]. Therefore, mode M1 is completely Y-polarized.

The measured Q-factor of the fundamental mode M1 as a function of the end-hole shift is plotted as shown in figure 5.18 (a). This was determined experimentally from the polarised emission spectra using a Lorentzian function to determine the full width half maximum linewidth $\lambda/\Delta\lambda$. The inset shows the emission spectra of the highest Q-factor (M1) cavity constructed. Here, the emission is fit to a Lorentzian function having a line width of 0.77 nm. We find that the Q-factor increases with increasing side hole shift, with the highest cavity Q-factor of 890 being obtained at $S/a = 0.28$.

Figure 5.18 (b) shows the relation between the peak position of the mode wavelength as a function to the side hole shift. It can be seen that as the cavity side holes are shifted outwards, the mode peak position undergoes a small red shift. The experimental data is compared to FDTD calculations, and it can be seen that only reasonable agreement is obtained due to imperfections in the fabrication of the 2D PC air holes.

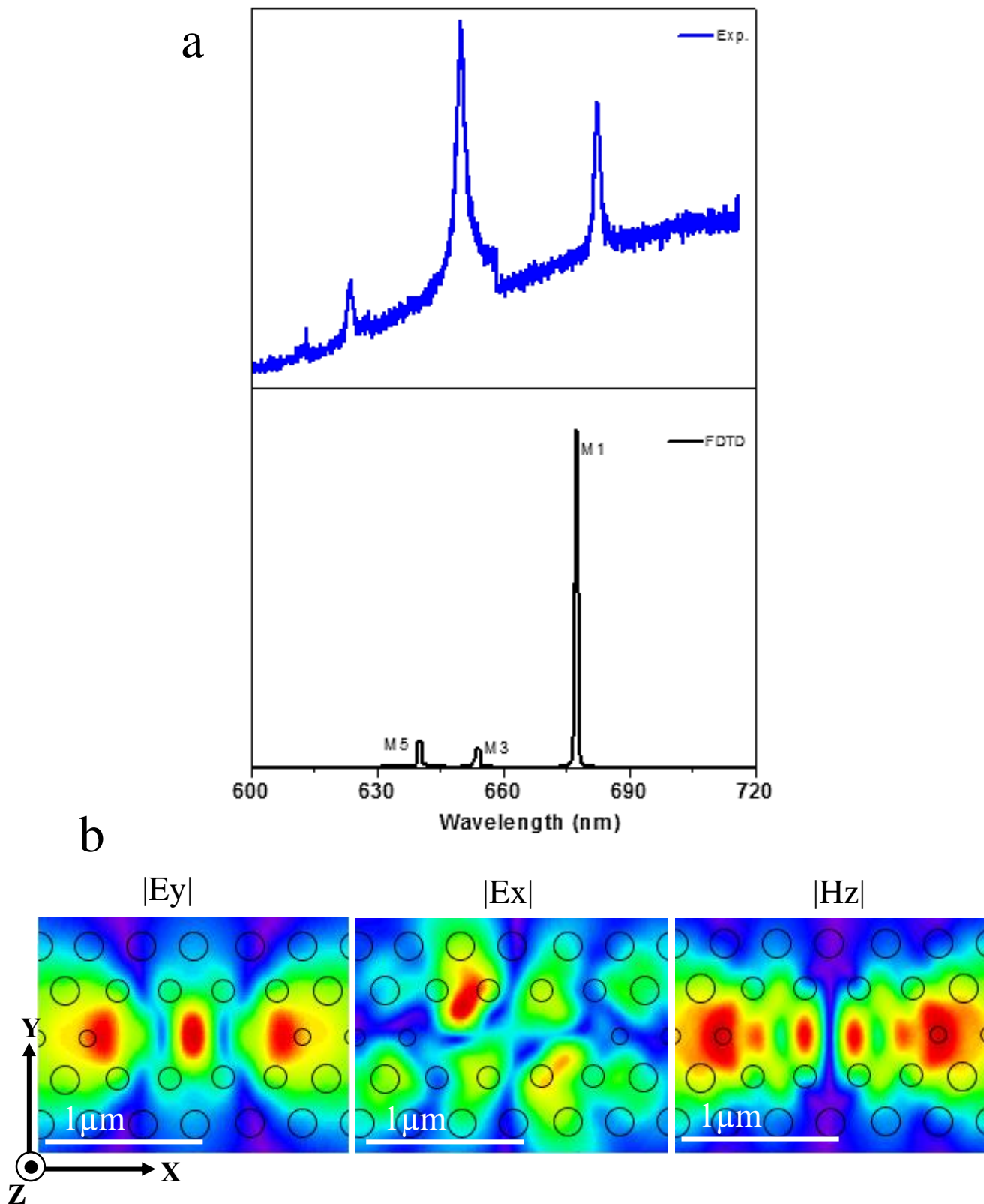


Figure 5.17: Comparison between the emission spectra of the measured Y-component modes and the simulated spectrum calculated using FDTD modelling. (b) Electromagnetic field distribution at the cavity surface at wavelengths corresponding to the fundamental mode M1.

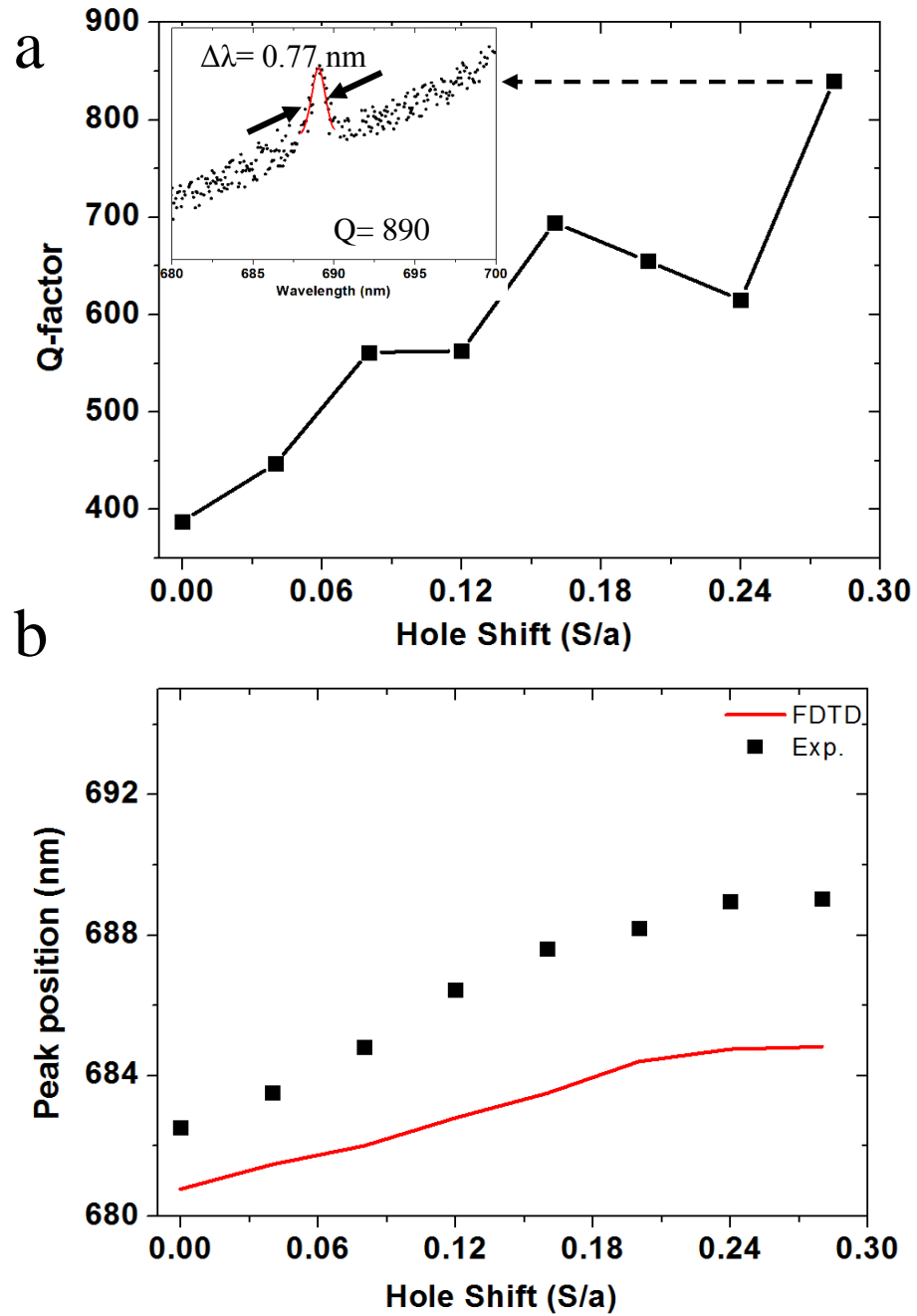


Figure 5.18: (a) Q-factor and (b) peak position of the fundamental mode as a function of the cavity side hole shift. The inset in part (a) shows the PL spectrum corresponding to a cavity having the maximum Q-factor. The red line in part (b) is the calculated wavelength of the M1 cavity mode calculated using FDTD.

5.8 Summary and Conclusions

Tuning the output spectra of an L3 nanocavity by resizing and changing the lattice constant of the PhC holes was studied both theoretically and experimentally. It was found that by reducing the hole size or increasing the lattice constant of 2D L3 nanocavity PhC, the optical modes can be red shifted. To create a high Q- factor L3 nanocavity, two mechanisms were explored; the first involved shifting the first hole on the both side of the cavity long axis outward from $S = 0$ to $S = 0.22a$. It was found that the cavity Q -factor of the fundamental mode M1 increased gradually to a value of $Q=260$ at 654 nm, for a side hole displacement of $S/a = 0.18$.

The second mechanism explored was modification of the size of the holes surrounding the L3 nanocavity. Here, the first hole on the both sides of the cavity long axis was displaced away from the cavity centre by a distance of S in the range ($0 \leq S/a \leq 0.28$). This red-shifted the fundamental mode M1 increased the Q -factor to 890 at a mode wavelength peak position of 683 nm. The Q -factor increased fourfolds in comparison with an unmodified cavity.

Similar structures to this will be explored for a range of applications in subsequent chapters in this thesis.

References

1. Y. Akahane, T. Asano, B. S. Song, S. Noda, “High-Q photonic nanocavity in two-dimensional photonic crystal”, *Nature* **425**, 944 (2003).
2. K. J. Vahala, “Optical microcavities,” *Nature* **424**, 839 (2003).
3. Pisanello, F., A. Quattieri, T. Stomeo, L. Martiradonna, R. Cingolani, A. Bramati, M. De Vittorio, “High-Purcell-factor dipole like modes at visiblewavelengths in H1 photonic crystal cavity”, *Optics Express*, **35**, 1509-1511 (2010).
4. K. Hennessy, A. Badolato, M. Winger, D. Gerace, M. Atature, S. Gulde, S. Falt, E. L. Hu, and A. Imamoglu, “Quantum nature of a strongly coupled single quantum dot-cavity system,” *Nature*, **445**, 896–899 (2007).
5. B. Ellis, M. A. Mayer, G. Shambat, T Sarmiento, J. Harris, E. E. Haller, J.Vuckovic, “Ultralow-threshold electrically pumped quantum dot Photonic-crystal nanocavity laser”, *Nature Photonics*, **5** , 297-300 (2011).
6. W-H. Chang, W-Y. Chen, H-S. Chang, T-P. Hsieh, J-I. Chyi, and T-M. Hsu, “Efficient Single-Photon Sources Based on Low-Density Quantum Dots in Photonic-Crystal Nanocavities”, *Physical Review Letters*, **96**, 117401 (2006).
7. W.-Y. Chen, W.-H. Chang, H.-S. Chang, T. M. Hsu, C.-C. Lee, C.-C. Chen, P. G. Luan, J.-Y. Chang, T.-P. Hsieh, and J.-I. Chyi, “Enhanced light emission from InAs quantum dots in single-defect photonic crystal microcavities room temperature,” *Applied Physics Letters*, **87**, 071111 (2005).

8. A. Badolato, K. Hennessy, M. Atature, J. Dreiser, E. L. Hu, P. M. Petroff, A. Imamoglu, “Deterministic Coupling of Single Quantum Dots to Single Nanocavity Modes”, *Science*, **308**, 1158-1161 (2005).
9. A. Majumdar, A. Papageorge, E. D. Kim, M. Bajcsy, H. Kim, P. Petroff, and J. Vuckovic, “Probing of single quantum dot dressed states via an off-resonant cavity”, *Physical Review* **B 84**, 085310 (2011).
10. Z. Wu, Z. Mi, P. Bhattacharya, T. Zhu, and J. Xu, “Enhanced spontaneous emission at 1.55 μm from colloidal PbSe quantum dots in a Si photonic crystal microcavity”, *Applied Physical Letters*, **90**, 171105 (2007).
11. T. Yoshie, J. Vuckovic, and A. Scherer, “High quality two-dimensional photonic crystal slab cavities”, *Applied Physics Letters*, **79**, 26, (2001).
12. H. Matsubara, S. Yoshimoto, H. Saito, Y. Jianglin, Y. Tanaka, S. Noda, “GaN Photonic-Crystal Surface-Emitting Laser at Blue-Violet Wavelengths”, *Science*, 319, 445-447 (2008).
13. M. Arita, S. Ishida, S. Kako, S. Iwamoto, and Y. Arakawa, “AlN air-bridge photonic crystal nanocavities demonstrating high quality factor”, *Applied Physical Letters*, **91**, 051106 (2007).
14. Z. Zhang, T. Yoshie, X. Zhu, J. Xu, and A. Scherer, “Visible two-dimensional photonic crystal slab laser,” *Applied Physical Letters*, **89**, 071102 (2006).
15. Wang, C.F., R. Hanson, D.D. Awschalom, E.L. Hu, T. Feygelson, J. Yang, and J.E. Butler, “Fabrication and characterization of two-dimensional photonic crystal microcavities in nanocrystalline diamond”, *Applied Physics Letters*, **91**, 201112 (2007).
16. A. Avoine, C. Vion, J. Laverdant, S. Bonnefont, O. Gauthier-Lafaye, L. Coolen, A. Maitre, “Photonic crystal cavity modes in the visible range

- characterized by scattering spectroscopy”, *Physical Review A* **82**, 063809 (2010).
17. M. Makarova, J. Vuckovic, H. Sanda, and Y. Nishi, “Silicon-based photonic crystal nanocavity light emitters,” *Applied Physics Letters*, **89**, 221101 (2006).
18. V. M.N. Passaro, “*Advances in Photonic Crystals*” 348 pages, Publisher: InTech, Chapters published, (2013), under CC BY 3.0 license DOI: 10.5772/47821.
19. Barth, M., J. Kouba, J. Stingl, L. chel, and O. Benson, “Modification of visible spontaneous emission with silicon nitride photonic crystal nanocavities”, *Optics Express*, **15**, 25, 17231-17240 (2007) .
20. H. R. Philipp, “Optical properties of silicon nitride”, *Journal of the Electrochemical Society*, **120**, 2, 295-300 (1973).
21. Y-J Fu, Y-S Lee, and S-D Lin, “Design and demonstration of high quality-factor H1-cavity in two-dimensional photonic crystal”, *Optics Letters*, **38**, 22, (2013).
22. Barth, M., N. Nusse, J. Stingl, B. Lochel, and O. Benson, “Emission properties of High-Q silicon nitride photonic crystal heterostructure cavities”, *Applied Physics Letters*, **93**, 021112 (2008).
23. Murshidy, M.M., A.M. Adawi, P.W. Fry, D.M. Whittaker, and D.G. Lidzey, “The optical properties of hybrid organic-inorganic L3 nanocavities”, *Journal of Optical. Society of America*, **B 27**, 215-221 (2010).
24. M. M. Murshidy, A. M. Adawi, P. W. Fry, D. G. Lidzey, “A one-dimensional photonic-crystal nanocavity incorporating a fluorescent molecular dye”, *Applied Physics Letters*, **97**, 153303 (2010).

25. M.W. McCutcheon and M. Loncar, “Design of a silicon nitride photonic crystal nanocavity with a Quality factor of one million for coupling to a diamond nanocrystal”, *Optics Express*, **16**, 23, 19136 (2008).
26. A.M. Adawi, A.R.A. Chalcraft, D.M. Whittaker, and D.G. Lidzey, "Refractive Index Dependence of L3 Photonic Crystal Nano-Cavities," *Optics Express*, **15**, 22, 14299-14305 (2007).
27. M. Kitamura, S. Iwamoto, and Y. Arakawa, “Enhanced light emission from an organic photonic crystal with a nanocavity,” *Applied Physics Letters*, **87**, 151119 (2005).
28. Y. Akahane, T. Asano, B-S. Song, and S. Noda, “Fine-tuned high-Q photonic-crystal nanocavity,” *Optics Express*, **13**, 1202 (2005).
29. Q. Gong, X. Hu, “Photonic crystals principles and applications”, CRC press, © Taylor and Francis Group, LLC, (2013).
30. A. Tandaechanurat, S. Iwamoto, M. Nomura, N. Kumagai, and Y. Arakawa, “Increase of Q-factor in photonic crystal H1- defect nanocavities after closing of photonic bandgap with optimal slab thickness”, *Optics Express*, **16**, 448 (2008).
31. S. G. Johnson, S. Fan, P. R. Villeneuve and J. D. Joannopoulos, “Guided modes in photonic crystal slabs,” *Physical Review B* **60**, 5751-5758 (1999).
32. <https://www.filmetrics.com/reflectance-calculator>.
33. Y.S. Peng, M.H. Yao, R.C. Li, Z.G. Wang, “Study of modes for two-dimensional L3 photonic crystal nanocavities”, *Optics Communications*, **285**, 1510–1513 (2012).
34. A. R. A. Chalcraft, S. Lam, D. O’Brien, T. F. Krauss, M. Sahin, D. Szymanski, D. Sanvitto, R. Oulton, M. S. Skolnick, A. M. Fox, D. M.

- Whittaker, H. Y. Liu, and M. Hopkinson, “Mode structure of the L3 photonic crystal cavity,” *Applied Physics Letters*, **90**, 241117 (2007).
35. S. Zhang, W. Zhou, X. Ye, B. Xu, and Z. Wang, “Cavity-Mode Calculation of L3 Photonic Crystal Slab Using the Effective Index Perturbation Method”, *Optical Review*, **20**, 5, 420–425 (2013).
36. J. D. Joannopoulos, S. G. Johnson, J. N. Winn, and R. D. Meade, “Photonic Crystals: Molding the Flow of Light”, (Princeton University Press, 2008).
37. M. Nomura, S. Iwamoto, M. Nishioka, S. Ishida, and Y. Arakawa, “Highly efficient optical pumping of photonic crystal nanocavity lasers using cavity resonant excitation”, *Applied Physics Letters*, **89**, 161111 (2006).
38. M. Nomura, S. Iwamoto, T. Yang, S. Ishida, and Y. Arakawa, “Enhancement of light emission from single quantum dot in photonic crystal nanocavity by using cavity resonant excitation”, *Applied Physics Letters*, **89** (2006) 241124.
39. M. Loncar, T. Yoshie, A. Scherer, P. Gogna and Y. Qiu, “Low-threshold photonic crystal laser”, *APPLIED PHYSICS LETTERS*, **81**, 15, (2002).
40. D. M. Beggs, L. O’Faolain, T. F. Krauss,” Accurate determination of the functional hole size in photonic crystal slabs using optical methods”, *Photonics and Nanostructures – Fundamentals and Applications*, **6**, 213–218 (2008).
41. M. Murshidy, “The optical properties of hybrid organic-inorganic photonic crystal nanocavities”, doctoral theses, University of Sheffield, 2010.
42. Y. Tanaka, T. Asano, Y. Akahane, B-S. Song, and S. Noda, “Theoretical investigation of a two-dimensional photonic crystal slab with truncated cone air holes”, *Applied Physics Letters*, **82**, 11, (2003).

43. M-K. Kim, J-K Yang and Y-H Lee, "Influence of Etching Slope on Two-Dimensional Photonic Crystal Slab Resonators", *Journal of the Korean Physical Society*, **50**, 4, 1027-1031 (2007).
44. R. Bose, X. Yang, R. Chatterjee, J. Gao, and Ch. W. Wong, "Weak coupling interactions of colloidal lead sulphide nanocrystals with silicon photonic crystal nanocavities near 1.55 μm at room temperature" *Applied Physics Letters*, **90**, 111117 (2007).
45. T. Tanabe, A. Shinya, E. Kuramochi, S. Kondo, H. Taniyama and M. Notomi, "Single point defect photonic crystal nanocavity with ultrahigh quality factor achieved by using hexapole mode", *Applied Physics Letters*, **91**, 021110 (2007).
46. A.M. Adawi, M.M. Murshidy, P.W. Fry, and D.G. Lidzey, "An Optical Nanocavity Incorporating a Fluorescent Organic Dye Having a High Quality Factor", *ACS Nano*, **4**, 6, 3039-3044 (2010).
47. K. Rivoire, A. Kinkhabwala, F. Hatami, W. T. Masselink, Y. Avlasevich, K. Müllen, W. E. Moerner, and J. Vučković, "Lithographic positioning of fluorescent molecules on High-Q photonic crystal cavities", *Applied Physics Letters* **95**, 123113 (2009).
48. Y. Lai, S. Pirotta, G. Urbinati, D. Gerace, M. Minkov, V. Savona, A. Badolato, and M. Galli, "Genetically designed L3 photonic crystal nanocavities with measured quality factor exceeding one million" *Applied Physics Letters*, **104**, 241101 (2014).
49. H. Sekoguchi, Y. Takahashi, T. Asano, and S. Noda, "Photonic crystal nanocavity with a Q-factor of ~ 9 million", *Optics Express*, **22**, 1, 916-924 (2014).

Chapter Six

A chemical sensor based on a photonic-crystal L3 nanocavity defined into a silicon-nitride membrane

6.1 Introduction

The small modal volume of a nanocavity combined with a strongly localized electromagnetic field provides an effective means to detect small changes in the local dielectric constant of the surrounding medium [1, 2]. This can be used to detect the binding of specific biological material [3-8] to a cavity surface, with such changes being detected through a shift in the wavelength of the various cavity modes. For a full review of the literature on this subject, the reader is referred to reference [9]. The majority of previous work on this subject has explored devices that utilize a silicon on insulator (SOI) chip as the medium into which the PC and cavity is defined. Here the combination of a high refractive index silicon layer ($n = 3.5$) positioned above a low index silicon oxide cladding ($n = 1.5$) provides tight optical confinement in the silicon, creating an effective waveguide structure for light around 1.3 to 1.5 μm .

Whilst SOI-based structures clearly offer the advantages of effective optical confinement and a well-developed platform for lithography, their operation at infra-red based wavelengths make them less sensitive to refractive-index changes resulting from the selective binding of many organic (carbon-based) materials. This is because organic materials often have a higher refractive index at UV or visible wavelengths (i.e. close to an electronic transition) [10]. It is clear however that the increased sensitivity to large changes in refractive index obtained by sensing materials at visible wavelengths will come at the price of

reduced cavity Q-factor, as the dielectric materials used to construct the cavity have lower refractive index and thus confine light less effectively [11]. Furthermore, the reduced refractive index of the cavity dielectric will also necessitate that such cavities operate in air rather than in an aqueous environment. This is in contrast to systems based on SOI, where the high refractive index contrast between silicon and water permits the formation of photonic crystals having an optical band-gap even when the structure is immersed in water. This will clearly limit the type of materials that could be sensed by a nanocavity operating at visible wavelengths to those carried by air. Nevertheless, there are plenty of applications for air-based detectors, such as the detection of air-borne pollutants, pathogens or explosive materials etc.

In this chapter, the use of low Q-factor nanocavities built using the material silicon nitride (SiN) are explored as optical sensors. It is demonstrated that such cavities can be used to detect the surface deposition of a molecular monolayer - corresponding to the binding of as little as 0.35 fg of material to the cavity surface. It is then demonstrated that by incorporating a thin functionalized polymer layer at the surface of a SiN L3 nanocavity, small changes in cavity volume can be detected as the polymer swells in response to exposure to an acidic vapor. It is argued that such SiN-based structures show promise as chemical and biochemical sensors having a sensitivity that is in many cases comparable to similar structures constructed using SOI. This chapter is partly based on work reported in the paper Deasy et al. [12], on which I am a second author.

6.2 Using Lumogen Red as a testbed

To explore the response of a nanocavity to a precise change in the thickness of a thin-film deposited onto a cavity surface, the Langmuir-Schaefer (LS) technique was used to deposit sequential monolayers of the molecular dye Lumogen Red (figure 6.1) onto the surface of cavity (1) with high precision. Note that the deposition of the Lumogen Red and the measurement of the optical properties of the L3 nanocavity were done in conjunction with Dr. Kieran Deasy¹ and Dr. Stuart Brittle**

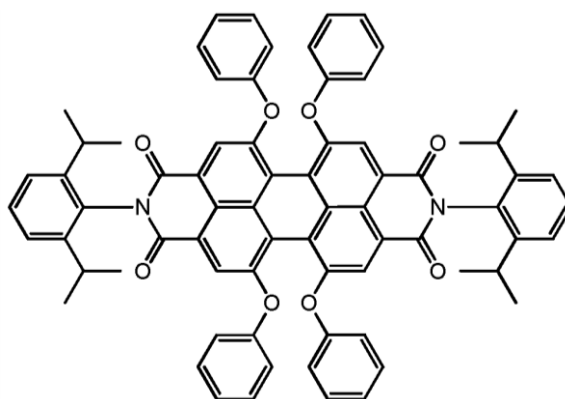


Figure 6.1: Chemical structure of Lumogen Red

The area per molecule of the LS deposited films was determined from an isotherm recorded during the compression of the Lumogen Red monolayers on the water sub-phase (see figure 6.2). Using this, the area subtended by each molecule at the water surface is calculated to be 1.5 nm². Spectroscopic ellipsometry was also used to determine the thickness of a single Lumogen Red monolayer and its average refractive index and these were found to be 1.2 nm and 1.65 respectively.

¹ Current address: Light-Matter Interactions Unit, OIST Graduate University, 1919-1 Tancha, Onna-son, Okinawa 904-0495, Japan.

** . Department of Physics and Astronomy, University of Sheffield, Sheffield, S3 7RH, United Kingdom.

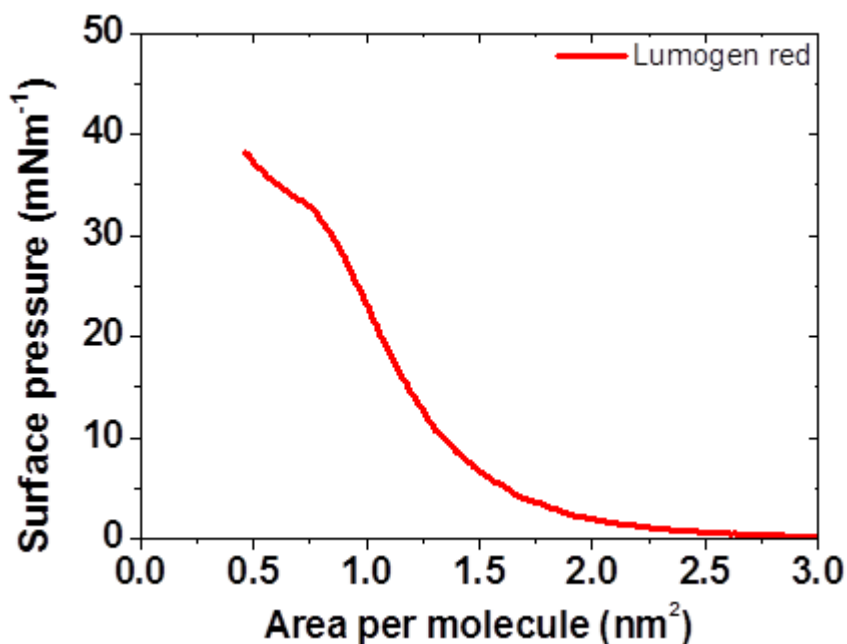


Figure 6.2: isotherm for monolayer compression of Lumogen Red

Lumogen Red has been explored previously in optical nanocavities [13, 14] and micropillars [15]. Lumogen Red is highly photostable, absorbs light efficiently at wavelengths below 600 nm, and emits fluorescence with high quantum efficiency from 575 nm to 750 nm, with a maximum at 600 nm [15]. In these experiments, Lumogen Red was used as it can be easily deposited on a surface with monomolecular precision, with its strong, red-fluorescence emission permitting the effect of a surface molecular layer on the optical mode wavelength of a SiN L3 nanocavity to be studied. Like many organic materials, Lumogen Red is expected to have a relatively low relative permittivity and thus acts as a reasonable model for a biomolecule [16]. Note however, a practical implementation of such cavities as a sensor would not include Lumogen Red. Rather, this can be achieved by coating the cavity surface with a material whose optical properties can be modified in response to chemical species present in their surrounding environment.

6.3 Experimental methods

To deposit functional organic films onto the nanocavities, the material of interest was dissolved in chloroform and spread on a clean water (Elga PURELab Option >15 M Ω cm) subphase surface in a NIMA BAM Langmuir trough. After evaporation of the chloroform solvent, the film was compressed to a surface pressure of 15 mN/m whilst a LS deposition was performed. Here the substrate was held almost parallel to the surface of the water and was then lowered until the entire surface of the substrate made contact with the liquid. It was then retracted vertically, with a molecular monolayer being transferred to the substrate. This process was repeated sequentially, with as many as 16 monolayers being deposited onto the nanocavity. Note, that as the substrates are retracted, they were deliberately tilted such that any remaining water drops on the surface could easily run off and be collected in one corner. The optical properties of the material of interest were explored using a M2000v, J.A. Woollam Co. ellipsometer, which permitted film thickness and refractive index to be determined by employing a Cauchy model to fit Ψ (the ratio of the amplitude of the incident and reflected light beams) and Δ (the ratio of the phase lag of the incident and reflected light beams). Spectroscopic ellipsometry was also used to characterise the change in refractive index and thickness as the film was exposed to an acidic vapour. Here a cotton bud was dipped into an acidic solution and held in close proximity to the cavity surface or a coated organic film.

6.4 L3 Cavity design.

The cavities explored were designed using a finite difference time domain (FDTD) engine (Crystalwave software supplied by Photon Design Ltd.), and were constructed such that the fundamental cavity mode was located at

approximately 650 nm [13]. Two different cavity designs were explored; cavity (1) was defined into a PhC having a hole diameter of $d = 0.6a$, with the holes at the end of the cavity long-axis shifted outwards by $S = 0.24a$, see Figure 6.3(a). Such techniques have been shown to reduce leaky modes from the cavity and thus improve cavity Q-factor [13], with the structures explored here having a Q-factor of $\sim 1,500$. In cavity (2) the four holes along the long axis of the cavity had a hole diameter of $d = 0.5a$, with the first three holes at either end of the cavity having a diameter of $0.4a$ and shifted by $S1 = 0.22a$, $S2 = 0.025a$ and $S3 = 0.18a$ respectively (as shown in Figure 6.3(c)). Here, the cavity Q-factor was lower at $\sim 1,000$. The distribution of the fundamental cavity mode as calculated using the FDTD model is plotted in Figures 6.3 (e) & (f).

6.5 Effect of Lumogen Red monolayers on L3 nanocavity mode wavelength

The photoluminescence (PL) emission from nanocavities was studied following excitation using a CW laser ($\lambda = 442$ nm). All measurements were made in air. By setting the spectrometer grating to zeroth-order, the system can also be used to create a direct, real-space fluorescence image of the nanocavity surface. This is shown in Figure 6.4 for a nanocavity before and after being coated by a series of Lumogen-Red molecular monolayers. It can be seen that a bright, emissive spot is detected in the center of the image that corresponds to the nanocavity region. The edge of the photonic crystal region is similarly bright, with emission resulting from enhanced optical scattering. In all cases, this image is used to define the region on the CCD detector over which emission was

recorded, allowing the optical properties of the nanocavity to be probed whilst limiting its sensitivity to the surrounding (non-cavity) regions.

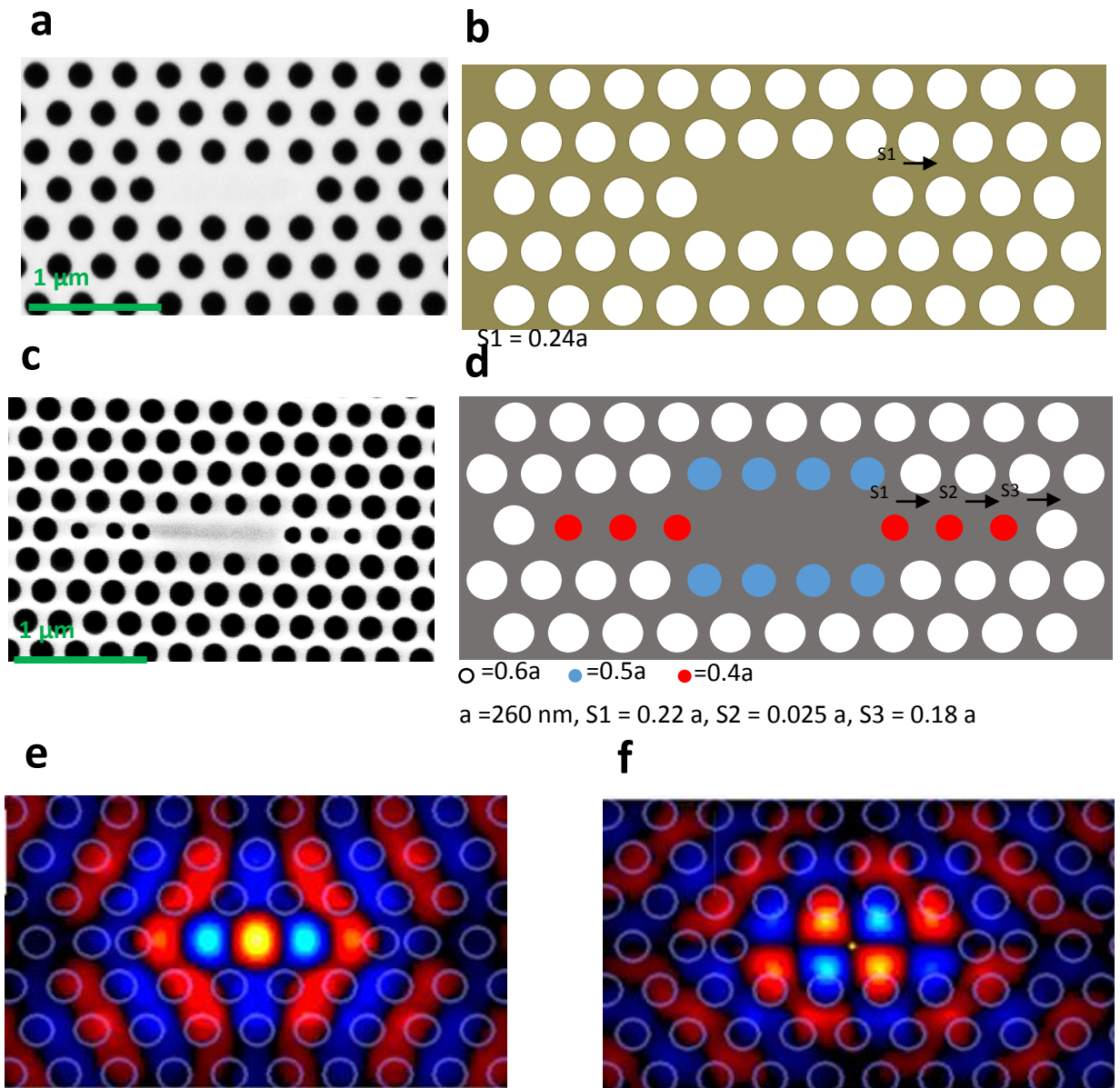


Figure 6.3: (a) and (c) show SEM images of L3 nanocavities (1) and (2) respectively fabricated into a 200 nm thick SiN membrane. Parts (b) & (d) show a schematic of the two types of L3 nanocavities used in these experiments (described in the text as cavity (1) and cavity (2) respectively). Parts (e) & (f) show an FDTD simulation of the E_x and E_z fields confined within the cavity respectively. Figure taken from reference [12].

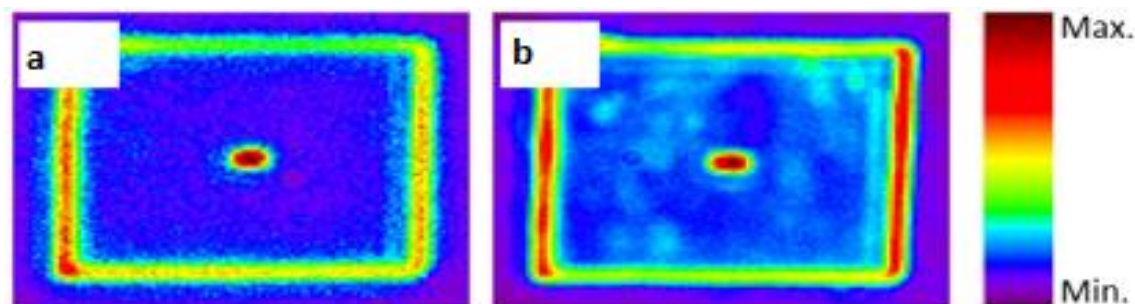


Figure 6.4: (a) & (b) show PL intensity images of the PC and nanocavity before and after coating with a number of Lumogen-Red monolayers. Here, the colour-scale of both images are normalized to the peak emission intensity. Figure taken from reference [12].

Figure 6.5 shows a series of PL spectra recorded from nanocavity (cavity 1) coated with an increasing number of molecular monolayers of Lumogen Red. Here, data is plotted around the wavelength of the fundamental cavity mode around 650 nm. Note, even in a cavity with no Lumogen Red present, luminescence from the cavity mode is still detected; an effect that originates from the weak intrinsic fluorescence of silicon nitride. It can be seen that the wavelength of the fundamental mode undergoes a red-shift as the number of monolayers increases, going from 650.8 nm when the cavity is coated with a single monolayer to 654.0 nm after 16 monolayers have been deposited. The intensity of the peak emission detected from the nanocavity and the peak emission wavelength is plotted as a function of the number of LS films deposited as shown in figure 6.6(a) and (b) respectively. Here, the peak intensity (wavelength) was obtained from the peak-to-peak of a Lorentzian function fit to each of the features shown in figure 6.5 after an emission background had been subtracted to account for the intrinsic fluorescence of the SiN.

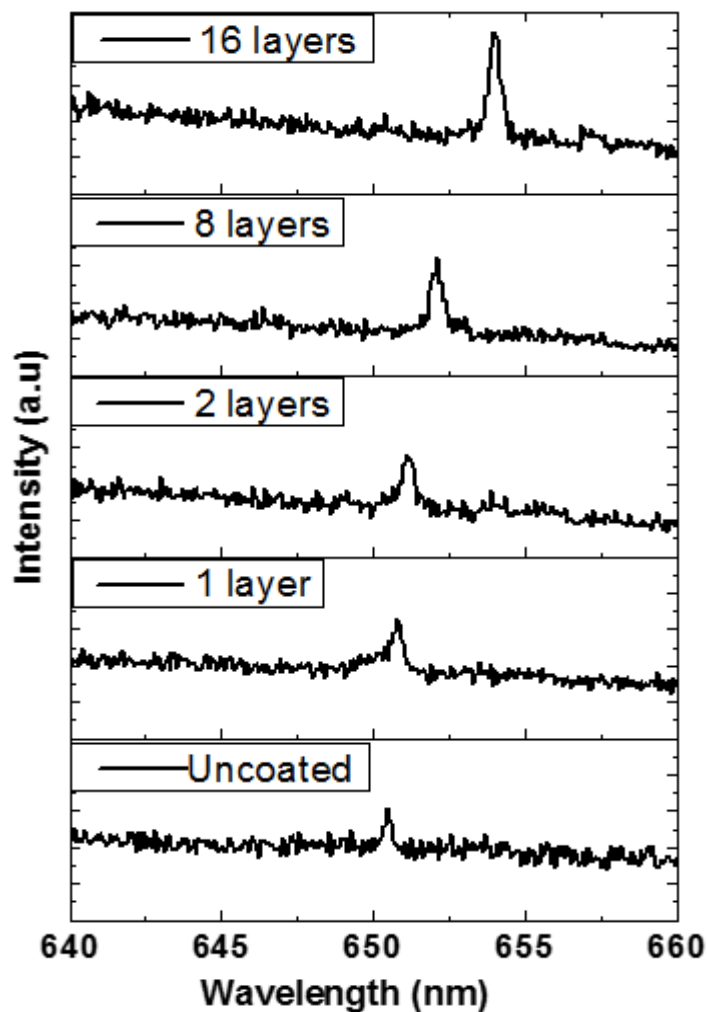


Figure 6.5: PL spectra for a Lumogen Red coated nanocavity as a function of the number of LS deposited monolayers. Figure taken from reference [12].

It can be seen that the luminescence emission is approximately linear as a function of the Lumogen Red layer thickness. To understand the origin of this dependence, FDTD modeling (not shown) was used to calculate the average value of the electromagnetic field throughout the organic layer. The model suggests that the average electromagnetic field intensity within this layer is approximately constant (to within $\pm 12\%$) over the range of film thicknesses explored here. This indicates that no significant changes in the coupling efficiency of the fluorescence emission to the cavity mode can be expected. It can be concluded therefore that the linear increase in luminescence observed as

a function of Lumogen Red layer thickness simply results from the fact that there is progressively more material at the nanocavity surface whose fluorescence is able to couple to the confined optical field. It can be seen in figure 6.6 (b) that the cavity mode undergoes a red-shift as Lumogen Red monolayers are deposited onto the cavity surface. Such a change in cavity mode wavelength results from a change in the overall thickness and effective refractive index of the nanocavity and surrounding photonic crystal. Similar effects have been previously observed following the deposition of materials such as xenon [17] or Al₂O₃ [18] onto a nanocavity surface or by using reversible refractive index changes in photochromic films to tune nanocavity wavelength [19].

The effect of the organic surface layer on the optical mode-structure of the cavity can be modeled using an FDTD model. Using this, the cavity mode wavelength was calculated as a function of the number of Lumogen Red monolayers using measured values of monolayer thickness (1.2 nm) and refractive index ($n = 1.65$) as input as shown in Figure 6.6 (b). This is plotted against measured cavity mode wavelength, with a good agreement achieved between the model and the experimental data.

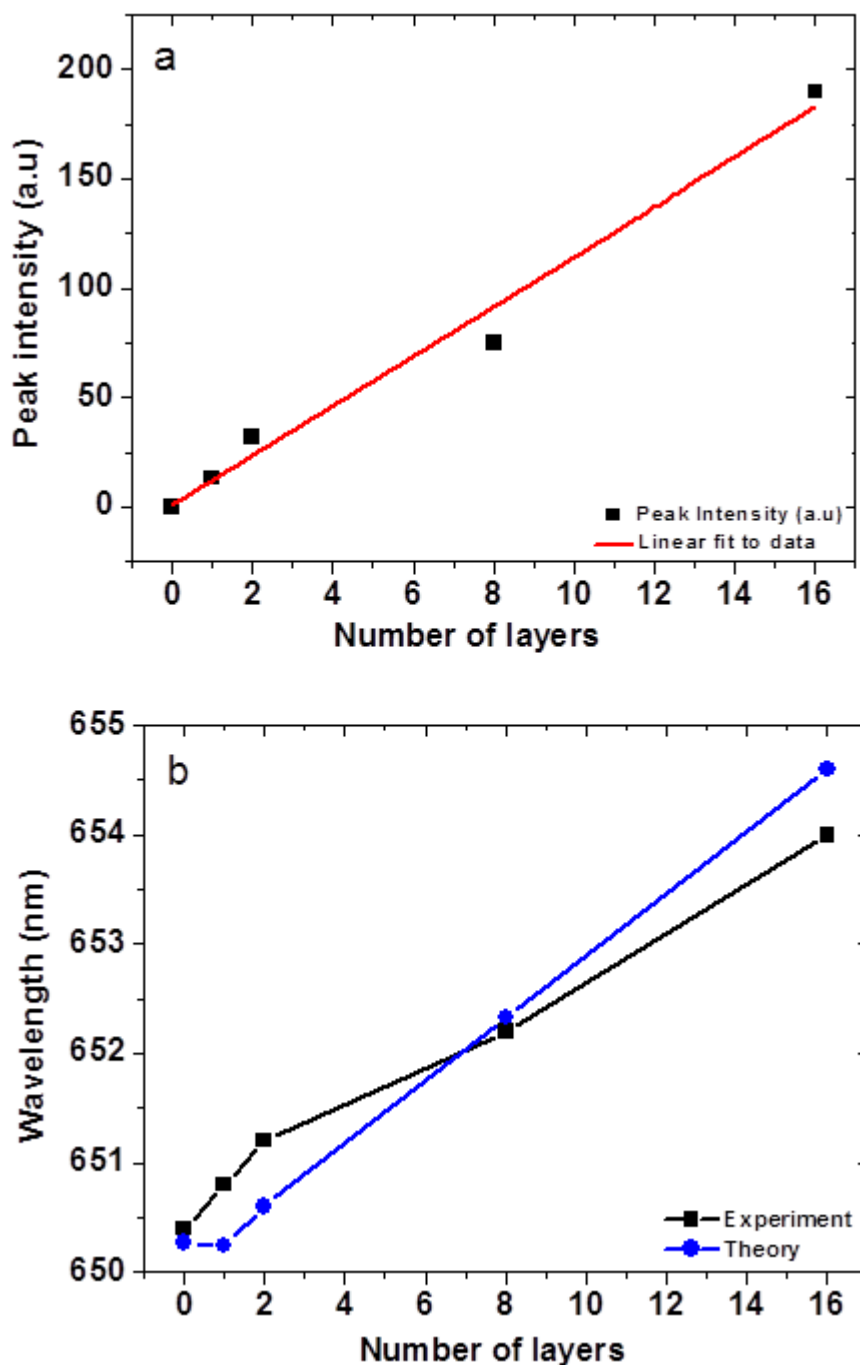


Figure 6.6: Part (a) shows the peak intensity of the Lumogen Red (LR) emitted via the fundamental cavity mode as a function of the number of molecular monolayers deposited onto the cavity surface. Part (b) shows the measured wavelength of the fundamental cavity mode of a nanocavity coated with Lumogen Red as a function of number of deposited monolayers. Data is compared with the results of an FDTD calculation plotted on the same wavelength scale. Figure taken from reference [12].

6.6 Detection limit vs. number of monolayers.

Returning to figure 6.5, it can be seen that as the thickness of the surface layer increases beyond a certain critical level (around 50 nm), the cavity mode starts to broaden appreciably. Indeed, the FDTD model indicates that the FWHM of a cavity coated with a 15 nm thick layer having a refractive index of ~ 1.80 increases from 1.04 to 3.44 nm as the thickness of this surface layer is increased to 60 nm. Such a broadening will clearly act to limit the effectiveness by which subtle changes in film thickness can be followed, and thus SiN L3 cavity are most appropriately used in conjunction with thin (< 50 nm) organic films.

The ability of the silicon-nitride based nanocavities to act as a simple optical sensor is therefore evident. The width of the cavity mode resonance in the cavities is 0.45 nm, and if a limit of detection sensitivity is detected as being half the cavity mode linewidth, then such structures should be sensitive to a mode shift of 0.225 nm. Using a simple linear fit, it is found that a spectral shift of 0.22 nm occurs following the deposition of a single Lumogen Red monolayer. This shift coincides with limit of detectability, indicating that the cavities can be used to detect films having an average thickness of a single monolayer. The surface area of the cavity is estimated to be 3×10^5 nm². This area is defined as the surface-area enclosed within the 10 holes that surround the cavity medium (defined by a line that runs through the centre of each of these holes). By estimating that each Lumogen Red molecule subtends an area of 1.5 nm², it is estimated that the cavity has a detection sensitivity of ~ 0.35 fg.

6.7 Using an L3 nanocavity as a Chemical Sensor.

In the following sections, an L3 nanocavity is explored as a simple chemical sensor. Here, the cavity is combined with a porphyrin based polymer and is used to detect an acidic vapour. As it is shown below, the optical properties of porphyrin are strongly modified by exposure to acidic vapour and they are found to be an ideal material to incorporate within a L3 nanocavity for sensor applications.

6.7.1 Porphyrins

Porphyrins are macrocyclic molecules, having a structure that consists of four pyrrole rings as shown in figure 6.7.

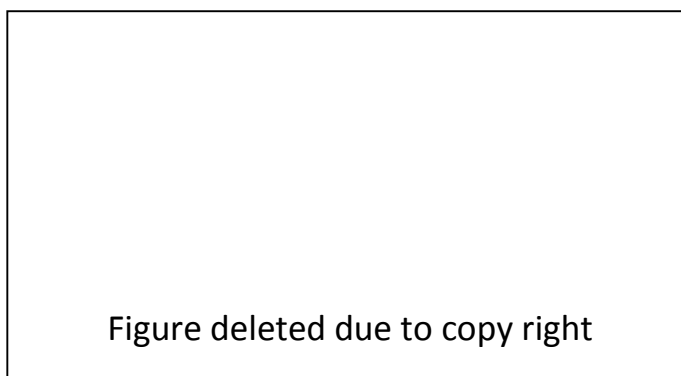


Figure 6.7: The chemical structure of the basic porphyrin ring [20]

Porphyrins have a high degree of conjugation and contain a large number of highly delocalized electrons [21], resulting in intense absorption at visible wavelengths. This feature makes such materials useful as sensor materials, particularly in sensors that detect changes in optical properties. The most common example of a porphyrin is an iron containing Porphyrin which is known as a heme. This component plays an important role in transporting oxygen in the blood. Porphyrins also have other important applications in other biological processes such as photosynthesis [22].

A series of porphyrins combining metal ions have been previously synthesized and explored [23]. Metalloporphyrins, can be synthesized by replacement of the two inner pyrrole (N-H bond) protons in a Porphyrin macrocyclic by a metal ion [24]. Porphyrins and metalloporphyrins act as a flexible system that can be used in different applications [25]. For example, metalloporphyrins have been used in photochemical processes especially photodynamic therapy (PDT) [26], and as chemical sensors for detecting different gaseous species [27-29].

6.7.2 Selection of Porphyrin materials as a chemical sensor to detect acid vapours.

In order to develop a nanocavity sensor, the optical response of a series free-based porphyrins and metalloporphyrins was explored on exposure to an acidic vapour.

The structure of the metalloporphyrins is shown in figure 6.8. Here, porphyrins containing Au, Co, Pt and Mg ions were explored, with bulky side groups attached to the molecule to aid solubility and reduce aggregation. A porphyrin based polymer called PP1 was also explored. The structure of polymer PP1 is shown in figure 6.9. PP1 is copolymer of tetraaminophenyl porphyrin and diaminodurene with the fluorinated dianhydride (with $x = 5\%$).

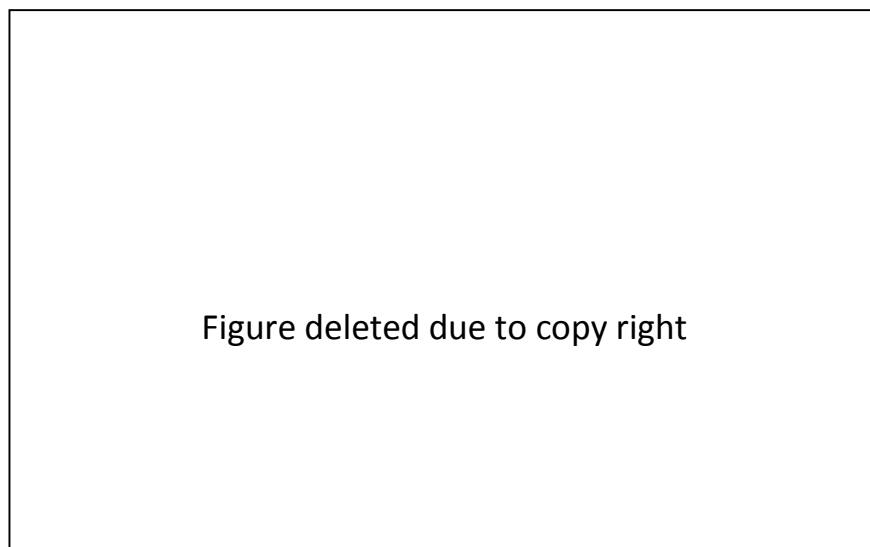


Figure 6.8: The chemical structure of metallized EHO (5, 10, 15, 20-Tetrakis (3, 4-bis (2-ethylhexyloxy) phenyl)-21H, 23H-porphine), Au EHO and Mg EHO Au [30]

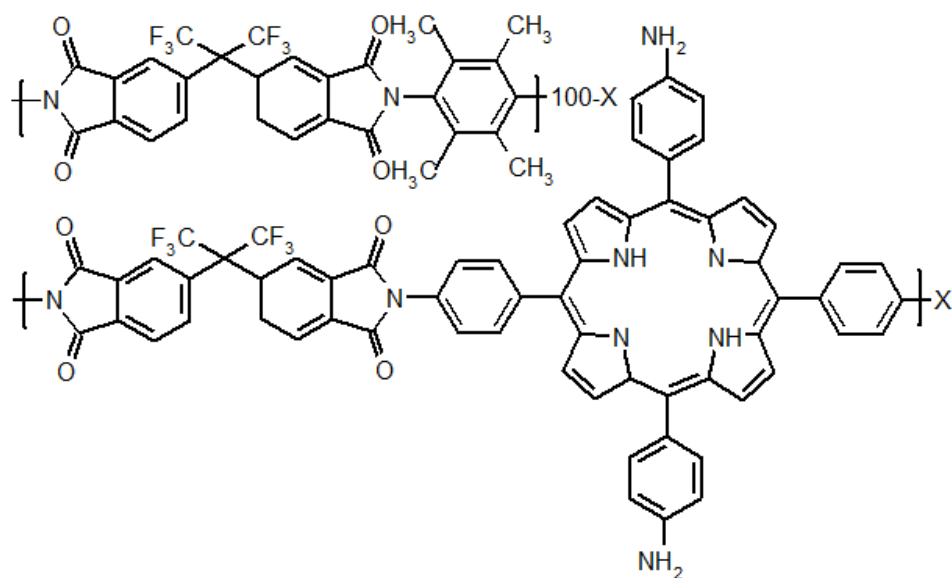


Figure 6.9: chemical structure of PP1 [12]

Here, the incorporation of the porphyrin moiety gives additional benefits from both the porphyrin ring itself and its amine substituents. Amines are readily protonated by acidic materials such as trifluoroacetic acid (TFA). The repulsion between the resultant ionized species is expected to cause the polymer to swell as well as change its refractive index.

To explore the use of porphyrin based compounds as sensor materials, a series of thin film were fabricated using spin coating on to a Si wafer. The thickness of the metalloporphyrins films were around 3.6 nm, with the PP1 thickness being 5.4 nm. Films were then exposed to a TFA vapour, for periods of up to 40 minutes, with the change in film layer thickness and refractive index being recorded using a spectroscopic ellipsometer. The exposure process was achieved by using a gas flow control system that connected to the ellipsometer. The dynamic change the thickness of a series of metalloporphyrins and the PP1 polymer as a function of vapor exposure time is shown in figure 6.10. The rate at which film thickness changed indicates that the material PP1 undergoes the most rapid swelling when exposed to the acidic vapor. Indeed, it can be seen that most porphyrins explored reach saturation point after 3 to 4 minutes after exposure, while increases in PP1 film thickness continued over the entire espouse process, with changes in thickness by as much as 10 nm evidenced. The origin of the different swelling rates is at present unknown.

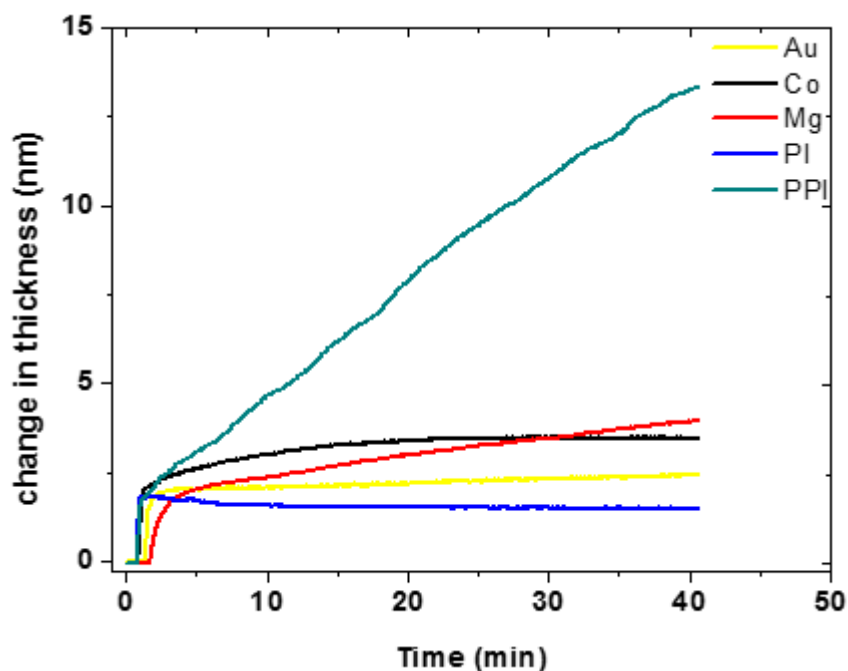


Figure 6.10: the increase in thickness of different polymer-based porphyrins. The high degree of responsiveness of PP1 is clearly evident in comparison to the other polymers tested.

6.7.3 PP1 layer thickness vs. vapor exposure

The result shown in figure 6.10 indicates that the PP1 polymer undergoes a large expansion on exposure to an acid vapor, making it a good candidate for application as a sensor material. It is apparent that the rate of swelling partially slows as a function of time following the initial exposure. Previous work suggests that changes in the optical properties of such films on exposure to a test gas saturates over a time-scale between 2 and 10 minutes [30, 32]. It is estimated that full swelling saturation time for a PP1 film is around 50 minutes (see figure 6.10), although as is shown below, a measurable response from the sensor is obtained after a TFA exposure of less than 30 seconds.

To confirm the results of the ellipsometry, the thickness change of a PP1 film was measured using AFM after it was exposed to TFA vapour. Here, a small scratch was made in a PP1 film with a series of images recorded at different times during the exposure as shown in figure 6.11. The results of the AFM measurements are in close agreement with ellipsometry measurements as illustrated in Table 6.1.

Table 6.1 Comparison of thickness change measurements recorded using ellipsometry and AFM

Exposure time (min)	Ellipsometry (nm)	AFM (nm)
10	4.8	7.5
30	10	9
60	14.8	15

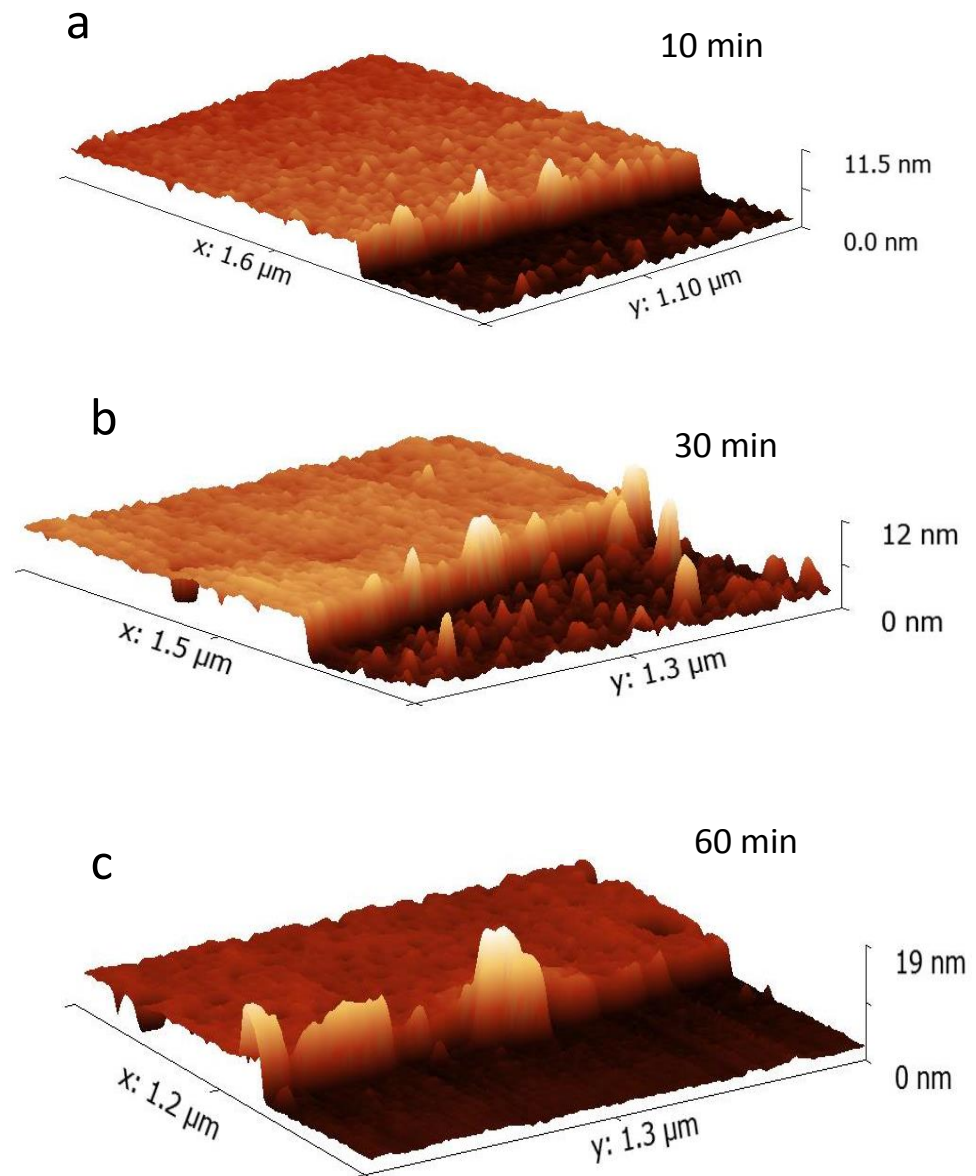


Figure 6.11: AFM images of a PP1 film during exposure to a TFA vapour. Here, scans were recorded after (a) 10 min, (b) 30 min and (c) 60 min.

6.8 Using an L3 nanocavity as a chemical sensor.

The results presented in section 6.2 demonstrated the ability of L3 cavities to act as a sensitive system to monitor changes in the thickness of an organic film deposited onto their surface. In the following sections, we develop this concept, and explore the optical properties of an L3 cavity coated with a thin film of PP1. To combine the PP1 polymer with a nanocavity, the LS technique was again used. Fluorinated-polyimide polymers have previously been explored for their sensing ability in simple thin-film format, with changes in spectral-position and intensity of fluorescence used to detect water, ethanol and isopropanol vapour [16].

6.8.1 Experimental results

In figure 6.12, the PL emission following laser excitation is plotted for an uncoated nanocavity and a nanocavity that was coated with 5 monolayers of PP1. Before coating the nanocavity, it is found that the fundamental cavity mode is located at 657.3 nm. After the LS deposition of the PP1, a strong peak is seen at 663.5 nm that originates from PP1 emission that is coupled into the fundamental cavity mode. In the same plot, the PL emission from the same cavity is shown after it has been exposed to a TFA vapor for 3 minutes. Note that the local TFA concentration during this exposure process was neither controlled nor measured. It can be seen that this exposure results in a red-shift of the cavity mode wavelength by (1.3 ± 0.3) nm to 664.8 nm. This change most probably results from a change in molecular conformation of the porphyrin polymer as a result of protonation of the amino groups. It appears that this red-shift is reversible; by heating the structure to 70°C in air for 5 minutes and then cooling it to room-temperature, the cavity mode blue-shifts to 663.3 nm. This process effectively ‘re-sets’ the optical sensor by raising the PP1 above its glass transition

temperature and facilitating the escape of trapped TFA. This then results in a re-ordering of PP1 molecular structure to its equilibrium conformation. Note that previous work has shown that this process is repeatable over at least 10 cycles [33], and that porphyrin polymers have a high degree of stability and that degradation is insignificant over the period of an entire year [34].

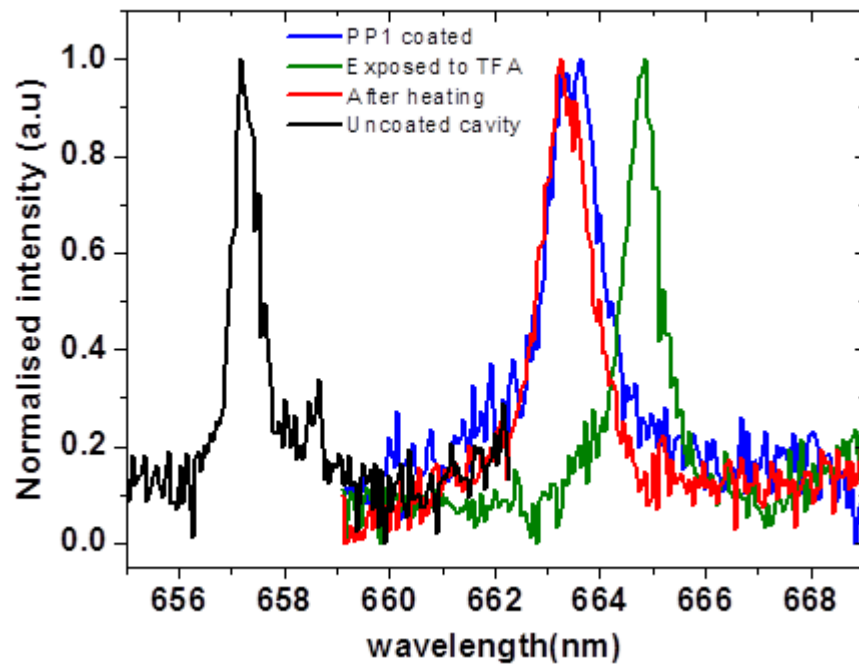


Figure 6.12: shows the PL emission from a nanocavity that has been coated with PP1. Here, data is shown for a cavity both before and after TFA vapour exposure. Data is also shown for the vapour-exposed cavity after it had been heated to 70°C and then returned to room temperature. Figure taken from reference [12].

6.8.2 Modelling cavity response.

FDTD calculations can be used to confirm the effect of the swelling of the PP1 polymer on the optical properties of the cavity. As input into the model, an L3 structure is assumed based on cavity design 2 as described earlier, with the cavity defined into a PhC made from a dielectric having a refractive index of 2.05. Onto this structure, a layer of various thickness is modelled having a refractive index

of 1.779 (approximating the PP1 layer) to determine the shift in the cavity mode wavelength. The results of the model are shown in figure 6.13, where the change in the simulated cavity mode wavelength is plotted as a function of surface layer thickness. It is predicted that the cavity mode wavelength undergoes a linear shift as the surface layer thickness increases.

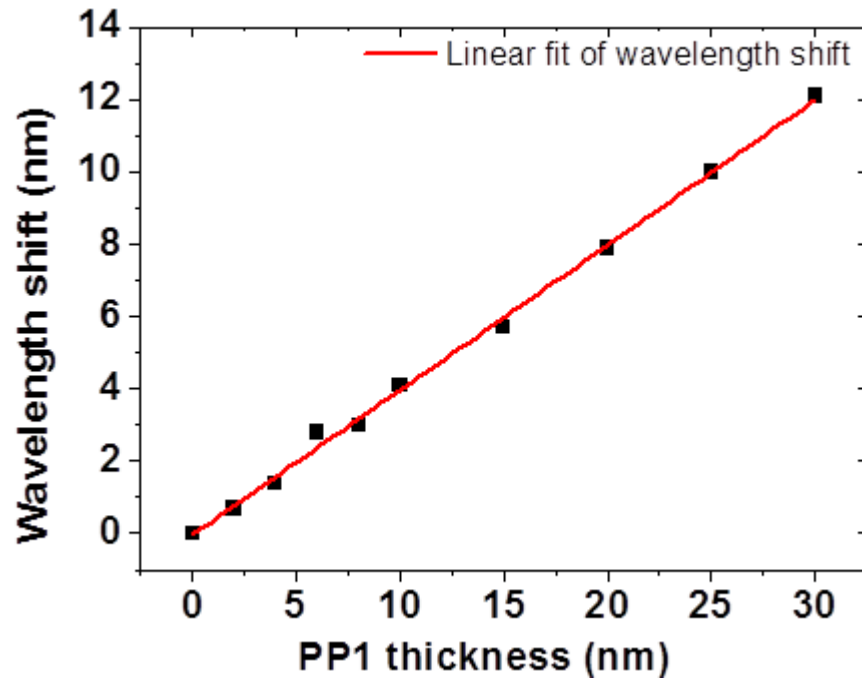


Figure 6.13: shows the result of an FDTD model that describes the shift in the cavity mode wavelength as a function thickness of the PP1 surface-layer. Figure taken from reference [12].

Experimentally, a shift in cavity mode wavelength of (1.3 ± 0.3) nm is detected, which the FDTD calculation indicates equates to a change in PP1 thickness of 3.25 nm. Using the ellipsometer measurements shown in figure 6.14 it can be seen that the PP1 film swells by 3.8 nm after a 3 minute TFA exposure (with its refractive index increasing from 1.779 to 1.798 (refractive index data not shown)); a value in good agreement with the thickness change determined on the basis of the shift in the cavity-mode. Any difference between the calculated and measured values is most easily accounted for by small changes in the refractive

index of the PP1 layer that occur as it swells that are not taken account in the calculations. Again using the half-width of the cavity mode linewidth as a limit for the detection resolution, it is estimated that a minimum change in the thickness of the PP1 surface layer of (1.4 ± 0.3) nm can be detected. Note that the model indicates that if the thickness of the PPI surface layer is instead fixed at 15 nm, a wavelength shift of $\Delta\lambda = 0.34$ nm is obtained for a change in refractive index of $\Delta n = 0.02$.

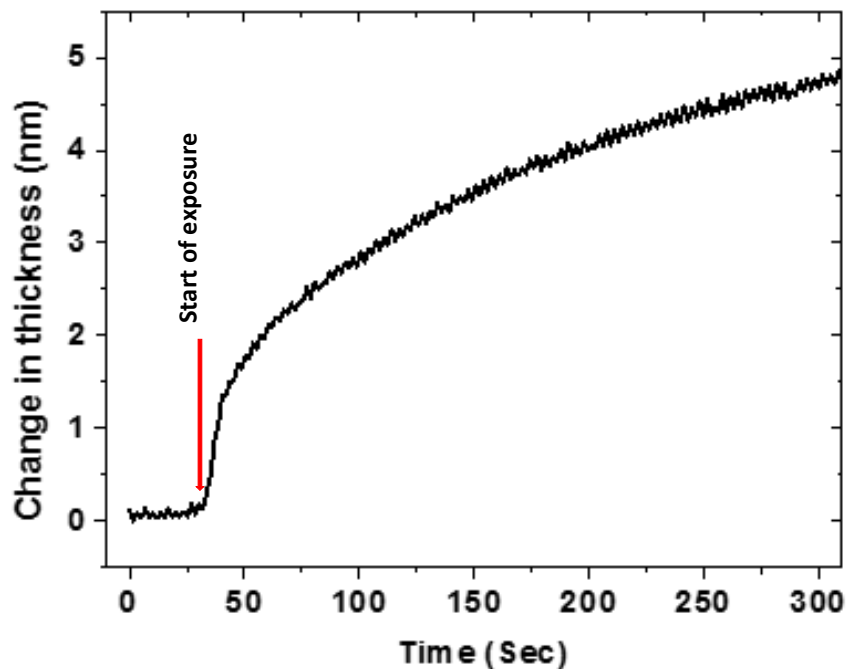


Figure 6.14: shows the increase in thickness of a control PP1 5 monolayers deposited on a silicon wafer using LS method as it is exposed to a TFA vapour over 30 sec. Here, thickness is determined via spectroscopic ellipsometer.

6.9 Conclusions

It has been shown that a SiN based nanocavity can be used to detect the deposition of a molecular monolayer onto its surface, and the swelling of a nanometer-thick porphyrin-based polymer film on a nanocavity surface as it is

exposed to an acidic vapour. Despite the fact that the nanocavity has a relatively low Q-factor, it is found that it has comparable sensitivity (in terms of its ability to detect the binding of fg quantities of material bound to the cavity surface) as other SOI-based nanocavity systems that operate at near infra-red wavelengths [9]. This sensitivity comes from the fact that the cavities operate at visible wavelengths (~ 650 nm) where the refractive index changes of the materials is relatively larger. It was also demonstrated that by coating the surface of the cavity with a thin-film of a porphyrin-based polymer, a swelling of the polymer could be detected through a shift in the cavity mode wavelength as the structure was exposed to an acidic vapor. The work demonstrates the applicability of silicon-nitride based photonic crystal nanocavities as simple optically-based chemical sensors. Indeed, other work has shown that porphyrin based materials have been used to selectively recognize a variety of different materials, including dopamine [35] and mercury (II) [36]. Sensors utilizing other polymers that undergo swelling can be envisaged to detect vapors such as chloroform [37] or ammonia [38]. To increase the sensitivity of the sensors further, it may be possible to coat or pattern a cavity surface with a molecular imprinted polymer (MIP) [39]. This technique can be used to imprint a surface thereby allowing it to selectively recognize and locally concentrate a particular molecular species. It is expected that by developing techniques to selectively pattern different MIP films or functionalized organic materials on a nanocavity surface, it will be possible to create a series of cavities integrated onto a single substrate that can selectively detect a range of target materials, permitting such structures to form the basis of an artificial nose.

References

1. D. F. Dorfner, T. Hurlimann, T. Zabel, L. H. Frandsen, G. Abstreiter, J. J. Finley, "Silicon photonic crystal nanostructures for refractive index sensing," *Applied Physics Letters*, **93**, 181103(2008).
2. C. Kang, C.T. Phare, Y. A. Vlasov, S. Assefa, S.M. Weiss, "Photonic crystal slab sensor with enhanced surface area", *Optics Express* **18**, 27930-27937 (2010).
3. S. Mandal, J. M. Goddard, D. Erickson, "A multiplexed optofluidic biomolecular sensor for low mass detection", *Lab on a Chip* **9**, 2924–2932 (2009).
4. D. Dorfner, T. Zabel, T. Hurlimann, N. Hauke, L. Frandsen, U. Ranta, G. Abstreiter, J. Finley, "Photonic crystal nanostructures for optical bio sensing applications", *Biosensors and Bioelectronics* **24**, 3688–3692 (2009).
5. M. Lee, P. M. Fauchet, "Two-dimensional silicon photonic crystal based bio sensing platform for protein detection," *Optics Express*, **15** 4530 – 4535 (2007).
6. M.G. Scullion, A. Di Falco, T.F. Krauss, "Slotted photonic crystal cavities with integrated microfluidics for biosensing applications," *Biosensors and Bioelectronics*, **27**, 101– 105 (2011).
7. W.-C. Lai, S. Chakravarty, Y. Zou, R.T. Chen, "Silicon nano-membrane based photonic crystal microcavities for high sensitivity bio-sensing," *Optics Letters*, **37** 1208-1210 (2012).

8. S. Pal, E. Guillermain, R. Sriram, B.L. Miller, P. M. Fauchet, "Silicon photonic crystal nanocavity-coupled waveguides for error-corrected optical biosensing," *Biosensors and Bioelectronics*, **26**, 4024–4031 (2011).
9. S. Pal, P.M. Fauchet, B.L. Miller, "1-D and 2-D Photonic Crystals as Optical Methods for Amplifying Biomolecular Recognition," *Analytical Chemistry*, **84**, 8900–8908 (2012).
10. M. Fox, "*Optical Properties of Solids*", Oxford University Press Inc, New York (2001).
11. A. M. Adawi, A. R. A. Chalcraft, D. M. Whittaker and D. G. Lidzey, "Refractive index dependence of L3 photonic crystal nano-cavities," *Optics Express* **15**, 14299 (2007).
12. K. Deasy, K. Sediq, S. Brittle, T. Wang, F. Davis, T. Richardson and D. Lidzey, "A chemical sensor based on a photonic-crystal L3 nanocavity defined in a silicon-nitride membrane", *Journal of Materials Chemistry C* **2**, 8700–8706 (2014).
13. A. M. Adawi, M. M. Murshidy, P. W. Fry and D. G. Lidzey, "An Optical Nanocavity Incorporating a Fluorescent Organic Dye Having a High Quality Factor," *ACS Nano* **4**, 3039 (2010).
14. M. M. Murshidy, A. M. Adawi, P. W. Fry and D. G. Lidzey, "A one-dimensional photonic-crystal nanocavity incorporating a fluorescent molecular dye," *Appl. Phys. Lett.* **97**, 153303 (2010).
15. A.M. Adawi, A. Cadby, L.G. Connolly, W.-C. Hung, R. Dean, A. Tahraoui, A.M. Fox, A.G. Cullis, D. Sanvitto, M.S. Skolnick, D.G. Lidzey, "Spontaneous emission control in micropillar cavities containing a fluorescent molecular dye," *Advance Material* **18**, 742-747 (2006).

16. M. K. Gilson and B. H. Honig, *Biopolymers*, “The dielectric constant of a folded protein”, **25**, 2097-2119 (1986).
17. S. Mosor, J. Hendrickson, B. C. Richards, J. Sweet, G. Khitrova, H. M. Gibbs, T. Yoshie, A. Scherer, O. B. Shchekin and D. G. Deppe, “Scanning a photonic crystal slab nanocavity by condensation of xenon,”, *Applied Physics Letter*, **87**, 141105 (2005).
18. S. Kiravittaya, H. S. Lee, L. Balet, L. H. Li, M. Francardi, A. Gerardino, A. Fiore, A. Rastelli and O. G. Schmidt, “Tuning optical modes in slab photonic crystal by atomic layer deposition and laser-assisted oxidation,” *Journal Applied Physics*, **109**, 053115 (2011).
19. D. Sridharan, R. Bose, H. Kim, G. S. Solomon and E. Waks, “A reversibly tunable photonic crystal nanocavity laser using photochromic thin film”, *Optics Express*, **19**, 5551 (2011).
20. M. O. Senge, A. A. Ryan, K. A. Letchford, S. A. MacGowan and T. Mielke, “Chlorophylls, Symmetry, Chirality, and Photosynthesis”, *Symmetry*, **6**, 781-843 (2014).
21. S. A. Brittle, T. H. Richardson, J. Hutchinson, C. A. Hunter, “Comparing zinc and manganese porphyrin LB films as amine vapour sensing materials”, *Colloids and Surfaces A: Physicochemical and Engineering Aspects*, **A 321**, 29-33 (2008).
22. R. Chandra, M. Tiwari, P. Kaur, M. Sharma, R. Jain and S. Dass, “Metalloporphyrins - applications and clinical significance”, *Indian Journal of Clinical Biochemistry*, **15**(Suppl), 183-199 (2000).
23. A. D. F. Dunbar, T.H. Richardson, A. J. McNaughton, J. Hutchinson, and C. A. Hunter, “Investigation of Free Base, Mg, Sn, and Zn Substituted Porphyrin

- LB Films as Gas Sensors for Organic Analytes” *Journal of Physics Chemistry*, **B 110**, 16646-16651(2006).
24. E. B. Fleischer, “Structure of porphyrins and metalloporphyrins”, *Chemical Research*, **3**, 3, 105–112 (1970).
25. K. S. Suslick, N. A. Rakow, M. E. Kosal and J. H. Chou, “The materials chemistry of porphyrins and metalloporphyrins”, *Journal of Porphyrins and Phthalocyanines*, **4**, 407–413 (2000).
26. A. Chiaviello, I. Postiglione and G. Palumbo, “Targets and Mechanisms of Photodynamic Therapy in Lung Cancer Cells: A Brief Overview”, *Cancers*, **3**, 1014-1041 (2011).
27. C. M. Dooling, O. Worsfold, T. H. Richardson, R. Tregonning, M. O. Vysotsky, C. A. Hunter, K. Kato, K. Shinbo, F. Kaneko, “Fast, reversible optical sensing of NO₂ using 5,10,15,20-tetrakis[3,4-bis(2-ethylhexyloxy)phenyl]-21H,23H-porphine assemblies”, *Journal of Material and Chemistry*, **11**, 392, (2001).
28. M. Tonezzer, A. Quaranta, G. Maggioni, S. Carturan, G. Della Mea, “Optical sensing responses of tetraphenyl porphyrins toward alcohol vapours: A comparison between vacuum evaporated and spin-coated thin films” *Sensors and Actuators B* **122**, 620–626 (2007).
29. J. Roales, J.M. Pedrosa, P. Castellero, M. Cano, T. H. Richardson, Á. Barranco, and A. R. Gonzalez-Elipé, “Selective Detection of Volatile Organic Compounds by Spectral Imaging of Porphyrin Derivatives Bound to TiO₂ Porous Films” *Applied Material Interfaces*, **4**, 5147–5154 (2012).
30. A. F. Gutiérrez, S. Brittle, T. H. Richardson and A. Dunbar, “A proto-type sensor for volatile organic compounds based on magnesium porphyrin molecular films *Sensors and Actuators*, **B 202**, 854-860 (2014).

31. S. Carturan, A. Quaranta, E. Negro, M. Tonezzer, M. Bonafini, G. Maggioni, G. Della Mea, “Optical response of 6FDA-DAD fluorinated polyimide to water and alcohols,” *Sensors and Actuators B* **118**, 393–398 (2006).
32. S. Brittle, T. H. Richardson, A. D. F. Dunbar, S. Turega and C. A. Hunter, “Alkylamine Sensing Using Langmuir-Blodgett Films of n-Alkyl-N-phenylamide-Substituted Zinc Porphyrins”, *Journal of Physics Chemistry*, **B 112**, 11278-11283 (2008).
33. T. H. Richardson, C. M. Dooling, L. T. Jones and R. A. Brook, “Development and optimization of porphyrin gas sensing LB films”, *Advances in Colloid and Interface Science*, **116**, 81-96 (2005).
34. J. M. Pedrosa, C. M. Dooling, T. H. Richardson, R. K. Hyde, C. A. Hunter, M. T. Martin and L. Camacho, “The optical gas-sensing properties of an asymmetrically substituted porphyrin”, *Journal of Material and Chemistry*, **12**, 2659-2664 (2002).
35. L. Wu, L. Feng, J. Ren and X. Qu, “Electrochemical detection of dopamine using porphyrin-functionalized graphene”, *Biosensors and Bioelectronics*, **34**, 57-62 (2012).
36. J. K. Choi, G. Sargsyan, A.M. Olive and M. Balaz, “Highly Sensitive and Selective Spectroscopic Detection of Mercury (II) in Water by Using Pyridylporphyrin–DNA Conjugates”, *Chemistry European Journal*, **19**, 2515-2522 (2013).
37. X.L. Zhang, Z.Y. Qin, X. Liu, B.L. Liang, N. Liu, Z. Zhou and M.F. Zhu, “Flexible sensing fibers based on polyaniline-coated polyurethane for chloroform vapor detection”, *Journal of Materials Chemistry A*, **1**, 10327-10333 (2013).

38. S. Banerjia, W. Penga, Y.-C. Kimb, N. Menegazzob and K. S. Booksh, “Evaluation of polymer coatings for ammonia vapor sensing with surface plasmon resonance spectroscopy” *Sensors and Actuators B: Chemical*, **147**, 255–262 (2010).
39. K. Haupt, A. V. Linares, M. Bompart and T. S. B. Bernadette, “Molecularly imprinted polymers”, *Topics in Current Chemistry*, **325**, 1-28 (2012).

Chapter Seven

Photonic-crystal L3 nanocavities containing plasmonic nanoparticles fabricated using a laser-printing technique

7.1 Introduction

Confining light in a volume commensurate with its corresponding wavelength is a key component in the growing field of nanophotonics. A nanocavity can permit control over the interactions of light with matter, allowing quantum electrodynamic effects to be used in a range of emerging optoelectronic devices [1, 2]. Such systems are of more than purely fundamental interest; nanophotonic structures can act as ultra-fast, ultra-compact laser devices [3], and when connected by optical waveguides in a photonic crystal could act as active communication elements, for example acting as single photon light-sources for quantum communication [4].

A number of reports detail the development of nanoscale metallic structures that support defined plasmonic modes [5, 6-10]. By placing two metallic nanoparticles onto the surface of a photonic-crystal cavity, it was shown that luminescence from a localized plasmon supported between the nanoparticles could be efficiently coupled into a cavity-mode [6]. Other work has demonstrated that a metallic nanorod grown on a nanocavity surface can act as an antenna to focus light to the apex of the nanorod [7]. This effect was utilized to create a platform to detect Raman emission from a single quantum dot placed at the nanorod apex. A tapered metallic waveguide defined on the surface a photonic crystal cavity has also been used to perform nanoscale chemical

mapping on a patterned Si / SiO₂ surface [15]. Here, it was argued that the photonic crystal cavity was able to collect light from an external laser and focus it to create surface plasmon-polaritons that propagated along the metallic waveguide. Taken together, these results suggest that (depending on their particular morphology and geometrical arrangement) plasmonic nanostructures defined on a nanocavity surface can either harvest light and couple energy (via a plasmon) to a cavity, or otherwise extract energy from a photonic crystal and convert it to a plasmon. Such effects may form the basis of new types of laser [11], with hybrid photonic-plasmonic crystals predicted to support optical modes having very large Q/V ratios [12]. Recently, Yi et al. showed that in a Si based hybrid plasmonic-photonic system, the Q factor of a L3 nanocavity is dependent on the relative position of the metal NP with respect to the cavity electric field distribution [9]. It was found that, the emission from the metal-NP dominated the nanocavity emission when it was located at the electric (or magnetic) field maxima (antinodes). Other work by Iwanaga et al. described the contraction of a stacked complementary (SC) plasmon-photonic crystal that acted as an efficient optical trap [13]. It was shown that coupling between plasmonic resonances and photonic guided modes resulted in the fabrication of a system having a large density of states and a high-quality factor.

In this chapter, the optical properties of printed gold nanoparticles (Au NP) has been explored within an L3 nanocavity. Here, an optical printing technique was used to place single 150 nm Au NPs within a cavity. Measurements of cavity mode linewidth made before and after NP patterning indicate a clear interaction between the cavity mode and the plasmonic modes of the NP. The experimental results are supported using FDTD calculations, and show that electromagnetic

energy stored within L3 nanocavity is dissipated through excitation of a localized surface plasmon. It is also demonstrated that such interactions are sensitive to the exact location of the NP within the cavity, with the interaction being maximized when the NP is placed over a region of high electromagnetic-field amplitude. The work presented in this chapter is based on the results of a collaboration with a group at Ludwig-Maximilians-Universität München (LMUM) published in a paper by Do et al [14], of which I am second author.

7.2 The optical characteristics of a single gold nanosphere

As the plasmonic elements in the structures, spherical Au nanoparticles were used having an average diameter 150 nm as shown in TEM image figure 7.1, and were patterned onto the nanocavity surface. The extinction spectrum of these NPs in water is shown in Figure 7.2. The spectrum is characterized by a broad dipolar plasmon resonance centred at 642 nm and by a quadrupolar plasmon resonance peaking at 545 nm; an observation consistent with other measurements on similar spherical gold colloids of similar size [15, 16]. Such NPs are an ideal system in order to explore the coupling of plasmonic and optical modes, as the dipolar mode is sufficiently broad to allow an effective overlap with the fundamental cavity mode wavelength that is positioned around 670 nm.

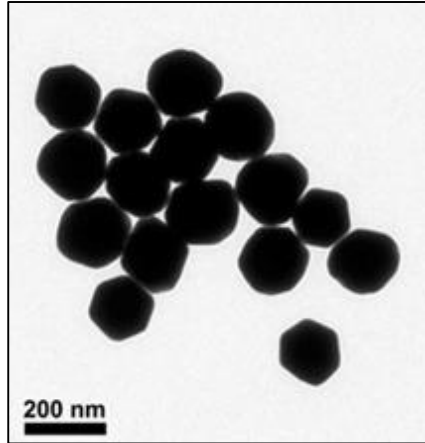


Figure 7.1: Transmission electron microscopy (TEM) image of the 150 nm spherical gold nanoparticles used in this work. Figure taken from [14]

7.3 Optical printing technique

An optical printing technique has been used to place individual NPs into an L3 nanocavity. This is a simple method having a high degree of control over the deposition of NPs onto a substrate surface. The simplicity of this technique results from the fact that it does not involve multiple steps to treat the substrate surface with patterning chemicals. In contrast, it can print individual NPs directly from a colloidal suspension onto a substrate with precision of tens of nanometers, and can additionally be used to control NP orientation using polarized light. The technique relies on optical forces (see section 4.12.1) in order to pick up an individual NP from the colloidal suspension, guide it toward the printing position, and then finally fix it on the substrate surface through van der Waals forces by overcoming the surface electrostatic repulsion force [17]. Optical printing is thus a promising technique that can be used in the production and development of various nanoscale devices and circuits. Despite such advantages, the technique

has a number of limitations when used to print a single gold nano sphere within a L3 nanocavity SiN based PhC, as discussed in section 6.4.2.

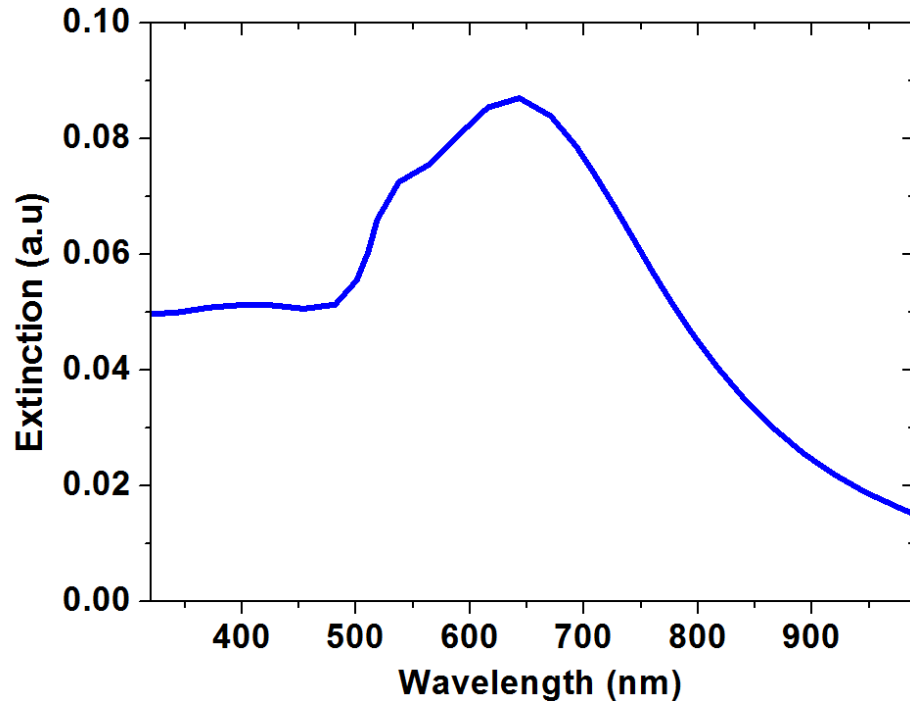


Figure 7.2: The extinction spectrum of the gold colloid measured in water.

7.4 Printing single gold nanosphere onto L3 nanocavity surface

An optical printing technique was used to accurately position a gold nanoparticle (NP) onto a sub-micrometer sized defect of an L3 photonic nanocavity. In this work, Jaekwon Do² did the optical printing of Au NP inside L3 nanocavity process, was done by using the experimental setup described in section 4.12.1.

1 Dr. Jaekwon Do. Photonics and Optoelectronics Group, Department of Physics and CeNS Ludwig-Maximilians-Universität München (LMUM), Munich, Germany

7.4.1 Silicon Nitride as a platform for gold nanoparticle printing

Silicon nitride (Si_xN_y) was used as the cavity dielectric as it is transparent at visible wavelengths. Such transparency makes it an ideal material to be used in conjunction with gold NPs that have a plasmon band peaking at visible wavelengths [18-20] (see Chapter 5).

7.4.2 Limitations to the laser printing technique

Two processes limit the patterning resolution. Firstly, during the printing process the NP experiences Brownian motion that causes a time-dependent fluctuation of the particle position in the focus of the printing laser. This effect is however relatively small and results in a fluctuation in position of the printed particles by a few 10's of nm [18]. A more significant process that limits the absolute printing resolution to around $1\mu\text{m}$ results from the accuracy by which a specific point on the surface (e.g. the centre of the nanocavity) can be aligned with the focus of the patterning laser.

While it is not possible to accurately control the relative position of an Au NP within an individual nanocavity, it was found that the positioning accuracy of the laser printing technique is sufficiently good such that $\sim 50\%$ of patterned cavities contained a single Au NP within the cavity defect. It was also found that optical printing technique could cause localized heating to both gold NPs and the SiN membrane (possibly melting them) when using printing laser at visible wavelength.

7.5 Experimental Results

The interaction between the plasmon supported by a single gold NP and the fundamental mode of an optical nanocavity was explored. Figure 7.3(a) shows a series of SEM images of 8 individual L3 nanocavities patterned with single Au NPs. In Figure 7.3(b) the fluorescence emission from the nanocavity is plotted that was generated from the cavity highlighted with a red-frame in part (a) both before (black-line) and after (red-line) laser-printing a single 150 nm Au NP. The observations presented here are representative of the general findings from at least 8 independent patterned cavities.

It can be seen that the fundamental cavity mode (having a peak wavelength of 687 nm) has a linewidth of 3.3 nm (corresponding to a Q-factor of 210). This value is broadened to 5.8 nm, red-shifted by 4 nm and reduced in amplitude by approximately 3.6 times by the presence of the printed Au NP. The interaction between the optical modes of the cavity and the Au NP can be understood using finite difference time domain modeling (FDTD) performed using MEEP software [19]. Figure 7.3(c) shows the results of the FDTD simulations for a nanocavity with, and without a 150 nm Au NP. It can be seen that there is a good qualitative agreement between the simulations and the experimental data, with the mode broadening and red shift reproduced in the calculations. Note however the spectral mismatch between the simulated and measured cavity most probably results from a combination of slightly non-uniform hole spacing, the effect of hole taper and a slightly different lattice constant than expected. The narrower linewidth predicted by the model results from the fact that incoherent scattering

due to surface roughness and imperfections in the photonic crystal are not taken into account.

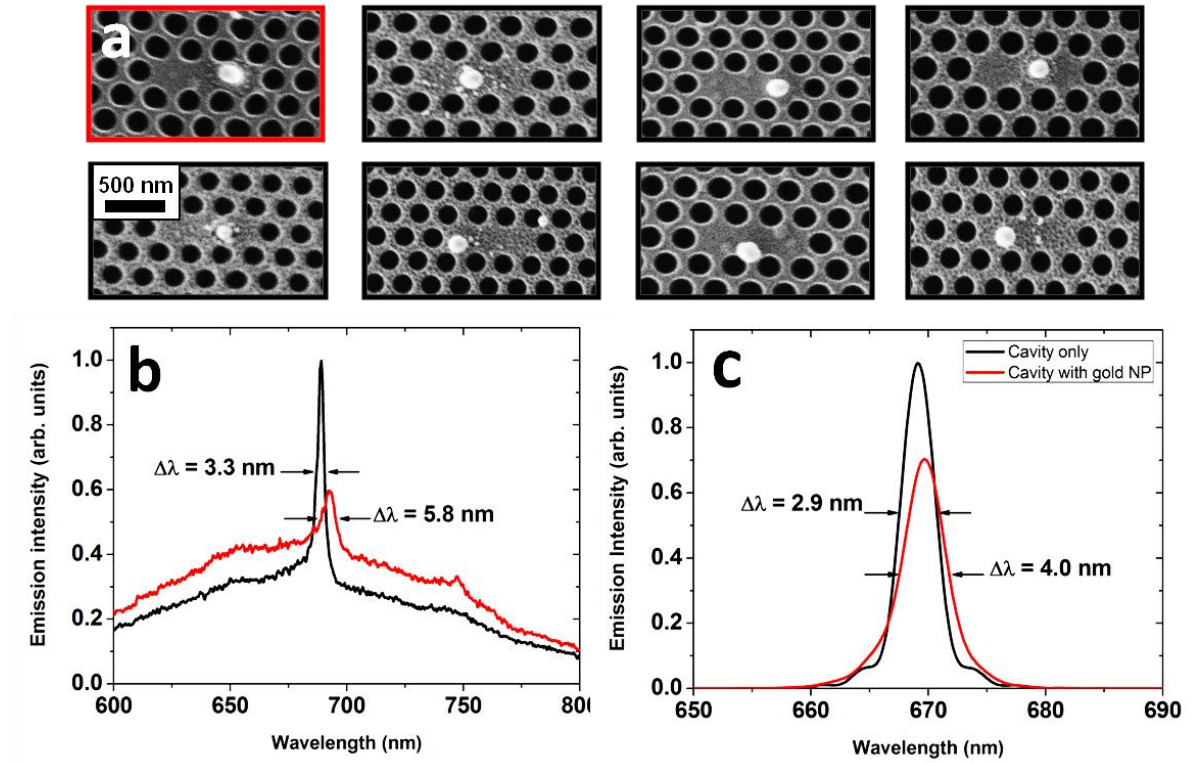


Figure 7.3: (a) SEM images of a series of nanocavities containing optically printed 150 nm gold nanoparticles. Parts (b) and (c) show respectively measured and modelled nanocavity emission for the top left cavity (highlighted with a red frame) before (black line) and after (red line) laser-printing the 150 nm Au NP. Figure reproduced from [14].

7.6 Theoretical calculations

The FDTD calculations were performed in collaboration with Dr. David Coles³. Damping and broadening of the cavity mode can be interpreted as resulting from a dissipative mechanism by which the EM field stored in the cavity drives the NP plasmon at the cavity mode frequency. This conclusion is reached based on FDTD simulations. Here, the time-dependent decay of the electromagnetic field and its interaction with the NP has been explored as shown in Figure 7.4. Here part (a) shows the calculated decay of the field at the centre of the cavity dielectric as a function of time for an ‘empty’ nanocavity and a nanocavity containing an Au NP. It can be seen that the presence of the NP reduces the lifetime of the EM field from 204 fs to 112 fs indicating that energy stored within the cavity is partially dissipated by driving the NP plasmon at the cavity mode frequency. Part (b) plots the EM field distribution throughout the cavity and NP system at a series of different times up to 500 fs following initial excitation. It can be seen that following the build-up of the field (taking ~ 150 fs), the EM field extends throughout the nanocavity and NP system and has a complex (non-trivial) distribution over the surface of the NP. This indicates that the EM field has in fact excited a superposition of different NP plasmon resonances. Time-reversal symmetry suggests that the reverse process should also be possible in which energy initially stored in a plasmon is then able to excite the optical field within the cavity. As shown in Figure 7.3 (a), a single Au NP can be printed onto a nanocavity surface, however the accurate positioning of the Au

³ Dr. David Coles. Now at Department of Materials, Hume-Rothery Building University of Oxford Parks Road, Oxford

NP within an individual nanocavity is less straightforward. To assess the effect of such uncertainty in position FDTD simulations were performed in which the location of the NP is systematically varied along the nanocavity long-axis (i.e. as a function of x for $y = 0$). In Figure 7.4 (c) the linewidth of the cavity mode emission is plotted (dependent on the degree of electronic interaction between the NP plasmon and the cavity) as a function of NP position, with data plotted as a function of lattice constant a . In addition, the electromagnetic field intensity ($|E_y|$) and the data overlaid on a background that shows the $|E_y|$ field intensity across the (x, y) plane of the cavity on the same length-scale was plotted. It can be seen that the linewidth of the cavity emission is closely correlated with $|E_y|$, indicating the high degree of position sensitivity that is required to maximize the electromagnetic interaction between the plasmon and the cavity mode. The NPs used have the peak of their dipolar plasmon mode positioned to shorter wavelengths (642 nm) than the fundamental cavity mode – although there is still substantial overlap resulting from its broad linewidth. To understand the effect of the energetic-mismatch, the interaction efficiency between the cavity and the NP was explored as a function of the energetic position of the cavity-mode. The simulations were achieved by varying the photonic-crystal lattice constant while keeping the relative hole size the same. This is shown in Figure 7.4(d), where is plotted the percent change in the linewidth of the NP-cavity emission (red squares) as a function of cavity-mode wavelength. For comparative purposes, the calculated extinction spectrum of a 150 nm spherical Au NP is also shown in Figure 7.4 (d), (black curve). Note in these simulations, the relative location of the NP is fixed at the centre (surface) of the nanocavity. It can be clearly seen that the cavity mode broadens significantly as it comes into resonance with the

peak of the dipolar-plasmon resonance, indicating stronger electromagnetic dissipation. For completeness, the effect of a 150 nm dielectric particle is plotted having the same optical constants as Polystyrene on the cavity mode. As expected, it can be seen that such a particle has a negligible effect on cavity mode broadening, indicating that interactions between the cavity mode and a nearby dielectric particle are relatively limited.

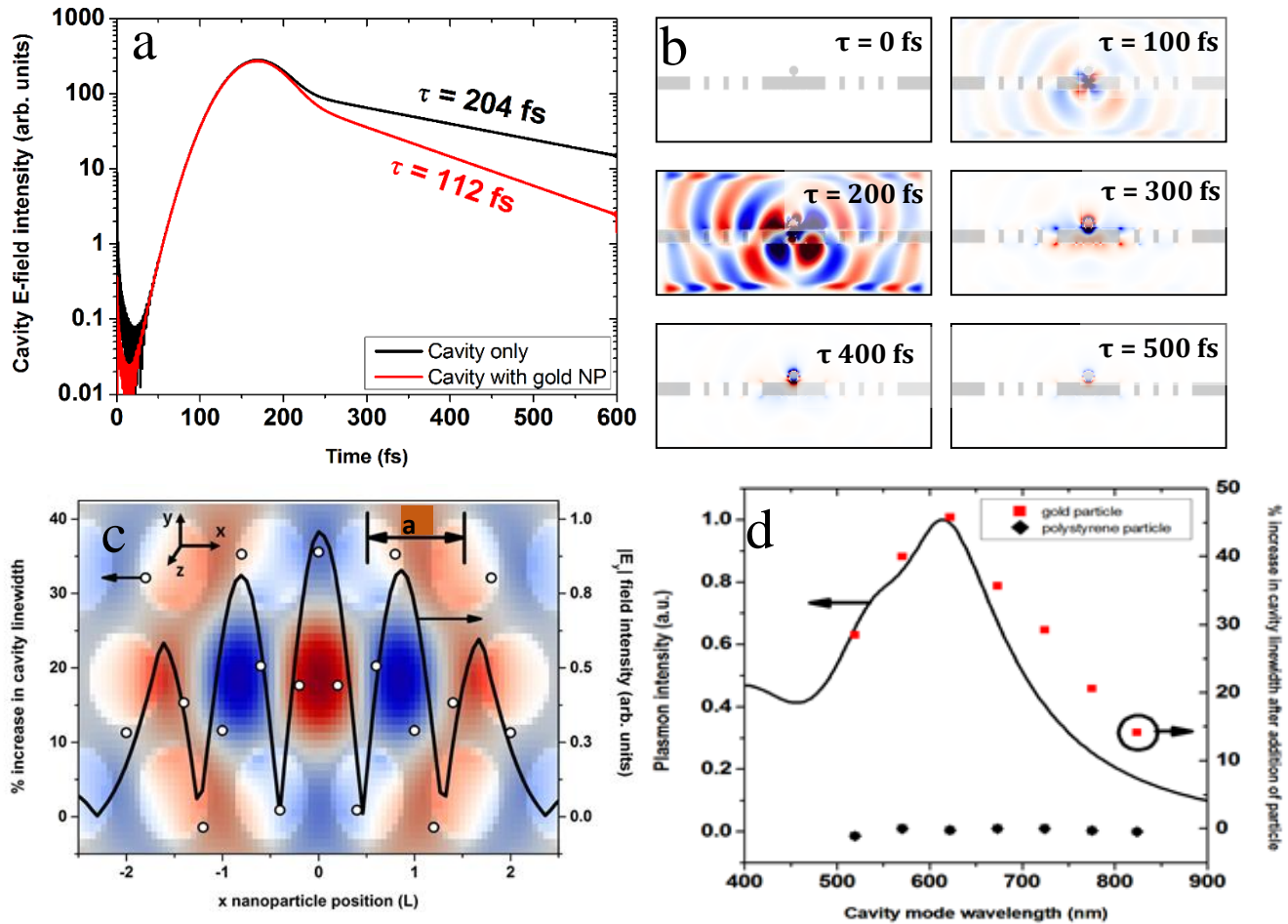


Figure 7.4: (a) FDTD modelled time-averaged dependent $|E_y|$ component of the cavity mode E-field at the centre of the nanocavity with (red line) and without (black line) a 150 nm gold nanoparticle placed centrally on the cavity surface. (b) $|E_z|$ component of electromagnetic field at the cavity mode wavelength (673 nm) through a cross section of the nanocavity- nanoparticle system at various time delays after excitation of the system. (c) Solid line: $|E_y|$ component of the cavity mode E-field as a function of position in x , where a is the photonic crystal lattice constant. Open circles: % increase in cavity linewidth as a function of the gold nanoparticle position in y . Background shows $|E_y|$ field distribution in the area of the cavity defect on the same scale. (d) Extinction spectrum of a single 150 nm gold nanoparticle as calculated using FDTD (black solid line). Red squares and black diamonds show the modelled percentage change in TE cavity mode linewidth for a 150 nm gold and 150 nm polystyrene nanoparticle respectively placed centrally on the cavity surface as a function of the cavity mode wavelength. Figure reproduced from [14].

7.7 Conclusions

An optical printing technique was used to place single 150 nm Au nanoparticles within an L3 nanocavity. Measurements of cavity mode linewidth made before and after NP patterning indicate a clear interaction between the cavity mode and the plasmonic modes of the NP. This is confirmed using FDTD simulations that show that energy initially stored in the nanocavity is dissipated through excitation of localized surface plasmons. The simulations performed also demonstrate that such interactions are sensitive to the exact location of the NP within the cavity, with the interaction being maximized when the NP is placed over a region of high electromagnetic-field amplitude. It is possible that by utilizing the ability of metallic and core-shell NPs to enhance fluorescence intensity [21, 22] by control over radiative rates, [23] it will be possible to harness such structures to design new types of low-threshold laser. The aqueous-based all-optical printing technique used to assemble a hybrid photonic-plasmonic nanostructure represents a significant advance, as it is much faster than serial pick-and-place or nano manipulation techniques that have been previously used to fabricate such structures, and importantly it could even be parallelized [32] to simultaneously position nanoparticles in multiple cavities. This process could be utilized to pattern (for example) inorganic nanocrystals and nanodiamonds into a nanocavity to create single photon emitters. Furthermore, this vertical printing technique eliminates the necessity for cavities to be designed with manipulation in mind, with NP printing possible in a range of different structures and architectures. Despite the fact that the technique does not allow accurate positioning of a NP within a single nanocavity, it allows single NPs to be loaded into a nanocavity. This ability will permit plasmons on a single NP to be directly

and selectively excited using relatively simple optical techniques. By using a waveguide structure defined into a PhC it should be possible to couple in a controllable fashion to a series of nanocavities that each contain a NP. Indeed, the strong attachment of the laser-printed Au NPs to the cavity surface suggests that photonic-NP structures could be integrated into a microfluidic device, opening up new possibilities as chemical and biochemical sensors.

However, the limitations of using optical printing technique to print gold NPs within SiN based L3 nanocavity have been discussed in section 7.3.2. For this reason, attention then focused on the development of efficient alternative techniques to place more accurately plasmonic NPs in a nanocavity. To do this electron beam lithography was developed as an efficient printing technique. As is shown in the following chapter this does not affect the optical properties of the plasmonic NPs and caused no physical damage to the cavity membrane, it can also be used with high precision to define NPs having different size and shape in a cavity.

References

- 1 J. M. Gerard, J. Gayral, “Strong Purcell Effect for InAs Quantum Boxes in Three-Dimensional Solid-State Microcavities”, *Journal of Light wave Technology*, **17**, 11, (1999).
- 2 T. Yoshie, A. Scherer, J. Hendrickson, G. Khitrova, H. M. Gibbs, G. Rupper, C. Ell, O. B. Shchekin & D. G. Deppe, “Vacuum Rabi splitting with a single quantum dot in a photonic crystal nanocavity”, *Nature*, **432**, 200-203 (2004).
- 3 H. Altug, Dirk Englund, J. Vučković, “Ultrafast photonic crystal nanocavity laser”, *Nature Physics*, **2**, 484 - 488 (2006).
- 4 K. J. Vahala, “Optical microcavities”, *Nature*, **424**, 839-846 (2003).
- 5 O. Benson, “Assembly of hybrid photonic architectures from nanophotonic constituents” *Nature*, **480**, 193–199 (2011).
- 6 M Barth, S Schietinger, S Fischer, J Becker, N Nusse, T Aichele, B Lochel, “Nanoassembled plasmonic-photonic hybrid cavity for tailored light-matter coupling”, *Nano letters*, **10**, 3, 891-895 (2010).
- 7 F. De Angelis, M. Patrini, G. Das, I. Maksymov, M. Galli, L. Businaro, L.C. Andreani, E. Di Fabrizio, “A Hybrid Plasmonic–Photonic Nanodevice for Label-Free Detection of a Few Molecules”, *Nano Letters*, **8**, 2321-2327 (2008).
- 8 F. De Angelis, G. Das, P. Candeloro, M. Patrini, M. Galli, A. Bek, M. Lazzarino, I. Maksymov, C. Liberale, L.C. Andreani, E. Di Fabrizio, “Nanoscale chemical mapping using three-dimensional adiabatic compression of surface plasmon polaritons”, *Nature Nanotechnology*, **5**, 67-72 (2010).

- 9 Y. Yi, T. Asano, Y. Tanaka, B-S Song, S. Noda, “Investigation of electric/magnetic local interaction between Si photonic-crystal nanocavities and Au meta-atoms”, *Optics Letters*, **39**, 19, (2014).
- 10 I. Mukherjee, G. Hajisalem, R. Gordon, “One-step integration of metal nanoparticle in photonic crystal nanobeam cavity”, *Optics Express*, **19**, 23, 22462 (2011).
- 11 R.-M. Ma, R.F. Oulton, V.J. Sorger, G. Bartal, X. Zhang, “Room-temperature sub-diffraction-limited plasmon laser by total internal reflection”, *Nature Materials*, **10**, 110-113 (2011).
- 12 X. Yang, A. Ishikawa, X. Yin, and X. Zhang, "Hybrid photonic-plasmonic crystal nanocavities," *ACS Nano*, **5**, 2831-2838 (2011).
- 13 M. Iwanaga and B. Choi, “Heteroplasmon Hybridization in Stacked Complementary Plasmo-Photonic Crystals”, *Nano Letters*, **15**, 1904–1910 (2015).
- 14 J. Do, K. N. Sediq, K. Deasy, D. M. Coles, J. Rodríguez-Fernández, J. Feldmann, and D. G. Lidzey, “Photonic Crystal Nanocavities Containing Plasmonic Nanoparticles Assembled Using a Laser-Printing Technique”, *Advanced Optical Mater*, **1**, 946–951 (2013).
- 15 K.L. Kelly, E. Coronado, L.L. Zhao, and G.C. Schatz, “The Optical Properties of Metal Nanoparticles: The Influence of Size, Shape, and Dielectric Environment”, *Journal of Physical Chemistry B* **107**, 668-677 (2003).
- 16 J. Rodríguez-Fernández, J. Pérez-Juste, F. J. García de Abajo, L. M. Liz-Marzán, “Seeded Growth of Submicron Au Colloids with Quadrupole Plasmon Resonance Modes” *Langmuir*, **22**, 7007-7010 (2006).

- 17 A. S Urban, A. A. Lutich, F. D Stefani, J. Feldmann, "Laser Printing Single Gold Nanoparticles". *Nano Letters* **10**, 4794-4798, (2010).
- 18 Murshidy, M.M., A.M. Adawi, P.W. Fry, D.M. Whittaker, and D.G. Lidzey, "The optical properties of hybrid organic-inorganic L3 nanocavities", *Journal of Optical Society of America B*, **27**, 215-221 (2010).
- 19 A.M. Adawi, M.M. Murshidy, P.W. Fry, and D.G. Lidzey, "An Optical Nanocavity Incorporating a Fluorescent Organic Dye Having a High Quality Factor," *ACS Nano*, **4**, 6, 3039-3044 (2010).
- 20 A.M. Adawi, A.R.A. Chalcraft, D.M. Whittaker, and D.G. Lidzey, "Refractive Index Dependence of L3 Photonic Crystal Nano-Cavities," *Optics Express*, **15**, 22, 14299-14305 (2007).
- 21 F. Tam, G.P. Goodrich, B.R. Johnson, N.J. Halas, "Plasmonic enhancement of molecular fluorescence", *Nano Letters*, **7**, 496-501 (2007).
- 22 P.P. Pompa, L. Martiradonna, A. Della Torre, F. Della Sala, L. Manna, M. De Vittorio, F. Calabri, R. Cingolani, R. Rinaldi, "Metal-enhanced fluorescence of colloidal nanocrystals with nanoscale control", *Nature Nanotechnology*, **1**, 126-130 (2006).
- 23 P. Anger, P. Bharadwaj, L. Novotny, "Enhancement and quenching of single-molecule fluorescence" *Physical Review Letters*, **96**, 113002 (2006).
- 24 S. Nedev, A.S. Urban, A.A. Lutich, J. Feldmann, "Optical Force Stamping Lithography", *Nano Letters*, **11**, 5066–5070 (2011).

Chapter Eight

The fabrication and characterization of gold nanoparticles and nanoparticle dimers and their incorporation into photonic nanocavities

8.1 Introduction

The ability to directly fabricate plasmonic nanostructures allows increased control over their optical properties. A complex arrangement such as coupled nanodisks can generate a localized and intense electromagnetic field, with the field being strongly enhanced in the gap between the particles. Here, the field produced is known to be highly sensitive to the local environment, allowing NP dimers to be used in many applications such as structures to enhance Raman scattering [1, 2], and as biosensors [3].

In this chapter, the optical response of isolated nanoparticles and nanoparticle dimers are studied. The effect of printing gold nanodisks inside an L3 nanocavity is then explored experimentally and by modelling. It is concluded that plasmonic dimers can have a significant effect on the optical properties of the confined electric field within L3 cavity. It is also shown using FDTD modelling that the field intensity can be significantly enhanced between the coupled dimer in comparison to that in an empty cavity or between nanodisks fabricated on a planar surface. This suggests that such plasmonic-photonic structures may be of potential interest as novel types of laser devices.

8.2 Single gold nanodisk.

To investigate the energy of localized surface plasmons (LSP) as a function of gold NP size, an array of single nanodisks was fabricated on a silicon nitride layer using EBL. All gold nanodisks had the same shape (ellipsoid) and the same height (≈ 100 nm). They were arranged in a square array having a lattice constant of $3 \mu\text{m}$ as shown in figures 8.1(a) & (b). The distance between the individual particles was far enough to reduce inter-particle interactions and also enables a single particle to be isolated and measured. In the experiments described, the long axis length, which is referred to as the nanoparticle size, was varied between 170 and 355 nm. SEM images were used to characterise the size of the NPs along the X and Y axis. Two mechanisms were used to determine the height of the NPs in the out of plane dimension (Z-axis). Firstly, the deposition crystal sensor that was fixed inside the thermal evaporation chamber was used to obtain an estimate of the thickness of the evaporated material. Secondly, AFM scans were used to directly image the NPs as in shown in figure 8.1(c). The gold nanodisks printed onto a SiN membrane were divided into three sets depending on their size and aspect ratio. The first set includes NPs having a size of 210, 230, 250 and 300 nm with an aspect ratio of 2.2. The second set included particles having sizes 280, 325 and 355 nm with an aspect ratio of 2.5. The last set was for particles having sizes of 170 and 190 nm with an aspect ratio of 1.6. Figures 8.2(a) and (b) show dark field measurements of scattered light from individual NPs and FDTD calculations respectively of scattered light from particles in the first set. Figure 8.2 (c), (d) and (e), (f) similarly plots measured and calculated scattering for the second and third sets of NPs.

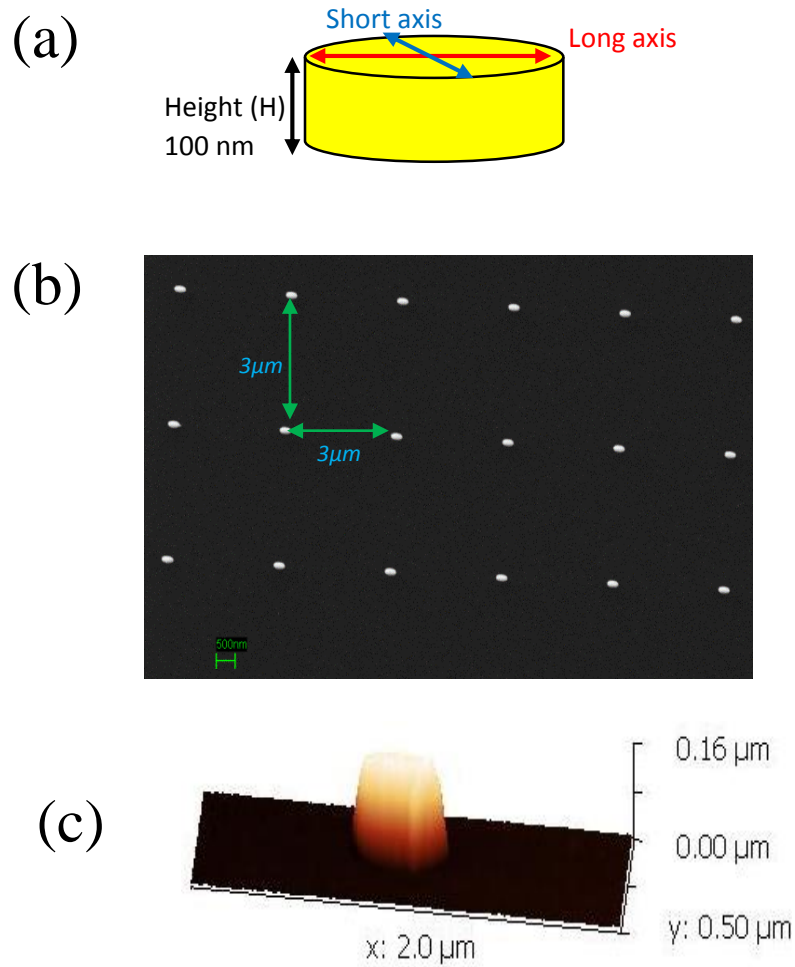


Figure 8.1: (a) Schematic illustrating the gold nanodisk dimensions. (b) SEM image of an array of printed single gold nanoparticles on a $(3\mu\text{m} \times 3\mu\text{m})$ lattice, (c) AFM image of a nanoparticle having a height of 100 nm.

In all cases, experimental scattering spectra are measured over the wavelength range 500-900 nm due to the spectral sensitivity of the spectrometer. FDTD calculations were however performed over a much wider range (up to 1200 nm). For all NPs, we observe a resonance between 650 and 800 nm. Our calculations indicate a scattering peak between 600 nm and 1000 nm. In most cases, we find reasonable agreement arrangement between measurements and theory, however in some cases a scattering peak is predicted at significantly longer wavelength

than is observed experimentally. The reason for this discrepancy is not understood.

Nevertheless, both experiment and modelling indicated that the peak position of the scattered light red-shifts as the particle size increases as shown in figure 8.2 and summarized in figure 8.3(a) and (b). This result shows the ability to tune the optical properties of metal NPs by changing their size.

For relatively large nanoparticles (as discussed in chapter two), the phase retardation of the oscillating electrons plays an important role in the determination of plasmon resonance [4], and the resonance peak undergoes a red-shift and it has a multimode character. In addition, for non-spherical nanoparticles, the SPR is modified and can be considered different from that of a spherical nanoparticle [5, 6] as longitudinal and transversal polarizations do not produce equivalent resonances. These modes mainly correspond to free electrons oscillating parallel or perpendicular to the NP long axis [7]. Additionally, the peak position of the scattered field is affected by the relative orientation of a nanoparticle and the excitation field. It has been observed that light scattered from the long axis of nanorods tends to be at red wavelengths, while it tends to be at green wavelength when scattered from the short axis [8].

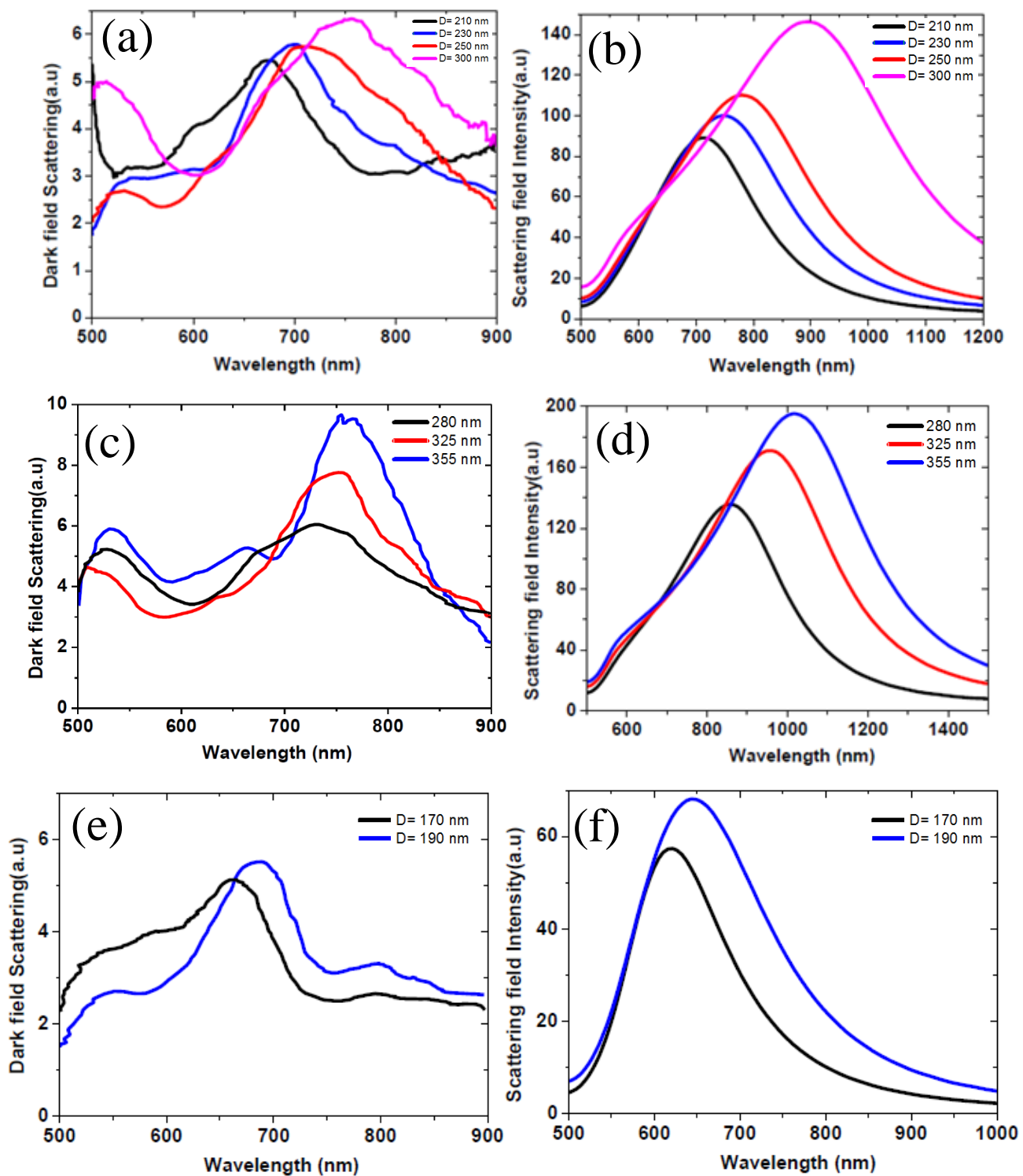


Figure 8.2: (a), (c), (e) Experimental measurement and (b), (d), (f) FDTD calculation of the scattered resonance peak position for the first, second and third set of NPs. Here, the first, second and third NP sets had an aspect ratio 2.2, 2.5 and 1.6 respectively. It can be seen that scattered light moves towards the red as the particle size increases.

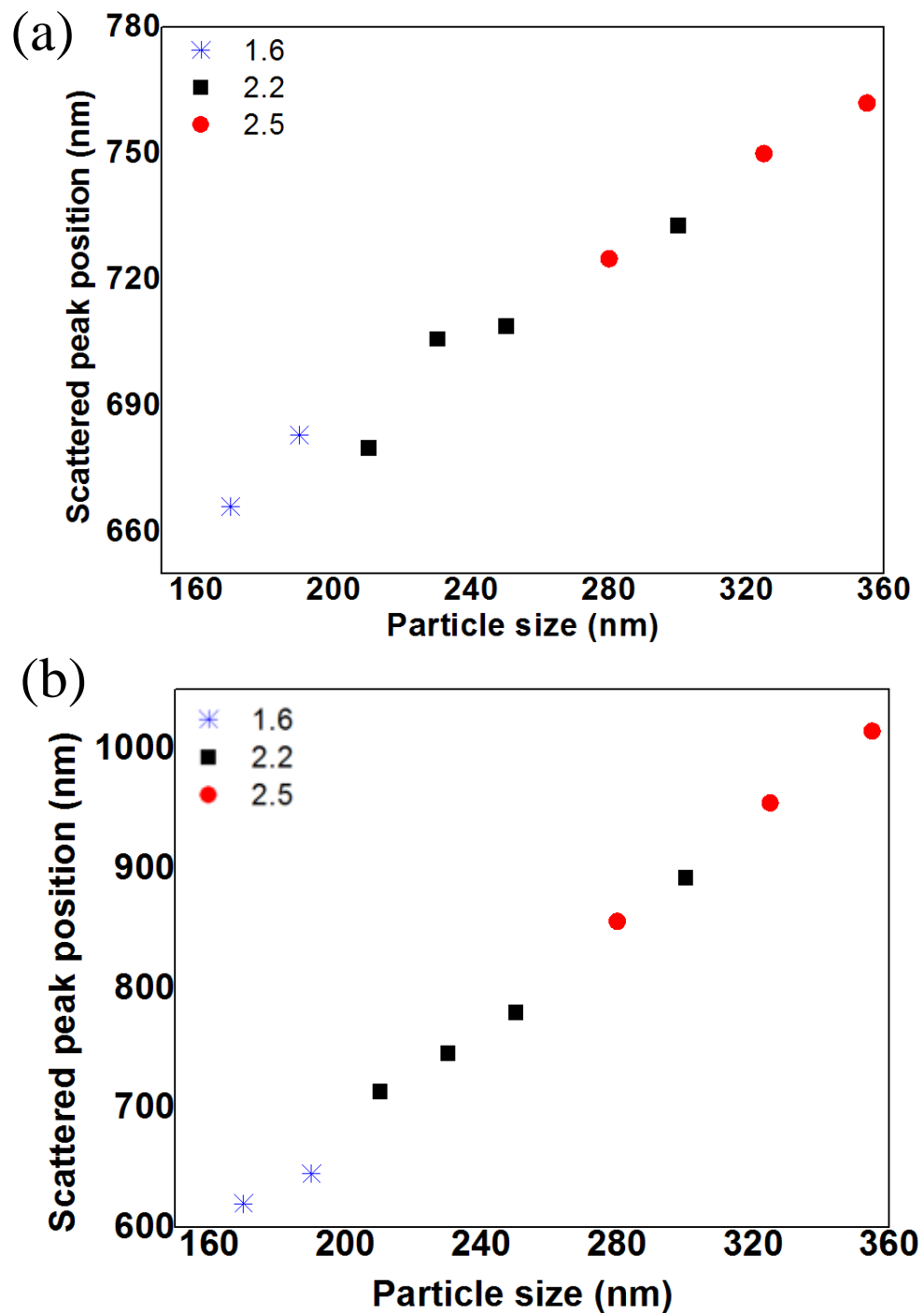


Figure 8.3: (a) Experimental measurement and (b) FDTD calculation of the peak scattering resonance position for different particle sizes having different aspect ratios. Particles are divided into three sets depending on their aspect ratios 1.6 (blue crosses), 2.2 (black squares) and 2.5 (red circles). The results show that the scattered peak position redshifts linearly with increasing particle size.

The longitude band modes of elongated NPs generally undergo a red-shift as the particle size and the aspect ratio increases, as $\omega_{res} \propto \frac{1}{R}$, where R is the aspect ratio (see chapter three, equation 2.25). This effect can be explained according to a mass-spring model. As the aspect ratio and the particle size increases, the separation between the ends of the particle increases, and thus the restoring force of the oscillating charges at the ends of particle (determining the oscillation frequency) is reduced [9, 10]. In other words, the oscillating charges suffer less damping [11] and the retardation effect increases as the particle size increases [5, 12].

It found that, the intensity of scattered field increases as the particle size increases (see chapter three section 3.5). Here, both calculations and measurements show a near field enhancement of the scattered field for all sets of gold nanodisks as the particle size increases, as illustrated in Figures 8.4 (a), (b).

8.3 Gold nanodisks dimers.

A high enhancement and strong localized optical near field can be created in a small volume by arranging a small gap between two or more metallic nanoparticles. For a very small gap (a few nanometres) between sharp antennas, an ultra-tight confinement and extreme near field enhancement can be achieved, known as a hotspot. Such hotspots can be used to study light matter interactions [13]. To explore the optical response of a pair nanoparticles, an array of dimer nanodisks were printed on a SiN membrane surface using EBL as shown in figures 8.5 (a) and (b). Experimentally, gold nanodisk dimers were created having a long axis length of 165 nm, an aspect ratio of 1.54 and a height of 100

nm, with such nanoparticles being separated by 70, 100, 155, 170 and 210 nm as shown in the SEM image in figure 8.5 (a).

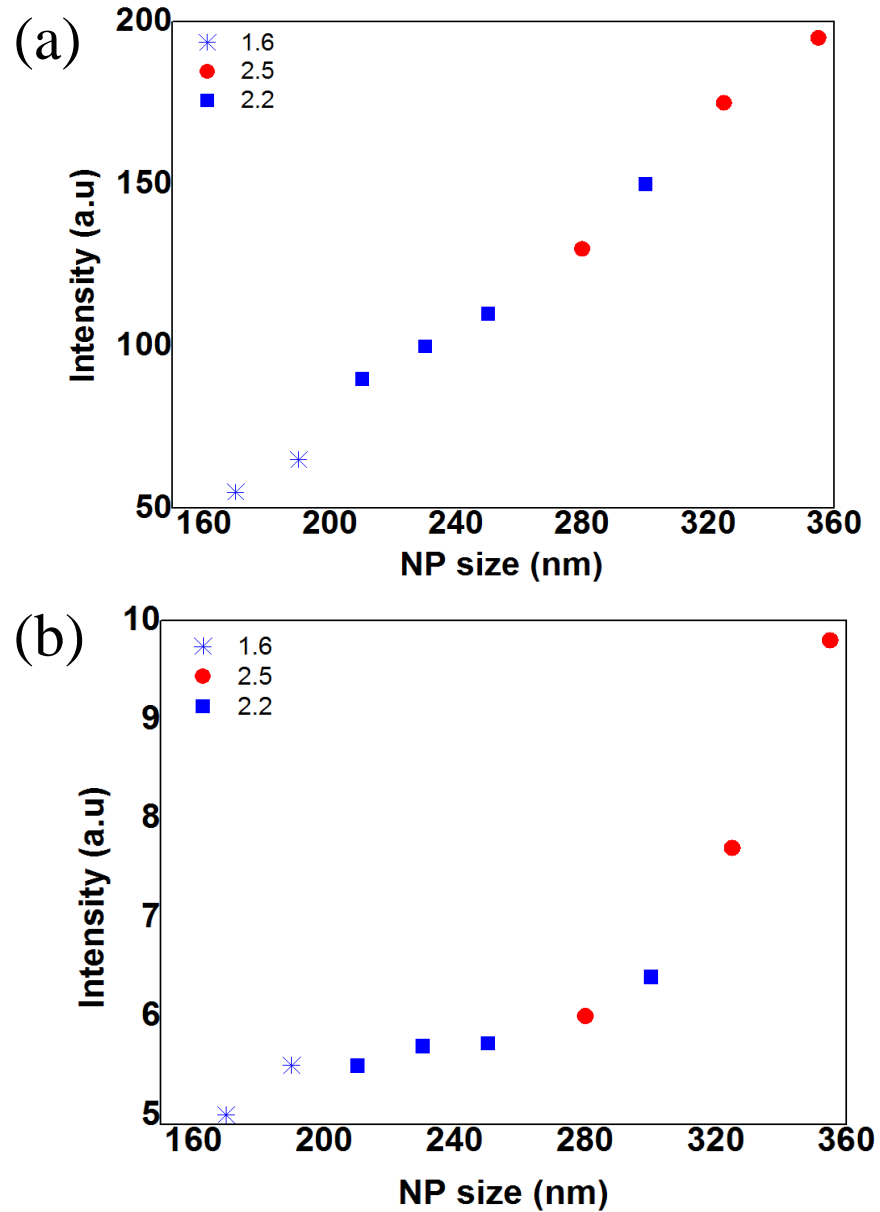


Figure 8.4: (a) Calculated and (b) dark field measurements of scattering intensity from individual gold nanodisks having different sizes. It is clear that the scattered field intensity is enhanced as the particle size increases.

Although EBL is a powerful tool to fabricate features around 100 nm, the fabrication of smaller particles can be challenging. The reason for this is the fact

that unexposed PMMA resist between the particles can receive a large electron beam dose [12]. This means that the PMMA in the gap becomes dissolved during the development process and consequently the gap between the nanodisks becomes filled with a thin gold layer. This results in the dimers actually having a dumbbell shape [14] as shown in the SEM image in figure 8.5 (b). In this case, we characterized the total length of the connected dimer as being twice the particle length (L) plus the contact length ($2L+D$) as illustrated in figure 8.6.

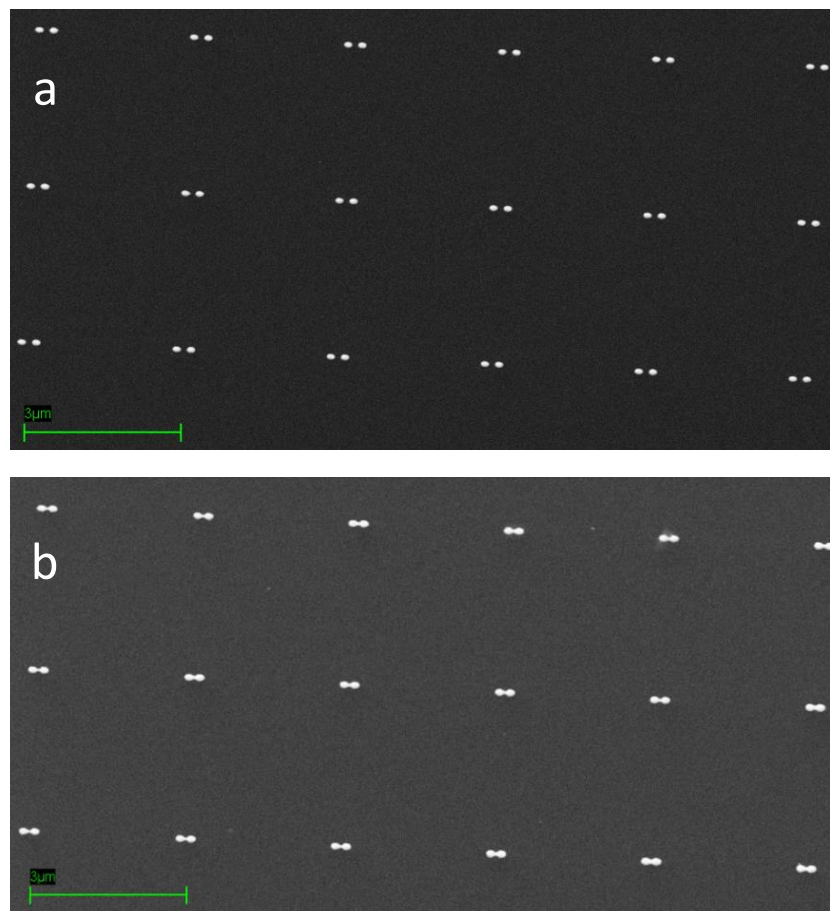


Figure 8.5: SEM image for separated nanodisk dimers part (a) and dumbbells part (b)

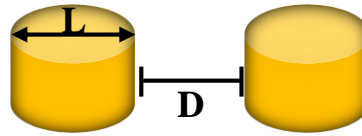


Figure 8.6. Schematic illustration of the nanodisk dimer length (L) and separation (D) between them

Dark field scattering measurements of gold dimer nanodisks indicate that the plasmon scattering resonance exhibits a red shift with decreasing separation as shown in figure 8.7 (a). This result is confirmed by previous studies [12, 15-21]. Specifically, we find that the peak resonance red-shifts by ≈ 75 nm as the distance between the coupled dimer decreases by 140 nm (from 210 nm to 70 nm). Figure 8.7 (b) is an SEM image showing the variation of separation between the metal NP dimers. Experimentally it is observed that the peak resonance becomes highly sensitive to small variations in the distance as the gap between the dimers is decreased [21]. Figure 8.7(c) summarizes the red shift in the peak resonance as the distance between the decreases.

The red shift in plasmon energy with decreasing separation can be explained through the spring-mass model [22, 23, 24] (see Chapter 3 section 3.4.5). Coupling between NPs occurs through introducing an extra spring in the gap that separates between them. This extra spring is produced as consequence of mutual charge induction on the opposite side of the particles, which produces a restoring force that modifies the oscillation frequency [9, 10]. As the distance between the dimers decreases, the charges on both sides of the gap that oscillate in-phase due to the induction effect will be highly localized and strongly attracted to each other. Phenomenologically, the red shift in the plasmon energy can be resulted from the reduction of the effective restoring force of the spring in the gap that leading to reduce the spring oscillation frequency [16, 25].

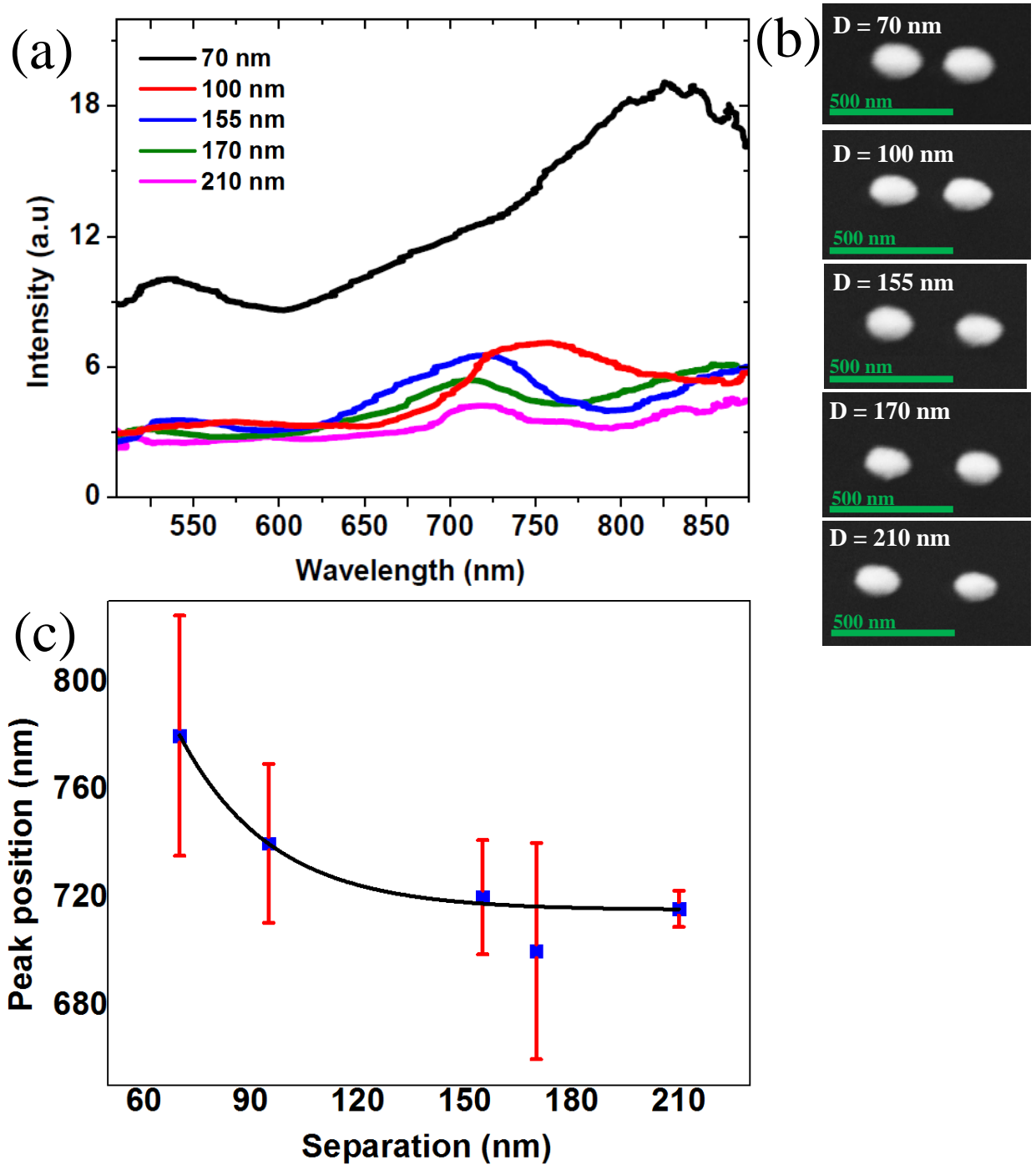


Figure 8.7: (a) Dark field scattering spectra of nanodisk dimers as a function of end to end separation. It can be seen that the peak red shifts as the separation distance between metal NPs decreases. (b) SEM image showing NP having variation in separation. (c) Experimental data showing the peak of the scattering wavelength as a function of separation between the metal dimers.

Moving the dimers into contact forms a dumbbell shape as shown in figure 8.8 (inset SEM image). In this case, the oscillating electrons tunnel through the region between them, resulting in a nonlocality of the charge distribution which effects the local dielectric constant [26]. Here, the scattering peak is dependent on the total length of the connected dimer, and acts as single particle rather than a separated dimer. Consequently, as the length of connected area increases, the scattered peak position undergoes a red shift as shown in figure 8.8.

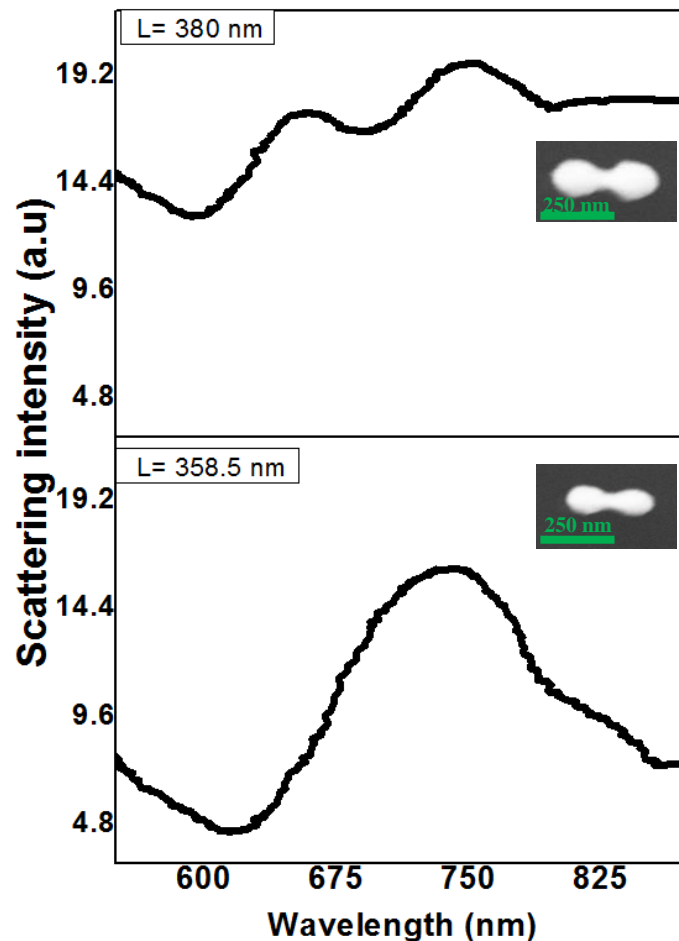


Figure 8.8: Dark field scattering spectra of connected gold nanodisk dimers as a function of dimer length. The scattered peak resonance can be seen to red shift as the dimer length increases.

The strength of the scattered field is also affected by the separation between metal dimers. It is observed that the intensity of the scattered field increases dramatically as the separation between the coupled particles is reduced as illustrated in figure 8.9. Here, it is found that the intensity increased 5 fold as the separation reduced from 210 nm to 70 nm. This large enhancement in the electric field confined between the dimers occurs as a result of large accumulation of charge around the inter-particle gap [27].

In addition, a slight increase in scattering intensity (by 1.3 times) from the dumbbell shaped dimers is observed experimentally with increasing dimer length; a result of increases in the extinction cross section [27]. Other studies have shown that the “neck” area can also help concentrate the electric field in a small spatial region [14].

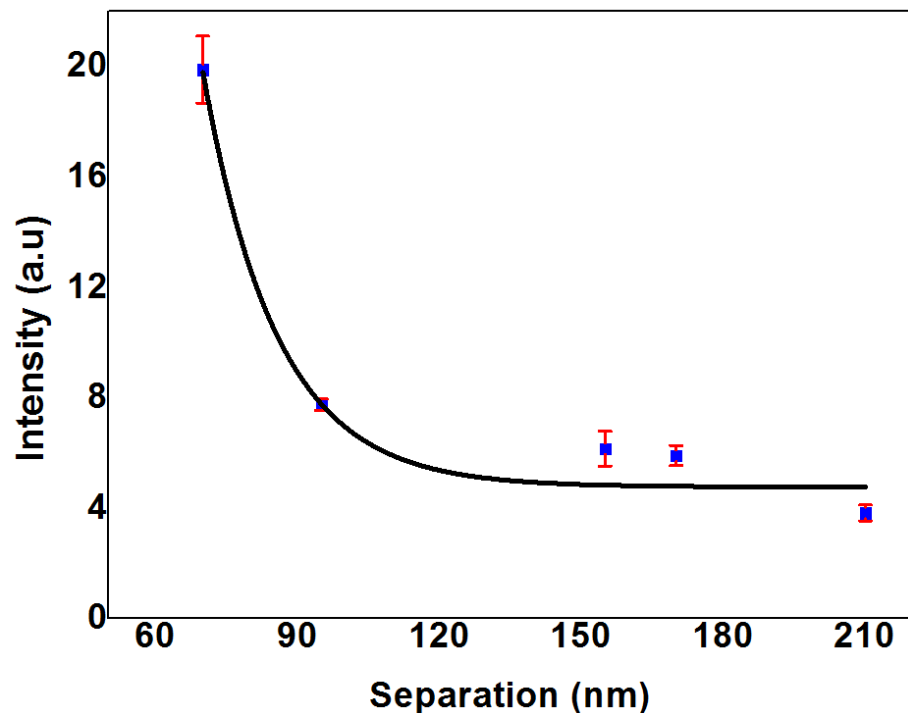


Figure 8.9: the intensity of scattered field gold nanodisk dimers as a function of the separation length. It can be seen that the intensity increases rapidly as the separation between dimer NPs decreases.

Here, we find that, dimeric NPs can scatter the incident light more intensely than a single NP. For example, relative scattering efficiency was measured from a single NP having a length of 170 nm with an aspect ratio of 1.6, and a nanodisk dimer having a length of 165 nm and an aspect ratio of 1.54 separated by 70 nm. It was found that the intensity of scattered field from the dimer was a factor of 2 times larger at $\lambda = 666$ nm and increased to a factor of 5 at $\lambda = 800$ nm in comparison with that of a single NP. It appears therefore, dimer NP configurations produce a greater light-matter interaction and can potentially act as structures in which there is a high local field intensity.

To exploit this effect, we have explored the interaction between the light confined in an L3 nanocavity and a plasmonic dimer. This study is the subject of the following sections.

8.4 Gold nanodisk dimers printed inside L3 nanocavity using EBL.

Dielectric photonic crystal nanocavities can confine light within a small volume. As demonstrated above, metal NPs can confine a surface plasmon close to their surface, but with such structures having a low quality factor. Attempts have been made to combine plasmonic nanostructures with PC nanocavities [29-33]. Such hybrid structures are predicted to enhance the local EM field; however, this is often accompanied by a reduction in the quality factor of the system [32].

In this work a hybrid plasmonic/photonic crystal system is explored. The effect of placing gold nanodisk dimers into a cavity having different NP separations on

the wavelength and intensity of cavity mode is discussed. Our measurements are compared with an FDTD model, with a reasonable agreement demonstrated.

8.5 Experimental methods

A silicon nitride based two dimensional photonic crystal L3 nanocavity was fabricated using EBL, and was defined into a hexagonal lattice having a lattice constant of 260 nm with a hole size of 142 nm. The thickness of the SiN slab was 200 nm. PL measurements of the cavity showed multi resonance peak modes polarized along both the long and short axis.

Gold nano disk dimers were patterned into the cavity having a long axis of 160 nm, an aspect ratio of 1.53 and a height of ~100 nm. The distance between the dimers was varied from 40, 60, 80 to 120 nm. Figure 8.10 shows an SEM image of gold nanodisk dimers printed onto an L3 nanocavity. The fabrication of such structures is explained in chapter 4 section 4.13.

PL measurements were made on representative cavities without gold nanodisk dimers, and cavities that contained the dimers. As a further check, the Au dimers were then removed from the nanocavities using a mixture of concentrated [nitric](#) and [hydrochloric acid](#) in a volume ratio of 1:3, and the cavity emission was re-measured. PL measurements of an L3 nanocavity without any nanodisk dimers indicated that the cavity supported four optical modes; M1 and M4 polarized in the Y direction and modes M2 and M3 polarized in the X-direction as shown in figure 8.11 (a). The experimentally measured cavity emission is compared with FDTD calculations (performed by Dr. David Coles University of Oxford) as shown in figure 8.11 (b).

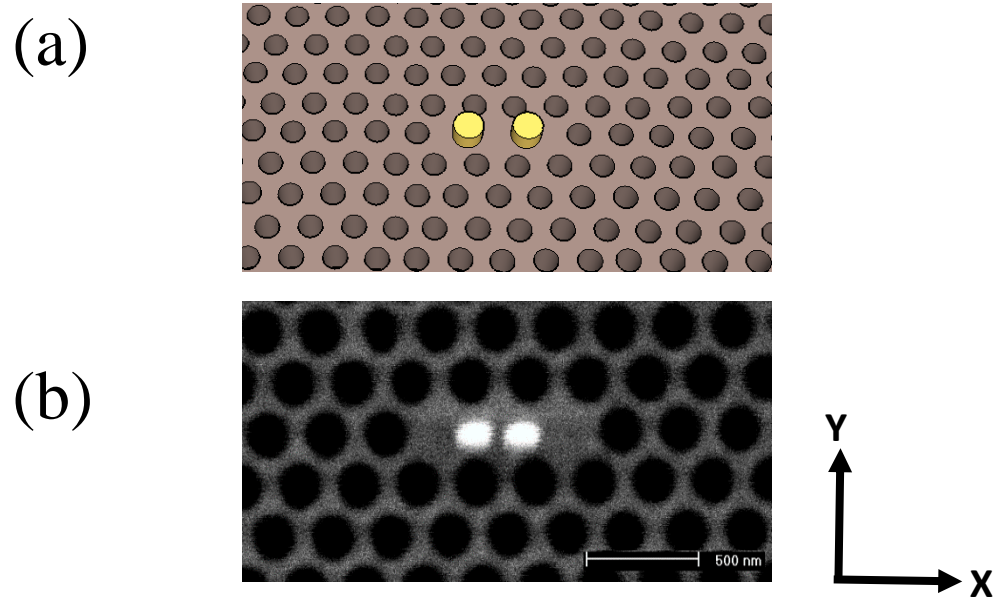


Figure 8.10. (a) Schematic and (b) SEM image of printed gold nanodisk dimer on an L3 nanocavity.

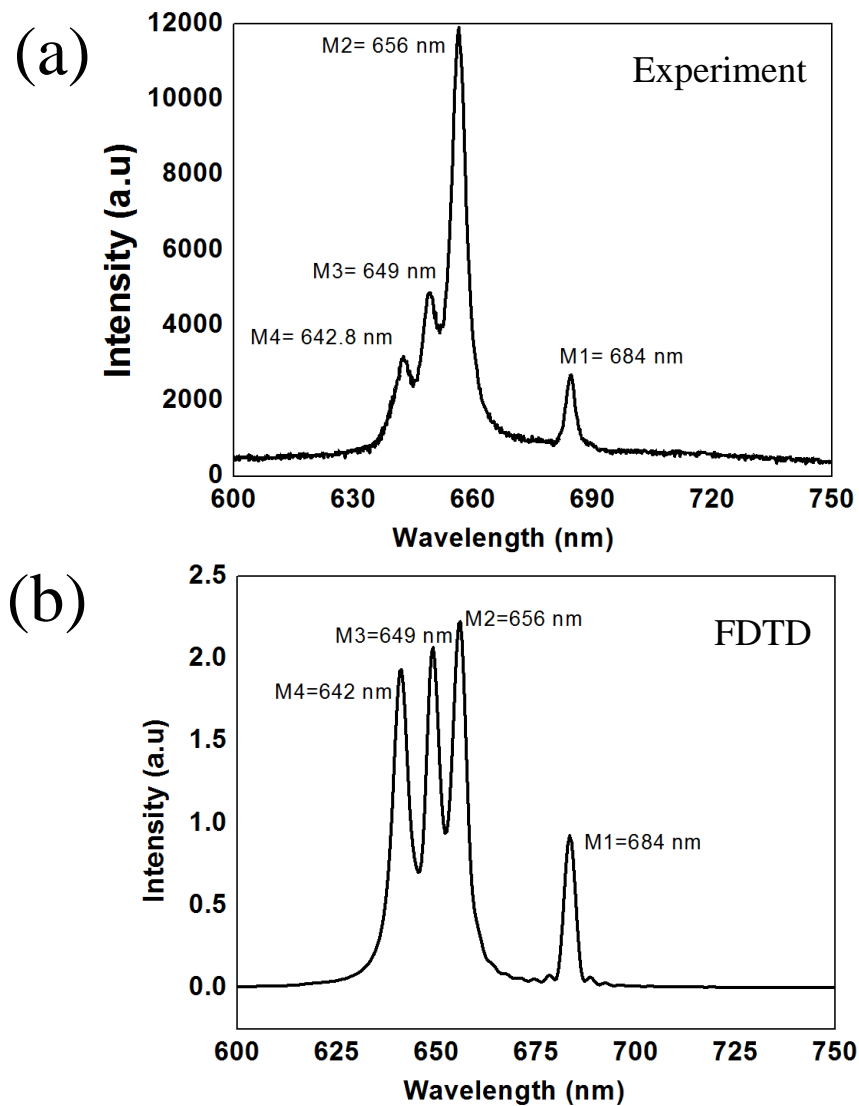


Figure 8.11: (a) Measured and (b) calculated optical mode structure of an L3 nanocavity without Au nanodisk dimers

8.6 Results and Discussions

The effect of the gold nanodisk dimers on the optical modes of the L3 nanocavity was explored by comparing the emission from the cavity either with the dimers or after they had been removed using an acid wash. Both FDTD calculations and experimental measurements are used to probe the optical properties of the cavity as a function of the relative spacing between the particles as shown in figure 8.12 (a) and (b). Here, we plot measured and modelled emission for a cavity with and without the dimers respectively. It can be seen that the model suggests the cavity modes tend to merge as the separation between the dimers increases, as shown in figure 8.12 (a). Note that due to the effects of broadening, mode M3 cannot be observed experimentally. Experimentally measured spectra are confirmed qualitatively by FDTD modelling, which shows that modes M2 to M4 are only poorly resolved and have a high degree of overlap.

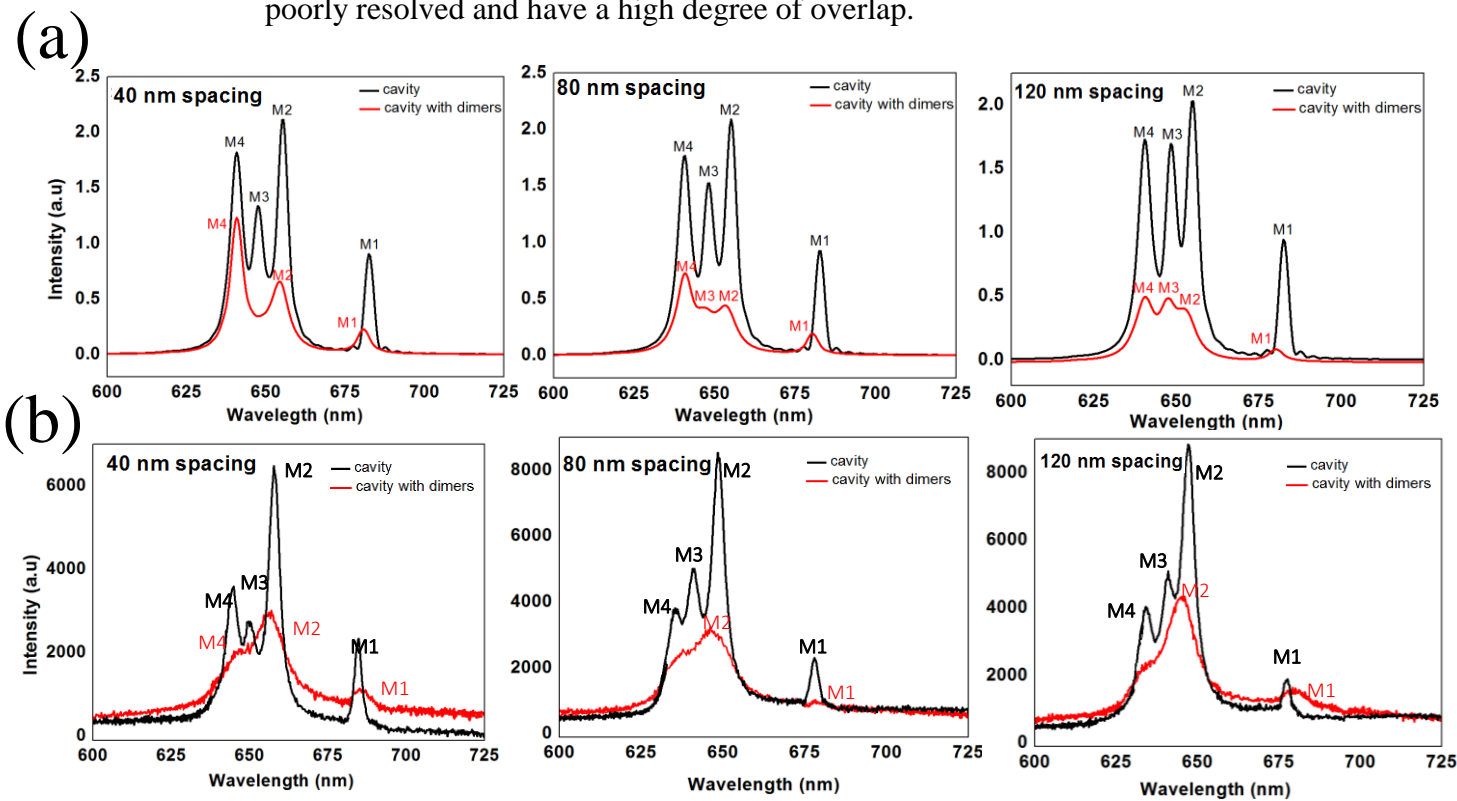


Figure 8.12: (a) FDTD, (b) measured optical mode from L3 nanocavity with and without gold dimers.

To quantify the effect of the gold nanodisk dimers on the cavity modes, we have explored the position of modes M1 and M2 before and after the gold nano disk dimers are fabricated into a cavity. Here, we determine a wavelength shift $\Delta\lambda$, where ($\Delta\lambda = \lambda_{\text{cavity with dimers}} - \lambda_{\text{cavity}}$) with this shift plotted as a function of the separation distance. Experimentally we find that the peak position of the fundamental mode M1 (Y- polarization see figure 8.13 (a)) is slightly red shifted in cavities containing NPs. Note however, this effect is small in comparison to the uncertainty of the experiment, and thus we conclude that this effect is probably not significant. In contrast, mode M2 (X-polarization) makes a progressive blue-shift towards shorter wavelengths as the dimer separation increases as shown in figure 8.13 (b).

We find however that the FDTD model (as shown in figure 8.12 (a) and (b)) indicates that the wavelength of modes M1 and M2 are expected to be slightly blue-shifted in cavities containing the plasmonic dimers compared with ‘empty’ cavities, and that the mode wavelength is not expected to change appreciably with particle separation. Despite some difference between the model and experimental observation the relatively small shifts observed here suggest that the plasmonic dimer is not expected to significantly modify the photon mode structure (energy or spatial extent) within the cavity.

The effect of placing plasmonic dimers inside a nanocavity can be further explored by measuring the change in the line width and thus Q-factor of the cavity modes. The Q-factor of a cavity containing plasmonic particles is known to be affected by the orientation of the particles in the cavity [29], their position with

respect to the EM field maxima within the cavity [33] and their relative separation.

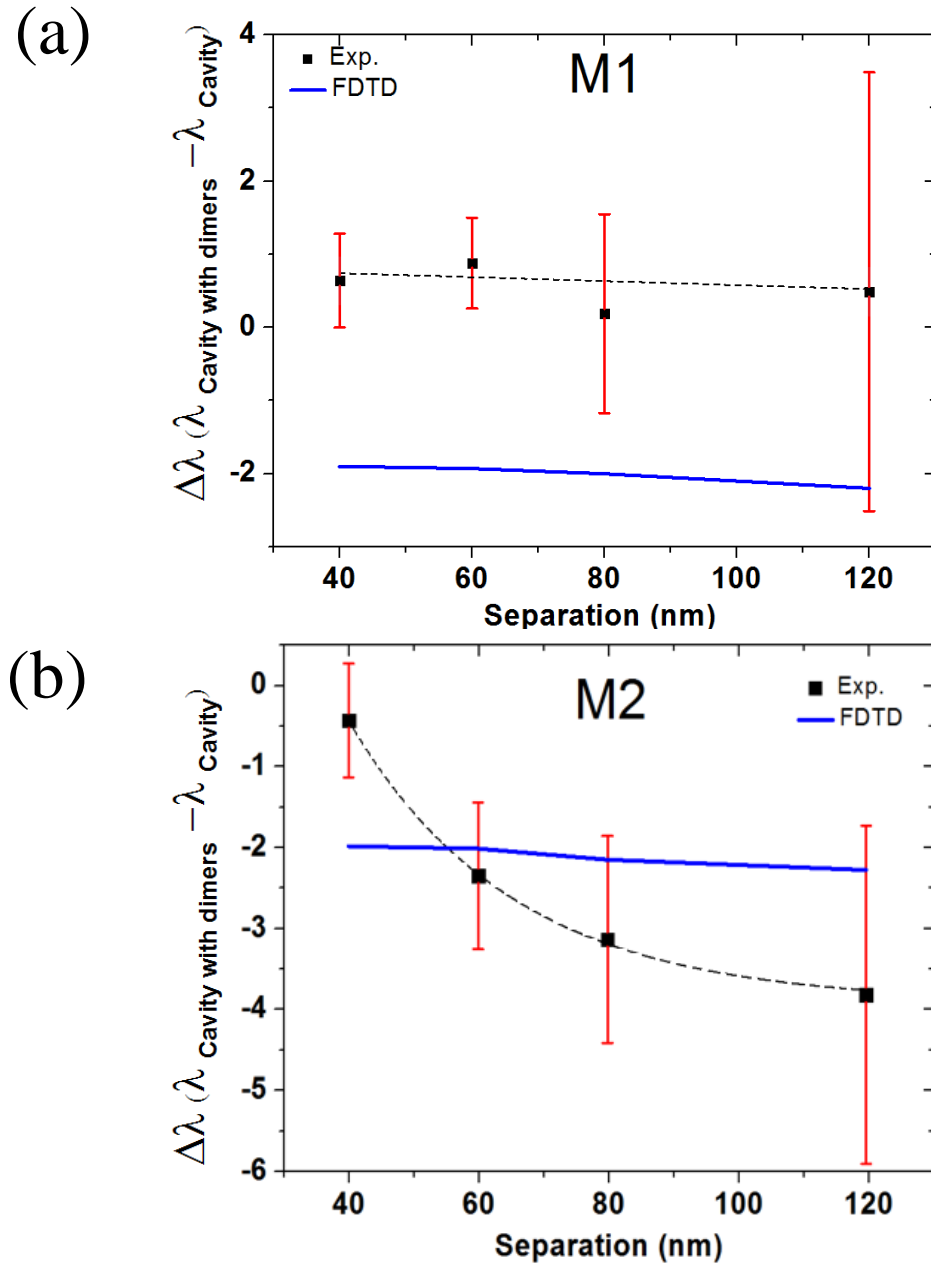


Figure 8.13: The shift in the peak position of modes M1 (part (a)) and M2 (part (b)) on addition of a nanoparticle dimer. Data is plotted as a function of dimer separation.

We can relate the cavity Q-factor to the cavity photon lifetime (τ) using [34]

$$\tau = \frac{Q\lambda}{\pi c}$$

Where λ is the cavity mode wavelength. From this, we can calculate the change in relative photon lifetime in the cavity as a function of dimer separation. We also predict photon lifetime within the cavity using our FDTD model as shown in figure 8.14 (a) and (b). Our model predicts that when the gold nanodisk dimer is orientated parallel to the corresponding cavity polarization, (mode M3 see part (b)), the cavity photon lifetime is reduced as the particle separation is reduced due to increased scattering and absorption by the dimer [33]. In contrast, mode M1 is polarized in a direction orthogonal to the dimer long axis, and thus the cavity photon lifetime is not predicted to undergo a significant reduction at reduced dimer separation, as shown in figure 8.14 (a). This suggests a reduced coupling between mode M1 and the plasmonic resonance [29].

We have also calculated the intensity of the E-field between the dimers (X and Y-polarized mode) with respect to the bare cavity and also dimers printed onto a bare SiN substrate as shown in figure 8.15 (a) and (b). For the X-polarized cavity M3 mode (see part (b)), we find that the EM field between dimers is enhanced significantly at small particle separation and decreases with increasing separation. We find that the field reaches its highest value at a particle separation of 30 nm as shown in figure 8.15 (b). This value is 8 times higher than that between dimers printed onto a bare SiN substrate. The model suggests therefore that orienting a plasmonic nano dimer to the photonic field polarization can create an electromagnetic hot spot between dimers having a relatively small separation. We believe therefore that, a hybrid metallic dimers / PC nanocavity system could

be used as a platform to fabricate optical devices to create a high near-field intensity which could potentially be used to control light-matter interactions at nanometre length scales. In contrast, the intensity of the EM field of the Y-polarization cavity mode (figure 8.15 (a)) between dimers is attenuated at small particle separations and increases by around 3.5 times with increasing separation.

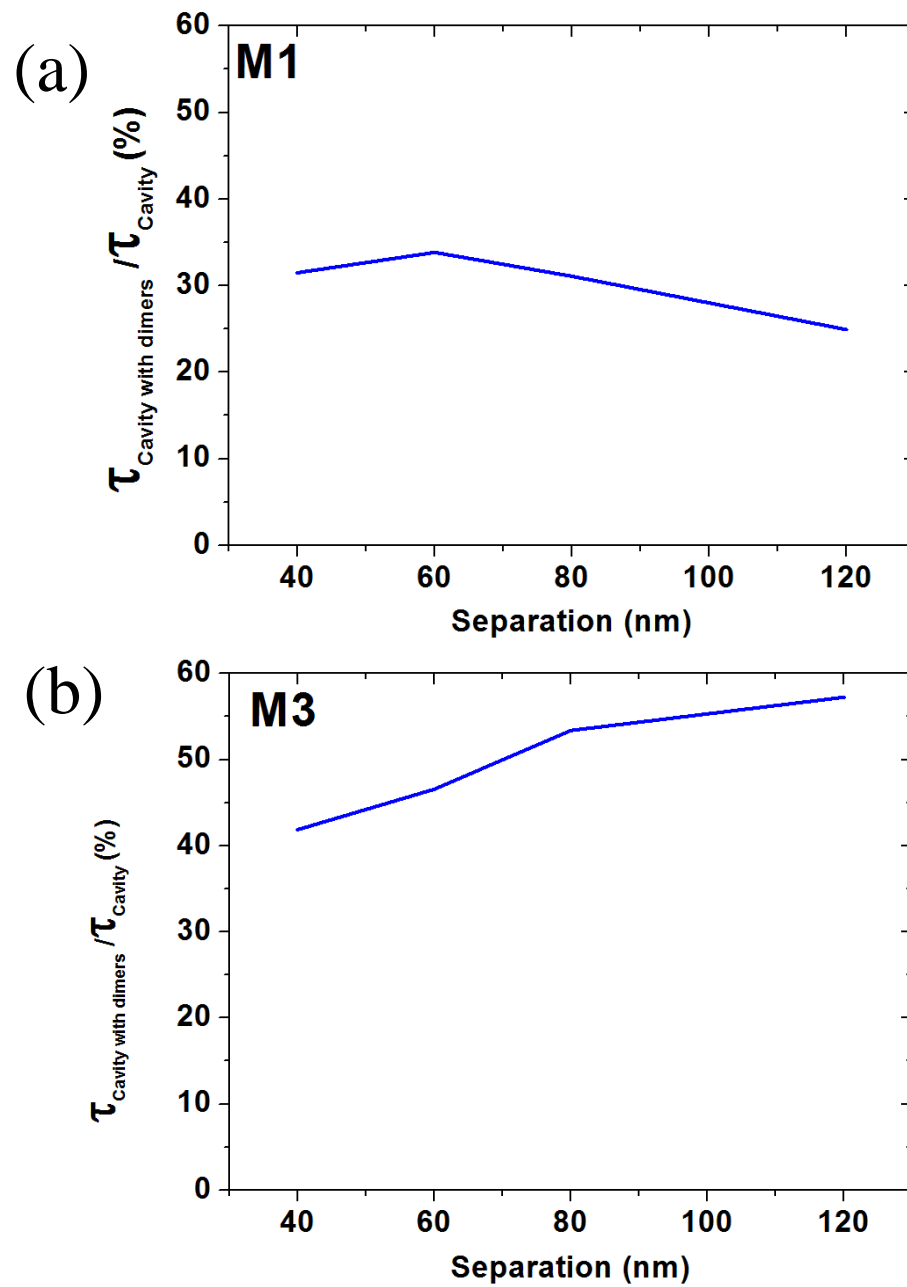


Figure 8.14: the reduction in the cavity mode lifetime with presence of dimers into an L3 nanocavity for (a) Y-polarized mode and (b) X-polarized mode.

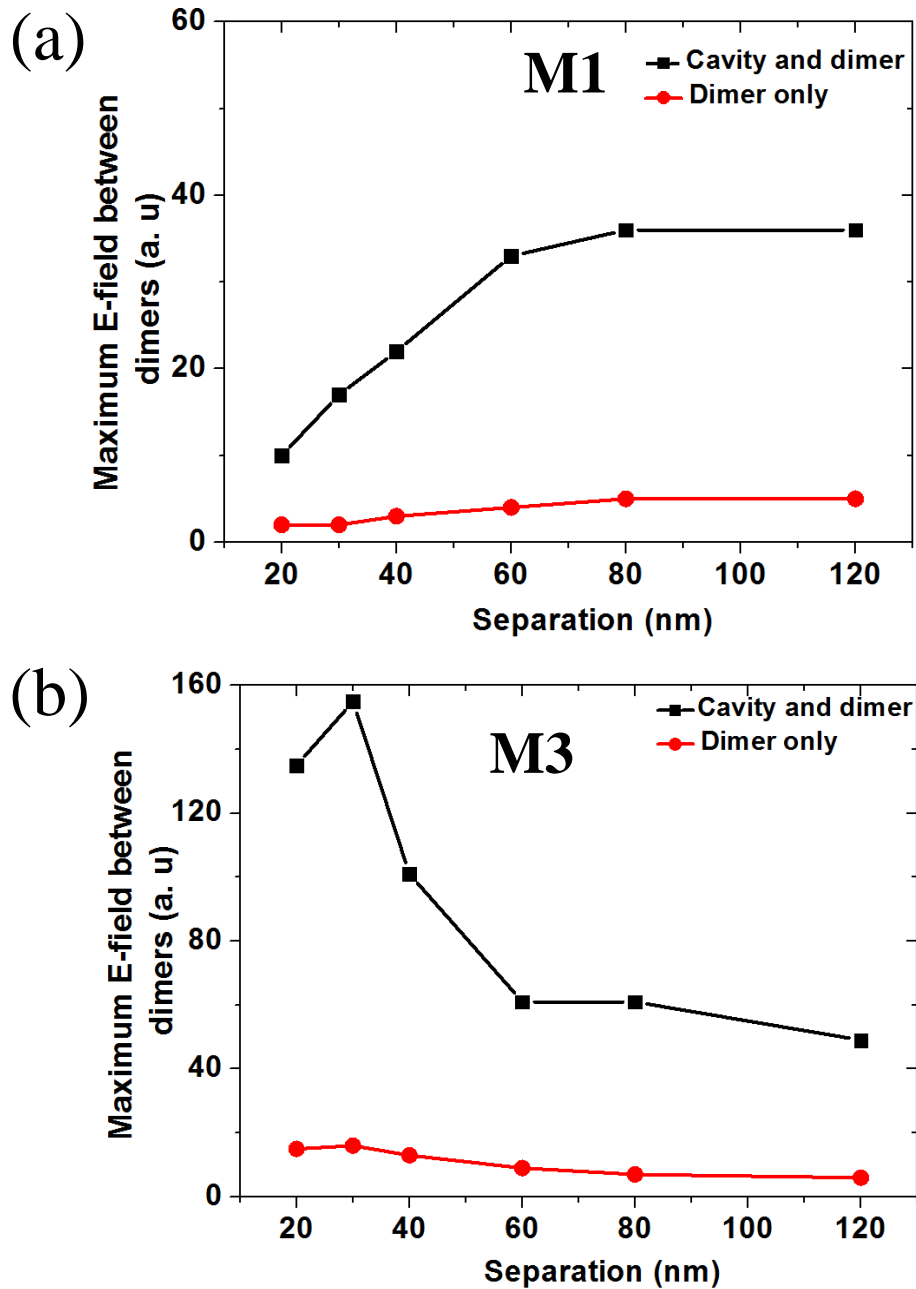


Figure 8.15: A comparison between electric field enhancement of a gold nanodisk dimer inside a L3 nanocavity (black squares) and those positioned on a SiN substrate (red circles) for both X and Y polarizations. (a) In the Y-polarization, the EM field between the dimers undergoes a reduction as the separation between dimers is reduced. (b) In the X-polarization the EM field between dimers (that is matched to the cavity polarization) within a L3 nanocavity is enhanced significantly as the separation between dimers is reduced.

8.7 Conclusions

Electron beam lithography has been used to print single and dimeric gold nanodisks on a bare SiN substrate. It was shown that the scattering plasmon resonance of single gold nanodisk red shifts and its scattering intensity increases with increasing particle size. In contrast, reducing the separation between the gold nanodisk pushes the scattering plasmon resonance to longer wavelengths and increases their scattering intensity.

The optical properties of hybrid plasmonic-photonic crystal L3 nanocavities are explored. Two cavity modes are selected for study; M1 polarized in the Y direction and M2, M3 polarized in the X direction. It is found that the energy and wavelength of the cavity modes are only weakly affected by the separation of the coupled dimers. The peak position and the photon lifetime of mode M1 does not undergo significant changes when nanoparticle dimers are introduced, which suggests reduced coupling between this mode and the plasmon resonance.

In contrast, mode M2 (X-polarization) shifts towards shorter wavelengths as the particle separation increases and the M3 mode photon lifetime is slightly reduced as the particle separation is decreased. This suggests a coupling between the optical mode and the plasmon resonance of the dimer.

FDTD calculations also confirm a coupling between a plasmon resonance and a cavity mode when they are polarized in the same direction. For small separations between the dimers our calculations indicated a significant enhancement of the EM field between the dimers when placed into an L3 nanocavity.

We believe that the structures fabricated here may form the basis of a new types of plasmonic/photonic laser. This would require some high gain material (e.g. an

organic semiconductor) to be incorporated into the cavity. Our concept is based on other work in which plasmonic nanostructures are used to create a high localized EM field within an ultra-small volume and thereby enhance lasing action. For example, studies showed that using an array of Au or Ag metal can improve the lasing action of an active medium by enhancing their rate of spontaneous emission [35, 36]. Unlike an isolated plasmonic NP, high ohmic losses at optical wavelengths can significantly be reduced by using a hybrid plasmonic dielectric waveguide system. Oulton et al [37] showed that a 5 nm gap between a CdS nanowire and an Ag layer can enhance the spontaneous emission rate by up to 6 times resulting a strong mode confinement and threshold-less lasing. In our study we find a field enhancement of up to 8 times between gold nanodisks can be achieved when they are introduced into an L3 nanocavity. Here, we propose that this high field enhancement could be combined with the optical feedback of an L3 cavity to make an efficient low-threshold nano-scale laser.

Reference

1. W. Li, P. H. C. Camargo, X. Lu, and Y. Xia, “Dimers of Silver Nanospheres: Facile Synthesis and Their Use as Hot Spots for Surface-Enhanced Raman Scattering”, *Nano Letters*, **9**, 1, 485-490 (2009).
2. Dong-Kwon Lim, Ki-Seok Jeon, H. M. Kim, Jwa-Min Nam & Y. D. Suh, “Nanogap-engineerable Raman-active nanodumbbells for single-molecule detection”, *Nature Materials*, **9**, 1, 60 – 67(2010).
3. J. N. Anker, W. P. Hall, O. Lyandres, N. C. Shah, J. Zhao and R. P. Van Duyne, “Biosensing with plasmonic nanosensors”, *Nature materials*, **7**, (2008).
4. N. Yamamoto, K. Araya, and F. J. García de Abajo, “Photon emission from silver particles induced by a high-energy electron beam”, *Physical Review B*, **64**, 205419 (2001).
5. S. Link, M. B. Mohamed, M. A. El-Sayed, “Simulation of the Optical Absorption Spectra of Gold Nanorods as a Function of Their Aspect Ratio and the Effect of the Medium Dielectric Constant” *Journal of Physics and Chemistry B*, **103**, 3073 (1999).
6. S. K. Ghosh and T. Pal, “Interparticle Coupling Effect on the Surface Plasmon Resonance of Gold Nanoparticles: From Theory to Applications”, *Chemical Review*, **107**, 11, 4797-4862 (2007).
7. C. J. Orendorff, T.K. Sau, and C. J. Murphy, “Shape-Dependent Plasmon-Resonant Gold Nanoparticles”, *Small*, **2**, 5, 636 – 639 (2006).
8. C. Sonnichsen, A. P. Alivisatos, “Gold Nanorods as Novel Nonbleaching Plasmon-Based Orientation Sensors for Polarized Single-Particle Microscopy”, *Nano Letters*, **5**, 2, 301-304 (2005).

9. G. W. Bryant, F. J. G. de Abajo, J. Aizpurua, “Mapping the Plasmon Resonances of Metallic Nanoantennas”, *Nano Letters*, **8**, 2, 631-636 (2008).
10. J. Aizpurua, G. W. Bryant, L. J. Richter, F. J. G. de Abajo, “Optical properties of coupled metallic nanorods for field-enhanced spectroscopy”, *Physical Review B* **71**, 235420 (2005).
11. M.B. Mohamed V. Volkov, S. Link, M. A. El-Sayed, “The ‘lightning’ gold nanorods: fluorescence enhancement of over a million compared to the gold metal”, *Chemical Physics Letters*, **317**, 517–523 (2000).
12. L. Gunnarsson, T. Rindzevicius, J. Prikulis, B. Kasemo, M. Kall, “Confined Plasmons in Nanofabricated Single Silver Particle Pairs: Experimental observations of Strong interparticle interactions”, *Journal of Physical Chemistry B*, **109**, 3, 1079-1087 (2005).
13. R. A. Puebla, L. M. L. Marzan, F. J. G. de Abajo, “Light Concentration at the Nanometre Scale”, *The Journal of Physical Chemistry Letters*, **1**, 2428–2434 (2010).
14. T. Atay, J. H. Song, A. V. Nurmikko, “Strongly interacting plasmon nanoparticle pairs: From dipole-dipole interaction to conductively coupled regime”, *Nano Letters*, **4**, 9, (2004).
15. E. Irissou, B. L. Drogoff, M. Chaker, D. Guaya, “Correlation between plasma expansion dynamics and gold-thin film structure during pulsed-laser deposition”, *Applied Physics Letters*, **80**, 10, (2002).
16. W. Rechberger, A. Hohenau, A. Leitner, J.R. Krenn, B. Lamprecht, F.R. Aussenegg, “Optical properties of two interacting gold nanoparticles”, *Optics Communications*, **220**, 137–141(2003).

17. K.-H. Su, Q.-H. Wei, X. Zhang, “Interparticle coupling effects on plasmon resonances of nano gold particles”, *Nano Letters*, **3**, 8, 1087-1090(2003).
18. F. J. G. de Abajo, “Nonlocal Effects in the Plasmons of Strongly Interacting Nanoparticles, Dimers, and Waveguides”, *Journal of Physical Chemistry C* **112**, 17983-17987 (2008).
19. H. Fischer, O. J. F. Martin, “Engineering the optical response of plasmonic nanoantennas”, *Optics Express*, **16**, 12, 9144-9154 (2008).
20. J. C. Jasapara, M. J. Andrejco, J. W. Nicholson, A. D. Yablon, Z. Varallyay, “Simultaneous direct amplification and compression of picosecond pulses to 65-kW peak power without pulse break-up in erbium fibre”, *Optics Express*, **15**, 26, 17494-17501 (2007).
21. P. K. Jain, W. Huang, M. A. El-Sayed, “On the Universal Scaling Behavior of the Distance Decay of Plasmon Coupling in Metal Nanoparticle Pairs: A Plasmon Ruler Equation”, *Nano Letters*, **7**, 7, 2080-2088 (2007).
22. N. Verellen, Y. Sonnefraud, H. Sobhani, F. Hao, V. V. Moshchalkov, P. Van Dorpe, P. Nordlander, S. A. Maier, “Fano Resonances in Individual Coherent Plasmonic Nanocavities”, *Nano Letters*, **9**, 7, 1663-1667 (2009).
23. J. Zuloaga, E. Prodan, P. Nordlander, “Quantum Description of the Plasmon Resonances of a Nanoparticle Dimer”, *Nano Letters*, **9**, 2, 887-891 (2009).
24. J. Zuloaga, E. Prodan, P. Nordlander, “Quantum Plasmonics: Optical Properties and Tunability of Metallic Nanorods”, *American Chemical Society, Nano*, **4**, 9, 5269–5276 (2010).
25. P Biagioni, J-S Huang, B Hecht, “Nanoantennas for visible and infrared radiation”, *Reporters on Progress in Physics*, **75**, 024402 (2012).

26. L. Slaughter, W-S Chang, S. Link, “Characterizing Plasmons in Nanoparticles and Their Assemblies with Single Particle Spectroscopy”, the Journal of Physical Chemistry Letters, **2**, 2015-2023 (2011).
27. R. A-Puebla, L. M. L.-Marzan, F. J. G. de Abajo, “Light Concentration at the Nanometer Scale”, the Journal of Physical Chemistry Letters, **1**, 2428-2434 (2010).
28. I. Romero, J. Aizpurua, G. W. Bryant, F. J. G. de Abajo, “Plasmons in nearly touching metallic nanoparticles: singular response in the limit of touching dimers”, Optics Express, **14**, 21, 9988-9999 (2006).
29. M. Barth, S. Schietinger, S. Fischer, J. Becker, N. Nüsse, T. Aichele, B. Löchel, C. Sönnichsen, and O. Benson, “Nanoassembled plasmonic-photonic hybrid cavity for tailored light-matter coupling,” Nano Letters, **10**, 3, 891–895 (2010).
30. F. De Angelis, M. Patrini, G. Das, I. Maksymov, M. Galli, L. Businaro, L. C. Andreani, and E. Di Fabrizio, “A hybrid plasmonic photonic nanodevice for label free detection of a few molecules,” Nano Letters, **8**, 8, 2321–2327 (2008).
31. M. Barth, N. Nüsse, B. Lochel and O. Benson, “Controlled coupling of a single-diamond nanocrystal to a photonic crystal cavity” Optics Letters, **34**, 1108–1110 (2009).
32. I. Mukherjee, G. Hajisalem, and R. Gordon, “One step Integration of metal nanoparticles in photonic crystal nanobeam cavity,” Optics, Express **19**, 23, 22462–22469 (2011).

33. Y. Yi, T. Asano, Y. Tanaka, B-S Song, and S. Noda, “Investigation of electric/magnetic local interaction between Si photonic-crystal nanocavities and Au meta-atoms”, *Optics Letters*, **39**, 19 (2014).
34. Y. Takahashi, H. Hagino, Y. Tanaka, B-SSong, T Asano, and S Noda, “High-Q nanocavity with a 2-ns photon lifetime”, *Optics Express*, **15**, 25, 17207-17213 (2007).
35. F. Van Beijnum, P. J. Van Veldhoven, E. Jan Geluk, M. J. A. de Dood, G. W. 't Hooft, and M. P. van Exter, “Surface plasmon lasing observed in metal hole arrays”, *Physical Review. Letters*, **110**, 206802 (2013).
36. W. Zhou, M. Dridi, J. Y. Suh, C. H. Kim, D. T. Co, M. R. Wasielewski, G. C. Schatz and T. W. Odom, “Lasing action in strongly coupled plasmonic nanocavity arrays” *Nature Nanotechnology*, **8**, 506–511 (2013).
37. R. F. Oulton, V. J. Sorger, T. Zentgraf, R-M Ma, C. Gladden, L. Dai, G. Bartal, X. Zhang, “Plasmon lasers at deep subwavelength scale”, *Nature*, **461**, (2009).

Conclusions and Suggestions for Further Work

9.1 Conclusion

In this thesis, two major topics were addressed. Firstly, the optical properties two-dimensional photonic crystal (2D PC) L3 nanocavities were discussed as well as routes to use such structure a chemical sensor. Secondly the optical properties of plasmonic nanostructures were described with such areas then brought together through the development of hybrid plasmonic-photonic nanocavities.

In Chapter 5, I investigated a number of parameters that affect the photoluminescence (PL) emission from SiN based L3 nanocavities, including the size of PC air holes and the lattice constant. It was found that by reducing the size of the air holes (D) and increasing the lattice constant (a) of 2D PC, the cavity modes can be shifted toward longer wavelengths. Two different approaches were discussed to increase the Q-factor of the nanocavity. The first approach involved shifting the long axis air holes at both ends of the cavity. By shifting the holes away from the cavity, the Q-factor of the cavity reached a value of 260 at 653.8 nm, for a side hole displacement of $0.18a$. The second approach involved modifying the size of air holes around the cavity. The results showed that the Q-factor increased to 890 at mode peak 682.5 nm by shifting first two air holes along the cavity axis by $0.28a$. This permitted a significant improvement in EM field intensity within the cavity to be gained in comparison with an unmodified cavity.

In Chapter 6, I explored the use of a SiN based nanocavity to follow the deposition of a nanometre-thick porphyrin-based polymer (PP1) film onto a cavity surface. This then permitted changes in its thickness resulting from

swelling as it was exposed to an acidic vapour to be detected through a shift in the cavity mode wavelength. It was found that the cavity modes red-shifted in a linear fashion as the layer thickness was increased, with a minimum change in the thickness of the PP1 surface layer of (1.4 ± 0.3) nm detected. In addition, FDTD calculations were used to confirm the experimental results and model changes in thickness and refractive index.

In Chapter 7, an optical printing technique was used to place single 150 nm gold nanoparticle (Au NP) within an L3 nanocavity. Measurements of cavity mode linewidth made before and after NP patterning indicate a clear interaction between the cavity mode and the plasmonic modes of the NP. The experimental results were again confirmed using FDTD calculations, and showed that energy initially stored in the nanocavity is dissipated through excitation of localized surface plasmons. The model also demonstrated that such interactions are sensitive to the exact location of the NP within the cavity, with the interaction being maximized when the NP is placed over a region of high electromagnetic-field amplitude.

In Chapter 8, gold nanodisks was printed onto a SiN membrane and into and L3 nanocavity using electron beam lithography (EBL). The optical properties of printed single and dimer gold nanodisk on bare SiN membrane were investigated both theoretically and experimentally. Results showed that the scattering plasmon resonance peak wavelength is strongly dependent on the particle size and aspect of ratio. While the separation between gold nanodisks dimer effects on the plasmon resonance peak position, in which it red shifted with decreasing the separation between coupled dimer. Finally, dimeric gold nanodisks with varied separation were placed inside an L3 nanocavity. It was

found that the optical properties of the cavity modes influenced by the nanodisks dimer orientation according to cavity polarization as well as the separation between them.

9.2 Future work

In this work, the physics and applications of PC L3 nanocavities have been explored. Further improvement in the ability of such cavities to react to changes in their local environment will be facilitated through the constructing of the structures having increased Q-factors.

Here, I believe that using different designs to modify a PC nanocavity with reduced sidewall (taper angle) of the PC air holes will have a great impact on the cavity Q-factor. By using such high Q-factor cavities together with positioning the intended sensor elements e.g. plasmonic elements, quantum dots controlled nanoparticles using high precision lithographic patterning techniques (e.g. dip-pen lithography) within the cavity will significantly increase the sensor capabilities of such PC L3 nanocavities. Such techniques can also be used to enhance the spontaneous emission rate of a single emitter (for example a single molecule) located at the maximum field of the optical mode within the cavity, with such quantum emitters having applications as an efficient nanoscale light sources.

Noble metal nanoparticles (NM NP) can provide significant enhancements of electromagnetic near fields. The intensity of such fields can be tuned by size, shape, and nanoparticle arrangement. Electron beam lithography is an efficient, flexible tool that enables the size and shape of NPs to be directly defined. A significant EM field enhancement within ultra-small volumes is

expected for a metal NPs printed within an L3 nanocavity when cavity the mode matches the NP peak plasmon resonance wavelength. Therefore, I believe that a hybrid plasmonic-PC device will potentially provide a method to easily create optical systems to study light-matter interactions or create sensor based devices using surface enhancement Raman spectroscopy (SERS).

Publications and presentations

Publications

1. Jaekwon Do, Khalid N. Sediq, Kieran Deasy, David M. Coles, Jessica Rodríguez Fernández, Jochen Feldmann, and David G. Lidzey, “Photonic-Crystal Nanocavities Containing Plasmonic-Nanoparticles Assembled Using a Laser-Printing Technique”, *Advanced Optical Materials*, **1**, 12, 946-951 (2013).
2. Kieran Deasy, Khalid N. Sediq, Stuart Brittle, Tao Wang, Frank Davis, Tim H. Richardson and David G. Lidzey, “A chemical sensor based on a photonic-crystal L3 nanocavity defined in a silicon-nitride membrane”, *Journal of Materials Chemistry C*, **2**, 8700–8706 (2014).
3. Khalid N. Sediq, D. Coles, and D.G. Lidzey, “ Fabrication of plasmonic nanostructures into nano-optical cavities using electron-beam lithography”, (Manuscript in preparation)

Presentations

1. Soft Matter group meeting, held at Millennium Galleries in Sheffield, September 2012, poster presentation.
2. UK Semiconductors and UK Nitride Consortium Summer Meeting, Sheffield Hallam University (9-10) July 2014, Oral presentation.